DYNAMICS OF SWIRLING JETS AND FLAMES

A Dissertation
Presented to
The Academic Faculty

By

Christopher M. Douglas

In Partial Fulfillment
of the Requirements for the Degree
Doctor of Philosophy in the
College of Engineering
George W. Woodruff School of Mechanical Engineering

Georgia Institute of Technology

May 2021

DYNAMICS OF SWIRLING JETS AND FLAMES

Thesis committee:

Dr. Timothy C. Lieuwen, chair
Aerospace Engineering
Georgia Institute of Technology

Dr. Benjamin L. Emerson
Aerospace Engineering
Georgia Institute of Technology

Dr. Cyrus K. Aidun
Mechanical Engineering
Georgia Institute of Technology

Dr. Santosh Hemchandra
Aerospace Engineering
Indian Institute of Science

Dr. Devesh Ranjan
Mechanical Engineering
Georgia Institute of Technology

Date approved: March 18, 2021

This thesis is dedicated to my mother, Julie Douglas,

who homeschooled my sisters and I until college.

ACKNOWLEDGMENTS

It is impossible not to acknowledge the many individuals who supported me in my doctoral studies.

Beginning in the academic world, I would first like to thank my undergraduate research advisor, Dr. Shannon Timpe from my years at Bradley University. It was Dr. Timpe who first suggested the idea of a PhD to me, and I am immensely grateful for the many hours of personal attention and professional mentorship he bestowed upon me during my time in his research group. Whether it be in regards to blues music (which of course must be played on vinyl) or experimental data analysis, Dr. Timpe has had a tremendous impact on my artistic judgments.

Next, I must thank Dr. Marty Morris, another Bradley University professor who also had a tremendous impact on me by introducing me to the study of fluid dynamics. I spent many long afternoons in Dr. Morris' office receiving so much advice regarding research, graduate school decisions, and even German beers. In particular, it was Dr. Morris who encouraged me to take additional graduate classes in mathematics during my undergraduate studies which proved to be an extremely wise investment.

Moving on to Georgia Tech, Dr. Tim Lieuwen has been role model and mentor for me since I first interviewed to join his research group. Dr. Lieuwen is a man I deeply admire both personally and professionally, and I have always benefited from his physical intuition and analytical chops. He has compared the scientific process to 'navigating through a dark forest', but, as anyone who has gone 'bushwhacking' with Tim will know, he greatly enjoys that activity both figuratively and literally. While completing any PhD necessitates some struggles, I have always been able to count on Tim's guidance to pull me through the lows and carry me into the highs. I am filled with gratitude for the opportunity to have been his student, and for the many conference trips and 'mini-sabbaticals' with Cambridge and IISc that he has generously sponsored.

Speaking of Cambridge and IISc, a very special thank you goes to Dr. Matthew Juniper and Dr. Santosh Hemchandra for briefly adopting me into their research groups during my visits to those institutions. Though my time with them both was short, I absorbed an immense amount of knowledge from their tutelage and I still treasure those experiences. A further thanks goes to Dr. Hemchandra for serving on my committee.

Dr. Ben Emerson, who is also on my thesis committee, has also been a huge influence on me. Dr. Emerson really took me under his wing in my early days in Tim's group, spending a huge amount of time educating me about hydrodynamic stability and many other subjects. He has also served as my chief accomplice at conferences and offered me important candid advice which has helped to shape my professional trajectory.

I am also thankful for the wisdom I've received from Dr. Vishal Acharya. Dr. Acharya has a vast knowledge of mathematics and high-performance computing and has been a tremendously important resource for me while I was developing the computational frameworks presented within this thesis. Even after the codes were written however, he continued to help me by graciously sharing computing time and resources with me, even at the cost of his own time.

I would also like to thank Dr. Cyrus Aidun and Dr. Devesh Ranjan for agreeing to serve on my thesis committee. Their helpful suggestions and careful inspection of my work has been of great benefit to both my thesis and my development.

Beyond my academic mentors, I cannot begin by acknowledging anyone else but my girlfriend, Kalina Paunovska. Kalina is a role model to me and her constant encouragement and love for me have contributed to this work just as much as the academic guidance granted by my mentors. Another loving thank you goes to my parents, Mark and Julie, and my sisters, Katie and Sarah. They all have been immensely supportive of me throughout this journey, and I am extremely grateful to have each of them in my life. Further loving thanks also goes to Kalina's parents, Nik and Natasa, who have essentially become a second set of parents to me. I love and thank you all.

My PhD would also not have been possible without the support of my community, peers, and friends. My fellow graduate students, friends, and teammates from the combustion lab, Tech, and beyond have all played an instrumental role to my mental health and happiness. Furthermore, many of my colleagues, such as Travis Smith, Vedanth Nair, Hanna Ek, Debolina Dasgupta, Nick Magina, Luke Humphrey, Jamie Lim, Kiran Manoharan, Jacob Sebastian, Chris Foley, Ianko Chterev, and surely others I've failed to mention have each provided helpful insights which advanced my work. I am so grateful to have had such wonderful people surrounding me over these years.

Finally, I would like to acknowledge the support from the Georgia Tech President's Fellowship and the Tau Beta Pi Anderson Fellowship. Computational resources which supported my work are also acknowledged from XSEDE through the National Science Foundation's Graduate Research Fellowship Program and from the National Center for Atmospheric Research through Cheyenne (doi:10.5065/D6RX99HX) under project number UGIT0028.

TABLE OF CONTENTS

LIST OF TABLES

LIST OF FIGURES

LIST OF ACRONYMS

CMOS Complementary Metal Oxide Semiconductor

DNS Direct Numerical Simulation

ECS Exact Coherent Structures

GMRES Generalized Minimal Residual

IP In Phase

LES Large Eddy Simulation

MOPA Master Oscillator Power Amplifier

OP Out of Phase

PIV Particle Image Velocimetry

PLIF Planar Laser-Induced Fluorescence

PSD Power Spectral Density

PVF Progress Variable Field

RANS Reynolds-Averaged Navier Stokes

TKE Turbulent Kinetic Energy

WKBJ Wentzel-Kramers-Brillouin-Jeffreys

SUMMARY

Even the simplest swirling jet flows possess an astonishing degree of complexity. This complexity is a two-edged sword, presenting both a unique opportunity to advance the science of fluid mechanics as well as a major barrier for a variety of engineering applications. In particular, swirling jet technologies have proven crucial for enabling the increased efficiencies and drastically-reduced emissions seen in modern combustion systems. However, the enhanced mixing and flame stability characteristics offered by swirling flow configurations are constrained by a relatively limited understanding of their dynamics, which continues to press the power and propulsion industry against the limits of reliable performance.

This research is comprised of two major, complimentary thrusts centered on the dynamics of swirling jets and flames. The first focuses on rigorously characterizing the behavior of laminar swirling jets and flames from a dynamical systems perspective using bifurcation analysis. These results offer several new insights into the physics of swirling jets, such as demonstrating bistability between competing low pressure regions and characterizing the bifurcation and nonlinear evolution of a variety of coherent limit-cycle structures from an initially steady state. The effect of combustion on these processes is also considered.

The second portion of the work addresses the more practical need for reliable low-order models of turbulent swirling jets and flames. A linear hydrodynamic-acoustic response framework is developed in order to predict the coherent response of a swirling reacting jet to external acoustics. This model is validated against measurements from acoustically-forced experiments, showing that many important aspects of the forced response can be characterized on the basis of very affordable computations. Using experimental data, the work also analyzes the relationship between large-scale coherent vortical structures and incoherent turbulent fluctuations, with a focus on assessing the ability of turbulence models to capture these interactions.

CHAPTER 1
INTRODUCTION

1.1 Motivation

This thesis describes an investigation into the hydrodynamics of swirling jets and flames via numerical methods and experimental analysis. Swirling jets host a suite of rich physics due to the complex interplay among axial and azimuthal shear layers, centrifugal instabilities, and propagating inertial waves. Though scientifically interesting in their own right, these flows are of crucial importance to the engineering of various modern technologies including gas turbine combustors, cyclonic separators, and aeronautical lift and control surfaces. Swirling jets are also a core feature of numerous natural flows including tornadoes, cyclones, and quasars. At a more fundamental level, even turbulent eddies in general are affected by many of the same phenomena as swirling jets, such as vortex breakdown.

Of these many applications, the main motivation for this work is derived from the power and propulsion sector. There, the enhanced mixing and flame stability characteristics offered by swirling jet burner configurations has directly contributed to the increased thermal efficiencies and drastically-reduced emissions seen in modern lean premixed combustion systems [1, 2]. However, an incomplete physical understanding of swirling flows continues to press the industry against the limits of reliable performance [3]. Increasingly lean burn conditions and complex nozzle arrangements, while necessary to meet ever more stringent emissions requirements, have resulted in a reliability tradeoff, leading to systems that are highly susceptible to adverse transient events such as thermoacoustic oscillations, flashback, and blowout. Such combustion instabilities can have significant negative impacts on system emissions, performance, and even structural integrity. For context about the scale of this problem, in ground-based gas turbines, up to 70% of non-fuel operating costs can

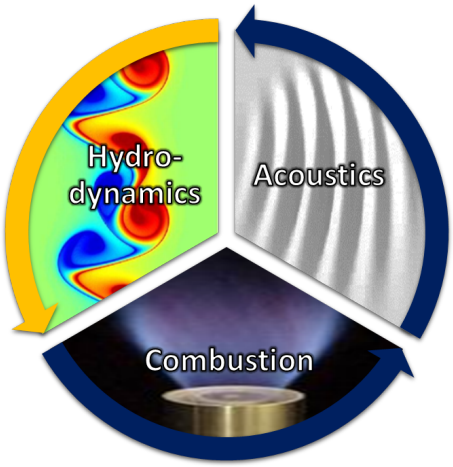

Figure 1.1: Schematic of the thermoacoustic combustion instability feedback loop. This thesis focuses on the hydrodynamic aspect of this process in swirling jet flows and flames.

be attributed to repairs and replacements associated with combustion instabilities [2].

Combustion instabilities encompass a diverse family of dynamic processes consisting of many possible driving mechanisms. Of these, the thermoacoustic coupling between hydrodynamic instabilities and unsteady heat release oscillations is one of the most widespread and yet also the most poorly understood [4]. In this process, shown schematically in Figure 1.1, acoustic disturbances excite fluid mechanic instabilities which manifest organized, large-scale vortical structures. These structures then disturb and interact with the flame, leading to heat release oscillations which can generate new acoustic disturbances and form a closed feedback loop. Previous PhD thesis projects by O'Connor and Smith [5, 6] have been devoted to understanding the thermoacoustic portion of such self-sustained cycles in lean premixed swirling flames. However, the natural hydrodynamic processes which link the acoustic and flame disturbances in swirling jets remain relatively poorly understood. This void serves as the primary motivation for the work in this thesis.

1.2 Literature review

1.2.1 Physics of laminar swirling jets

Non-reacting setting

One of the most salient hydrodynamic features of swirling flows is the phenomenon of vortex breakdown. Vortex breakdown occurs when the axial flow along or near the vortex axis abruptly stagnates beyond a certain level of swirl. In most swirling flow configurations, this phenomenon is associated with exchanges of stability and multistability among various axisymmetric and spiral states [7, 8]. A classic early example is Lambourne & Bryer's [9] famous photograph, shown in Figure 1.2, of the flow over a delta wing exhibiting simultaneous 'spiral' and 'bubble' breakdown patterns. Throughout the literature of swirling flows, significant effort has been exerted to categorize the observed forms of vortex breakdown into relatively few canonical types, and to relate these different classifications by the physical mechanisms underpinning their behaviors.

In the inviscid limit, columnar swirling flows (*i.e.* axisymmetric rotating flows with bulk axial motion and zero radial velocity) are subject to at least three independent instability mechanisms that interact to control the overall stability behavior. First is centrifugal instability which occurs due to a local imbalance between the centrifugal force and the radial pressure gradient. This mechanism is related to the Rayleigh criterion which states that purely rotational flows are only linearly stable to axisymmetric perturbations if the angular momentum increases monotonically outward [10, 11]. Centrifugal instability is well-known to affect swirling jets, where it interacts with axial and azimuthal shear and inertial wave propagation [12]. In the linear limit, asymptotic analyses have shown that this mechanism tends to most strongly amplify helical modes with wavenumber vectors that are oriented along the direction of zero strain of the base flow [13, 14].

Next, the Kelvin-Helmholtz instability arises due to velocity shear. For columnar flows without swirl, only axial shear is present, and the shear mechanism is related to Rayleigh's

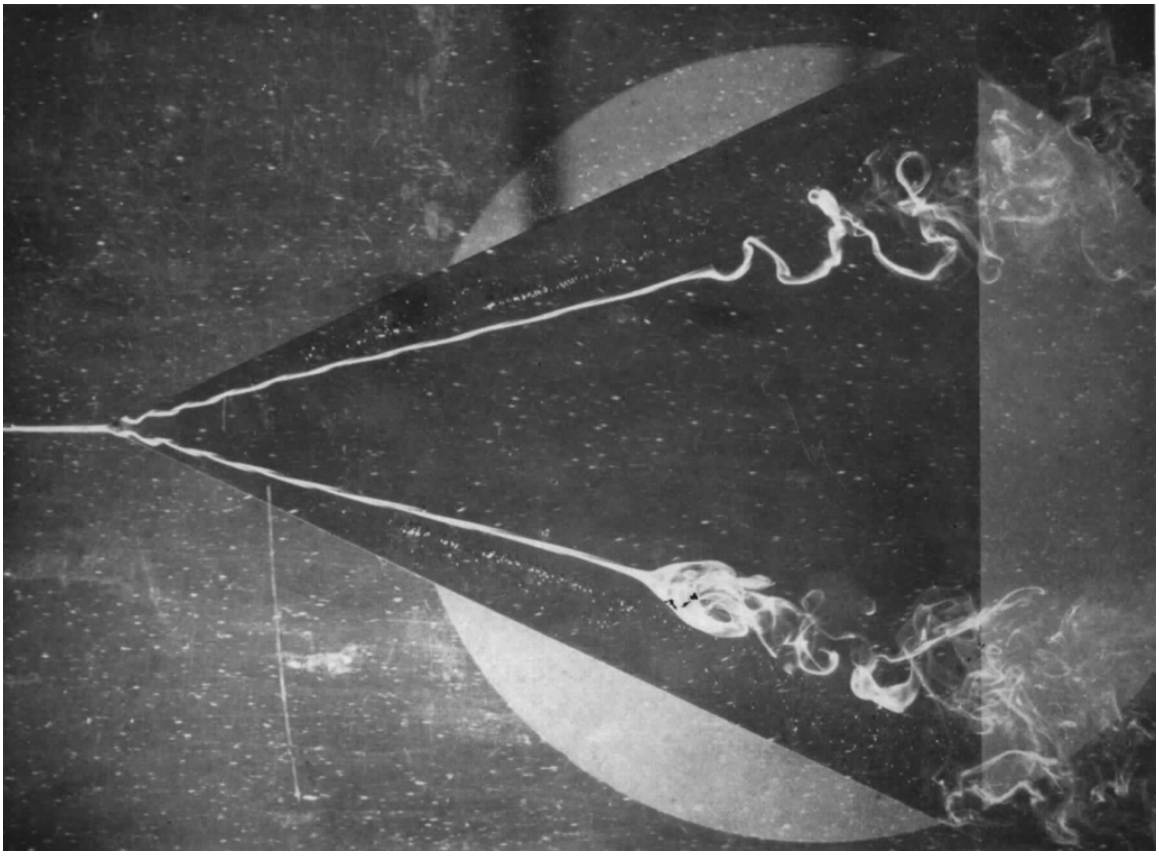

Figure 1.2: Photograph showing different manifestations of vortex breakdown in the flow over a delta wing in a water tunnel. Reproduced from Lambourne & Bryer [9].

well-known inflection point theorem [15, 16]. An analogous theorem also holds for vortices without axial flow where only azimuthal shear is present [15]. More generally, however, columnar flows with swirl experience shear with both axial and azimuthal components. Under the so-called 'tilting shear' approximation [17], which neglects curvature effects, it has been shown that the shear mechanism in swirling flows tends to selectively amplify helical disturbances where the wavenumber vector is aligned with the direction of maximal strain of the base flow [18, 17]. More generally, curvature effects allow the two shear components to interact with centrifugal and Coriolis effects.

Finally, inertial waves influence the stability of swirling jets. In the specific case of a streamwise-invariant flow with uniform axial velocity and solid body rotation, the shear and centrifugal instability mechanisms are inactive, and the Coriolis force gives rise to pure

traveling Kelvin waves [19]. The propagation of these waves may be super- or sub-critical[1] with respect to the axial flow depending on the level of swirl, but they are all neutrally-stable under the assumption of axial inhomogeneity [20, 21]. However, if the streamwise invariance is broken, for example by certain streamwise boundary conditions, subcritical inertial waves can interact with the asymmetry, leading to both axisymmetric and spiraling instabilities [22, 23]. This basic mechanism is closely related to the nonlinear phenomenon of vortex breakdown, though the overall vortex breakdown process is more delicate in flow situations where the shear and centrifugal mechanisms are also active.

This thesis is directed towards swirling jets in less idealized situations, where viscosity and geometry, in addition to generating their own new physics, prohibit any clean separation of the basic mechanisms discussed above. The first efforts to understand such flows appeared in the 1960's and were primarily motivated by engineering applications in swirl-stabilized combustion. Early studies of swirling jets [24] focused heavily on developing empirical correlations for the macroscopic flow characteristics based on measured turbulence statistics. Though controlled fundamental experiments were commonplace at the time in confined swirling flows such as vortex tubes [25, 26] and rotating cylinders [27], it was not until over two decades later that studies began to investigate the physical processes underlying these statistics in unconfined swirling jets. For example, influential work by Farokhi et al. [28] highlighted the effect of swirl and forcing *distribution* (and not just magnitude) on the flow characteristics. Other authors such as Panda & McLaughlin [29] and Martin & Meiburg [30] expanded on these ideas, advancing a dynamical systems perspective toward the behavior of swirling jets which emphasized the role of coherent vortical structures and instabilities over turbulence statistics.

Within this paradigm, the LadHyX group performed a series of experiments examining the dynamics of transitional water jets discharging from a rotating pipe into a large tank. Beginning with the study by Billant et al. [31], they systematically explored the vortex

[1] These terms refer only to the propagation speeds of inertial waves relative to the bulk flow speed and are unrelated to the bifurcation classifications from dynamical systems with the same names.

breakdown process at various Reynolds numbers as a function of the swirl ratio. A key contribution of that research was the description of the "conical" form of vortex breakdown and the bistable relationship between it and the more well-known "bubble" form over a certain range of swirl and Reynolds numbers. Time-domain simulations have corroborated this interpretation of the cone and bubble as bistable breakdown states in swirling jets [32, 33], but the relationship between these states has not yet been clearly shown.

Another feature of the LadHyX experiments was the use of planar flow visualization techniques along multiple measurement planes. These methods were used by Billant et al. [31] to provide a clearer perspective of the jet's three-dimensional dynamics compared to earlier line-of-sight observations. In particular, their visualizations detailed a spiral flow structure of azimuthal periodicity $|m| = 2$, shown in Figure 1.3, which rotated in time in the same direction as the imposed rotation. This instability appeared at swirl ratios well below those associated with the formation of any central stagnation point and diminished at higher levels of swirl as either conical or bubble-type breakdown emerged. In certain conditions after breakdown, the flow was dominated by asymmetric, $|m| = 1$, spiral structures. Note that throughout the range of swirl ratios examined by Billant et al. [31], unsteady "Kelvin-Helmholtz-like billows" were also present, though these structures were not a major focus of that study.

In a later study using the same experimental apparatus, Loiseleux & Chomaz [34] focused more specifically on the system's behavior before vortex breakdown. They described three distinct pre-breakdown regimes where a variety of unsteady axisymmetric and spiral structures exchange dominance with varying swirl. In the non-swirling case, the shear layer rolled up into nominally axisymmetric ring structures due to the Kelvin-Helmholtz instability. In the first regime, at low swirl numbers, co-rotating spiral structures began to be favored over the primary vortex rings, though both were present, presumably due to secondary instability. The azimuthal periodicity of the dominant asymmetric structures gradually decreased with increasing swirl until reaching a transitional stage where axisym-

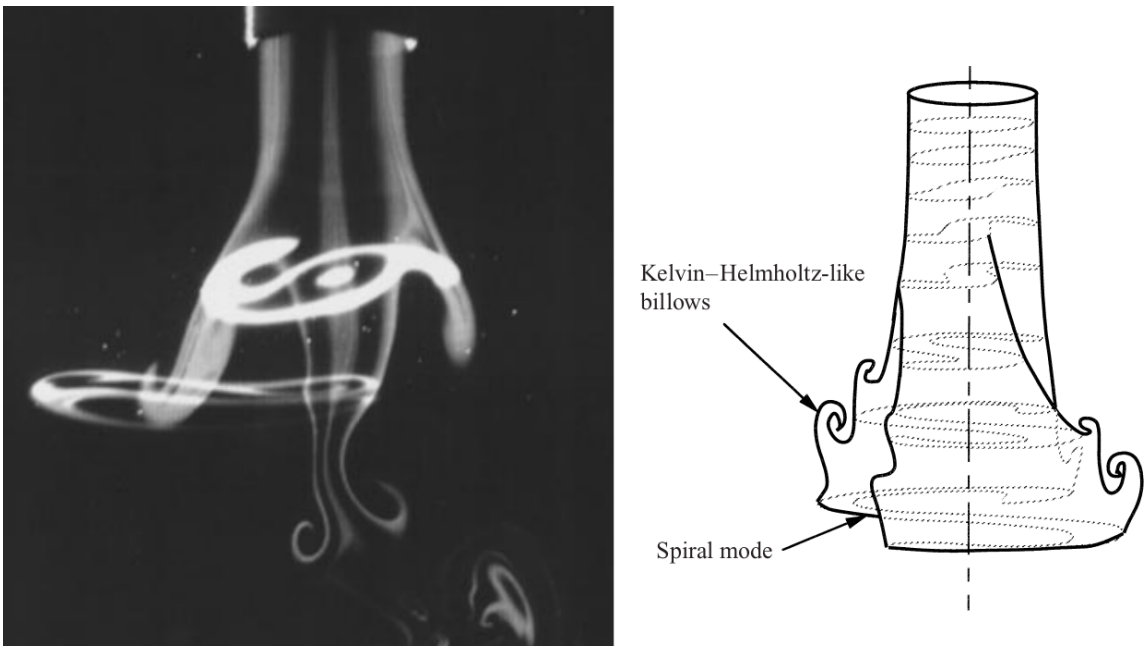

Figure 1.3: Fluorescent dye visualization of the spiral $|m| = 2$ instability via laser sheets in the meridional plane and in a slanted plane from the horizontal (left) and corresponding schematic (right). Reproduced from Billant et al. [31].

metric ring structures again dominated. In the second regime, the co-rotating $|m| = 2$ spiral instability reported by Billant et al. [31] strongly dominated the flow dynamics, eliminating any distinction between primary versus secondary instability. Finally, in the third regime immediately preceding vortex breakdown, a distinct counter-rotating motion with $|m| = 1$ periodicity appeared in addition to other intermittent axisymmetric and three-dimensional structures of similar amplitude.

Similar experimental descriptions of deterministic flow structures in swirling jets have also been detailed by Liang & Maxworthy [35, 36]. Their observations agree qualitatively with the earlier studies by the LadHyX group, while providing more quantitative insight into the dynamics thanks to improved velocimetry techniques. In particular, spectral analysis suggested that the axisymmetric oscillations emphasized by Gallaire & Chomaz [37] are primarily excited by external noise, suggesting a passive amplifier role for the $m = 0$ pulsations associated with convective instability. In contrast, they argued that the pre-breakdown $|m| = 2$ and post-breakdown $|m| = 1$ instabilities also reported by Billant et al. [31] repre-

sent self-excited flow oscillations that are present independent of external noise. This point is further supported by the lack of receptivity of this swirling jet to $|m| = 2$ forcing, as observed in the experiments of Gallaire et al. [38]. Based on their observations, Liang & Maxworthy [35] further characterized the bifurcations underlying the self-excited instabilities by fitting their measured oscillation amplitude-swirl ratio relationship to an unforced supercritical Landau equation model. Despite a relatively high level of background noise, they found evidence that both instabilities are associated with supercritical Hopf bifurcations and determined approximate critical swirl values for each.

Ruith et al [39] performed a comprehensive numerical investigation of unconfined swirling flow using the vortex model from Grabowski & Berger [40]. Based on both axisymmetric and three-dimensional unsteady simulations, Ruith et al. [39] systematically surveyed the parameter space and noted the emergence of steady, axisymmetric vortex breakdown and its eventual instability toward spiraling vortical structures associated with either $|m| = 2$ or $|m| = 1$. Thanks to their detailed study, the Grabowski-Berger vortex has become a standard flow for analysis of swirling flow dynamics [41, 42, 43, 44]. However, it is important to note that this vortex model does not capture all aspects of the flows found in a broad class of physically-interesting swirling jet applications. For instance, the Grabowski-Berger vortex is defined by a fixed parallel inflow condition which exhibits substantial axial co-flow over the entire radial extent of the domain. Swirling jets, in contrast, are typically surrounded by nominally quiescent surroundings. As a result of key differences like this, the relationship between the dynamics of the Grabowski-Berger vortex model and those of many swirling jets realized in the laboratory or in practical hardware is unclear.

Recently, Moise & Mathew [45] performed nonlinear simulations of a different fixed vortex model which is more representative of this broader class of swirling jets. They documented a variety of characteristic flow states and, as expanded upon in a subsequent paper [33], described hysteresis with respect to swirl among these states. However, their choice of Cartesian coordinates and periodic lateral boundary conditions were observed

to introduce certain spurious dynamics, and the specific interpretation of their results in relation to earlier experimental observations is not fully apparent.

Reacting setting

The presence of combustion convolutes the physics of swirling jets significantly compared to the non-reacting case. Unsteady structures such as those discussed above also appear in reacting jets and can profoundly affect the combustion process in a number of ways such as by initiating flame wrinkles and responding to thermoacoustic feedback. The flame itself plays an active role in these dynamics, explicitly modifying the flow field through gas expansion. This leads to baroclinic, buoyant, and dilatation effects which constitute additional physical mechanisms that complement and interact with the centrifugal, shear, and Coriolis mechanisms discussed previously. However, unlike the mechanisms present in the nonreacting case, the baroclinic and dilatation mechanisms cannot be isolated and studied independently in a columnar flow. Buoyancy effects, which are separable in the same manner as the prior mechanisms, will be not be considered in this thesis, as they are typically unimportant in industrial-scale combustion systems.

The exclusion of buoyancy, which may seem a limiting restriction, is actually an important step in exposing the other hydrodynamic behaviors of swirling jets. For example, Gotoda et al. [46] avoided buoyancy effects by performing an experimental investigation of rich ($\phi = 1.43$) swirling methane-air flames in a rotating Bunsen burner apparatus in microgravity. As shown in Figure 1.4, these authors observed that the flame exhibited a stable 'conical' shape at low swirl and a stable 'plateau' shape at high swirl separated by an intermediate interval of swirl where the flame was unstable and irregularly shaped. While their instrumentation did not permit precise descriptions of these unsteady features, their work does emphasize the role of hydrodynamic instability on the flame's unstable behavior. Furthermore, the appearance of the 'plateau' flame suggests the presence of a steady vortex breakdown feature in the flow field just downstream of the flame.

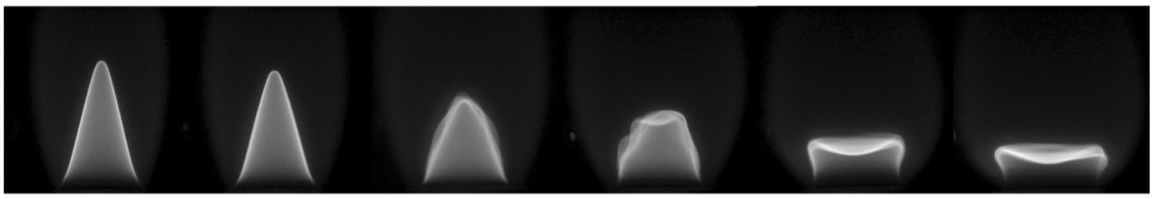

Figure 1.4: Photographs illustrating the structure of laminar swirling Bunsen flames in microgravity as a function of swirl. Note that the swirl number definition accompanying this image is different from the convention used in the rest of this thesis. Reproduced from Gotoda et al. [46].

The influence of distributed exothermic reactions on the phenomenon of steady axisymmetric vortex breakdown has been studied by Rusak, Kapila, and Choi [47, 48]. Using asymptotic analysis and numerical simulations of inviscid lean, premixed, diffuse swirling flames in a finite-length pipe, they demonstrated a non-monotonic relationship between the reaction's exothermicity and the critical level of swirl required to achieve vortex breakdown. In the case of weakly-exothermic, ultra-diffuse premixed flames, they used an asymptotic analysis of the vorticity transport equation to argue that baroclinic effects dominate the effect of gas expansion and reduce the critical amount of swirl necessary for vortex breakdown compared to a non-reacting flow. However, they also show that for less-lean flames, this trend is reversed. In those more exothermic situations, dilatation due to the flame's heat release accelerates the flow in the streamwise direction and interacts with other baroclinic effects to resist the onset of vortex breakdown. Claims of experimental support for this theory of vortex breakdown in reacting flows have been advanced by Umeh et al. [49], who applied a similar vorticity budget analysis to time-averaged flowfields measured across a range of lean equivalence ratios in a turbulent swirl-stabilized combustor. However, the results in this thesis will show that these arguments are somewhat oversimplistic, as real flames have many different controlling factors beyond the exothermicity such as thickness and flame speed which have a hugely influential role on the flame and flow behavior.

A preliminary investigation on the origin and control of hydrodynamic instabilities in

swirling flames has been performed by Qadri [50]. Qadri's work is based on steady simulations, linear stability analysis, and structural sensitivity analysis of an unconfined vortex model which included a mixture fraction formulation to model diffusion flames. His results considered two specific strongly-swirling flow configurations both with and without significant axial co-flow. In both cases, the steady flowfields featured a clear axisymmetric 'bubble'-type vortex breakdown region and were unstable to co-rotating, counter-winding $|m| = 1$ spiral disturbance modes. However, the structural characteristics of these modes were very different. In the case with strong co-flow, the flame was unstable to a high-frequency, short-wavelength mode with a similar origin and structure to instabilities seen in other nonreacting studies [39, 43]. In contrast, in the more jet-like case without strong co-flow, the flame was unstable to a low-frequency, long-wavelength mode caused by density fluctuations at the flame base. This structural characteristic implies that the mode is related to an intrinsic linear instability of the flame and not to a typical jet instability. This further suggests that the hydrodynamic instabilities of reacting jets may include a broader set of instabilities than their nonreacting counterparts.

It should be acknowledged at this point that there are very few fundamental and theoretical investigations of reacting swirling jets. Overwhelmingly, the swirl flows community has focused on strongly turbulent conditions, likely for practical reasons. Indeed, flashback and blowoff severely restrict the range of parameters suitable for experimental investigations of any premixed laminar flame [51], and such issues are only exacerbated in the case of rotating flows due to the enhancement of flame propagation speeds along a vortex axis [52]. Furthermore, virtually all engineering applications of swirling jets involve turbulent flow situations. Nonetheless, it does seem that significant room for advancement could arise from more fundamental studies of reacting swirling flames in laminar, non-buoyant flow regimes.

1.2.2 Features of turbulent swirling jets and flames

Significance of coherent structures

After the onset of turbulence, swirling jets and wakes exhibit even more complex behavior. In some cases, barely any distinguishable structure exists, while others exhibit certain patterns that roughly resemble the laminar unsteady motions. Over the last half-century, a considerable effort has been invested in isolating and investigating the coherent motions in turbulent flows and flames of the latter type using the triple decomposition [53]. The coherent structures often form organized, nearly-periodic oscillations despite seemingly random behavior at the finer scales, creating spectral peaks in otherwise broadband turbulence [54, 55, 56, 57]. Such structures take many forms, including axisymmetric and helical oscillations of shear layers and precession, oscillation, and pulsation of vortex breakdown features [57, 3, 54, 55, 58]. An example of such coherent turbulent structures, taken from Huang & Yang [59], is shown in Figure 1.5. When reactions are introduced, local flame wrinkles and periodic strain introduced by coherent motions manifest themselves on the combustion process through dynamic propagation, stabilization, quenching, and re-ignition of flames [60, 61, 62, 63, 64] as well as generation of and response to narrowband acoustics [2, 65]. If the thermoacoustic feedback to the coupled flow dynamics is positive, combustion instability ensues, and coherent structures can drive high-amplitude heat release and pressure oscillations.

Following recent advances in dynamical systems theory and computational capabilities, the context of deterministic coherent structures in turbulence has evolved rapidly since the early 2000's. Despite the bewilderingly-high dimensionality of high-Reynolds number turbulent swirling flames, low-dimensional invariant manifolds exist in the state space [66, 67]. Such attractors physically represent Exact Coherent Structures (ECS): unstable non-chaotic solutions to the governing equations which exhibit definite spatiotemporal symmetries. Moreover, from a dynamical systems perspective, these structures emerge gradu-

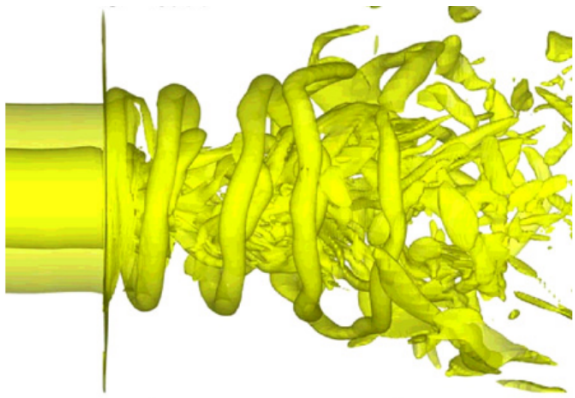

Figure 1.5: Iso-vorticity contours derived from a simulation of a lean premixed flame in a turbulent annular swirling jet. Reproduced from Huang & Yang [59].

ally. Inexact, but nonetheless organized, coherent structures arise physically whenever the system's state-space trajectory frequently visits the vicinity of an ECS (without perfectly collapsing onto it) [68].

Perhaps unsurprisingly, identification of the invariant manifolds relevant to a given turbulent state is nontrivial, and the unstable nature of ECS means that they do not exactly manifest themselves physically. Instead, theoretical efforts to interpret coherent structure in turbulence often invoke the idea of a Koopman expansion, which represents complex nonlinear state-space dynamics using a linearly-evolving but infinite-dimensional basis [69, 70]. In general, the Koopman operator possesses a continuous spectrum of nonorthogonal Koopman eigenfunctions residing in a Hilbert space. Its utility stems from the fact that non-chaotic motions (*i.e.* ECS) may be represented by discrete eigenfunctions of a finite-dimensional Koopman operator with an appropriate choice of basis. Further, a truncated linear Koopman operator converges to the fully-nonlinear dynamics as the chaotic trajectory coalesces toward an invariant manifold [71].

Thus, the classical method of isolating 'inexact' coherent structures from broadband turbulence through the triple decomposition, which lacked theoretical underpinnings at its inception, is indeed a rigorous method to decompose the dynamics of a turbulent attractor in many practical situations [72]. Furthermore, Koopman and linear global stability modes

and eigenvalues are equivalent when the Koopman expansion is discrete, which implies that global stability modes can approximate the nonlinear dynamics when coherent structures appear [73, 74]. This perspective also theoretically relates the unsteady features in laminar flows to coherent structures in turbulent flows with the same mean profile, provided the disorganized fluctuations of broadband turbulence are properly captured [75]. Consequently, mean flow stability analysis has proven to be a powerful predictive tool for many inert shear flows including turbulent swirling jets [76, 77, 78, 79].

Despite their utility toward deciphering high-dimensional fluid motions, it should be emphasized that coherent structures alone cannot paint a complete picture of turbulent flow dynamics. One important reason for this is the 'phase-jitter' phenomenon, whereby incoherent fluctuations cause cycle-to-cycle variations in the spatial location of otherwise coherent structures. This effect results in a spatial smearing of the resulting time- and phase-averages, which can lead to drastic underestimates in the overall strength and extent of the identified coherent structures in comparison to the instantaneous flow [80]. Such considerations are particularly relevant to reacting flows, where strong turbulent fluctuations can instantaneously overstretch the flame, leading to transient local extinction events which may fundamentally alter the flame behavior [61, 62].

Implications for Low-Order Modeling

Despite the valuable insights gleaned from deterministic views of turbulence, the development of affordable predictive tools for turbulent swirling flows and flames continues as a major challenge in simulations. The size and Reynolds numbers of reacting swirling jet problems are intractable for comprehensive Direct Numerical Simulation (DNS) – even with projected improvements in computing power for the foreseeable future. As such, the field relies extensively on reduced-order modeling efforts such as Large Eddy Simulation (LES), Reynolds-Averaged Navier Stokes (RANS) solvers, and numerous hybrid approaches. While these modeling strategies necessarily incorporate major simplifications

to the nonlinear equations that govern fluid motion and flame propagation, they can be capable of reasonable predictions of combustor outputs and macroscale flow features, which rationalizes their use.

Central to any low-order method are the particular turbulence and chemistry sub-models chosen for the application. LES is a well-demonstrated method that directly models those eddies containing a significant portion of a flow's kinetic energy, but invokes sub-grid scale scalar mixing models to account for dissipation and chemistry [3]. Unfortunately, even when technically feasible, LES can be prohibitively expensive for design and other applications, which motivates simpler methods. RANS solvers provide such simplification by modeling, rather than simulating, even the large eddy structures; thus, they rely on a suitable closure to model the so-called Reynolds stress. These closures typically rely on tenuous assumptions relating mean and fluctuating quantities to describe turbulence, chemistry, and turbulence-chemistry interactions, but are orders of magnitude cheaper than LES [3]. Submodels are also relevant for mean flow stability analyses of turbulent swirling flames which must incorporate turbulence and chemistry models to capture the effects of disorganized turbulent fluctuations in the vicinity of the attractor [77, 75]. Whatever the case, the ability of the particular turbulence submodel to capture the physical characteristics of turbulence is critical for the full scheme to accurately represent the global dynamics.

As an example, identification of the correct flame anchoring location is a particular challenge in reacting flows. The strain rate field plays an important role in the combustion characteristics of swirl-stabilized flames, largely due to its influence on flame anchoring locations. A kinematic balance of the local flow velocity and the local flame speed determines the spatiotemporal dynamics of the propagating flame front. However, the local strain rate influences the local burning velocity, and can actually render regions of the flow field non-combustible where the strain rate magnitude exceeds the extinction strain rate of the mixture. Hence, a poorly-tuned model may select a region of the flow such as a thin shear layer as the flame anchoring location, when in fact this region is unable to support

combustion.

A turbulence submodel must be evaluated rigorously to determine its validity. This can be accomplished by comparing mean flow properties between a modeling result and experiments or DNS. However, such *a posteriori* approaches evaluate the entire low-order method rather than just the turbulence submodel, making generalization difficult. A more general approach is to directly apply the turbulence model to experimental measurements or DNS results and compare the output stresses from the model against the actual stresses of the known field. These *a priori* approaches to characterizing turbulence models have become an extensive area of research as new turbulence modeling techniques continue to emerge. A typical approach is to use DNS to obtain the velocity gradients necessary to model the Reynolds stress or sub-grid closure and then compare the model and experiment [81].

Numerous studies on DNS of simple reacting and non-reacting turbulent flows have demonstrated shortcomings in many standard turbulence models, but experimental comparisons with systems inaccessible to DNS remain sparse. This is partly due to the difficulty of resolving the required three-dimensional velocity gradients with traditional velocimetry techniques. Nonetheless, advanced PIV techniques such as holographic PIV, multi-plane PIV, and tomographic PIV all offer the possibility of resolving 3-D gradients within a small volume using finite differencing, and they have been applied for this purpose by a handful of authors in non-reacting flow fields [82, 83]. Such techniques have also been demonstrated in reacting fields, but not yet at a spatiotemporal resolution sufficient for determination of the complete strain rate tensor [84]. Previous studies have quantified strain rate fields and inferred their impact on the observed flame stabilization position in reacting swirling jets [85, 86, 87, 64]. However, these studies have not assessed or compared their measured Reynolds stresses with turbulence model predictions.

1.3 Objectives

The key objectives of the research undertaken in this thesis are fourfold. First, this thesis aims to elucidate the steady and time-periodic nonlinear dynamical behaviors of non-reacting swirling jets in the laminar regime. Despite their significance, obtaining detailed and repeatable characterizations of the swirling jet parameter space via experiments or conventional time-marching computations remains challenging. This is due partly to the sheer variety of different flow patterns that have been reported across the literature, but also to the multistability and hysteresis which can relate distinct states. Without a deeper understanding of the overall parameter space, any observation must be taken in the specific context of the flow configuration, including the initial conditions, confinement, external noise sources, and geometrical variations. This work, presented in chapter 3, seeks to provide a more comprehensive "taxonomy" of swirl flow configurations and dynamics in order to relate different observations by a more general set of behaviors using numerical bifurcation analysis.

The second objective builds on the first by extending a similar analysis to reacting laminar swirling jets. As mentioned in subsection 1.2.1, reacting swirling jets are relatively poorly-understood compared to their non-reacting counterparts. This fundamental study, given in chapter 4, addresses important similarities and differences between the reacting and non-reacting settings, with the aim of providing a framework which complements the understanding gained from the non-reacting case.

Next, this work will move on to low-order modeling of turbulent swirling jet systems. The third objective is to asses the utility of hydrodynamic stability analysis as a tool from which to interpret the results of turbulent experiments. This investigation will focus on a highly-turbulent, transversely-forced swirling flame configuration that was previously investigated experimentally in Smith's thesis [6]. These results, provided in chapter 5, will demonstrate that a relatively simple linear hydrodynamic model can capture many

important aspects of the coherent forced response expressed by a highly turbulent reacting swirling jet, suggesting it can also explain the physical selection processes underlying these dynamics.

The fourth and final objective of this thesis is to assess the ability of simple turbulence models to reproduce the Reynolds stress fields required for low-order modeling of forced and unforced turbulent jets and flames. These results, given in chapter 6, offer insight into the interplay among coherent vortices, broadband turbulence, and unsteady flames, which all contribute to the overall macroenvironment within a turbulent combustor. Additionally, the presented experimentally-measured Reynolds stress fields serve as a platform from which to evaluate turbulence models for future low-order modeling efforts in swirling flames.

CHAPTER 2
THEORETICAL AND NUMERICAL APPROACH

This chapter outlines the different modeling approaches undertaken in this thesis. The first section describes the flow configuration and numerical branch tracing and bifurcation analysis methods used to characterize the nonlinear dynamics of the laminar flow situations studied in chapter 3 and chapter 4. Then, in the second section, a triple decomposition-based mean flow stability framework is developed in order to interpret the coherent forced response of experimentally-measured turbulent flows. These results are presented in chapter 5.

2.1 Laminar problems

2.1.1 Flow configuration

The laminar models considered in this thesis simulate non-reacting and reacting flow situations consisting of viscous swirling jets discharging from a long, straight, rotating pipe into a semi-infinite domain Ω as depicted in figure Figure 2.1. In either case, conventional cylindrical-polar coordinates defined by $\boldsymbol{x} = (x, r, \theta)$ are adopted with the origin located at the center of the pipe exit. All quantities are dimensionless; the lengths being normalized by the pipe diameter $D = 2R$ and the velocities by the steady, mass-averaged flow U through the pipe. Hence, the flow may be parameterized by the swirl ratio $S = \omega_p R/U$ and the Reynolds number $Re = DU/\nu$ where ω_p is the rotation rate of the pipe and ν is the fluid's kinematic viscosity.

In the simpler case of a homogeneous, non-reacting flow, the fluid's density and viscosity are constant and its motion is described completely by the state vector $\boldsymbol{q} = (\boldsymbol{u}, p)^{\mathrm{T}}$ consisting of the velocity $\boldsymbol{u} = (u_x, u_r, u_\theta)^{\mathrm{T}}$ and pressure p fields. Together, their evolu-

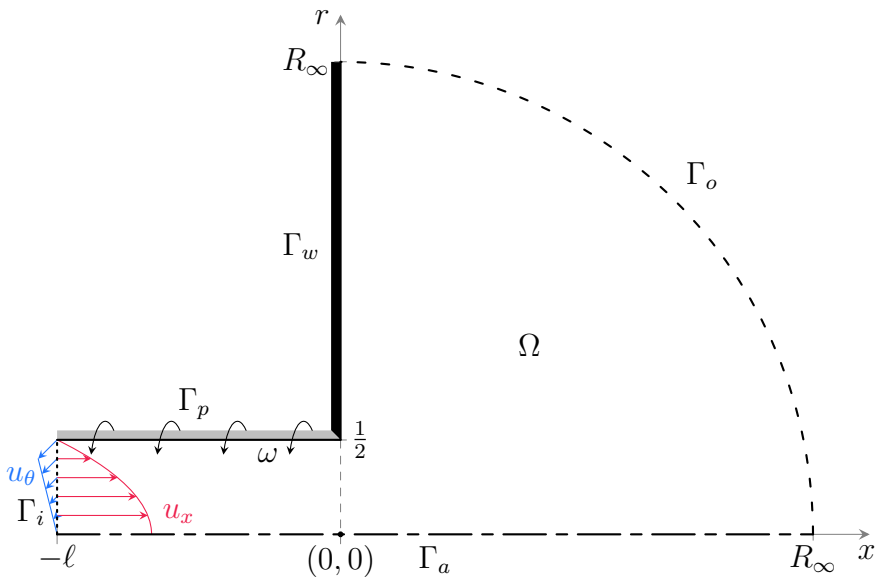

Figure 2.1: Schematic of the meridional plane of the axisymmetric domain Ω with boundary Γ.

tion in the domain proceeds according to the incompressible Navier-Stokes and continuity equations,

$$\frac{\partial \boldsymbol{u}}{\partial t} + \boldsymbol{u} \cdot \boldsymbol{\nabla} \boldsymbol{u} = -\boldsymbol{\nabla} p + \frac{1}{Re} \nabla^2 \boldsymbol{u}, \tag{2.1a}$$

$$0 = \boldsymbol{\nabla} \cdot \boldsymbol{u}. \tag{2.1b}$$

In the reacting flow case, the flow geometry remains the same but the governing equations are generalized to account for many of the key additional physical processes which come into play in the context of lean premixed flames. As the focus of this work is on the hydrodynamic aspects of reacting flow, the chemistry model is restricted to a simple, single-step fuel-limited mechanism which greatly simplifies the modeling effort without sacrificing some important features of real flames. The chosen model is derived from conservation of mass, species, momentum, and energy and an equation of state following Poinsot & Veynante [88]. A similar model has been used by Rusak, Choi, & others in their work on reacting swirling pipe flows [47, 48, 89].

The following is a brief description of the assumptions underlying this model; a complete derivation with further details can be found in Appendix A. Chemistry is modeled by a single-step, irreversible, fuel-limited premixed reaction with a rate determined by the Arrhenius law. The products and reactants are assumed to have equal molecular weights, and to behave as perfect gases. The Soret, Dufour, and pressure gradient diffusion effects are all neglected, as is radiation. Asymptotically small Mach numbers are considered, such that the pressure and viscous heating terms in the energy equation vanish, and the pressure splits into a constant leading-order thermodynamic pressure which is used in the equation of state and a higher-order hydrodynamic pressure correction which enforces energy conservation. A Lewis number of one is assumed to relate the species concentration and temperature by the flame Progress Variable Field (PVF) Θ which varies from zero in the reactants to one in the products. In the reacting case, the state vector is given by $\boldsymbol{q} = (\Theta, \boldsymbol{u}, p)^{\mathrm{T}}$, and the resulting dimensionless system is,

$$\frac{1}{1+\Delta T\Theta}\left(\frac{\partial\Theta}{\partial t}+\boldsymbol{u}\cdot\boldsymbol{\nabla}\Theta\right) = Da\left(\frac{1-\Theta}{1+\Delta T\Theta}\right)\exp\left(\frac{-Ze\,(1+\Delta T)\,(1-\Theta)}{1+\Delta T\Theta}\right) + \frac{1}{Pe}\nabla^2\Theta, \quad (2.2a)$$

$$\frac{1}{1+\Delta T\Theta}\left(\frac{\partial\boldsymbol{u}}{\partial t}+\boldsymbol{u}\cdot\boldsymbol{\nabla}\boldsymbol{u}\right) = -\boldsymbol{\nabla}p+\frac{1}{Re}\nabla^2\boldsymbol{u}, \quad (2.2b)$$

$$0 = \boldsymbol{\nabla}\cdot\boldsymbol{u}-\frac{\Delta T}{1+\Delta T\Theta}\left(\frac{\partial\Theta}{\partial t}+\boldsymbol{u}\cdot\boldsymbol{\nabla}\Theta\right). \quad (2.2c)$$

Here, ΔT is the exothermicity (i.e. the temperature difference between the burned and unburned fluid), $Ze = T_a\Delta T/(1+\Delta T)^2$ is the Zeldovich number based on the Arrhenius activation temperature T_a, $Pe = DU/\mathcal{D}$ is the Péclet number based on the mixture's constant diffusivity $\mathcal{D}$, and $Da = (\mathcal{A}D/U)\exp\left(-Ze(1+\Delta T)/\Delta T\right)$ is the Dahmköhler number based on the Arrhenius frequency factor $\mathcal{A}$. Note that in case $\Delta T = 0$, the system decouples and becomes equivalent to Equation 2.1 with an additional passive scalar equation for Θ. Within this formulation, analytical estimates for the unstretched laminar flame

speed and thickness, due to Williams [90], are given by,

$$S_L^0 \approx \frac{1}{Ze}\sqrt{\frac{2Da}{Pe}}\left(1+\frac{1.344-1.656\Delta T}{Ze(1+\Delta T)}\right) \qquad \text{and} \qquad \delta_F^0 \approx \frac{1}{S_L^0 Pe}. \tag{2.3}$$

A complete listing of the boundary conditions associated with Equation 2.1 and Equation 2.2 are given in Table 2.1. Axial flow is controlled by a prescribed steady mass flux through the pipe, and no-slip conditions are enforced for all velocity components on the rotating pipe wall Γ_p and the fixed exit-plane wall Γ_w. Conceptually, the inlet pipe is sufficiently long such that a region exists where the flow is fully-developed but exit effects are negligible. The upstream boundary Γ_i is located at some $x = -\ell$ in this fully-developed region where the distribution of axial and azimuthal velocity is fixed to match the Poisseuille solution. In the reacting case, the incoming fluid at Γ_i is assumed to consist of pure reactants, and all walls $\Gamma_p \cap \Gamma_w$ are assumed to be adiabatic. Note that instead of rigidly enforcing a parallel inflow at Γ_i, less-restrictive Neumann conditions are enforced on the radial component of velocity to minimize inlet reflections and scattering of upstream-propagating vorticity disturbances and inertial waves [91]. On the central axis Γ_a, three-dimensional symmetry constraints based on a Fourier expansion along θ are derived from parity considerations for each velocity component in the limit of $r \to 0$ for each azimuthal wavenumber m [92]. The jet exits the pipe into a semi-infinite reservoir which is truncated to the large but finite radius R_∞ for practical purposes. The particular configuration used for this paper is specified by the values $\ell = 4$ and $R_\infty = 40$ which were selected on the basis of a parameter independence analysis presented in Appendix B.

To accurately model the unconfined flow, transparent constraints along the open boundary Γ_o are required. As emphasized by several authors [93, 41], such conditions must not only allow flow to passively exit the domain without generating wave reflection artifacts but must also enable free entrainment from the far-field. A constraint which satisfies both of these requirements in non-swirling flows and emerges naturally in the vari-

Table 2.1: List of boundary conditions. Note that, in the non-reacting case, $\rho \equiv 1$ and the conditions on Θ are ignored. In the reacting case, $\rho = (1 + \Delta T \Theta)^{-1}$.

Boundary		Constraints			
Inlet, Γ_i		$u_x = 2 - 8r^2$	$\partial_x u_r = 0$	$u_\theta = 2Sr$	$\Theta = 0$
Pipe, Γ_p		$u_x = 0$	$u_r = 0$	$u_\theta = S$	$\partial_r \Theta = 0$
Wall, Γ_w		$u_x = 0$	$u_r = 0$	$u_\theta = 0$	$\partial_x \Theta = 0$
	$m = 0$:	$\partial_r u_x = 0$	$u_r = 0$	$u_\theta = 0$	$\partial_r \Theta = 0$
Axis, Γ_a	$\lvert m \rvert = 1$:	$u_x = 0$	$\partial_r u_r = 0$	$\partial_r u_\theta = 0$	$\Theta = 0$
	$\lvert m \rvert \geq 2$:	$u_x = 0$	$u_r = 0$	$u_\theta = 0$	$\Theta = 0$
Open, Γ_o		$\left(-\tilde{p}\boldsymbol{I} + Re^{-1}\boldsymbol{\nabla u}\right) \cdot \boldsymbol{n} - \frac{1}{2}\rho \boldsymbol{u} \min\left(0, \boldsymbol{u} \cdot \boldsymbol{n}\right) = 0$			$\boldsymbol{n} \cdot \boldsymbol{\nabla} \Theta = 0$

ational formulation of Equation 2.1 is the well-known free-outflow condition given by $\left(-p\boldsymbol{I} + Re^{-1}\boldsymbol{\nabla u}\right) \cdot \boldsymbol{n} = 0$, where $\boldsymbol{I}$ is the identity matrix and $\boldsymbol{n}$ is the outward unit normal vector. However, this condition raises two major concerns for the strongly-swirling and recirculating flows considered here. First, the free-outflow condition requires the normal derivative of the normal flow component to exactly balance the pressure along the boundary. In a scenario where centrifugal effects due to swirl induce a physical variation in pressure along the open boundary, the free-outflow condition will generate nonphysical flow gradients to match this variation. Second, when there is inward flow across the boundary, the free-outflow condition does not restrict the energy entering the domain and may lead to ill-posedness.

To mitigate these problems, other studies employing free-outflow conditions for investigations of open swirling flows have employed extended computational domains with artificial sponge layers. That approach seeks to avoid the aforementioned concerns by using large amounts of artificial dissipation to rapidly develop the flow to a purely-outward Poiseuille form with negligible azimuthal velocity before it reaches the outflow boundary. While effective, such treatment adds design challenges and computational expenses associated with the parameters of the sponge layer and the increased domain size. This work takes a different approach. The boundary stress issue is avoided by excluding the centrifugal pressure variations from the normal stress balance on the boundary, while ill-posedness is avoided using a robust directional outflow condition which remains well-posed even with

substantial entrainment from the domain exterior. More specifically, to decouple the centrifugal pressure from the outflow boundary condition, the modified pressure $\tilde{p} = p - p_o$ is defined along the open boundary. Here, p_o is a scalar potential which characterizes the centrifugal pressure variations along Γ_o via the relation,

$$\boldsymbol{\nabla} p_o \cdot \boldsymbol{t} = \left. \frac{u_\theta^2}{r} \right|_{\Gamma_o}, \quad \text{or} \quad \boldsymbol{\nabla} p_o \cdot \boldsymbol{t} = \frac{1}{1 + \Delta T \Theta} \left. \left(\frac{u_\theta^2}{r} \right) \right|_{\Gamma_o}, \tag{2.4}$$

in the non-reacting and reacting cases, respectively. Here, $\boldsymbol{t}$ is the positively-oriented unit tangent vector along Γ_o. Since Equation 2.4 only defines p_o up to a constant, $p_o = 0$ at $\Gamma_w \cap \Gamma_o$ may be chosen for uniqueness. Then, saving the details for the next section, p_o is excluded from the pressure term in the open boundary condition so that centrifugal pressure variations are decoupled from the flow gradients on the boundary.

To address the issue of recirculating flow from the domain exterior, the directional outflow condition,

$$\left(-p\boldsymbol{I} + Re^{-1} \boldsymbol{\nabla} \boldsymbol{u} \right) \cdot \boldsymbol{n} - \frac{1}{2} \boldsymbol{u} \min\left(0, \boldsymbol{u} \cdot \boldsymbol{n}\right) = 0. \tag{2.5}$$

is adopted for the non-reacting case, following [94]. Similarly, the reacting case uses the requirement,

$$\left(-p\boldsymbol{I} + Re^{-1} \boldsymbol{\nabla} \boldsymbol{u} \right) \cdot \boldsymbol{n} - \frac{1}{2} \left(\frac{\boldsymbol{u} \min\left(0, \boldsymbol{u} \cdot \boldsymbol{n}\right)}{1 + \Delta T \Theta} \right) = 0. \tag{2.6}$$

These conditions are identical to the conventional Neumann-type free-outflow condition along any part of the open boundary with a local outflow (where $\boldsymbol{u} \cdot \boldsymbol{n} > 0$). However, wherever back flow occurs, dissipation related to the weak form of the nonlinear advection term appears, which yields a stable Robin-type condition. This, in turn, bounds the energy influx while still respecting the important exchange of mass and momentum across the open boundary. Furthermore, the existence of weak solutions under the directional outflow condition has been proven [95], and its numerical accuracy relative to other approaches has

been demonstrated [96].

Combining the directional outflow condition with the centrifugal pressure decoupling approach yields the modified directional outflow boundary condition given in Table 2.1. This condition is applied along the entirety of the open boundary Γ_o. In the absence of swirl, this constraint reduces exactly to the directional outflow condition, and further to the free-outflow condition if the flow is also purely outward across Γ_o. In the reacting case, standard Neumann conditions are used along Γ_o for the flame PVF.

2.1.2 Discretization

The numerical methods are derived from the variational forms of Equation 2.1 and Equation 2.2, which include the boundary conditions of Table 2.1 and the constraint of Equation 2.4. To remove the coordinate singularity at $r = 0$, Equation 2.1a (in the non-reacting case) or Equation 2.2a and Equation 2.2b (in the reacting case) are first multiplied by the radial coordinate [97]. Then, taking the standard real or complex L^2 inner product $\langle \bullet, \bullet \rangle_\Omega$ and introducing test functions $\check{\boldsymbol{q}}$, an integral is taken over the domain, leading to the weak formulation. In the non-reacting case, the problem consists of seeking in the appropriate spaces $\boldsymbol{q}$ such that for all $\check{\boldsymbol{q}}$:

$$\left\langle r\check{\boldsymbol{u}}, \frac{\partial \boldsymbol{u}}{\partial t} + \boldsymbol{u} \cdot \boldsymbol{\nabla} \boldsymbol{u} \right\rangle_\Omega + \left\langle \boldsymbol{\nabla}(r\check{\boldsymbol{u}}), -p\boldsymbol{I} + \frac{1}{Re}\boldsymbol{\nabla}\boldsymbol{u} \right\rangle_\Omega + \langle \check{p}, \boldsymbol{\nabla} \cdot \boldsymbol{u} \rangle_\Omega + \left\langle r\check{\boldsymbol{u}}, p_o \boldsymbol{n} - \frac{1}{2}\boldsymbol{u} \min(0, \boldsymbol{u} \cdot \boldsymbol{n}) \right\rangle_{\Gamma_o} + \left\langle \check{p}_o, \boldsymbol{\nabla} p_o \cdot \boldsymbol{t} - \frac{u_\theta^2}{r} \right\rangle_{\Gamma_o} = 0. \quad (2.7)$$

Likewise, in the reacting case, the problem consists of finding $\boldsymbol{q}$ such that for all $\check{\boldsymbol{q}}$:

$$\begin{aligned}
&\left\langle r\check{\Theta}, \frac{1}{1+\Delta T\Theta}\left(\frac{\partial\Theta}{\partial t}+\boldsymbol{u}\cdot\boldsymbol{\nabla}\Theta-Da\,(1-\Theta)\exp\left(\frac{-Ze\,(1+\Delta T)\,(1-\Theta)}{1+\Delta T\Theta}\right)\right)\right\rangle_{\Omega}\\
&\quad+\left\langle\boldsymbol{\nabla}(r\check{\Theta}), \frac{1}{Pe}\boldsymbol{\nabla}\Theta\right\rangle_{\Omega}+\left\langle r\check{\boldsymbol{u}}, \frac{1}{1+\Delta T\Theta}\left(\frac{\partial\boldsymbol{u}}{\partial t}+\boldsymbol{u}\cdot\boldsymbol{\nabla}\boldsymbol{u}\right)\right\rangle_{\Omega}+\langle\check{p}, \boldsymbol{\nabla}\cdot\boldsymbol{u}\rangle_{\Omega}\\
&\quad+\left\langle\boldsymbol{\nabla}(r\check{\boldsymbol{u}}), -p\boldsymbol{I}+\frac{1}{Re}\boldsymbol{\nabla}\boldsymbol{u}\right\rangle_{\Omega}-\left\langle\check{p}, \frac{\Delta T}{1+\Delta T\Theta}\left(\frac{\partial\Theta}{\partial t}+\boldsymbol{u}\cdot\boldsymbol{\nabla}\Theta\right)\right\rangle_{\Omega}\\
&\quad+\left\langle r\check{\boldsymbol{u}}, p_o\boldsymbol{n}-\frac{\boldsymbol{u}\min(0,\boldsymbol{u}\cdot\boldsymbol{n})}{2\,(1+\Delta T\Theta)}\right\rangle_{\Gamma_o}+\left\langle\check{p}_o, \boldsymbol{\nabla}p_o\cdot\boldsymbol{t}-\frac{u_\theta^2}{r\,(1+\Delta T\Theta)}\right\rangle_{\Gamma_o}=\;0
\end{aligned} \tag{2.8}$$

Note that weak form of the modified directional outflow condition described above results in a boundary integral along Γ_o which is simplified by the application of the divergence theorem to the viscous and pressure terms of Equation 2.1.

The spatial discretisation consists of a Delaunay triangulation of the meridional plane constructed using GMSH [98]. After experimentation with several different meshes, a triangulation was selected for Ω with $\ell = 4$ and $R_\infty = 40$ which features $140\,055$ elements. Finally, an inf-sup stable discrete problem is formed by projecting the weak formulation of Equation 2.7 onto the basis of Taylor-Hood ($\mathbb{P}_2 \times \mathbb{P}_1$) finite elements associated with the mesh using FreeFEM [99]. The velocity $\boldsymbol{u}$ and pressure p are defined respectively on bi-quadratic and bi-linear elements over the full domain Ω, while the centrifugal pressure p_o is defined on linear elements along only the boundary Γ_o. In the reacting cases, the progress variable Θ is also defined on bi-quadratic elements over Ω. In the non-reacting case, the resulting discrete flow states have $915\,839$ total degrees of freedom. The reacting case has $1\,197\,481$ degrees of freedom. Further details of the mesh and an assessment of the robustness of the results to the selected discretisation are provided in Appendix B.

2.1.3 Solution Approach

Though the actual implementation is based on the weak form, (e.g. the autonomous nonlinear system for the non-reacting case in Equation 2.7), for convenience of notation, further discussion will make use of the strong state-space form,

$$\mathcal{M}\left(\boldsymbol{q};\Delta T\right)\frac{\partial \boldsymbol{q}}{\partial t}+\mathcal{R}\left(\boldsymbol{q};Re,S,Pe,\Delta T,Da,Ze\right)=0, \tag{2.9}$$

where $Re, S, \ldots$ are parameters and the strong forms of the mass and steady system operators are $\mathcal{M}$ and $\mathcal{R}$, respectively; they are defined in Appendix C. In the nonreacting case, all parameters but *Re* and *S* are irrelevant and $\mathcal{M}$ is a constant mass matrix. This notation neglects several important aspects of the weak form, including the boundary conditions and the restriction of Equation 2.4 to Γ_o. In the parallel implementation, all problems are abstracted to the linear algebra level by FreeFEM [99, 100] and solved in a distributed manner using PETSc [101] based on direct factorization via MUMPS [102] except where noted otherwise.

In the inert case, the flow is initialized using the solution to the steady linear Stokes system (i.e. $Re = 0$). From this initial point, solutions at other parameter values can be straightforwardly identified using the approaches described below. Unlike the non-reacting case, the reacting flow system is strongly nonlinear even in the $Re \to 0$ limit due to the heat release term. This demands special considerations in order to reliably initialize the reacting flowfield. To "ignite" the flame, the following sequence of steps is performed. First, the flowfield is initialized with the linear, inert Stokes solution (i.e. $\Delta T = Re = 0$). Next, the exothermicity is gradually increased from zero at a reduced Zeldovich number until a well-defined flame front appears. Once this flame is apparent, the remaining parameters are incrementally adjusted until their target values are reached using the continuation methods detailed below.

Identification and continuation of equilibrium states

Since the geometry and boundary conditions are agnostic to θ and t, the steady states $\boldsymbol{q}_0(x, r)$ of this flow represent axisymmetric fixed points of Equation 2.9. Such solutions are commonly termed "base flows" in the context of linear stability analysis but will be referred to as "steady states" in this thesis to avoid ambiguity. Hence, $\boldsymbol{q}_0$ is defined as an equilibrium satisfying,

$$\mathcal{R}_0(\boldsymbol{q}_0; Re, S, \ldots) = 0, \tag{2.10}$$

where the 0-subscript on $\mathcal{R}_0$ is used to indicate a restriction of the steady three-dimensional operator $\mathcal{R}$ to its axisymmetric Fourier component. A similar m-subscript convention is used throughout this thesis to indicate the restriction of any three-dimensional operator to the m-th component of its azimuthal Fourier decomposition by formally replacing any partial derivatives along θ with the product $\mathrm{i}m$.

One simple strategy to find $\boldsymbol{q}_0$ is by locking the values of all parameters and using Newton's method to iteratively refine an initial guess $\boldsymbol{q}_0$ for the steady flow. In this approach, the correction $\delta\boldsymbol{q}_0$ to the initial guess is then determined by solving the linear problem,

$$\mathcal{J}_0(\boldsymbol{q}_0)\,\delta\boldsymbol{q}_0 = \mathcal{R}_0(\boldsymbol{q}_0), \tag{2.11}$$

where $\mathcal{J}$ is the Jacobian operator. Following each iteration, the state is updated as $\boldsymbol{q}_0 \leftarrow \boldsymbol{q}_0 - \delta\boldsymbol{q}_0$, and the process is repeated until the norm of the residual converges within $\|\mathcal{R}_0\| < 10^{-10}$.

While sufficient for such purposes as initializing a solution branch, the straightforward approach outlined above is not always robust for continuation of a branch along a parameter. In general, nonlinear systems may exhibit multiple solutions at identical parameter values, and the domain of convergence for Newton's method shrinks as the Jacobian matrix becomes singular near a bifurcation point. A more suitable approach for such systems

involves tracing branches of $\boldsymbol{q}_0$ using a predictor-corrector scheme which can "jump" over singularities [103]. Methods of this type treat both the state vector $\boldsymbol{q}_0$ and a continuation parameter α (for example, $Re, S, \ldots$) as unknowns in Equation 2.10 and require an additional constraint to compensate for this new degree of freedom.

The continuation approach employed here relies on a predictor-corrector scheme with a tangent predictor step and a Moore-Penrose corrector sequence. For the predictor step, it exploits the fact that the null vector associated with the augmented Jacobian matrix at a point on the solution curve lies tangent to the solution curve at that point. More precisely, the null vector $\boldsymbol{y} = \left(\boldsymbol{y}_{\boldsymbol{q}}, y_\alpha\right)^{\mathrm{T}}$ satisfies,

$$\boldsymbol{y} \in \ker\left(\left[\mathcal{J}_0\left(\boldsymbol{q}_0, \alpha\right), \frac{\partial \mathcal{R}_0\left(\boldsymbol{q}_0, \alpha\right)}{\partial \alpha}\right]\right) \tag{2.12}$$

where the vector $\partial \mathcal{R}_0 / \partial \alpha$ is approximated via finite differences. To determine $\boldsymbol{y}$ and fix its orientation with respect to the parameter, the approach proceeds by setting $y_\alpha = -1$ and solving

$$\mathcal{J}_0\left(\boldsymbol{q}_0, \alpha\right) \boldsymbol{y}_{\boldsymbol{q}} = \frac{\partial \mathcal{R}_0\left(\boldsymbol{q}_0, \alpha\right)}{\partial \alpha}. \tag{2.13}$$

Thus, a linear prediction for a new point on the solution curve is obtained by taking $\left(\boldsymbol{q}_0, \alpha\right) = \left(\boldsymbol{q}_0, \alpha\right) + h\left(\boldsymbol{y}_{\boldsymbol{q}}, y_\alpha\right) / \|\boldsymbol{y}\|$ where h is a parameter which controls the size and orientation of the predictor step. To enable accurate branch tracing without the expense of needlessly small steps, the magnitude of h must be adjusted throughout the continuation process. The chosen approach uses an adaptive scaling for h based on the convergence behavior of the previous corrector sequence following [104] and described below. Furthermore, to ensure a consistent sense of direction along the solution branch, the sign of h must be flipped when a limit point is traversed. This is achieved by monitoring the sign of the inner product between the null vectors associated with each consecutive pair of solution points. When these points lie on either side of a saddle-node bifurcation, the inner product is negative and the sign of h is reversed.

Following each predictor step, a nonlinear correction sequence is required to converge from the predicted point to a true equilibrium solution $\boldsymbol{q}_0$. For this, a Moore-Penrose approach is adopted where each Newton iteration of the corrector is constrained to be orthogonal to the kernel of the augmented Jacobian matrix at the current point. Thus, at each iteration, a solution must be obtained for the bordered linear system,

$$\begin{pmatrix} \mathcal{J}_0\left(\boldsymbol{q}_0, \alpha\right) & \dfrac{\partial \mathcal{R}_0\left(\boldsymbol{q}_0, \alpha\right)}{\partial \alpha} \\ \boldsymbol{y}_{\boldsymbol{q}}^{\mathrm{T}} & y_\alpha \end{pmatrix} \begin{pmatrix} \Delta \boldsymbol{q}_0 \\ \Delta \alpha \end{pmatrix} = \begin{pmatrix} \mathcal{R}_0\left(\boldsymbol{q}_0, \alpha\right) \\ 0 \end{pmatrix}. \tag{2.14}$$

While Equation 2.14 could be directly assembled and solved at each iteration, this approach is avoided for two reasons. First, since it contains $\boldsymbol{y}$, the augmented system matrix in Equation 2.14 requires the solution of Equation 2.13 prior to its assembly at each iteration. Second, the presence of the dense vectors $\boldsymbol{y}_{\boldsymbol{q}}^{\mathrm{T}}$ and $\mathcal{J}_\alpha$ on the borders of this augmented system matrix greatly complicate its overall structure compared to the sparse Jacobian matrix $\mathcal{J}_0$ underlying the conventional system in Equation 2.11.

Instead, a block elimination strategy is adopted to treat Equation 2.14 without explicitly forming the bordered system. This begins by separately solving Equation 2.13 and Equation 2.11. Since these systems involve the same $\mathcal{J}_0$, only a single sparse matrix must be assembled and factored to solve both problems. Then, using some algebra based on the Schur complement, the solution to Equation 2.14 is deduced as

$$\Delta \alpha = \frac{\boldsymbol{y}_{\boldsymbol{q}}^{\mathrm{T}} \delta \boldsymbol{q}_0}{1 + \boldsymbol{y}_{\boldsymbol{q}}^{\mathrm{T}} \boldsymbol{y}_{\boldsymbol{q}}}, \tag{2.15a}$$

$$\Delta \boldsymbol{q}_0 = \delta \boldsymbol{q}_0 - \boldsymbol{y}_{\boldsymbol{q}} \Delta \alpha. \tag{2.15b}$$

From here, the state is updated as $\left(\boldsymbol{q}_0, \alpha\right)^{\mathrm{T}} \leftarrow \left(\boldsymbol{q}_0, \alpha\right)^{\mathrm{T}} - \left(\Delta \boldsymbol{q}_0, \Delta \alpha\right)^{\mathrm{T}}$ and the process is repeated until reaching the same convergence tolerance of $\|\mathcal{R}_0\| < 10^{-10}$. For further efficiency gains, this corrector sequence is treated as a Newton-chord iteration where a single factorization of $\mathcal{J}_0$ from the first corrector iteration is reapplied to the remaining

iterations until convergence. Once convergence is achieved, the null vector from the last corrector iteration is then reused in the next predictor step.

As indicated above, well-designed adaptive step controls for the predictor are a key aspect of robust continuation methods. Nonetheless, strict convergence conditions are also needed for the corrector to ensure robust and accurate branch tracing. The requirements used here include:

i. a monotonic convergence of the residual norm during the corrector iterations,

ii. a decrease in the norm of the correction by at least a factor of two in each iteration,

iii. a norm of the first correction smaller than one,

iv. an angle between consecutive tangent vectors of less than 30°, and

v. no more than ten corrector iterations per step.

If any of these conditions fail to be met during the corrector process before the residual norm reaches the allowed tolerance, the step is rejected, and a new corrector sequence begins from a predictor with half the original step size. Otherwise, the converged step is accepted, and the step size for the next predictor is scaled based on requirements (ii-iv) as described in [104].

Stability analysis of steady states

The stability of axisymmetric equilibrium solutions to Equation 2.9 is assessed by the long-time asymptotic evolution of superimposed three-dimensional infinitesimal perturbations $\acute{\boldsymbol{q}}$ to $\boldsymbol{q}_0$. Due to the underlying symmetries of the flow system, any solution to Equation 2.9 can be expanded as a superposition of modes $\hat{\boldsymbol{q}}_m$ associated with azimuthal wavenumber m, growth rate σ, and frequency f according to,

$$\breve{\boldsymbol{q}}\left(x,r,\theta,t\right) \propto \hat{\boldsymbol{q}}_m\left(x,r\right) e^{\mathrm{i}m\theta+(\sigma+\mathrm{i}2\pi f)t} + \hat{\boldsymbol{q}}_m^*\left(x,r\right) e^{-\mathrm{i}m\theta+(\sigma-\mathrm{i}2\pi f)t}, \tag{2.16}$$

where * denotes complex conjugation and $\breve{\boldsymbol{q}}$ is arbitrarily small. In general, the modal decomposition given above is not immediately useful for analysis as the modes are nonlinearly coupled and may be strongly non-orthogonal at finite times. However, under the particular circumstances associated with this stability analysis, namely the arbitrary smallness of the disturbances and the asymptotic scaling of time, the modes in Equation 2.16 are both independent and orthogonal. From this standpoint, they are therefore equivalent to the eigenmodes of Equation 2.9 when linearized about $\boldsymbol{q}_0$ and subjected to homogeneous forms of the boundary conditions listed in Table 2.1. As a result, the overall stability characteristics of any $\boldsymbol{q}_0$ can be deduced from the spectrum of the generalized eigenvalue problem,

$$\lambda \mathcal{M} \hat{\boldsymbol{q}}_m + \mathcal{J}_m \left(\boldsymbol{q}_0 \right) \hat{\boldsymbol{q}}_m = 0, \tag{2.17}$$

where $\lambda = \sigma + \mathrm{i}2\pi f$ is the eigenvalue. If the real part of every eigenvalue of Equation 2.17 satisfies $\sigma < 0$, then $\boldsymbol{q}_0$ is stable; otherwise, it is unstable. For broad-spectrum calculations, Equation 2.17 is solved with the shift-and-invert technique using the Krylov-Schur method in SLEPc [105] to within a tolerance of $\| \lambda \mathcal{M} \hat{\boldsymbol{q}}_m + \mathcal{J}_m \hat{\boldsymbol{q}}_m \| < 10^{-6} \| \hat{\boldsymbol{q}}_m \|$. Then, if needed, the dominant eigenvalues are refined individually using power iteration to ensure convergence within a tolerance of 10^{-10}.

It is worth pointing out here that even if $\boldsymbol{q}_0$ is classified as stable according to the definition above, some perturbations may exhibit very large transient growth due to nonnormality before eventually converging to the dominant eigenmode in the long-time limit [106, 107]. As exemplified by the study of harmonically-forced coaxial jets at low swirl by Montagnani & Auteri [108], this linear transient growth mechanism opens pathways for subcritical and noncritical exchanges of stability for certain perturbations of small but finite size through nonlinear processes.

Some comments are also worthwhile in regards to the morphology of the eigenmodes. First, it should be emphasized that the form of Equation 2.16 is fully general for the system at hand and does not constrain the three-dimensional structure of the perturbations.

As a result, the sense of winding of non-axisymmetric disturbance modes is not always clear. This is in contrast to "weakly-global" approaches, such as that presented in the next section, which restrict the perturbations to strictly helical forms constrained by a uniform axial wavenumber (*i.e.* helical pitch) across each axial station, thereby imposing a definite sense of winding. Second, due to fact that the perturbations are real, the conjugate symmetry $\hat{\boldsymbol{q}}_m = \hat{\boldsymbol{q}}^*_{-m}$ holds for the modes of Equation 2.16. This guarantees that any mode associated with properties (m, σ, f) has an equivalent conjugate with $(-m, \sigma, -f)$. Consequently, this thesis takes $m \leq 0$ without loss of generality.

Finally, a remark is worthwhile on the sense of rotation of the perturbations. The azimuthal phase velocity of the perturbations is given by $-2\pi f/m$ according to Equation 2.16. Since the rotation of the pipe is positive with respect to the right hand rule along the x-axis, non-axisymmetric structures with $f > 0$ rotate in the same direction as the pipe due to the choice of $m \leq 0$. Henceforth, such structures will be simply referred to as co-rotating, while those with $f < 0$ will be termed counter-rotating. Unsteady $m = 0$ structures do not have a sense of rotation due to axisymmetry. In order to avoid confusion with regards to the various sign conventions used in existing studies, results will be reported exclusively in terms of unsigned values for the azimuthal periodicity $|m|$ and use the frequency to indicate the rotation direction of non-axisymmetric structures with respect to the pipe's rotation.

Identification and continuation of local bifurcation points

By definition, a generic local bifurcation point simultaneously satisfies Equation 2.10 and Equation 2.17 with $\sigma = 0$. Thus, bifurcation points correspond to solutions of the system,

$$\mathcal{R}_0\left(\boldsymbol{q}_0, \alpha\right) = 0, \tag{2.18a}$$

$$\mathcal{L}_m\left(\boldsymbol{q}_0, f, \alpha\right)\hat{\boldsymbol{q}}_m = 0, \tag{2.18b}$$

where $\mathcal{L}_m(\boldsymbol{q}_0, f, \alpha) = \mathrm{i}2\pi f\mathcal{M} + \mathcal{J}_m(\boldsymbol{q}_0, \alpha)$. With the addition of a normalization condition to fix the amplitude and phase of the bifurcating eigenmode, a Newton method to solve Equation 2.18 can be easily derived. However, the most straightforward approach requires the explicit formation and factorization of a large bordered matrix associated with a fully-augmented linearized system at each iteration. To reduce computational cost, our implementation leverages an exact block Crout decomposition similar to that used in LOCA [109] which breaks the large system into smaller, more tractable pieces.

In the general case of a non-axisymmetric Hopf bifurcation (*i.e.* a codimension-1 bifurcation associated with nonzero m and f), the solution process requires the resolution of Equation 2.11, Equation 2.13, and three complex sub-problems given by,

$$\mathcal{L}_m(\boldsymbol{q}_0, f, \alpha)\,\hat{\boldsymbol{w}}_m = \mathcal{H}_m(\hat{\boldsymbol{q}}_m)\,\delta\boldsymbol{q}_0, \tag{2.19a}$$

$$\mathcal{L}_m(\boldsymbol{q}_0, f, \alpha)\,\hat{\boldsymbol{b}}_m = \frac{\partial\mathcal{L}_m(\boldsymbol{q}_0, f, \alpha)\,\boldsymbol{q}_m}{\partial\alpha} - \mathcal{H}_m(\hat{\boldsymbol{q}}_m)\,\boldsymbol{y}_{\boldsymbol{q}}, \tag{2.19b}$$

$$\mathcal{L}_m(\boldsymbol{q}_0, f, \alpha)\,\hat{\boldsymbol{c}}_m = \mathrm{i}2\pi\mathcal{M}\hat{\boldsymbol{q}}_m, \tag{2.19c}$$

where $\hat{\boldsymbol{w}}_m$, $\hat{\boldsymbol{b}}_m$, and $\hat{\boldsymbol{c}}_m$ are intermediate solution vectors. In Equation 2.19, the vector $\partial\mathcal{L}_m\boldsymbol{q}_m/\partial\alpha$ is approximated via finite differences and $\mathcal{H}$ is the Hessian tensor derived from $\mathcal{L}_m$ which is given explicitly in Appendix C. Importantly, this forward substitution process only requires the sparse matrices $\mathcal{J}_0$ and $\mathcal{L}_m$ to be assembled and factored once at each iteration. Then, the required correction can be deduced from back substitution as,

$$\Delta f = \frac{\mathrm{Im}\left\{\hat{\boldsymbol{q}}_m^{\mathrm{H}}\hat{\boldsymbol{b}}_m\right\}\left(1 - \mathrm{Re}\left\{\hat{\boldsymbol{q}}_m^{\mathrm{H}}\hat{\boldsymbol{w}}_m\right\}\right) + \mathrm{Re}\left\{\hat{\boldsymbol{q}}_m^{\mathrm{H}}\hat{\boldsymbol{b}}_m\right\}\mathrm{Im}\left\{\hat{\boldsymbol{q}}_m^{\mathrm{H}}\hat{\boldsymbol{w}}_m\right\}}{\mathrm{Im}\left\{\hat{\boldsymbol{q}}_m^{\mathrm{H}}\hat{\boldsymbol{b}}_m\right\}\mathrm{Re}\left\{\hat{\boldsymbol{q}}_m^{\mathrm{H}}\hat{\boldsymbol{c}}_m\right\} - \mathrm{Re}\left\{\hat{\boldsymbol{q}}_m^{\mathrm{H}}\hat{\boldsymbol{b}}_m\right\}\mathrm{Im}\left\{\hat{\boldsymbol{q}}_m^{\mathrm{H}}\hat{\boldsymbol{c}}_m\right\}}, \tag{2.20a}$$

$$\Delta\alpha = \frac{1 - \mathrm{Re}\left\{\hat{\boldsymbol{q}}_m^{\mathrm{H}}\hat{\boldsymbol{w}}_m\right\} - \mathrm{Re}\left\{\hat{\boldsymbol{q}}_m^{\mathrm{H}}\hat{\boldsymbol{c}}_m\right\}\Delta f}{\mathrm{Re}\left\{\hat{\boldsymbol{q}}_m^{\mathrm{H}}\hat{\boldsymbol{b}}_m\right\}}, \tag{2.20b}$$

$$\Delta\boldsymbol{q}_0 = \delta\boldsymbol{q}_0 - \boldsymbol{y}_{\boldsymbol{q}}\Delta\alpha, \tag{2.20c}$$

$$\hat{\boldsymbol{q}}_m = \hat{\boldsymbol{w}}_m + \hat{\boldsymbol{b}}_m\Delta\alpha - \hat{\boldsymbol{c}}_m\Delta f. \tag{2.20d}$$

To complete the iteration, the state is updated $(\boldsymbol{q}_0, \alpha, f)^{\mathrm{T}} \leftarrow (\boldsymbol{q}_0, \alpha, f)^{\mathrm{T}} - (\Delta\boldsymbol{q}_0, \Delta\alpha, \Delta f)^{\mathrm{T}}$ and $\hat{\boldsymbol{q}}_m \leftarrow \hat{\boldsymbol{q}}_m / \|\hat{\boldsymbol{q}}_m\|$. This procedure is repeated until the norm of the residual of Equation 2.18 converges within the tolerance, (*i.e.* until $\sqrt{\|\mathcal{R}_0\|^2 + \|\mathcal{L}_m\hat{\boldsymbol{q}}_m\|^2} < 10^{-10}$).

Note that in the special case of a limit point, the algorithm above can be significantly simplified. In that case, all arithmetic is real and $\mathcal{J}_0 = \mathcal{L}_m$ since $m = f = 0$. Thus, only one matrix factorization is required, and Equation 2.19c and Equation 2.20a can be omitted since $\hat{\boldsymbol{c}}_m$ and δf are zero.

After a bifurcation point is identified with respect to the primary parameter α, its associated neutral curve may be traced along a second parameter β using predictor-corrector methods. This thesis adopts a zeroth-order approach where the predictor increments β by some amount h and takes the first step in the Newton scheme for Equation 2.18 using Equation 2.19 and Equation 2.20. Then, the corrector completes the remaining Newton iterations subject to the same requirements given in subsubsection 2.1.3, and h is adjusted according to the same adaptive strategy. When necessary, continuation around codimension-2 bifurcation points is achieved by exchanging the roles of the parameters α and β in this procedure.

Identification and continuation of periodic orbits

Following a Hopf bifurcation, a family of periodic solutions to Equation 2.9 branches from the axisymmetric equilibrium. Expanding these solutions into a temporal-azimuthal Fourier series truncated at level N allows the discrete representation,

$$\boldsymbol{q}(x, r, \theta, t) = \bar{\boldsymbol{q}}_0(x, r) + \sum_{j=1}^{N} \left[\hat{\boldsymbol{q}}_{jm}(x, r)\, e^{\mathrm{i}jm\theta + \mathrm{i}2j\pi ft} + \hat{\boldsymbol{q}}^*_{jm}(x, r)\, e^{-\mathrm{i}jm\theta - \mathrm{i}2j\pi ft}\right], \quad (2.21)$$

where $\bar{\boldsymbol{q}}_0$ represents the time- and azimuth-mean flow and the $\hat{\boldsymbol{q}}_{jm}$ represent the various harmonic components of the nonlinear oscillation. Note that the comments regarding the morphology and rotation of the eigenmodes given in subsubsection 2.1.3 also apply to the

Fourier components in this expansion.

Substituting the expansion of Equation 2.21 into Equation 2.9 and evaluating the result in Fourier space yields a discrete time-azimuthal spectral representation of the unsteady Navier-Stokes system governing periodic orbits. The resulting "harmonic-balanced" [110] system for the non-reacting case is,

$$\mathcal{R}_0\left(\bar{\boldsymbol{q}}_0\right) + \sum_{j=1}^{N} \mathcal{H}_0\left(\hat{\boldsymbol{q}}_{jm}^*\right)\hat{\boldsymbol{q}}_{jm} = 0, \quad (2.22a)$$

$$\frac{1}{2}\sum_{j=1}^{k-1} \mathcal{H}_{km}\left(\hat{\boldsymbol{q}}_{(k-j)m}\right)\hat{\boldsymbol{q}}_{jm} + \mathcal{L}_{km}\left(\bar{\boldsymbol{q}}_0, kf\right)\hat{\boldsymbol{q}}_{km} + \sum_{j=k+1}^{N} \mathcal{H}_{km}\left(\hat{\boldsymbol{q}}_{(j-k)m}^*\right)\hat{\boldsymbol{q}}_{jm} = 0, \quad (2.22b)$$

where Equation 2.22b is written for $k = 1, 2, \ldots, N$ and any terms involving harmonics higher than level N are discarded by the truncation. Here, the summations account for the coupling effect of Reynolds stresses resulting from nonlinear interactions among the various harmonics. More specifically, the mean Reynolds stress term in Equation 2.22a describes the steady, axisymmetric forcing generated by accumulating the interactions of each unsteady component with its corresponding conjugate. Similarly, the oscillatory Reynolds stress terms in Equation 2.22b describe the unsteady forcing associated with each Fourier component via sum and difference harmonic interactions. Note that Equation 2.22 is only valid as written here for the non-reacting case. The system for the reacting case is more complex due to triadic nonlinear interactions and is not considered in this thesis.

Since Equation 2.9 is autonomous, the frequency f of the orbit is unknown and must be determined in a coupled manner with $\boldsymbol{q}$ during the solution process. To uniquely define the solution with respect to a fixed phase reference along the orbit, the integral phase condition [111] is utilized to yield the additional constraint,

$$\sum_{j=1}^{N} j\left(\hat{\boldsymbol{q}}_{jm}^{\mathrm{H}}\mathcal{M}\hat{\boldsymbol{q}}_{jm}^* - \hat{\boldsymbol{q}}_{jm}^{\mathrm{H}}\mathcal{M}\hat{\boldsymbol{q}}_{jm}\right) = 0. \quad (2.22c)$$

Accordingly, the nonlinear system of Equation 2.22 is fully-specified.

One strategy to solve Equation 2.22 is to fix all parameters and iteratively refine an initial guess for a periodic orbit. This is analogous to the procedure for steady states associated with Equation 2.11. For convenience, the following notation is introduced for the N-th order discrete Fourier representation of a harmonic-balanced quantity with an azimuthally m-periodic fundamental component in real arithmetic,

$$\tilde{\boldsymbol{q}}_m^N = \left(\bar{\boldsymbol{q}}_0, \mathrm{Re}\left\{\hat{\boldsymbol{q}}_m\right\}, \mathrm{Im}\left\{\hat{\boldsymbol{q}}_m\right\}, \ldots, \mathrm{Re}\left\{\hat{\boldsymbol{q}}_{Nm}\right\}, \mathrm{Im}\left\{\hat{\boldsymbol{q}}_{Nm}\right\}\right)^{\mathrm{T}}. \tag{2.23}$$

The solution process is based on a block factorization scheme which algebraically isolates Equation 2.22c from the augmented system. In each step, it first finds intermediate vectors $\tilde{\boldsymbol{v}}_m^N$ and $\tilde{\boldsymbol{a}}_m^N$ which satisfy,

$$\tilde{\mathcal{J}}_m^N\left(\tilde{\boldsymbol{q}}_m^N, f\right)\tilde{\boldsymbol{v}}_m^N = \tilde{\mathcal{R}}_m^N\left(\tilde{\boldsymbol{q}}_m^N, f\right), \tag{2.24a}$$

$$\tilde{\mathcal{J}}_m^N\left(\tilde{\boldsymbol{q}}_m^N, f\right)\tilde{\boldsymbol{a}}_m^N = \frac{\partial\tilde{\mathcal{R}}_m^N\left(\tilde{\boldsymbol{q}}_m^N, f\right)}{\partial f}, \tag{2.24b}$$

where $\tilde{\mathcal{R}}_m^N\left(\tilde{\boldsymbol{q}}_m^N, f\right)$ is the combined residual of Equation 2.22a and Equation 2.22b in real arithmetic, $\tilde{\mathcal{J}}_m^N\left(\tilde{\boldsymbol{q}}_m^N, f\right) = \partial\tilde{\mathcal{R}}_m^N/\partial\tilde{\boldsymbol{q}}_m^N$ is the associated real Jacobian matrix given by,

$$\begin{bmatrix} \mathcal{J}_0\left(\bar{\boldsymbol{q}}_0\right) & \mathrm{Re}\left\{\mathcal{H}_0\left(\hat{\boldsymbol{q}}_m^*\right) + \mathcal{H}_0^*\left(\hat{\boldsymbol{q}}_m\right)\right\} & \mathrm{Im}\left\{-\mathcal{H}_0\left(\hat{\boldsymbol{q}}_m^*\right) + \mathcal{H}_0^*\left(\hat{\boldsymbol{q}}_m\right)\right\} & \cdots \\ \mathrm{Re}\left\{\mathcal{H}_m\left(\hat{\boldsymbol{q}}_m\right)\right\} & \mathrm{Re}\left\{\mathcal{L}_m\left(\bar{\boldsymbol{q}}_0, f\right) + \mathcal{H}_m^*\left(\hat{\boldsymbol{q}}_{2m}\right)\right\} & \mathrm{Im}\left\{-\mathcal{L}_m\left(\bar{\boldsymbol{q}}_0, f\right) + \mathcal{H}_m^*\left(\hat{\boldsymbol{q}}_{2m}\right)\right\} & \cdots \\ \mathrm{Im}\left\{\mathcal{H}_m\left(\hat{\boldsymbol{q}}_m\right)\right\} & \mathrm{Im}\left\{\mathcal{L}_m\left(\bar{\boldsymbol{q}}_0, f\right) + \mathcal{H}_m^*\left(\hat{\boldsymbol{q}}_{2m}\right)\right\} & \mathrm{Re}\left\{\mathcal{L}_m\left(\bar{\boldsymbol{q}}_0, f\right) - \mathcal{H}_m^*\left(\hat{\boldsymbol{q}}_{2m}\right)\right\} & \ddots \\ \vdots & \vdots & \ddots & \ddots \end{bmatrix}, \tag{2.25}$$

and $\partial\tilde{\mathcal{R}}_m^N/\partial f = 2\pi\left(0, -\mathcal{M}\mathrm{Im}\left\{\hat{\boldsymbol{q}}_m\right\}, \mathcal{M}\mathrm{Re}\left\{\hat{\boldsymbol{q}}_m\right\}, \ldots, -N\mathcal{M}\mathrm{Im}\left\{\hat{\boldsymbol{q}}_{Nm}\right\}, N\mathcal{M}\mathrm{Re}\left\{\hat{\boldsymbol{q}}_{Nm}\right\}\right)^{\mathrm{T}}$. The resolution of Equation 2.24 relies on iterative Krylov subspace methods as discussed below, and a significant savings is realized by applying the same factorization of the preconditioner during the iterations for both equations.

Once intermediate vectors are obtained from Equation 2.24, the corrections which com-

plete the Newton step for Equation 2.22 are determined via,

$$\delta f = \frac{\left(\tilde{\boldsymbol{\phi}}_m^N\right)^{\mathrm{T}} \tilde{\boldsymbol{v}}_m^N}{\left(\tilde{\boldsymbol{\phi}}_m^N\right)^{\mathrm{T}} \tilde{\boldsymbol{a}}_m^N} \tag{2.26a}$$

$$\delta\tilde{\boldsymbol{q}}_m^N = \tilde{\boldsymbol{v}}_m^N - \tilde{\boldsymbol{a}}_m^N \delta f, \tag{2.26b}$$

where $\tilde{\boldsymbol{\phi}}_m^N = \left(0, \mathcal{M}\Re\left\{\hat{\boldsymbol{q}}_m\right\}, -\mathcal{M}\Im\left\{\hat{\boldsymbol{q}}_m\right\}, \ldots, N\mathcal{M}\Re\left\{\hat{\boldsymbol{q}}_{Nm}\right\}, -N\mathcal{M}\Im\left\{\hat{\boldsymbol{q}}_{Nm}\right\}\right)^{\mathrm{T}}$ is a phase reference derived by linearizing Equation 2.22c. Then, the solution is updated $\left(\tilde{\boldsymbol{q}}_m^N, f\right) \leftarrow \left(\tilde{\boldsymbol{q}}_m^N, f\right) - \left(\delta\tilde{\boldsymbol{q}}_m^N, \delta f\right)$, and the process is repeated until the norm of the residual of Equation 2.22 converges within the tolerance.

After a branch of periodic solutions has been identified, parametric continuation is performed using a Moore-Penrose predictor-corrector scheme in a similar manner to the approach based on Equation 2.14. In the case where the periodic state is initialized from a Hopf point, the initial null vector is simply the bifurcating eigenvector. However, in general, the harmonic-balance null vector $\tilde{\boldsymbol{y}} = \left(\tilde{\boldsymbol{y}}_{\boldsymbol{q},m}^N, \tilde{y}_f, \tilde{y}_\alpha\right)^{\mathrm{T}} \in \ker\left(\tilde{\mathcal{J}}_m^N, \partial\tilde{\mathcal{R}}_0^N/\partial f, \partial\tilde{\mathcal{R}}_m^N/\partial\alpha\right)$ is determined by setting $\tilde{y}_\alpha = -1$ and solving Equation 2.24b and

$$\tilde{\mathcal{J}}_m^N\left(\tilde{\boldsymbol{q}}_m^N, f, \alpha\right)\tilde{\boldsymbol{b}}_m^N = \frac{\partial\tilde{\mathcal{R}}_0^N\left(\tilde{\boldsymbol{q}}_m^N, f, \alpha\right)}{\partial\alpha}, \tag{2.27}$$

where $\partial\tilde{\mathcal{R}}_m^N/\partial\alpha$ is approximated via finite differences. Then, using the Schur complement, the null vector is found as,

$$\tilde{y}_f = \frac{\left(\tilde{\boldsymbol{\phi}}_m^N\right)^{\mathrm{T}} \tilde{\boldsymbol{b}}_m^N}{\left(\tilde{\boldsymbol{\phi}}_m^N\right)^{\mathrm{T}} \tilde{\boldsymbol{a}}_m^N} \tag{2.28a}$$

$$\tilde{\boldsymbol{y}}_{\boldsymbol{q},m}^N = \tilde{\boldsymbol{b}}_m^N - \tilde{\boldsymbol{a}}_m^N \tilde{y}_f. \tag{2.28b}$$

Once the null vector is known, the prediction is obtained as in subsubsection 2.1.3 using the step parameter h. Next, the Moore-Penrose correction orthogonal to the null vector is

determined by solving the augmented problem,

$$\begin{pmatrix} \tilde{\mathcal{J}}_m^N\left(\tilde{\boldsymbol{q}}_m^N, f, \alpha\right) & \frac{\partial \tilde{\mathcal{R}}_m^N\left(\tilde{\boldsymbol{q}}_m^N, f, \alpha\right)}{\partial f} & \frac{\partial \tilde{\mathcal{R}}_m^N\left(\tilde{\boldsymbol{q}}_m^N, f, \alpha\right)}{\partial \alpha} \\ \left(\tilde{\boldsymbol{\phi}}_m^N\right)^{\mathrm{T}} & 0 & 0 \\ \left(\tilde{\boldsymbol{y}}_{\boldsymbol{q},m}^N\right)^{\mathrm{T}} & \tilde{y}_f & \tilde{y}_\alpha \end{pmatrix} \begin{pmatrix} \Delta\tilde{\boldsymbol{q}}_m^N \\ \Delta f \\ \Delta\alpha \end{pmatrix} = \begin{pmatrix} \mathcal{R}_m^N\left(\tilde{\boldsymbol{q}}_m^N, f, \alpha\right) \\ 0 \\ 0 \end{pmatrix}. \quad (2.29)$$

As in the steady case, Equation 2.29 is broken up and solved using a bordering algorithm. The null vector is determined using Equation 2.24b, Equation 2.27, Equation 2.28, and Equation 2.26a to find $\tilde{\boldsymbol{a}}_m^N$, $\tilde{\boldsymbol{b}}_m^N$, $\tilde{y}_f$, $\tilde{\boldsymbol{y}}_{\boldsymbol{q},m}^N$, and δf, respectively. Then, Equation 2.24a is solved and the Moore-Penrose Newton correction is backed out algebraically via

$$\Delta\alpha = \frac{\left(\tilde{\boldsymbol{y}}_{\boldsymbol{q},m}^N\right)^{\mathrm{T}} \tilde{\boldsymbol{v}}_m^N + \left[y_f - \left(\tilde{\boldsymbol{y}}_{\boldsymbol{q},m}^N\right)^{\mathrm{T}} \tilde{\boldsymbol{a}}_m^N\right] \delta f}{1 + \left(\tilde{\boldsymbol{y}}_{\boldsymbol{q},m}^N\right)^{\mathrm{T}} \tilde{\boldsymbol{y}}_{\boldsymbol{q}} + y_f^2}, \quad (2.30a)$$

$$\Delta f = \delta f - y_f \Delta\alpha, \quad (2.30b)$$

$$\Delta\tilde{\boldsymbol{q}}_m^N = \tilde{\boldsymbol{v}}_m^N - \tilde{\boldsymbol{a}}_m^N \Delta f - \tilde{\boldsymbol{b}}_m^N \Delta\alpha. \quad (2.30c)$$

Finally, the solution and null vector are updated as before until reaching convergence. For efficiency, the same factorization of the preconditioner is applied for all of the corrector iterations, and the continuation process follows the same convergence requirements and adaptive sizing strategy as described in subsubsection 2.1.3.

The solution process for Equation 2.22 is handled entirely in the spectral domain. For each limit cycle, the order N of the scheme is initialized at $N = 4$ and refined based on an iterative process which ensures that the highest resolved harmonic contains less than 1% of the total unsteady kinetic energy in the domain. If the amplitude of the highest harmonic exceeds this threshold, the value of N is increased by one and the continuation process for that cycle is repeated from the beginning. Using this approach, the highest order required for any limit cycle considered in this thesis was $N = 6$, with higher oscillation amplitudes typically requiring higher N.

As mentioned above, the numerical procedure itself is based on straightforward ex-

tensions of the fixed-parameter and predictor-corrector methods discussed in subsubsection 2.1.3. Nonetheless, unlike the earlier systems which could be efficiently solved using distributed direct methods combined with block factorization algorithms, Equation 2.22 is not amenable to direct Newton approaches due to the large size and block-dense structure of its associated Jacobian matrix (see Equation 2.25). To avoid such costs, this work resorts to iterative Newton-Krylov approaches. While a detailed analysis and optimization of these numerics is beyond the scope of this thesis, after some exploration, it was found that the Generalized Minimal Residual (GMRES) algorithm [112] is both a computationally tractable and numerically robust approach when used in conjunction with a suitable preconditioner and a backward-stable projection step. The implementation used here leverages a block-Jacobi right preconditioner based on memory-efficient low-rank approximate factorizations for the blocks along the main diagonal of the Jacobian matrix using the block low-rank capability of MUMPS [102]. After applying the preconditioner, the Arnoldi iterations are performed using the iteratively-refined Gram-Schmidt routine available in PETSc [101]. With this approach, the dimension of the Krylov subspace required to attain convergence of the linear systems ranges from $O(10)$ to $O(100)$, with faster convergence occurring when harmonic interactions are small and the diagonal blocks are dominant. As far as the results are concerned however, these numerical details are only of minor importance since convergence of Equation 2.22 is defined using the same threshold as the previous systems (*i.e.* an overall residual norm below 10^{-10}).

2.2 Turbulent problem

This section focuses on developing a mean flow stability analysis framework for modeling the response of measured turbulent, reacting, swirling jets to external acoustic forcing. The main objective is to predict the hydrodynamic response of the turbulent system to imposed acoustic excitation based only on experimental measurements from the unforced flow and a physics-based model which will be formulated below.

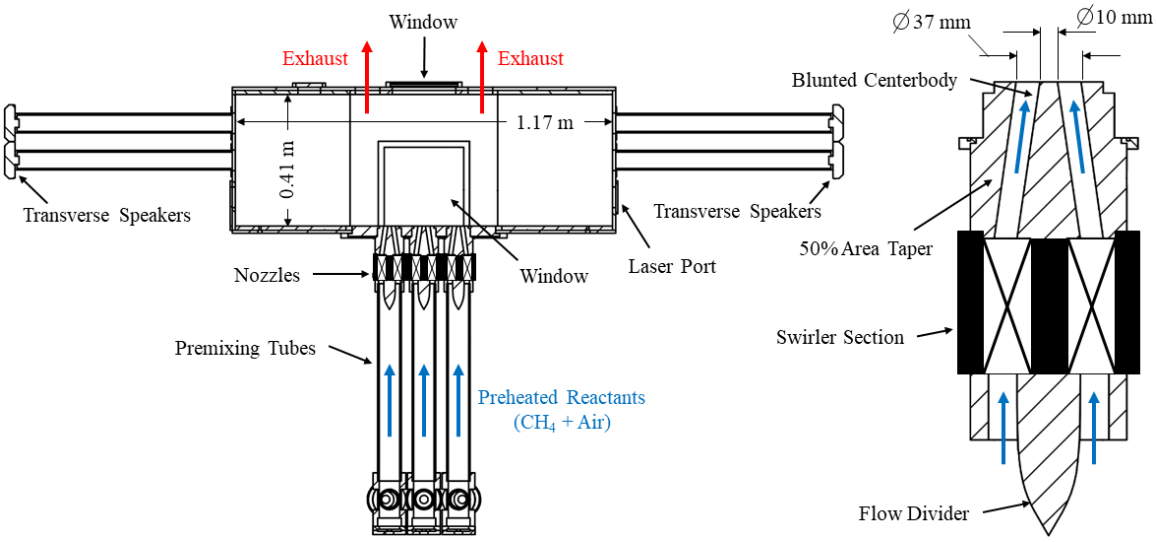

Figure 2.2: Schematic of experimental facility and nozzle geometry.

2.2.1 Facility

Before moving on to the modeling approach, a brief overview of the experimental facility is helpful for context. The measurements which will form the basis of this analysis have been reported previously in the works of Smith [6, 113, 114] and were all obtained in the experimental apparatus shown in Figure 2.2. This optically-accessible facility features a linear array of swirled annular nozzles with fuel and air flow rates that can be controlled independently. The combustor box has a high aspect ratio cross-section to accommodate transverse planar acoustic waves and is equipped with speakers to independently excite longitudinal and transverse acoustics. This design emulates an "unwrapped" version of the environment within industrial gas turbine annular combustors where transverse acoustic waves can have a significant influence on the system behavior [115]. The test facility is also outfitted with an electric heater that is used to preheat the combustor's air supply. High-speed planar measurement techniques including stereoscopic PIV and synchronized OH-PLIF were used for flow and flame characterization. Further details of the diagnostics and test conditions will be described in chapter 5 and chapter 6.

2.2.2 Linearization scheme

In the case of laminar flow discussed in section 2.1, the stability analysis was presented to determine the asymptotic time evolution of infinitesimal perturbations (which arise spontaneously) to steady solutions of the governing equations. This resulted in an eigenvalue problem for the perturbations (Equation 2.17) which is linear with respect to the axisymmetric steady flow. Conversely, in the approach derived here, the linearization is performed about the time-average of an unsteady flowfield rather than a true equilibrium of the governing equations, and the perturbations are imposed by external acoustic forcing. Mathematically, these are both very important distinctions which require special modifications to yield a rigorous approach.

The treatment presented here follows the argument outlined by Tammisola & Juniper [77] for non-reacting flows and applied to a reacting flow by Manoharan et al. [78]. It is based on the triple decomposition proposed by Hussain & Reynolds [53, 116, 117] which separates the fluctuating part of the usual mean/fluctuating Reynolds decomposition into coherent and incoherent parts, i.e.

$$\psi\left(\boldsymbol{x},t\right)=\overline{\psi}\left(\boldsymbol{x}\right)+\widetilde{\psi}\left(\boldsymbol{x},t\right)+\acute{\psi}\left(\boldsymbol{x},t\right), \tag{2.31}$$

for any quantity $\psi\left(\boldsymbol{x},t\right)$. The steady part is defined by the weighted time-average,

$$\overline{\psi}\left(\boldsymbol{x}\right)=\lim_{T\to\infty}\int_{0}^{T}w\left(\boldsymbol{x},t\right)\psi\left(\boldsymbol{x},t\right)\,\mathrm{d}t, \tag{2.32}$$

where $w\left(\boldsymbol{x},t\right)$ is some weighting function. The coherent part is based on the ensemble-average of zero time-mean periodic structures with frequency f at the same point of phase (i.e. the phase-average less the time-mean). The weighted phase-average is defined as,

$$\left\langle\psi\right\rangle\left(\boldsymbol{x},t\right)=\lim_{N\to\infty}\sum_{n=0}^{N}w\left(\boldsymbol{x},t+\frac{n}{f}\right)\psi\left(\boldsymbol{x},t+\frac{n}{f}\right), \tag{2.33}$$

leading to the following definition for the coherent oscillations,

$$\widetilde{\psi}\left(\boldsymbol{x},t\right)=\left\langle\psi\right\rangle\left(\boldsymbol{x}\right)-\overline{\psi}\left(\boldsymbol{x}\right). \tag{2.34}$$

Finally, the incoherent part $\acute{\psi}\left(\boldsymbol{x},t\right)$ consists of the leftover fluctuations unexplained by the sum of the mean and coherent parts. With these definitions and no further assumptions, the time- and phase-averages of incoherent quantities are exactly zero, meaning that the triple decomposition is an exact and complete representation of the turbulent flowfield.

Based on the definitions above, the identification of the mean and coherent parts of the flow is straightforward. The time mean is directly determined by averaging the available data over time. For determination of the coherent part of the flow, the appropriate approach depends on the way the data is sampled. If data is available at a constant sampling frequency, as will be the case in chapter 5, the output of Equation 2.33 is equivalent to a Fourier transform, and the phase averaging operation can be directly determined using the discrete Fourier transform. However, in the case where the sampling is not uniformly spaced in time, as in chapter 6, the Fourier transform cannot be directly applied and a more general phase averaging approach is needed. In that case, the phase average is determined by directly evaluating Equation 2.33 in the time domain, using a small phase tolerance to ensure a sufficient number of samples are collected in each phase ensemble.

The turbulent flow will be assumed to be governed by the same low-Mach number reacting equations presented above in Equation 2.2. However, as the flow is measured rather than modeled, it is difficult to identify flame parameters (here *Da* and *Ze*) which reflect the true flame's behavior with any reasonable degree of certainty. To avoid generating spurious effects related to this uncertainty, the reaction term will be ignored in the present model by setting $Da=0$, meaning that all identified instabilities will be completely hydrodynamic in origin. Nonetheless, it should be emphasized that neglecting the reaction term in the stability equations does not equate to neglecting reactions altogether. The effects of com-

bustion and heat release are still captured through their various effects on the experimental mean flowfield. Only the role of heat release *perturbations* is neglected in the final model. Following this assumption, it is convenient to rewrite Equation 2.2 in terms of the density ρ and temperature T instead of the flame PVF. The new system, which is completely equivalent to Equation 2.2 for $Da = 0$, is,

$$\frac{\partial \rho}{\partial t} + \boldsymbol{\nabla} \cdot (\rho \boldsymbol{u}) = 0, \tag{2.35a}$$

$$\rho \left(\frac{\partial \boldsymbol{u}}{\partial t} + \boldsymbol{u} \cdot \boldsymbol{\nabla} \boldsymbol{u} \right) = -\boldsymbol{\nabla} p + \frac{1}{Re} \nabla^2 \boldsymbol{u}, \tag{2.35b}$$

$$\boldsymbol{\nabla} \cdot \widetilde{\boldsymbol{u}} = \frac{1}{Pe} \nabla^2 T \tag{2.35c}$$

$$1 = \rho T. \tag{2.35d}$$

To formulate the mean flow stability analysis, all of the variables in Equation 2.35 are first expanded in terms of the triple decomposition. Here, as in Manoharan et al. [78], a Favré averaging approach is used, where the decompositions for ρ and p are based on unweighted averages (i.e. $w = 1$) and the decompositions for $\boldsymbol{u}$ and T are based on mass averages (i.e. $w = \rho/\overline{\rho}$ and $w = \rho/\langle\rho\rangle$ for the time- and phase-averages, respectively). The equations governing the coherent oscillation are identified by taking the difference of the ensemble-averaged and time-averaged equations and invoking the assumption that the incoherent fluctuations represent a zero-mean stochastic process. Note that the mean flow is determined directly from the experiments and does not need to be modeled, hence there

is no need of the time-averaged equations. Thus, the nonlinear coherent equations are,

$$\frac{\partial\widetilde{\rho}}{\partial t} + \boldsymbol{\nabla}\cdot(\widetilde{\rho}\,\overline{\boldsymbol{u}}) + \boldsymbol{\nabla}\cdot(\overline{\rho}\,\widetilde{\boldsymbol{u}}) = 0, \tag{2.36a}$$

$$\overline{\rho}\left(\frac{\partial\widetilde{\boldsymbol{u}}}{\partial t} + \widetilde{\boldsymbol{u}}\cdot\boldsymbol{\nabla}\overline{\boldsymbol{u}} + \overline{\boldsymbol{u}}\cdot\boldsymbol{\nabla}\widetilde{\boldsymbol{u}}\right) + \widetilde{\rho}\,\overline{\boldsymbol{u}}\cdot\boldsymbol{\nabla}\overline{\boldsymbol{u}} = -\boldsymbol{\nabla}\widetilde{p} + \frac{1}{Re}\nabla^2\widetilde{\boldsymbol{u}} - \boldsymbol{\nabla}\cdot\widetilde{(\rho\widetilde{\boldsymbol{u}}\widetilde{\boldsymbol{u}})} - \boldsymbol{\nabla}\cdot\widetilde{(\rho\acute{\boldsymbol{u}}\acute{\boldsymbol{u}})}, \tag{2.36b}$$

$$\boldsymbol{\nabla}\cdot\widetilde{\boldsymbol{u}} = \frac{1}{Pe}\nabla^2\widetilde{T} - \boldsymbol{\nabla}\cdot\widetilde{\left(\rho\widetilde{\boldsymbol{u}}\widetilde{T}\right)} - \boldsymbol{\nabla}\cdot\widetilde{\left(\rho\acute{\boldsymbol{u}}\acute{T}\right)}, \tag{2.36c}$$

$$0 = \overline{\rho}\widetilde{T} + \widetilde{\rho}\overline{T}. \tag{2.36d}$$

Comparing Equation 2.36 with Equation 2.35, it is clear that the Faveré averaging process has resulted in two new sets of terms which appear on the right hand side of Equation 2.36b and Equation 2.36c. Specifically, the terms $\nabla\cdot\widetilde{(\rho\widetilde{\boldsymbol{u}}\widetilde{\boldsymbol{u}})}$ and $\nabla\cdot\widetilde{\left(\rho\widetilde{\boldsymbol{u}}\widetilde{T}\right)}$ capture the coherent effect of coherent oscillations nonlinearly interacting with themselves and their harmonics. Additionally, the terms $\nabla\cdot\widetilde{(\rho\acute{\boldsymbol{u}}\acute{\boldsymbol{u}})}$ and $\nabla\cdot\widetilde{\left(\rho\acute{\boldsymbol{u}}\acute{T}\right)}$ describe the statistical coherent effect of self-interactions among incoherent fluctuations.

At this stage, the coherent equations require additional assumptions to yield a closed system for the coherent oscillation. To achieve this, it is first assumed that the coherent component of the self-interactions among the fundamental coherent oscillation and its harmonics is negligible such that $\nabla\cdot\widetilde{(\rho\widetilde{\boldsymbol{u}}\widetilde{\boldsymbol{u}})} = \nabla\cdot\widetilde{\left(\rho\widetilde{\boldsymbol{u}}\widetilde{T}\right)} = 0$. Crucially, without these terms, the coherent system is linear with respect to the coherent flow components. This subtlety is an important distinction between the turbulent mean flow stability analysis and the classical linear stability analysis adopted for laminar flows. Whereas the linearity of the classical approach hinges on the asymptotic smallness of the perturbations, the mean flow stability analysis instead depends on the much weaker assumption that coherent effect of the coherent harmonic interactions is negligible, regardless of the coherent oscillations' amplitude.

Next, Boussinesq's hypothesis is invoked such that the coherent transport of momentum by incoherent motions can be modeled using the mean eddy viscosity $\overline{\mu}_T(\boldsymbol{x})$. Practically, this assumption amounts to the requirements that,

$$\overline{\rho \acute{\boldsymbol{u}} \acute{\boldsymbol{u}}} = \tfrac{2}{3}\overline{k}\boldsymbol{I} - 2\overline{\mu}_T \overline{\boldsymbol{S}} \tag{2.37}$$

$$\widetilde{\rho \acute{\boldsymbol{u}} \acute{\boldsymbol{u}}} = \tfrac{2}{3}\widetilde{k}\boldsymbol{I} - 2\overline{\mu}_T \widetilde{\boldsymbol{S}} - 2\widetilde{\mu}_T \overline{\boldsymbol{S}}, \tag{2.38}$$

where $k = \frac{1}{2}\rho(\boldsymbol{u} - \overline{\boldsymbol{u}}) \cdot (\boldsymbol{u} - \overline{\boldsymbol{u}})$ is the Turbulent Kinetic Energy (TKE) and $\boldsymbol{S} = \boldsymbol{\nabla u} + (\boldsymbol{\nabla u})^{\mathrm{T}} - \frac{1}{3}(\boldsymbol{\nabla} \cdot \boldsymbol{u})\boldsymbol{I}$ is the deviatoric stress tensor. Following Tammisola & Juniper [77], the TKE and eddy viscosity are assumed to be unaffected by the coherent oscillation such that $\widetilde{k} = \widetilde{\mu}_T = 0$. The value of the mean eddy viscosity is then determined by projecting the measured Reynolds stress tensor from the experiments onto the scalar eddy viscosity model of Equation 2.37. This process results in an overdetermined system of equations which is satisfied in the least-squares sense via the relationship,

$$\overline{\mu}_T = -\frac{\left(\overline{\rho \acute{\boldsymbol{u}} \acute{\boldsymbol{u}}} - \frac{2}{3}\overline{k}\boldsymbol{I}\right) : \overline{\boldsymbol{S}}}{2\overline{\boldsymbol{S}} : \overline{\boldsymbol{S}}}, \tag{2.39}$$

where $\overline{\rho \acute{\boldsymbol{u}} \acute{\boldsymbol{u}}}$, $\overline{k}$, and $\overline{\boldsymbol{S}}$ are evaluated directly from the measurements. Altogether, the resulting model for the coherent transport of momentum by incoherent fluctuations is,

$$\widetilde{\rho \acute{\boldsymbol{u}} \acute{\boldsymbol{u}}} = -2\overline{\mu}_T \widetilde{\boldsymbol{S}}. \tag{2.40}$$

Similarly, the coherent thermal energy transport by incoherent motions is treated with a gradient diffusion model based on a constant turbulent Prandtl number assumption. In this approach, the turbulent thermal transport is captured by the same behavior, resulting in the dimensionless turbulent diffusion coefficient $\overline{\mathcal{D}}_T = \overline{\mu}_T$.

Applying the above simplifications to Equation 2.36, the coherent equations are closed and yield a linear system governing the dynamics of coherent oscillations in a turbulent

flow. Eliminating Equation 2.36d by substitution, the resulting linearized equations are,

$$\frac{\partial \widetilde{\rho}}{\partial t} + \boldsymbol{\nabla} \cdot (\widetilde{\rho}\,\overline{\boldsymbol{u}}) + \boldsymbol{\nabla} \cdot (\overline{\rho}\,\widetilde{\boldsymbol{u}}) = 0, \tag{2.41a}$$

$$\overline{\rho}\left(\frac{\partial \widetilde{\boldsymbol{u}}}{\partial t} + \widetilde{\boldsymbol{u}} \cdot \boldsymbol{\nabla}\overline{\boldsymbol{u}} + \overline{\boldsymbol{u}} \cdot \boldsymbol{\nabla}\widetilde{\boldsymbol{u}}\right) + \widetilde{\rho}\,\overline{\boldsymbol{u}} \cdot \boldsymbol{\nabla}\overline{\boldsymbol{u}} = -\boldsymbol{\nabla}\widetilde{p} + \frac{1}{Re}\boldsymbol{\nabla} \cdot \left[\left(1 + \overline{\mu}_T\right)\boldsymbol{\nabla}\widetilde{\boldsymbol{u}}\right], \tag{2.41b}$$

$$\boldsymbol{\nabla} \cdot \widetilde{\boldsymbol{u}} = -\frac{1}{Pe}\boldsymbol{\nabla} \cdot \left[\left(1 + \overline{\mathcal{D}}_T\right)\boldsymbol{\nabla}\left(\frac{\widetilde{\rho}}{\overline{\rho}^2}\right)\right]. \tag{2.41c}$$

Finally, under the further assumption of an axisymmetric mean flow, the normal modes expansion of Equation 2.16 may be introduced as an ansatz for the coherent oscillations (i.e. setting $\breve{\boldsymbol{q}} = \widetilde{\boldsymbol{q}}$). Note that even though the experimental configuration is not axisymmetric (see Figure 2.2), prior work has demonstrated that the mean flow is highly axisymmetric within the region of interest [113]. Therefore, Equation 2.41 can be cast in the form of the global linear eigenvalue problem given in Equation 2.17, thereby allowing the frequency and structure of natural coherent oscillations in the turbulent flow to be approximated by a linear analysis about the axisymmetric mean flow.

2.2.3 Weakly-global hydrodynamic stability analysis

Though useful for determining the natural (i.e. unforced) coherent flow dynamics, the homogeneous linear eigenvalue problem derived above is not suitable on its own for determining the coherent response due to acoustic forcing. One possible remedy for this issue would be to directly introduce a harmonic external forcing term to the governing equations, such that the response could be determined by solving a boundary value problem. Such a modification would, however, require detailed knowledge of the spatial distribution of the imposed forcing throughout the domain. At the small Mach numbers which characterize the flows considered in this thesis, the forcing effect from the external acoustics are strongly localized to the nozzle boundaries, where acoustic reflections induce small, coherent shear layer vortices that may be amplified or diminished as they convect along the flow. Unfortunately, due to the practical limitations of optical diagnostics, it is difficult to obtain

detailed flow measurements in these regions as the nozzle is not optically-accessible. Thus, a different approach is needed.

Another idea would be to separate the overall system response into separate 'inner' and 'outer' systems. In this framework, as noted by [78], the global approach expressed in the eigenvalue problem derived above represents a homogeneous 'outer' problem, which is valid throughout most of the domain where the localized forcing is insignificant. Then, an additional inhomogeneous 'inner' problem, valid at the locations near the nozzle boundaries where the acoustic coupling is present, would need to be formulated and solved. While local estimates of the forcing effects may be possible to obtain in very limited spatial regions, this approach would be challenging to formulate in a consistent way as the separate solutions which result from the inner and outer problems would need to match smoothly at the interface between their respective regions.

Rather than pursuing these ideas, the analysis considered here will leverage a so-called 'weakly-global' approach to analyze the response of the flow to acoustic forcing. This simpler technique is based on the Wentzel-Kramers-Brillouin-Jeffreys (WKBJ) theory of Chomaz et al. [118] and constructs weakly-global solutions for the natural hydrodynamic eigenmodes of the flow using a sequence of local parallel-flow stability analyses. In the unforced context of the weakly-global theory, these local analyses can be used to determine the natural "wavemaker" location and frequency in the flow, as shown by Juniper & Pier [119]. In the forced situation considered here, however, the imposed excitation represents the sole wavemaker for the hydrodynamic stability problem, provided the flow is not self-excited [74]. Thus, a leading-order prediction of the forced response may be determined through the WKBJ approach based on an imposed wavemaker located at the most upstream point resolved by the measurements and with a frequency equal to the forcing frequency [78]. Since it only requires local stability analyses, this method has the additional benefit of not requiring streamwise boundary conditions, which could represent a significant source of error in a fully-global framework due to the limited spatial extent of

the measurements.

Before moving on, it is worth briefly mentioning that the framework outlined above hinges on the assumption that the flow is not self-excited. If self-excited (i.e. "globally unstable") behavior were to be detected, on the other hand, the weakly-global analysis would become significantly more delicate as the forcing region would only represent one of the possible wavemaker regions [74, 119]. However, as will be shown in chapter 5, no self-excited behavior was detected for the flow considered in this thesis, indicating that such approaches are not necessary in the context of this particular analysis.

To proceed with formulating the local parallel-flow problems at each axial position, the WKBJ ansatz is introduced such that the modes of Equation 2.16 can be expressed in terms of local modes as,

$$\hat{\boldsymbol{q}}_m\left(x,r\right) = \hat{\boldsymbol{q}}_{Lm}\left(r;x\right)\exp\left(\mathrm{i}\int_{x_0}^{x} k(x')\,\mathrm{d}x'\right) \tag{2.42}$$

where k is the slowly-varying axial wavenumber, x_0 is the position of the wavemaker, and $\hat{\boldsymbol{q}}_{Lm}$ are the local modes where x appears as a parameter rather than an argument. As pointed out by Wang & Rusak [22] this ansatz is also associated with an assumption of axial homogeneity which prevents inertial waves propagating along the central axis from accumulating at streamwise boundaries. However, in the present approach, this corollary assumption is desirable since it further minimizes the influence of the uncertain streamwise boundary conditions on the hydrodynamic behavior.

Next, the mean flow is assumed to vary slowly in the axial direction (in the same manner as k) such that mean flow streamwise derivatives and radial velocities are negligible in the Jacobian $\mathcal{J}_m\left(\overline{q}_0\right)$ operator, and x again appears as a parameter rather than an argument. With these assumptions incorporated, the local eigenvalue problems which appear at each x can be deduced from the the global eigenvalue problem written in Equation 2.17 as,

$$\left[-\mathrm{i}\omega\mathcal{M} + \mathcal{A}_0 + k\mathcal{A}_1 + k^2\mathcal{A}_2\right]\hat{\boldsymbol{q}}_{Lm}\left(r;x\right) = 0. \tag{2.43}$$

Here, to avoid confusion with the global form of the Jacobian operator used in the previous section, $\mathcal{J}_m$ has been decomposed into $[\mathcal{A}_0(r;m) + k\mathcal{A}_1(r;m) + k^2\mathcal{A}_2(r;m)]$, and the complex frequency $\omega = -2\pi f + \mathrm{i}\sigma$ has been defined to be consistent with classical local stability literature [74, 120, 121]. In Equation 2.43, $\mathcal{A}_0$ is an operator which represents the part of $\mathcal{J}_m$ which is constant with respect to k, $\mathcal{A}_1$ represents the part which is linear, and so on. Each of these operators is defined explicitly in Appendix C.

Equation 2.43 is a local dispersion relationship which governs the hydrodynamic flow behavior at each x. Therefore, in the classical stability analysis framework, the local temporal stability is deduced by solving Equation 2.43 as a linear eigenvalue problem for complex ω given real k, the local spatiotemporal stability is determined by solving Equation 2.43 for the stationary points where $\partial\omega/\partial k = 0$ with ω and k complex, and local spatial stability is determined by solving Equation 2.43 as a quadratic eigenvalue problem for k with an imposed real ω [120, 121].

Determination of the weakly-global mode is achieved by solving Equation 2.43 as a spatial eigenvalue problem for a single real frequency ω_f (the external excitation frequency) over a sequence of axial positions to obtain a sequence of $\hat{\boldsymbol{q}}_{Lm}$ and k, and then the global mode shape is reconstructed from this sequence using Equation 2.42. Due to the quadratic nature of the spatial eigenvalue problem, each local spatial solution has two branches of solutions which propagate in opposite directions along x. Here, the wavemaker is considered to represent the upstream forcing at the burner lips where the hydrodynamics and acoustics are coupled. Therefore, in this work, the weakly-global mode will be constructed from the downstream-propagating solution branch such that it represents a leading-order solution to the forced response problem.

It is worth mentioning that if local self-excited behavior (i.e. absolute instability) were to be detected, the weakly-global analysis becomes significantly more involved. In that case, special care is needed to ensure that the local absolute instability is not influential enough to lead to weakly-global instability. To do this, the eigenvalue of the natural global

mode could be approximated by fitting the sequence of saddle points to a rational polynomial and identifying the stability of the related weakly-global mode by analytic continuation onto the complex x plane following [119]. However, as will be shown in chapter 5, no local self-excited behavior was detected for the flow considered in this thesis, indicating that such approaches are not necessary.

2.2.4 Numerical methods

The weakly-global hydrodynamic stability problem described above is solved using the pseudospectral Chebyshev collocation method, a technique which has been used extensively to study the local hydrodynamic stability of swirling flows [76, 122, 123]. In the current application, a staggered grid is employed to avoid the need for artificial pressure boundary conditions [124]. This grid employs a Chebyshev-Gauss-Lobatto quadrature for the velocity and density variables and a Chebyshev-Gauss quadrature for the pressure variable. As will be discussed below, the problems are considered in an unbounded radial domain to avoid confinement effects [92]. Points in the physical space r are mapped to collocation points in the computational space $\xi = [-1, 1]$ using a modified, two-parameter version of the algebraic mapping function proposed by Fabre & Jacquin [125]. The mapping used here is defined by,

$$r\left(\xi\right) = \frac{\alpha\xi\left(\xi^2 + 1\right)}{\left(\xi^2 - 1\right)\left(\xi^2 + 1 - \beta\right)}, \tag{2.44}$$

where α controls the spreading of the collocation points and β controls the clustering of the collocation points. It is equivalent to the mapping used by [125] for $\beta = 0$. The inclusion of the clustering parameter in Equation 2.44 was necessary to appropriately resolve the important gradients in the mean flow with a reasonable number of collocation points. In this work, $\alpha = 1/4$ and $\beta = 3/4$ are selected such that at least 50% of the collocation points are positioned on the interval $r = [0.1, 1]$, where the mean flow variation is strongest.

To pose the local stability problems, boundary conditions must be enforced along r. However, an approximation is needed to enforce these conditions as the experimental measurement window does not extend to the actual physical boundaries of the flow apparatus. Conveniently, near the outer edge of the measurement plane, it was observed that the mean flow is always comprised of nearly stagnant unburned fluid [6]. Therefore, the mean flow velocities at radial locations beyond the measurement window will assumed to be zero and the associated fluid properties will be chosen as those of the reactants. To avoid generating artificial boundary effects, this interval of stagnant fluid is then extended to infinity, where the perturbations are required to vanish in the limit $r \to \infty$ via Dirichlet conditions which mandate $\hat{\boldsymbol{q}}_{lm} = 0$ at $\xi = \pm 1$. To enforce the proper constraints on the axis, symmetry conditions are enforced at $r = \xi = 0$. These conditions are determined by the even or oddness of m and exploit the parity of the Chebyshev polynomials and each component of $\hat{\boldsymbol{q}}$[92]. For odd (conversely, even) m, the density, axial velocity, and hydrodynamic pressure perturbations have odd (even) parity and the radial and azimuthal velocity perturbations have even (odd) parity. A major benefit of enforcing symmetry in this way is that a scheme with N collocation points can handle odd Chebyshev expansions up to order $2N + 1$ and even expansions up to order $2N$. This effectively reduces the size of the required computational domain by half. For this study, convergence tests showed that $N = 150$ collocation points are suitable to accurately and affordably compute all of the eigenvalues and eigenvectors of interest.

Regarding the numerical approach, all of the eigenvalue problems in this work are solved using the QZ and QR algorithm implementations within the Matlab `eig` and `eigs` functions, respectively. Even when the computational grid is very highly resolved, the raw eigenvalue spectra may contain spurious and poorly-resolved solutions due to the discretization and floating-point arithmetic [76, 123]. These problematic eigenvalues are filtered from the eigenvalue spectrum by applying the following selection criteria: (i) neglecting eigenvalues associated with axial phase speeds that are greater than 10^6 times the

nominal flow speed, (ii) discarding eigensolutions that do not vanish as $r \to \infty$ using the criterion of Parras & Fernandez-Feria [123] with a cutoff value of 10^{-6}, and (iii) removing eigenvalues whose relative error in phase speed when computed with $N = 150$ and $N = 135$ collocation points is 1% or larger.

Temporal analysis

The temporal stability analysis involves the direct solution of Equation 2.43 as a generalized eigenvalue problem for ω with k given. As standard solvers are available for this formulation, no additional manipulation is necessary.

Spatiotemporal analysis

The spatiotemporal problem is solved using a variant of the algorithm proposed by Deissler [126], which finds saddle points where $\partial\omega/\partial k = 0$ using a gradient-descent stepping algorithm on the complex k-ω manifold. To facilitate this process, the dispersion relationship of Equation 2.43 is manipulated to yield an analytical expression for the group velocity. To do this, Equation 2.43 is differentiated with respect to k to yield,

$$\left[-\mathrm{i}\frac{\partial\omega}{\partial k}\mathcal{M} + \mathcal{A}_1 + 2k\mathcal{A}_2\right]\hat{\boldsymbol{q}}_{Lm} + \left[-\mathrm{i}\omega\mathcal{M} + \mathcal{A}_0 + k\mathcal{A}_1 + k^2\mathcal{A}_2\right]\frac{\partial\hat{\boldsymbol{q}}_{Lm}}{\partial k} = 0. \tag{2.45}$$

Then, after left-multiplying by the adjoint (left) eigenvector $\hat{\boldsymbol{q}}^{\dagger}_{Lm}$ and using the identity $\hat{\boldsymbol{q}}^{\dagger H}_{Lm}\left[-\mathrm{i}\omega\mathcal{M} + \mathcal{A}_0 + k\mathcal{A}_1 + k^2\mathcal{A}_2\right]\hat{\boldsymbol{q}}_{Lm} = 0$, Equation 2.45 can be rearranged to find,

$$\frac{\partial\omega}{\partial k} = \frac{\hat{\boldsymbol{q}}^{\dagger\mathrm{H}}_{Lm}\left[\mathcal{A}_1 + 2k\mathcal{A}_2\right]\hat{\boldsymbol{q}}_{Lm}}{\mathrm{i}\hat{\boldsymbol{q}}^{\dagger\mathrm{H}}_{Lm}\mathcal{M}\hat{\boldsymbol{q}}_{Lm}}. \tag{2.46}$$

Using a similar approach, the following expression for $\partial^2\omega/\partial k^2$ can be derived,

$$\frac{\partial^2\omega}{\partial k^2} = \frac{\hat{\boldsymbol{q}}^{\dagger\mathrm{H}}_{Lm}\left[2\left(-\mathrm{i}\frac{\partial\omega}{\partial k}\mathcal{M} + \mathcal{A}_1 + 2k\mathcal{A}_2\right)\frac{\partial\hat{\boldsymbol{q}}_{Lm}}{\partial k} + 2\mathcal{A}_2\hat{\boldsymbol{q}}_{Lm}\right]}{\mathrm{i}\hat{\boldsymbol{q}}^{\dagger\mathrm{H}}_{Lm}\mathcal{M}\hat{\boldsymbol{q}}_{Lm}}, \tag{2.47}$$

where $\partial\hat{\boldsymbol{q}}_{Lm}/\partial k$ is determined from Equation 2.45 as,

$$\frac{\partial\hat{\boldsymbol{q}}_{Lm}}{\partial k} = \left[-\mathrm{i}\omega\mathcal{M} + \mathcal{A}_0 + k\mathcal{A}_1 + k^2\mathcal{A}_2\right]^+ \left[-\mathrm{i}\frac{\partial\omega}{\partial k}\mathcal{M} + \mathcal{A}_1 + 2k\mathcal{A}_2\right]\hat{\boldsymbol{q}}_{Lm}, \tag{2.48}$$

and $[\cdot]^+$ denotes the Moore-Penrose pseudoinverse. In practice, Equation 2.48 is solved using the `lsqminnorm` function in Matlab.

Based on the above equations, a simple iterative algorithm to converge to a saddle point from a given initial wavenumber k and a guessed initial eigenvalue ω_0 proceeds as follows. First, Equation 2.43, Equation 2.46, and Equation 2.47 are solved to obtain ω, $\hat{\boldsymbol{q}}_{Lm}$, $\hat{\boldsymbol{q}}^\dagger_{Lm}$, $\partial\omega/\partial k$, and $\partial^2\omega/\partial k^2$ at the current point k. Next, the modulus and argument of the gradient-descent step are deduced as,

$$|\delta k| = \min\left(\left|\frac{\partial\omega/\partial k}{\partial^2\omega/\partial k^2}\right|, \delta k_{\max}\right),$$

and

$$\angle\delta k = \angle\left(-\frac{\partial\omega/\partial k}{\partial^2\omega/\partial k^2}\right),$$

respectively, where $\delta k_{\max} = 0.01$ is a step length threshold which aids numerical stability by avoiding excessively large steps. Finally, the step is completed by taking $k \leftarrow k + \delta k$, and the process is repeated until $\partial\omega/\partial k < 10^{-10}$.

Spatial analysis

The spatial eigenvalue problem, which seeks the spectrum of complex k with ω given, is solved directly via the companion matrix method. This approach recasts the eigenvalue problem of Equation 2.43 (which is quadratic in k) as a generalized eigenvalue problem of twice the original size, but where the eigenvalue k appears linearly. This is achieved by introducing the augmented eigenvector $\hat{\boldsymbol{Q}}_{Lm} = \left(\hat{\boldsymbol{q}}_{Lm}, k\hat{\boldsymbol{q}}_{Lm}\right)^{\mathrm{T}}$ to Equation 2.43. Then,

Equation 2.43 can be rearranged to yield,

$$\left[k \begin{pmatrix} \mathcal{A}_1 & \mathcal{A}_2 \\ \boldsymbol{I} & 0 \end{pmatrix} + \begin{pmatrix} -\mathrm{i}\omega\mathcal{M} + \mathcal{A}_0 & 0 \\ 0 & \boldsymbol{I} \end{pmatrix} \right] \hat{\boldsymbol{Q}}_{Lm} = 0. \tag{2.49}$$

In Equation 2.49, the first row of the augmented matrix blocks enforces Equation 2.43, while the second enforces the definition of $\hat{\boldsymbol{Q}}_{Lm}$. Incidentally, though not indicated in Equation 2.49, the last row and column of the augmented matrix and augmented mass matrix may be safely discarded since there are no k^2 terms associated with the pressure in this formulation. By augmenting the system in this way, the spatial eigenvalue problem can be solved using standard eigenvalue solvers. After solving, the redundant lower half of $\hat{\boldsymbol{Q}}_{Lm}$ can be freely discarded.

CHAPTER 3
BIFURCATION ANALYSIS OF NON-REACTING FULLY-DEVELOPED SWIRLING JETS

This chapter describes a numerical bifurcation analysis of an unconfined, incompressible, laminar swirling jet using the configuration and tools developed in chapter 2. While the configuration considered here is similar in many respects to the experimental setups used at LadHyX [31] or by Liang & Maxworthy [35, 36], there are some important distinctions. First, unlike the top-hat flow profiles seen in these experimental studies, this jet issues from a fully-developed rotating pipe flow. This choice eliminates any significant dependence of the jet's velocity profile on the length of the inlet pipe. Second, the present configuration places the reservoir wall flush with the pipe exit. Conversely, the experimental studies cited above have injected the jet into the domain some distance past the containing wall. Finally, those swirling jet experiments were performed in a closed tank with a lateral and axial extent on the order of ten times the jet diameter. The exact relevance of this level of confinement to the experimentally-observed dynamics is unknown, but numerical evidence does indicate that swirling flows are surprisingly sensitive to far-field boundary conditions [93, 41]. In contrast, the model studied here uses open boundary conditions which simulate an unconfined jet.

The contents of this chapter are currently pending publication at the Journal of Fluid Mechanics as an article I co-authored with Benjamin Emerson and Timothy Lieuwen [127].

3.1 Characterization of steady states

This section characterizes the equilibrium solutions represented by the steady axisymmetric flow in the (Re, S)-parameter space. These nonlinear solution branches are traced using the Moore-Penrose continuation method described in chapter 2 with either S or Re as the

free parameter. Once identified, the stability of the steady solutions is determined using eigenvalue calculations, and any apparent instabilities are tracked to their corresponding bifurcation points. In order to monitor the evolution of the steady flow as the parameters are varied, the minimum of the velocity along the central axis, $\min u_x(x, 0)$, is extracted from each equilibrium solution. This allows steady solutions exhibiting centrally-located recirculation features to be easily identified as those having $\min u_x(x, 0) < 0$.

3.1.1 Rotation effects

The investigation begins by characterizing the development of the steady flow with varying *S* at a fixed Reynolds number of $Re = 100$. A bifurcation diagram, synthesized from a total of 155 distinct steady solutions and eigenvalue calculations, is shown in Figure 3.1 along with visualizations of representative flow and eigenmode patterns. The diagram reveals a solution curve which may be divided into three segments connected by two saddle-node bifurcations at $S_B = 2.103$ and $S_F = 2.046$. At this Reynolds number, the only unstable eigenvalues are associated with $m = 0$ and appear on the real axis such that $f = 0$. Thus, the steady flow is everywhere stable toward both non-axisymmetric and oscillatory disturbances, and the eigenvectors associated with the unstable eigenvalues are real and axisymmetric.

The first portion of the solution branch exists on the interval $0 \leq S \leq S_B$ and is linearly stable. At $S = 0$, the solution (point 1 in Figure 3.1) represents a nonswirling, quasi-columnar jet which dissipates as it proceeds downstream and entrains the ambient fluid. As *S* is increased from 0, rotation enhances entrainment in the shear layer surrounding the jet, decreasing $\min u_x(x, 0)$ as *S* increases. Despite this additional mixing, the jet remains quasi-columnar (point 2 in Figure 3.1) until $S \sim 2.06$, when a central deceleration region characterized by streamlines bulging away from the jet axis gradually starts to emerge. At $S = 2.089$ (point 3 in Figure 3.1), the deceleration in this region becomes sufficient to form a stagnation point on the central axis at $x = 2.54$, followed immediately by the emergence

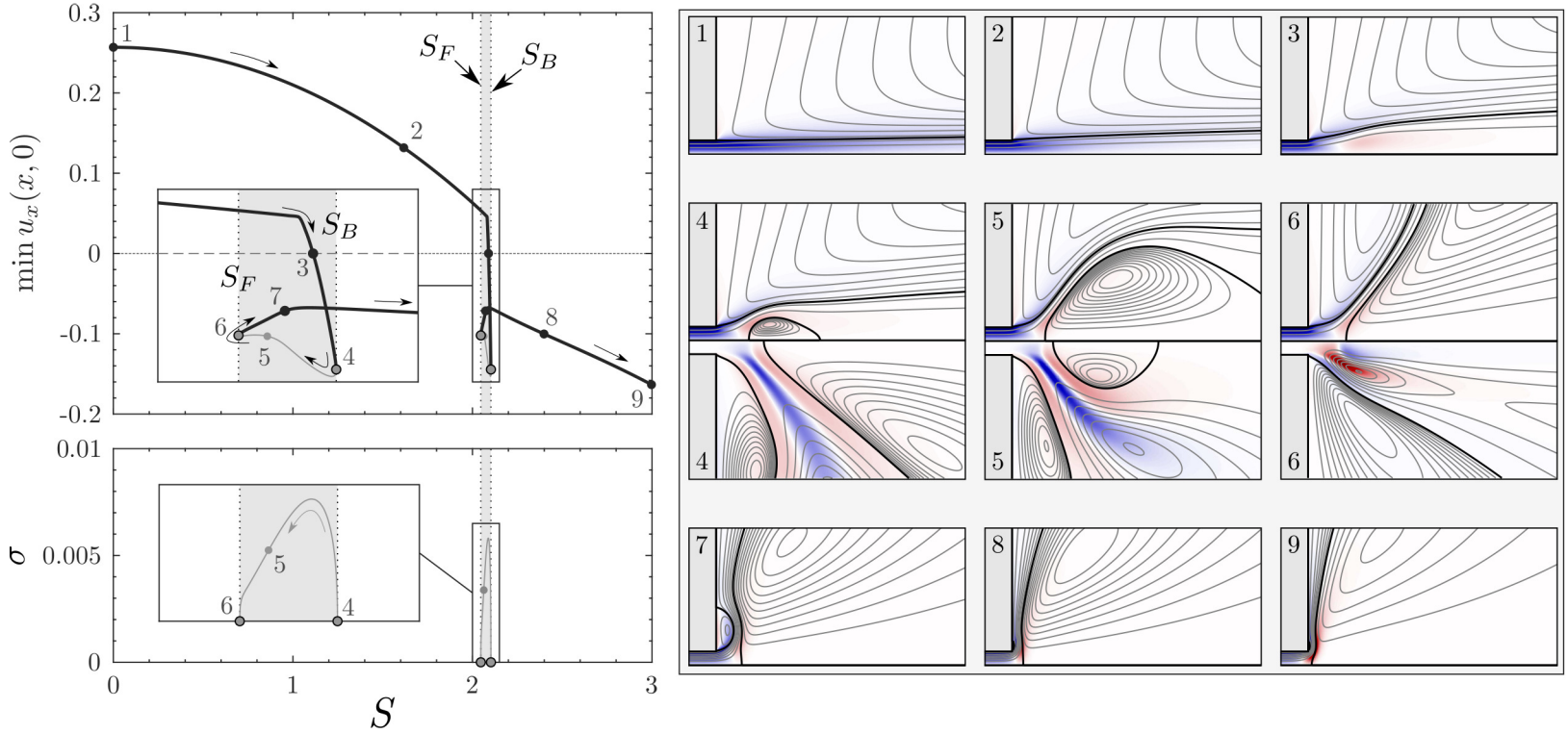

Figure 3.1: (left) $Re = 100$ bifurcation diagrams showing how the minimum centreline velocity of the steady flow and the growth rate of the non-stable eigenvalues change with S. Frequencies are not shown since all non-stable eigenvalues have $f = 0$. Thick black and thin gray curves indicate the respective stable and unstable solution branches. Saddle-node bifurcation points (labeled 4 and 6) are filled in gray. (right) Meridional projections of axisymmetric streamfunction isolines and azimuthal vorticity contours over $(x, r) \in [-1, 9] \times [0, 5]$ for selected steady flow fields (upper half-plane) and, when non-stable, eigenmodes (lower half-plane) as indicated in the diagrams. Stagnation streamlines are shown in black.

of a small central pocket of recirculating flow. This recirculation zone, a clear manifestation of vortex breakdown, swells and creeps upstream as the rotation increases until reaching $S = S_B$, where the first segment terminates as the solution curve turns backwards on itself with respect to S at a saddle-node bifurcation.

The saddle-node bifurcation at $S = S_B$ also marks the upper bound of the second portion of the solution curve which exists for $S_F < S < S_B$. Along this segment, the radial and axial extent of the ellipsoidal recirculation zone apparent in the solution at $S = S_B$ (point 4 in Figure 3.1) expands dramatically as the rotation decreases. This expansion is accompanied by a gradual reduction in the concavity of the forward portion of the central recirculation zone, causing the jet to flatten into a conically-spreading sheet as it flows around the front of the stagnation region (point 5 in Figure 3.1). By $S = 2.05$, the widening recirculation region becomes mildly convex, spreading the jet outwards along an increasingly diverging trajectory with respect to the axis, due to the increasing entrainment of the ambient fluid. During this transition, intensifying recirculation between the diverging jet and the wall develops into a pronounced outer ring vortex surrounding the jet. With only a slight further decrease in rotation, the jet flares open even further, bending back toward the wall, impinging upon it, and then attaching to it via the Coandă effect. The point of intersection between the wall and the outer stagnation streamline moves rapidly inwards as S makes its final approach to S_F. When the second segment ends at $S = S_F$ (point 6 in Figure 3.1), the stagnation streamline delimiting the boundary between the outer ring vortex and the jet intersects the wall at $r = 11.3$. Notably, this reattachment point is similar in radius to the vessels commonly used for controlled experimental studies [31, 35], suggesting that non-small confinement effects will be present even for large experimental domains.

As indicated by the positive real eigenvalues shown in Figure 3.1, the solutions along the second segment of the solution curve are unstable and repel disturbances. Because of this saddle-like nature, these solutions do not correspond to practically-observable flow

states. Nonetheless, important physical insights can still be gleaned from their behavior. In particular, no steady solutions containing a bubble-type recirculation zone (point 4 in Figure 3.1) exist for $S > S_B$, indicating that the flow transitions abruptly to a new nonlinear attractor as the rotation is increased beyond S_B. Similarly, the steady solutions exhibiting strong outer recirculation zones (point 6 in Figure 3.1) do not exist at rotation rates below S_F. Furthermore, the inward curvature apparent in the structure of the critical eigenvector at $S = S_F$ bears a distinct qualitative resemblance to the quasi-columnar flow states along the first solution segment (e.g. point 3 in Figure 3.1). The same is true of the critical eigenvector at $S = S_B$ with respect to the third segment described below. Overall, these results clearly demonstrate that an interval of hysteresis exists between the bistable steady states from S_F to S_B as indicated by the background shading in the bifurcation diagram of Figure 3.1.

The third and final segment along the $Re = 100$ solution curve exists as a stable solution for $S \geq S_F$. As S increases following the second saddle-node bifurcation, the separation vortex surrounding the jet contracts, and the jet is pulled even more strongly towards the wall. Beyond $S \sim 2.4$, the axial flow beyond the pipe is almost completely suppressed, and the jet instead proceeds radially outward along the wall immediately after exiting the pipe. At even higher $S > 3$, a region of reversed axial flow begins to extend upstream into the inlet pipe, signaling the onset of vortex breakdown within the pipe. In the present case of $Re = 100$, the emergence of pipe breakdown happens smoothly, and the solution segment remains single-valued for $S > 3$. However, at higher $Re \gtrsim 250$, the pipe vortex breakdown process was observed to involve a sequence of two saddle-node bifurcations separated by a saddle solution, consistent with the theory of Wang & Rusak [22]. Nevertheless, as the focus of this study is on swirling jets and since vortex breakdown in pipes has been well-studied elsewhere, the presented results are limited to rotation rates low enough to avoid the issue of vortex breakdown in the pipe. Even so, the analysis extended well into the pipe breakdown regime up to $S = 5$ to search for additional solution folds and branch

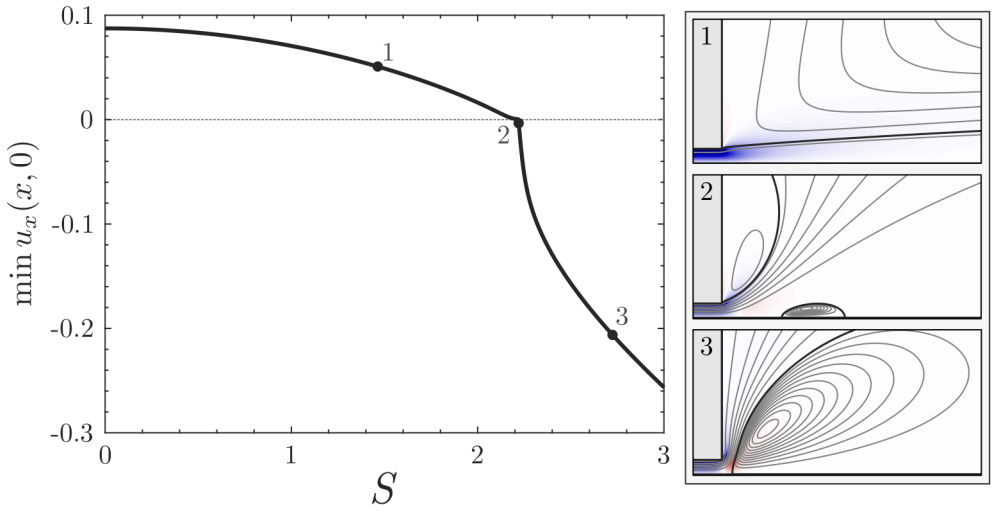

Figure 3.2: (left) Bifurcation diagram showing the progression of the minimum centreline velocity with varying S at $Re = 40$ and (right) three representative visualizations of the steady flow. Eigenvalues are not shown since all satisfy $\sigma < 0$. Visualizations follow the format from Figure 3.1.

connections relevant at lower S values, though none were found.

With this basic picture in mind, the study will now move on to other Reynolds numbers, beginning with the lower value of $Re = 40$. The bifurcation diagram for this more viscous case, which represents 67 point solutions, is shown in Figure 3.2. Unlike at $Re = 100$, a stable, single-valued solution curve exists for all S at $Re = 40$. As the rotation increases in this case, the steady flow smoothly evolves through flow states that are qualitatively quite similar to those at $Re = 100$. In particular, without undergoing any bifurcations, the $Re = 40$ flow structure progresses from a quasi-columnar swirling jet at low S to a breakdown state with both inner and outer recirculation zones at $S \sim 2.2$, and finally to a radial jet along the wall at higher S.

Conversely, at the higher Reynolds number of $Re = 200$, the dynamics are significantly more elaborate. The bifurcation diagram for this case synthesizes 422 point solutions and is shown in Figure 3.3. In contrast to the previous cases which both exhibit at least one stable steady solution for each value of S, the axisymmetric steady flow at $Re = 200$ is unstable for an appreciable range of swirl due to the presence of various three-dimensional instabilities.

The quasi-columnar steady flow associated with the nonswirling jet at $Re = 200$ is linearly stable. As rotation is increased from zero, the entrainment rate of the ambient fluid rises, and the steady flow's dominant eigenvalues become progressively less stable. The upper stability limit for this first solution branch is marked by a Hopf bifurcation at $S_U = 1.3$ due to an almost stationary $|m| = 2$ mode. This initial instability represents a nearly-helical co-winding spiral with a relative amplitude that slowly grows and then decays with increasing x. As S increases, the primary instability is followed by several more Hopf bifurcations associated with various slowly co- and counter-rotating $|m| = 2$ modes and one more rapidly counter-rotating $|m| = 1$ mode as S continues to increase. By $S = 1.6$, the steady quasi-columnar flow has nine unstable eigenmodes. It is clear at this point that three-dimensionality and oscillation will feature in the time evolution from the unstable quasi-columnar steady state for $S > S_U$. Nonetheless, it is worth emphasizing that the unstable eigenmodes are not intended nor expected to represent the true dynamics of the nonlinear system on its eventual attractor. Even in the initial evolution toward this attractor, non-normality may lead to algebraic (rather than exponential) growth of disturbances and very different linear dynamics than otherwise suggested by the eigenmodes [106, 107]. This point will be revisited in section 3.2 where the limit cycle behavior which follows instability is considered.

Beyond the quasi-columnar regime, the development of the unstable steady flow at $Re = 200$ is very similar to the axisymmetric vortex breakdown process described for $Re = 100$. Namely, as the rotation increases beyond $S \sim 2$, the flow along the centreline smoothly decelerates, stagnates, and recirculates. Next, the steady solution curve forms a pleat via a pair of saddle-node bifurcations at $S_B = 2.086$ and $S_F = 2.018$ wherein the steady flow's dominant feature transitions from a small central recirculation "bubble" to a large ring-shaped separation vortex along the outer wall with decreasing swirl. Finally, as the rotation begins to increase again just beyond S_F, the size of the outer separation vortex shrinks and the jet is pulled more quickly toward the wall. However, unlike at $Re = 100$, the steady flow

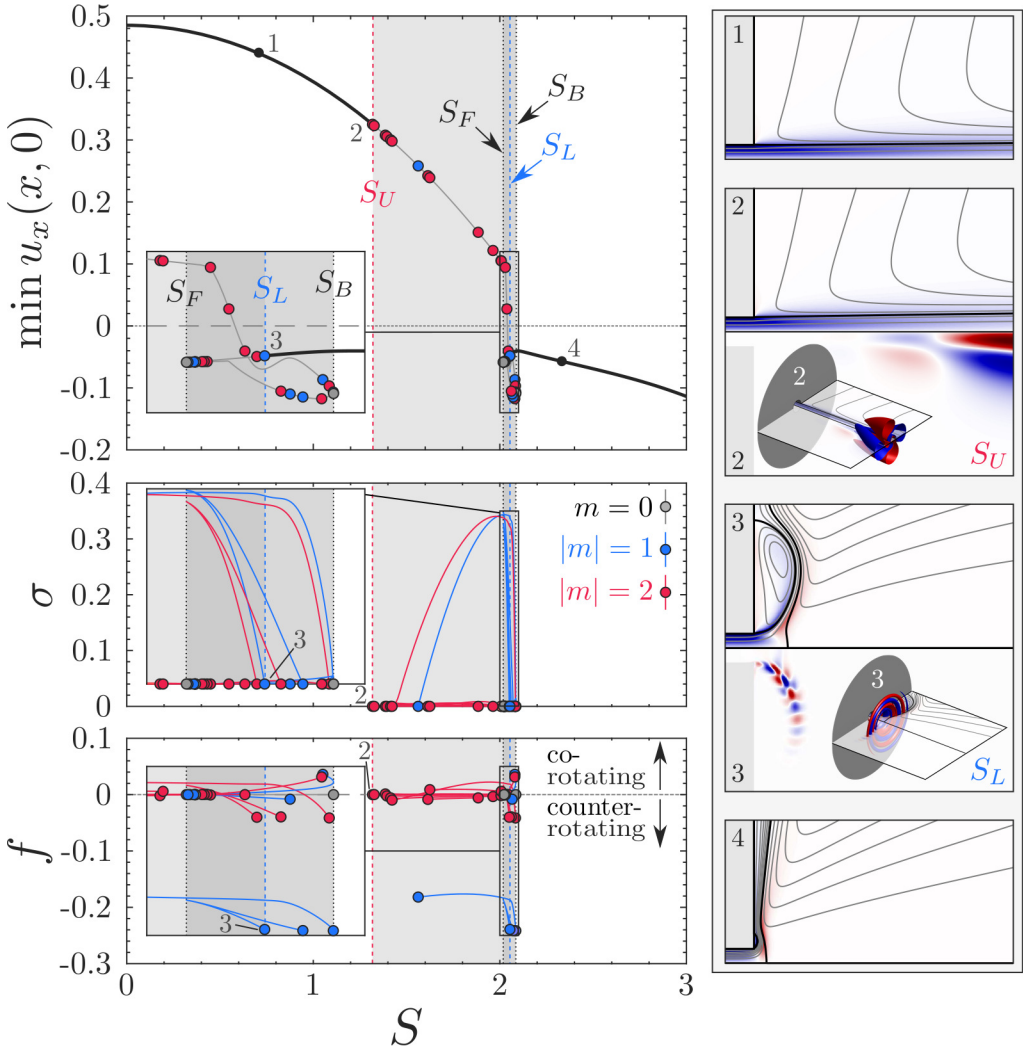

Figure 3.3: (left) Bifurcation diagram for $Re = 200$ showing how the minimum centreline velocity of the steady flow and the growth rate and frequency of the non-stable eigenvalues develop with S. Thick black and thin gray curves indicate the respective stable and unstable steady solution branches. Bifurcation points are outlined in black and filled according their azimuthal periodicity as indicated. (right) Representative visualizations of the steady flow along the stable solution branches and at the critical points S_U and S_L using the format from Figure 3.1. Critical disturbance modes are visualized by only their azimuthal vorticity fields in the meriodional plane since the streamfunction is undefined in three dimensions. Isometric views of the three-dimensional azimuthal vorticity fields are also shown via isocontours at levels corresponding to $\pm 20\%$ of the maximum.

in the present case remains unstable to a multitude of non-axisymmetric and oscillatory disturbances throughout this process, indicating that any practically-observable dynamics should differ quite dramatically from this steady, axisymmetric scenario. Nonetheless, after the final saddle-node bifurcation at S_F, the growth rates of the unstable modes gradually decrease, and the stability of the steady solution curve is eventually restored as S increases. The lower bound of the second interval of stability of the steady flow is marked by a Hopf bifurcation associated with a counter-rotating $|m| = 1$ mode at $S_L = 2.054$. Due to the strongly nonparallel nature of the steady flow in this regime, the co-winding spiral pattern of the critical mode is not helical in nature. This investigations found no evidence of any further instabilities for $S > S_L$ at $Re = 200$.

3.1.2 Reynolds number effects

Next, the study considers the Re dependence of the steady flow at fixed pipe rotation rates. Three bifurcation diagrams, obtained for $S = 1.8$, $S = 2.05$, and $S = 2.3$, are presented in Figure 3.4. Note that calculations are extended up to $Re = 1000$ in each case to search for additional solution folds or branch connections relevant to the lower Re values shown. Before detailing the specifics of each case individually, it is worthwhile to highlight how relatively modest changes in the pipe rotation rate can fundamentally change how the steady flow evolves as Re is varied. This is in contrast to the previous section which revealed that – precluding any instabilities – the evolution of the steady flow with varying rotation is qualitatively similar at different Reynolds numbers. Moreover, while there is a clear stabilizing effect of viscosity, both the critical Re and the structure of the critical modes varies significantly from case to case.

All of the fixed-S cases exhibit similar behavior for $Re \lesssim 10$. Beginning at the Stokes ($Re \leftarrow 0$) limit, the system is elliptic and linear, and the viscous swirling flow emerges from the pipe and quickly dissipates without ever forming a separating shear layer or recirculation zone. As Re increases to ~ 10, a shear layer forms that separates from the pipe's lip

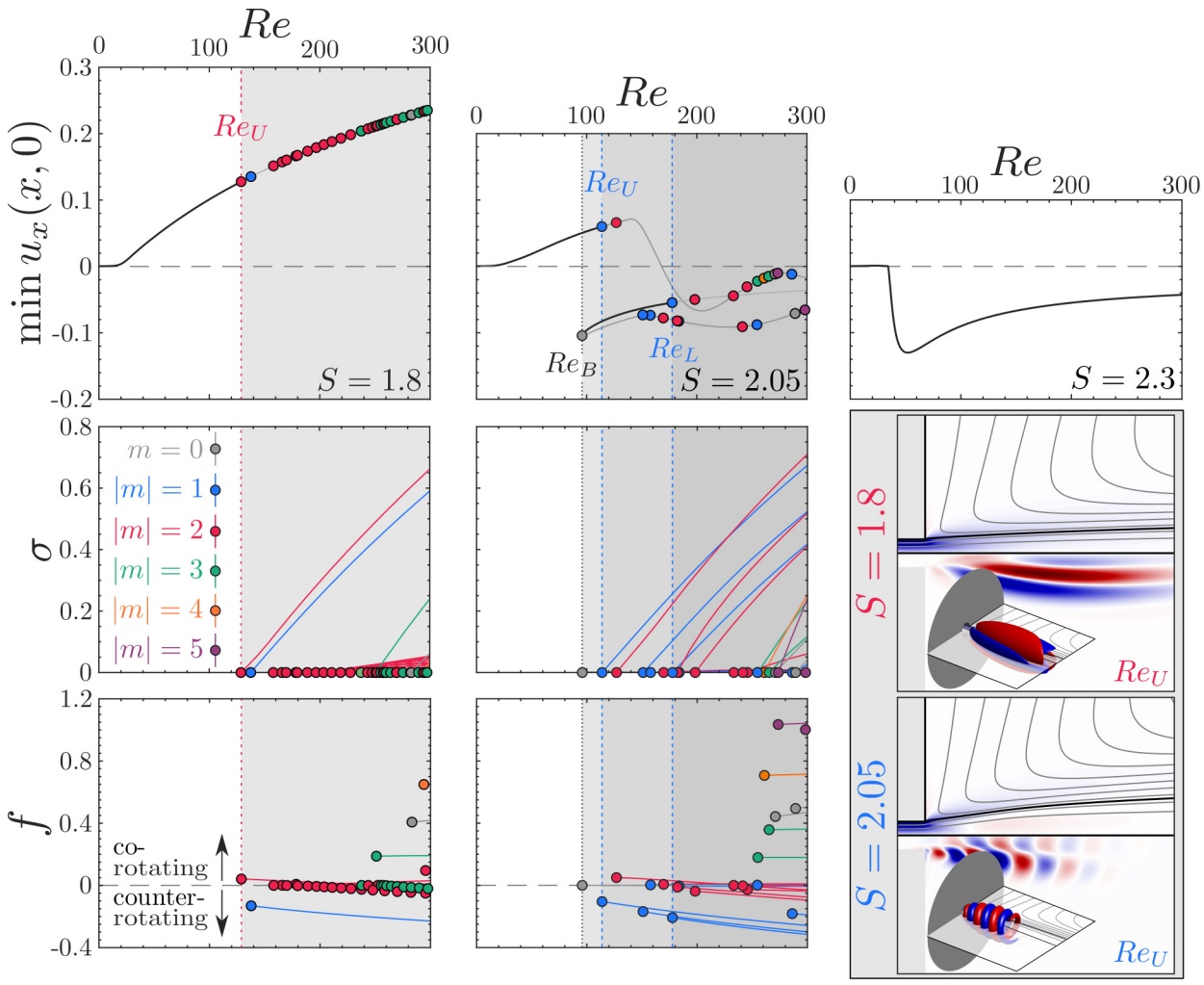

Figure 3.4: (top row) Bifurcation diagrams showing how the steady flow's minimum centreline velocity develops with *Re* for $S = 1.8$, $S = 2.05$, and $S = 2.3$. Bifurcation points are outlined in black and filled according their azimuthal periodicity as indicated. (lower-left) Development of the growth rate and frequency of the non-stable eigenvalues for $S = 1.8$ and $S = 2.05$. (lower-right) Visualizations of the steady flow and critical disturbance modes at Re_U for $S = 1.8$ and $S = 2.05$ using the format from Figure 3.3. The solutions at points Re_F and Re_L for $S = 2.05$ are not shown due to their respective similarity to point 4 in Figure 3.1 and point 3 in Figure 3.3.

at $x = 0$. In addition, nonlinearity gives rise to centrifugal effects proportional to S^2 which cause the jet to expand radially-outward. Note that, as mentioned in subsection 2.1.1, the shape and thickness of the boundary layers in the pipe are essentially independent of the Reynolds number since the incoming flow is fully-developed. Instead, the primary effect of increasing *Re* is to reduce the role of viscosity after the flow exits the rotating pipe.

With the exception of very low Reynolds numbers, where it dissipates too quickly to form a distinct jet, the steady flow at $S = 1.8$ takes the form of a quasi-columnar swirling jet without any noticeable deceleration along the central axis (see pattern 2 from Figure 3.1). In this case, the value of $\min u_x(x, 0)$ reported in Figure 3.4 is equivalent to the centreline velocity at the domain exit $u_x(R_\infty, 0)$ which slowly rises with increasing *Re* as the dissipation decreases. The axisymmetric equilibrium manifold at $S = 1.8$ is single-valued for all relevant *Re*. However, this steady flow solution only remains stable up to $Re_U = 128.8$. At this point, the steady flow experiences a Hopf bifurcation associated with a co-rotating $|m| = 2$ mode. The already-unstable steady flow then experiences a second Hopf bifurcation at $Re = 137.7$ associated with a counter-rotating $|m| = 1$ mode. As *Re* increases further, the flow becomes even more unstable, both due to the rising growth rates of the existing modes and due to new instabilities which occur in subsequent bifurcations.

At $S = 2.05$, the jet has up to three steady solutions for the range of *Re* investigated. These include one solution curve connected to the Stokes solution in the $Re \to 0$ limit, and a pair of solutions disconnected from the first which stem from a saddle-node bifurcation at $Re_F = 95.82$. Setting aside the issue of instability for a moment, the upper solution branch represents a quasi-columnar jet flow for $Re \lesssim 140$. As *Re* increases beyond this value, the streamlines along the axis bulge outwards until a central bubble-type recirculation zone gradually emerges at $Re \sim 168$ without bifurcation. For $Re > 168$, the recirculation zone enlarges and eventually gives way to various multi-cellular recirculation features similar to those found in the axisymmetric simulations of Ruith et al. [39]. However, since these steady solutions are strongly unstable to a broad range of three-dimensional disturbances,

they will not be investigated in detail here. In contrast to the upper solution branch, both solutions of the pair which appear at Re_F always exhibit at least one central stagnation point. At $Re = 100$ and $Re = 200$, these fixed-S solutions correspond to the second and third solution segments from the fixed-Re results described in the previous section. As was the case there, the saddle solution (lower gray curve in Figure 3.4) exhibits a transitional structure between bubble-type and cone-type central recirculation features (see pattern 5 and 6 from Figure 3.1), while the node solution (lower black curve in Figure 3.4) represents a flared-open cone structure dominated by a strong outer ring vortex (see patterns 6 and 7 from Figure 3.1). Qualitatively, these structures persist as Re varies, though the recirculation zones become significantly larger as Re increases.

Returning to the question of stability, the steady flow at $S = 2.05$ is stable and single-valued until the saddle-node bifurcation at Re_F. The newly-born saddle solution branch is unstable with respect to non-oscillatory $m = 0$ perturbations throughout its existence, but both of the other branches remain linearly stable until Hopf bifurcations occur at $Re_U = 113.8$ on the quasi-columnar solution branch and at $Re_L = 177.6$ on the lower branch. Unlike the $S = 1.8$ case which had a leading instability associated with $|m| = 2$, the bifurcations in this case are both associated with counter-rotating $|m| = 1$ modes. Shortly after their leading $|m| = 1$ instability, both of the now-unstable branches experience additional bifurcations associated with co-rotating $|m| = 2$ modes followed by a variety of others.

Finally, the study considers the case of $S = 2.3$. At this high level of rotation, the steady solution curve is again single-valued over the relevant range of Reynolds numbers. As Re increases away from the Stokes limit, the flow quickly transitions into a radial wall jet solution with an enormous central recirculation zone (similar to pattern 8 from Figure 3.1). The fluid's inertia increasingly resists this abrupt lateral reorientation of the flow, resulting in the formation of a ring-shaped separation vortex surrounding the pipe exit (similar to pattern 7 from Figure 3.1) which grows with Re. The strongly swirling flow remains stable

well beyond the critical Reynolds numbers of previous cases, eventually succumbing to a co-rotating $|m| = 1$ Hopf bifurcation at $Re = 348.4$.

3.1.3 Discussion: Overall steady flow characteristics

Having separately considered the steady flow's behavior at constant *Re* and *S*, the analysis of the steady flow is concluded with a more holistic perspective toward its overall dynamics. The single-parameter bifurcation curves discussed previously represent one-dimensional slices cut from a two-dimensional manifold of steady solutions over the (Re, S) parameter space. Likewise, the bifurcation points from the earlier diagrams are extended into neutral curves delimiting the steady flow's dynamically distinct regions. Taken together, this analysis synthesizes calculations from over 20 000 distinct steady states. The resulting three-dimensional bifurcation diagram is presented in Figure 3.5 along with a stability map formed by projecting the neutral curves from the solution manifold onto the *Re*-*S* plane. The stability map provides a comprehensive overview of the dynamics of the free swirling jet steady flow over the region $(Re, S) \in [0, 0] \times [300, 3]$ while the bifurcation diagram provides a more detailed representation of the state space topology for $(Re, S) \in [40, 1.8] \times [200, 2.3]$.

Figure Figure 3.5 indicates that bistability between two distinct axisymmetric steady states exists over a range of swirl and Reynolds numbers. This transition to bistable behavior is triggered by a codimension-2 cusp bifurcation at $(Re, S) = (47.10, 2.175)$, well before any of the oscillatory linear modes are destabilized. These results shed light on the different physics and sequences of bifurcations between laterally confined and unconfined flows. In confined flow situations, bistability typically occurs between steady columnar and breakdown states, as demonstrated theoretically [128, 22, 97] and evidenced experimentally [26]. Thus, vortex breakdown in confined flows is typically associated with an abrupt, hysteretic transition as the swirl parameter increases. In this unconfined flow, however, bistability is *not* associated with the initial occurrence of vortex breakdown. Rather,

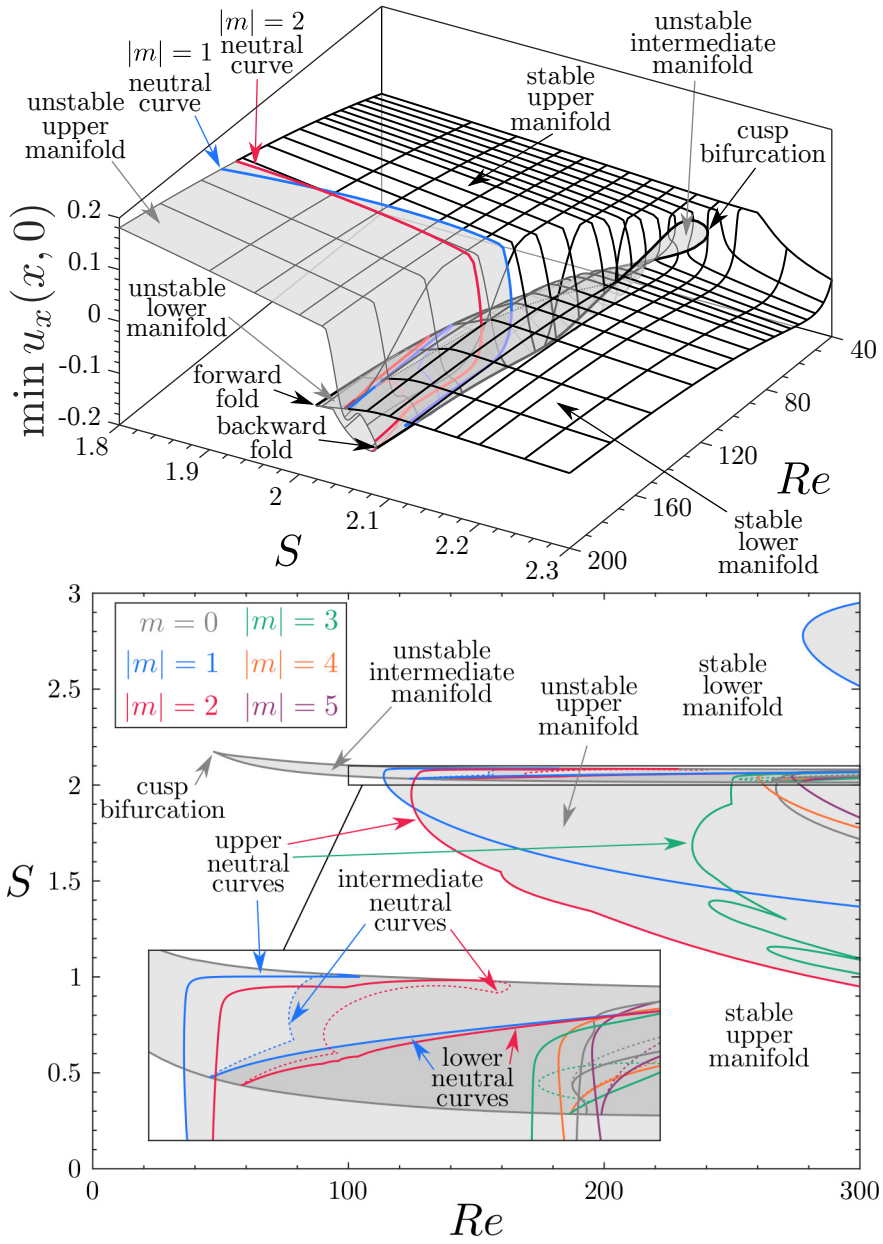

Figure 3.5: (top) Three-dimensional bifurcation diagram and (bottom) two-dimensional stability map for the swirling jet steady flow. Each neutral curve delimits the locus of critical points corresponding to each value of m; criticality occurs at the outermost neutral curve along the manifold.

it results from a competition and interaction between the secondary recirculating flow surrounding the jet and the central recirculation zone as described in subsection 3.1.1. As the central recirculation zone grows in size, its relative strength compared to the outer recirculation zone decreases, resulting in a sudden transition from a breakdown state with a small central bubble to a wall-jet state with a small ring-shaped separation vortex around the pipe exit as S increases beyond S_B. This distinction raises an important practical consideration: what radius is required of a closed experimental apparatus to approximate an unconfined flow? While the effect of lateral confinement has not been directly investigated in this study, the results along the intermediate and lower solution manifolds show significant radial flow across the open boundary which would clearly be affected by the introduction of a solid lateral wall for $Re > 50$. This suggests that any experimental device attempting to avoid confinement effects should at least exceed the radial extent of the unconfined domain used in this study. The topic of confinement will be returned to in the concluding remarks in section 3.3.

The results should also be contrasted with results from unconfined swirling flows with widespread axial co-flow. Meliga et al. [42] have shown that the steady solution manifold for the Grabowski-Berger vortex is single-valued for $Re \leq 300$ and that a central recirculation zone appears gradually in the flowfield as the swirl parameter increases. This qualitatively different result from those reported here appears to stem from the axial co-flow surrounding the vortex center in that model, which suppresses the formation of an outer recirculation zone. This, in turn, prevents the competing physics which lead to bistability and hysteresis of the steady flow. This suggests that if the velocity of the co-flow surrounding the jet is decreased, a threshold will be reached where an outer recirculation region can form and potentially give rise to bistable behavior. While it does not appear that any other studies have directly investigated this idea, Moise & Mathew [45] have explored the dynamics of the more jet-like 'Maxworthy' swirling flow model with a widespread, but very weak axial co-flow fixed to 1% of the core velocity. They presented evidence of hys-

teresis between bistable breakdown states similar to those detailed in this study, supporting the idea that the presence of an outer recirculation zone, enabled by a sufficiently weak axial co-flow, is necessary for bistability of the unconfined steady flow.

The diagrams in Figure 3.5 also reveal that, for $S \leq 3$ and $Re \leq 300$, the initial transition to unsteady behavior always originates at Hopf bifurcations associated with either $|m| = 1$ or $|m| = 2$ depending on the local flow state and parameter values. Nonetheless, particularly at higher *Re*, additional instabilities of other azimuthal periodicities bifurcate from the unstable steady flow at parameter values beyond the primary $|m| = 1$ or $|m| = 2$ instabilities. For example, the Hopf bifurcations associated with $m = 0$ occur at parameter values well beyond the critical values of the leading non-axisymmetric modes. Even though $|m| = 1$ has a lower minimum critical *Re*, it is clear from the diagrams that $|m| = 2$ is typically destabilized at lower values of swirl on the upper manifold. Regardless, the steady solution manifold is unstable toward both modes over an appreciable portion of the parameter space which is not limited to the quasi-columnar flow regime. This will be explored further in the following section which focuses on the periodic solution branches.

3.2 Characterization of limit cycle states

This section focuses on the structure and dynamics of the time-periodic solutions originating from Hopf bifurcations of the steady flow. These nonlinear solution branches are traced using the harmonic balance Moore-Penrose continuation method described in subsubsection 2.1.3. This technique plainly reveals saddle-node bifurcations of limit cycles and allows identification of multi-stable periodic states. However, temporal behaviors beyond those characterized here are certainly likely, as periodic orbits which are disconnected from the steady flow solution manifold have not been sought, determined the Floquet stability of the identified periodic states, or considered quasi-periodic or chaotic dynamics.

Compared to the steady flows examined previously, the flow topology and nonlinear dynamics of the periodic solution branches tends to be significantly more complex. Nonethe-

less, as in section 3.1, the minimum of the axial velocity on the central axis, $\min u_x(x,0)$, is again useful for monitoring the evolution of the overall flow structure as the parameters are varied due to its relation to the vortex breakdown phenomenon. Importantly, even though the flowfields are unsteady, this minimum represents a static value corresponding to the axisymmetric mean flow component in order to satisfy continuity for non-axisymmetric oscillations. In addition to the minimum axial velocity along the centreline, periodic solutions are also monitored through the frequency and amplitude of the periodic oscillation. Henceforth, the reported frequency and azimuthal periodicity values for a given limit cycle correspond to its fundamental oscillation. It should be noted, however, that the limit cycles do contain higher temporal and azimuthal harmonics due to nonlinearity which are accounted for in these results. The limit cycle amplitude is defined by the unsteady energy norm $\|\acute{\boldsymbol{u}}\| = \|\boldsymbol{u} - \bar{\boldsymbol{u}}\|$ which includes contributions from the fundamental oscillation and all resolved harmonics over the full computational domain.

3.2.1 The quasi-columnar jet regime

This study begins by characterizing the dynamics of the periodic orbits in the quasi-columnar flow regime. As apparent from the previous section, and particularly Figure 3.5, for $S \lesssim 2$, the flow assumes a quasi-columnar jet structure, and the steady solution manifold is single-valued. In this low-swirl regime, the steady flow experiences its primary linear instability via Hopf bifurcations associated with $|m| = 1$ and $|m| = 2$ modes above certain critical parameter values. According to Figure 3.4, as the Reynolds number increases beyond $\sim$160, a number of additional $|m| = 2$ (and, eventually, $|m| = 3$ and other) modes bifurcate from the quasi-columnar steady flow, which each give rise to their own distinct periodic solution branches. It is also clear from Figure 3.3 that these new limit cycle branches exist and overlap for an increasingly wide range of swirl as the Reynolds number progresses. To start, relatively low Reynolds numbers are considered to focus the analysis on the *leading* $|m| = 1$ and $|m| = 2$ periodic orbits in the quasi-columnar regime. The bifurcation dia-

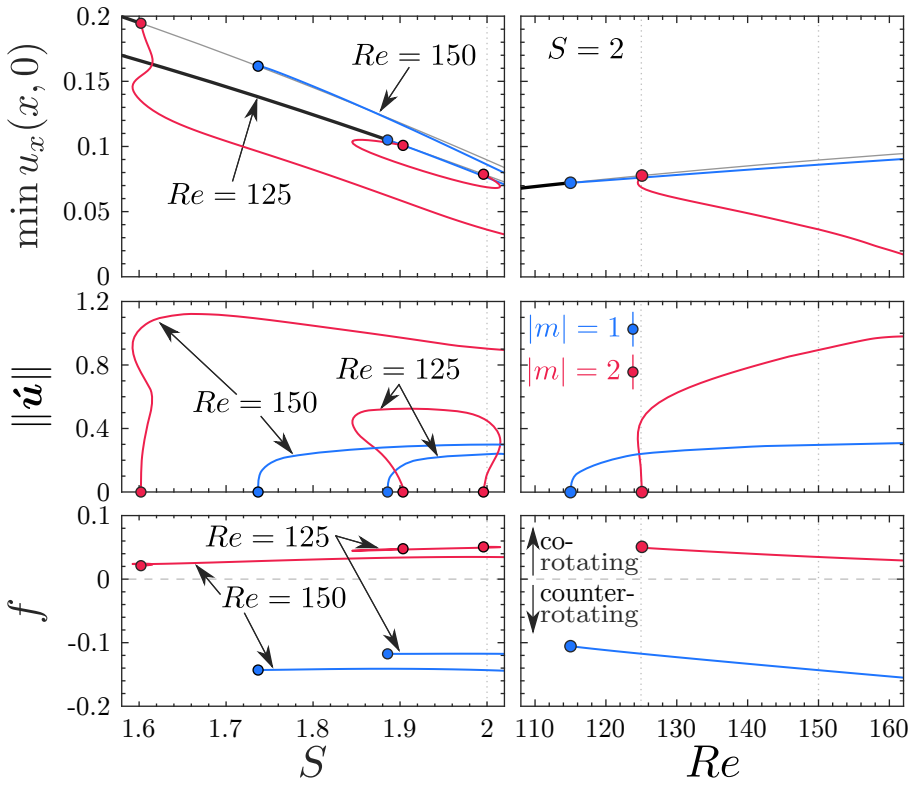

Figure 3.6: Bifurcation diagrams showing the evolution of the minimum centreline velocity, amplitude, and frequency of the periodic solutions (left) with varying S for $Re = 125$ and $Re = 150$ and (right) with varying Re for $S = 2$. The steady solution curves are shown for reference in black, while the blue and red curves correspond to the $|m| = 1$ and $|m| = 2$ periodic solution curves, respectively. Outlined circles represent Hopf bifurcation points. The dotted light vertical lines indicate the intersections of the parameter sweeps at $(Re, S) = (125, 2)$ and $(150, 2)$. The periodic solutions at $(Re, S) = (150, 2)$ are visualized in Figure 3.7.

grams for this case are presented in Figure 3.6. The dynamics of the quasi-columnar flow at higher-Re will be considered near the end of this section.

In Figure 3.6, as S increases, criticality of the steady flow occurs via a supercritical Hopf bifurcation associated with the counter-rotating $|m| = 1$ mode at $S = 1.886$. As S increases along the newly-born $|m| = 1$ periodic solution curve, the amplitude of the limit cycle grows, while its frequency remains nearly constant. The $|m| = 1$ cycle persists beyond the quasi-columnar regime and remains present as higher swirl induces mean flow stagnation and vortex breakdown. Further discussion of these higher-S dynamics is reserved for subsection 3.2.3. Just beyond the leading critical point of the $|m| = 1$ oscil-

lation, the quasi-columnar steady flow curve at $Re = 125$ experiences an additional Hopf bifurcation at $S = 1.903$ associated with $|m| = 2$. In this case, the bifurcation is subcritical, and the amplitude of the $|m| = 2$ limit cycle grows with decreasing S until reaching a saddle-node bifurcation at $S = 1.845$. Continuing along this $|m| = 2$ solution curve, a second saddle-node bifurcation is reached at $S = 2.015$, shortly before the branch terminates at another Hopf bifurcation of the steady flow at $S = 1.996$. The oscillation frequency of the $|m| = 2$ oscillation remains nearly constant with varying S. The multivaluedness displayed by the $|m| = 2$ cycle suggests a possible interval of multistability with respect to the steady flow and the $|m| = 1$ and $|m| = 2$ cycles. In addition, the fact that the $|m| = 1$ and $|m| = 2$ cycles coexist for an appreciable range of swirl suggests that a quasiperiodic orbit containing elements of both cycles could exist nearby in the state space. However, this is a speculation which requires further analysis to evaluate.

At $Re = 150$, the $|m| = 1$ and $|m| = 2$ limit cycles present in the previous case remain relevant, but with slightly different dynamics compared to the more viscous case. First, both cycles exist over a greater range of swirl than at $Re = 125$. In particular, for $Re = 150$, the $|m| = 2$ cycle bifurcates at $S = 1.602$, well before the $|m| = 1$ cycle at $S = 1.737$. The evolution of the $|m| = 2$ cycle is also associated with slightly more complex nonlinear behavior which manifests itself as a pleated (rather than folded) solution curve with respect to S as the amplitude increases. Finally, unlike before, the $|m| = 2$ cycle persists beyond the quasi-columnar regime and up to higher swirl levels associated with stagnation and recirculation of the mean flow. This will be further discussed in subsection 3.2.3. However, even in the quasi-columnar regime, the $|m| = 2$ cycle is clearly associated with a significant reduction in flow along the centreline.

The evolution of the periodic flow with varying Re at $S = 2$ is also shown in Figure 3.6 to provide some context about the periodic solution manifolds which connect the solutions curves at $Re = 125$ and $Re = 150$. At $S = 2$, the $|m| = 1$ cycle appears first at $Re = 115.0$ followed by the $|m| = 2$ oscillation at $Re = 125.1$. In this case, the supercritical and

subcritical bifurcation behavior described above for the respective $|m| = 1$ and $|m| = 2$ limit cycles with varying *S* is preserved when *Re* is the free parameter. The minimum *Re* associated with the saddle node bifurcation of $|m| = 2$ cycle occurs at $Re = 124.5$. While the oscillation frequency of these orbits did not change appreciably with varying *S*, a clear decrease of f is observed for both cycles as *Re* increases in this case.

Now, a description of the morphology of the periodic flow states in this flow regime is presented. At the parameter values discussed in this section, the mean flow structure of all limit cycles remains quasi-columnar (*i.e.* $\min u_x(x, 0) = u_x(R_\infty, 0)$), and the unsteady flow patterns are not strongly affected by the parameters. Figure 3.7 presents mean and instantaneous flow visualizations of the $|m| = 1$ and $|m| = 2$ limit cycles at $(Re, S) = (150, 2)$ along with a depiction of the corresponding steady flow. Note that the phase references selected to define $\theta = 0$ and $t = 0$ for these visualizations are arbitrary due to the system's θ and t invariance. This invariance property also allows the time evolution of non-axisymmetric structures to be understood equivalently by rotation. In forward time, translation along θ proceeds in the opposite direction as the motion of the unsteady structures due to the convention that the signed value of m be non-positive.

Beyond their distinct azimuthal periodicities, the $|m| = 1$ and $|m| = 2$ limit cycles correspond to completely different patterns of unsteady flow which lead to major differences in their overall structure and dynamics. The leading $|m| = 1$ limit cycle is associated with Kelvin-Helmholtz-like roll-up of the shear layer surrounding the jet. On an instantaneous basis, this limit cycle manifests itself as a nearly-helical, counter-rotating, co-winding flow structure concentrated near the pipe exit. Based on this topology, it seems likely that the $|m| = 1$ oscillation is driven primarily by the shear mechanism discussed in subsection 1.2.1. The $|m| = 1$ oscillation does not significantly alter the quasi-columnar jet's mean momentum distribution over the parameter range studied here; *i.e.*, there is relatively small topological difference between the axisymmetric mean flow associated with the $|m| = 1$ limit cycle and the corresponding steady flow at identical parameter values.

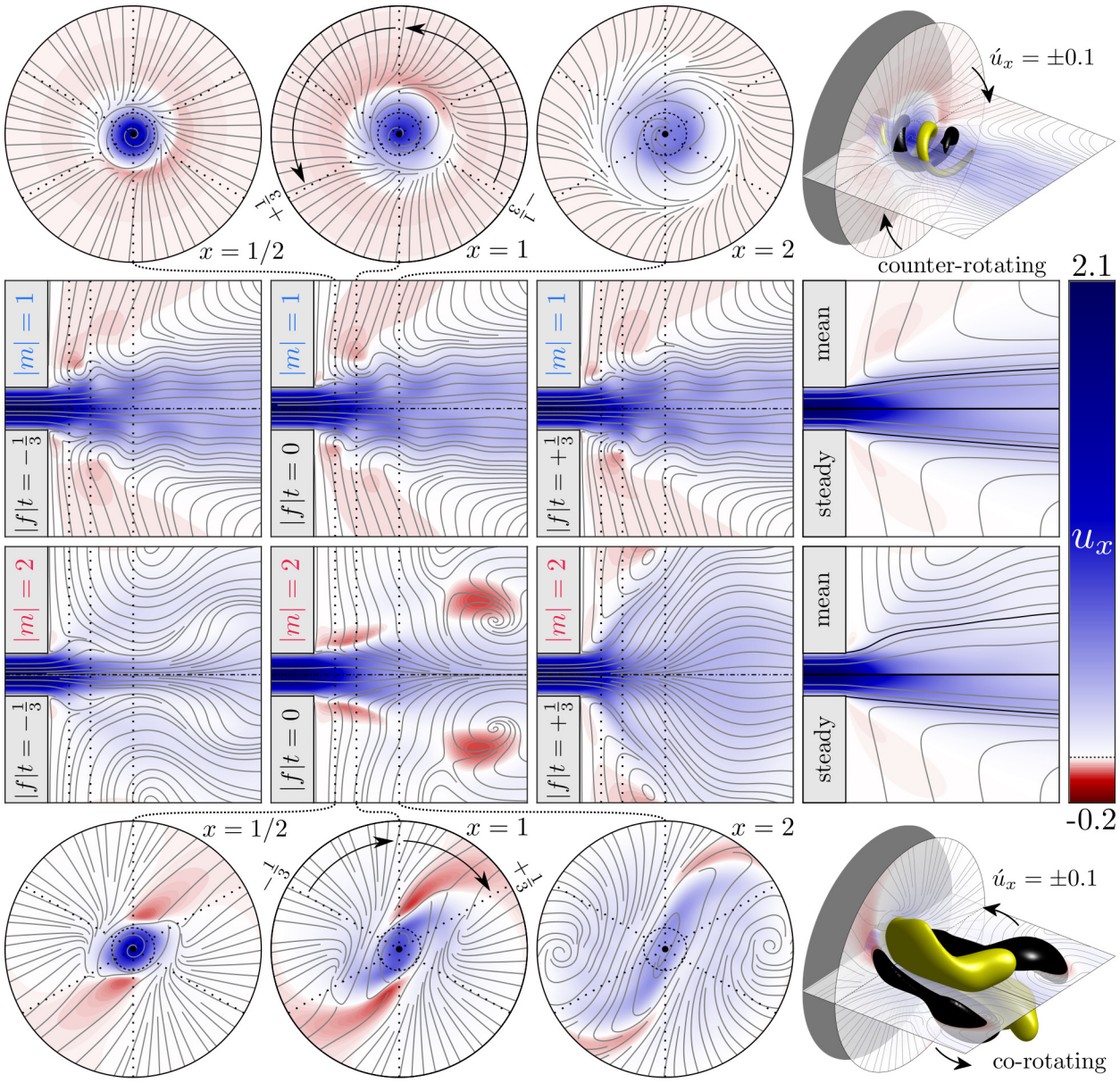

Figure 3.7: Visualizations of $|m| = 1$ (top two rows) and $|m| = 2$ (bottom two rows) limit cycle oscillations at $(Re, S) = (150, 2)$ via streamlines and axial velocity contours over $(x, r, \theta) \in [-1, 5] \times [0, 3] \times [0, 2\pi]$. The top and bottom image sequences show (from left to right) axial slice planes at $x = 1/2, 1, 2$ of the instantaneous flow as viewed from downstream along with a three-dimensional isometric view. The middle image sequences show meridional slice planes at three equally-spaced phase points with time increasing from left to right, followed by a comparison of the associated mean (top half) and steady (bottom half) flow. The dashed circle on each axial slice plane indicates the position of the pipe wall. The dotted lines show the intersection of the axial and meridional planes at each point of phase, with arrows in the axial planes indicating how these lines move with time. The yellow and black surfaces in the isometric views represent the respective positive and negative isocontour values indicated in the figure.

This similarity between the steady and mean flowfields is further demonstrated by the small effect of the $|m| = 1$ oscillation on $\min u_x(x, 0)$ as apparent in the previous bifurcation diagrams (Figure 3.6).

The leading $|m| = 2$ limit cycle represents an oscillation of the swirling jet which is strikingly similar to the pre-breakdown $|m| = 2$ instability described in the experiments of Billant et al. [31]. The unsteady flow consists features a large, co-rotating spiral structure which yields distinctive trident- and S-shaped flow patterns when visualized via meridional and axial slice planes, respectively. Unlike the relatively small and almost helical vortex roll-up associated with the $|m| = 1$ oscillations, the $|m| = 2$ limit cycle features substantial velocity fluctuations which extend several diameters axially and radially from the pipe exit. This reach leads to much higher entrainment of the fluid surrounding the jet than is present in either the steady flow or the $|m| = 1$ limit cycle states. Because the jet's momentum is vigorously redistributed radially outward by these oscillations, there are significant differences between the topology of the mean flow states and the corresponding steady flow states. Even though the mean flow associated with the $|m| = 2$ oscillations is quasi-columnar at $Re = 150$ in the sense that there is no centreline stagnation zone, the additional mixing provided by the unsteady flow leads to a region of strongly non-parallel flow in the vicinity of the pipe exit. This abrupt deflection of the mean flow leads to a significant reduction in the minimum centreline velocity associated with the $|m| = 2$ limit cycle as shown in Figure 3.6. Nonetheless, as the Reynolds number increases and the oscillation amplitude rises, the growing momentum deficit near the centreline eventually produces a stagnation point, triggering vortex breakdown.

Before ending this section, it is worth briefly addressing the periodic solutions present in the quasi-columnar regime at higher Reynolds numbers. Many of the periodic orbits in this portion of the parameter space feature multi-valued solution manifolds, and their structures are associated with a broad range of wavenumbers and frequencies. For this reason, this section only provides some illustrative examples of the numerous limit cycles

which come into existence as *Re* increases. For example, consider the dynamics of the quasi-columnar flow at $Re = 300$. Figure 3.8 displays a bifurcation diagram showing the dynamics of certain characteristic oscillations with $0 \leq |m| \leq 5$ alongside corresponding visualizations. Note that the presented cycles with $m = 0$, $|m| = 1$, $|m| = 4$, and $|m| = 5$ are the only periodic solutions with those wavenumbers which were found to bifurcate on this parameter interval. Conversely, many $|m| = 2$ and $|m| = 3$ instabilities exist in addition to those shown.

The $|m| = 1$ and $|m| = 2$ limit cycles shown in the bifurcation diagram of Figure 3.8 emerge from the same neutral curves as those studied at lower *Re*. At $Re = 300$, the dynamics and structure of these periodic solutions remain qualitatively similar to their lower-*Re* analogues, though the oscillation amplitudes and their effects on the mean flowfield become more pronounced. Given their similarity to the previous situations, this discussion will focus on solutions with other wavenumbers, beginning with $m = 0$. The axisymmetric oscillation bifurcates in a subcritical manner from the steady flow at $S = 1.718$ but its solution curve almost immediately turns forward in a saddle-node bifurcation at $S = 1.711$. This oscillation leads to the formation of axisymmetric vortex rings near the pipe exit which propagate downstream along the jet's shear layers. Like the $|m| = 1$ shear layer oscillations studied above, the $m = 0$ limit cycle has an almost negligible effect on the mean flow. However, compared to the $|m| = 1$ 'bending' oscillations, these $m = 0$ 'bulging' structures are both more stable (in the sense that they require higher *Re* and *S* values to bifurcate) and weaker (as their overall amplitude is smaller). The clear difference between these results and those in experiments which favor axisymmetric vortex shedding at low swirl conditions [31, 35] is noteworthy. This distinction is likely related to the jet exit profile, as those experiments tend to have thinner boundary layers while the jet profile used here is fully-developed. As shown by Batchelor & Gill [16] and Michalke [129], the inviscid linear dynamics of fully-developed jets are dominated by $|m| = 1$ disturbances, while jets with thinner boundary layers tend to prefer $m = 0$ instability modes. This point sug-

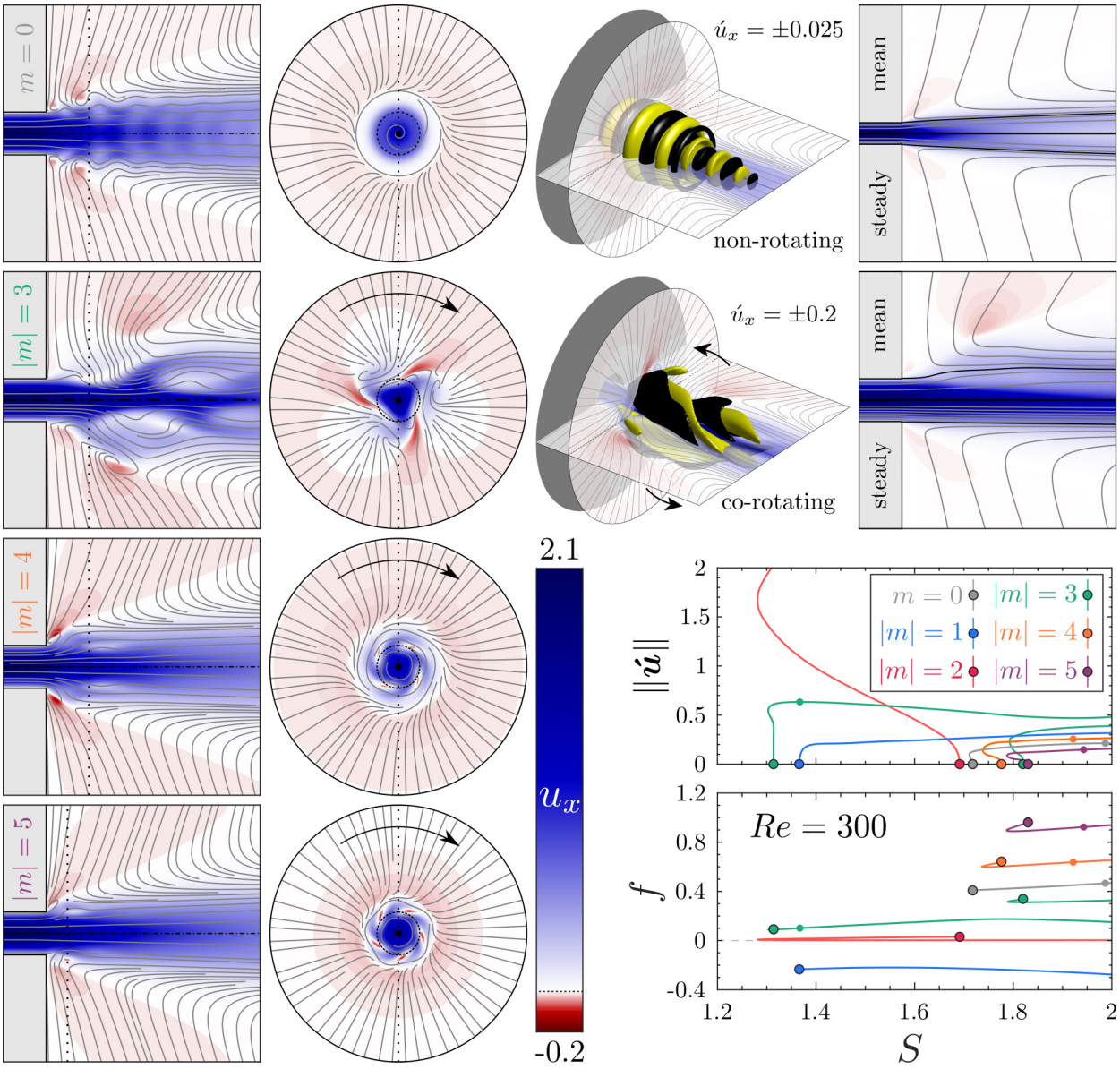

Figure 3.8: Visualizations of selected limit cycles at $Re = 300$ at the points indicated by the small points in the corresponding bifurcation diagram. Flow visualizations follow the format of Figure 3.7, though only a single meridional and axial slice plane is shown for each solution. Recall that the arrows on the axial slice planes indicate the motion of the dotted line showing the plane intersections, not the motion of the flowfield. Three-dimensional representations are also provided in the case of the $m = 0$ and $|m| = 3$ limit cycles.

gests a meaningful direction for future work which is expounded in the concluding remarks in section 3.3.

Figure Figure 3.8 also highlights the role of higher-wavenumber oscillations in the dynamics at $Re = 300$. All of the oscillations with $|m| \geq 3$ shown here exhibit subcritical behavior as their amplitude increases from their associated critical points, but supercritical bifurcations were also observed in other cases not shown. While the amplitudes of these $|m| \geq 3$ instabilities are clearly dwarfed by the $|m| = 2$ 'Billant' instability discussed earlier for all relevant *S*, their dynamics may still be to physical situations. In particular, the emergence of the $|m| = 3$ oscillation at relatively low *S* and high *Re* in these results is qualitatively consistent with the experimental observations of Billant et al. [31] and Liang & Maxworthy [35], though their transitions occurred at significantly higher Reynolds numbers. This indicates that a periodic attractor with $|m| = 3$ which bifurcates from the steady flow could be responsible for their observed transition. Furthermore, the demonstrated existence of other limit cycle states with even higher-periodicities suggests that such structures may represent relevant attractors for certain other high-*Re* conditions.

3.2.2 The wall-jet regime

After the flow transitions from a quasi-columnar jet to the wall-jet regime, the steady flow solution manifold once again becomes single-valued for $S \gtrsim 2.2$. As shown in Figure 3.5, a funnel-shaped, co-rotating and counter-winding $|m| = 1$ spiral instability appears in this high swirl regime for sufficiently high *Re*. Note that this instability belongs to a different neutral curve than any of the other $|m| = 1$ modes described in this study. Though other instabilities will certainly appear in this flow regime at higher parameter values, no additional bifurcations were detected for $S \leq 3$ and $Re \leq 300$.

A bifurcation diagram and visualization of the mean and instantaneous flow for the $|m| = 1$ limit cycle in the wall-jet regime at $Re = 300$ is presented in Figure 3.9. This limit cycle bifurcates in a supercritical manner with respect to its neutral curve and remains

single-valued for $Re \leq 300$. Its frequency increases proportionally with S and does not change substantially with Re. The oscillation consists of a co-rotating radial spiral structure which exists primarily along the shear layer separating the spreading jet from the centrally-recirculating fluid. This is clearly different from the $|m| = 1$ shear layer instabilities covered earlier which instead feature oscillations which are localized to the shear layer separating the jet from the outer recirculating fluid. Nonetheless, this oscillation does not significantly influence the mean distribution of momentum, as can be seen by comparing the steady and time averaged flow. Unlike the instabilities analyzed earlier, this limit cycle generates a small, but noticeable, motion in the pipe immediately upstream of the dump plane due to a slight precession of the leading stagnation point near the exit plane. This suggests that at parameter values beyond those investigated here, the onset of breakdown in the pipe may be linked to three-dimensional (rather than axisymmetric) motions due to downstream conditions related to the dynamics of the free jet after it exits the pipe. This bears certain similarities to the three-dimensional scenarios for vortex breakdown of columnar flows in finite-length rotating pipes discussed by Wang et al. [23]. Their linear analysis focused on the dynamics of propagating Kelvin waves which are trapped by the asymmetric streamwise boundary conditions and showed that, in certain cases, the primary instability in swirling pipe flow is non-axisymmetric. The configuration studied here, on the other hand, is much more complex, involving additional physical mechanisms both within and beyond the pipe as well as nonlinear effects.

3.2.3 The vortex breakdown regime

In this section, the focus is turned to the various periodic states present at intermediate swirl levels where the steady flow transitions from a quasi-columnar jet to a lateral jet along the dump plane wall. According to Figure 3.5, the steady flow solution manifold in this regime is characterized by multivaluedness over $2 \lesssim S \lesssim 2.1$. The drastic changes in steady flow topology and recirculation characteristics associated with the vortex breakdown phe-

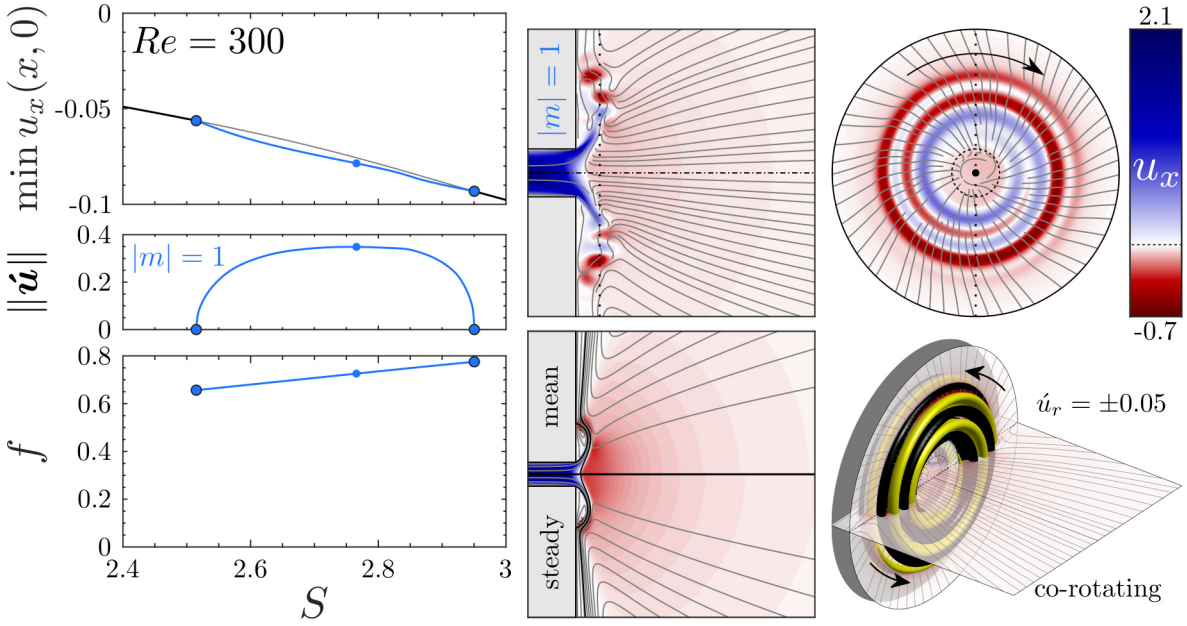

Figure 3.9: (left) Bifurcation diagram for the $|m| = 1$ limit cycle in the wall-jet regime at $Re = 300$ showing the evolution of the minimum centreline velocity, amplitude, and frequency with S. (right) Instantaneous and mean flow visualizations using the format of Figure 3.7 at the point indicated on the diagrams. Only one phase point of the instantaneous flow is shown. Note that the three-dimensional isocontours from this figure onward correspond to radial velocity fluctuations, unlike the isocontours for axial velocity fluctuations shown in the previous figures.

nomenon correspond to similarly dramatic shifts in the behavior of the periodic solutions. As before, the number of periodic solutions present at intermediate swirl rises dramatically as the Reynolds number increases. For practical reasons, the analysis in this section is therefore limited to $Re \leq 200$.

Beginning with the case of $Re = 150$, the evolution of the periodic solutions with changing S are shown in the bifurcation diagrams and visualizations of Figure 3.10. The solutions detailed in this diagram begin near the end of the quasi-columnar flow regime at $S = 2$. As the rotation is increased beyond this value, the vortex breakdown phenomenon begins to manifest itself on the periodic and steady solutions. However, compared to the steady solutions, the periodic solutions clearly require a higher value of S in order to form a central recirculation zone. This is likely because the increased mixing associated with the oscillations resists the central momentum deficit required to yield an internal stagnation

point under these conditions. Nonetheless, once the central recirculation zone does form, the $|m| = 1$ and $|m| = 2$ oscillations are both rapidly quenched as the bubble enlarges. The demise of the $|m| = 2$ oscillation involves complex dynamics featuring a pleated pair of saddle-node bifurcations with the first occurring almost immediately after the appearance of the central stagnation point. Thus, the $|m| = 2$ solution curve is multivalued for a small range of S as the amplitude decreases and S approaches the terminal bifurcation at $S = 2.081$. The dynamics of the $|m| = 1$ oscillation are more straightforward. After the recirculation zone forms, the $|m| = 1$ oscillation amplitude decreases uniformly with increasing swirl until disappearing via Hopf bifurcation at $S = 2.086$. Importantly, the $|m| = 1$ and $|m| = 2$ oscillations both destabilize before the first saddle-node bifurcation of the steady flow is encountered at $S_B = 2.089$. This leads to a brief interval of stability of the steady flow corresponding to a steady "bubble" breakdown state.

As S decreases along the intermediate solution manifold after reaching S_B, the steady solution curve is initially only unstable with respect to a non-oscillatory $m = 0$ mode as discussed in subsection 3.1.1. However, Hopf bifurcations associated with $|m| = 1$ and $|m| = 2$ occur at $S = 2.050$ and $S = 2.038$, respectively, giving rise to periodic solutions. These oscillations feature non-axisymmetric cone-shaped central recirculation zones which are clearly different from the bubble-shaped recirculation zones associated with their analogues along the upper solution manifold. Nonetheless, the unsteady structures and frequencies associated with both oscillations remain qualitatively similar to the $|m| = 1$ and $|m| = 2$ structures from before. Along the $|m| = 1$ periodic solution curve, the amplitude and frequency of the cycle initially increases with decreasing S until a saddle-node bifurcation is reached at $S = 2.031$. This saddle-node of the $|m| = 1$ cycle is separate from the saddle-node bifurcation at $S_F = 2.025$ associated with the steady flow. Next, the $|m| = 1$ solution curve reverses course, and both the amplitude and frequency of the $|m| = 1$ oscillation decrease with increasing S until finally terminating in a Hopf bifurcation at $S = 2.043$. The $|m| = 2$ oscillation bypasses the saddle-node bifurcation of the

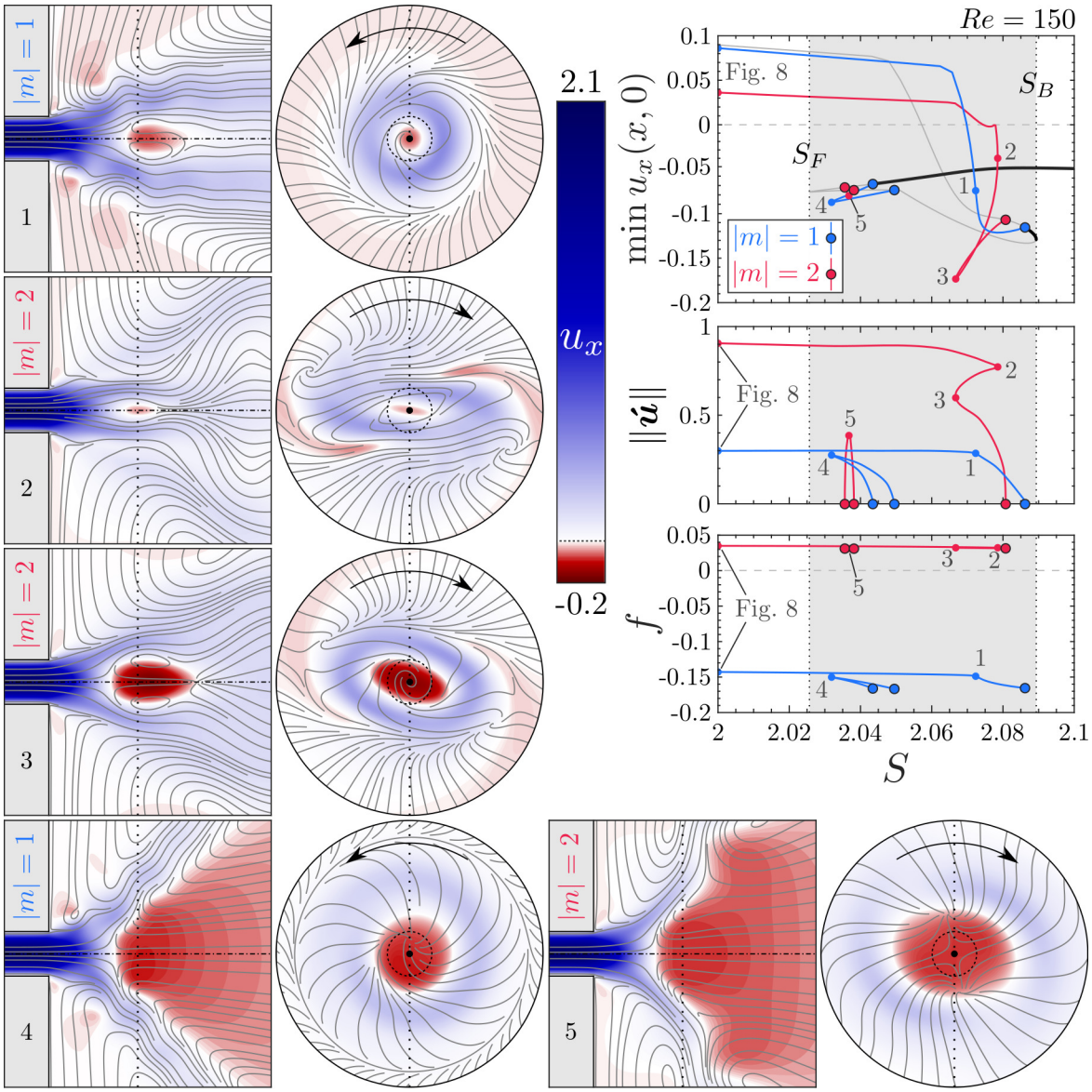

Figure 3.10: Bifurcation diagram for $Re = 150$ at intermediate swirl showing the evolution of the minimum centreline velocity, amplitude, and frequency with S along with instantaneous and mean flow visualizations using the format of Figure 3.7 at the indicated points. Only one phase point of the instantaneous flow is shown.

steady flow with no saddle-node bifurcation of its own; it is single-valued for the entirely of its small range of existence between $S = 2.038$ and $S = 2.035$. Thus, as S decreases from its initial bifurcation point along the intermediate steady flow manifold, the amplitude of the $|m| = 2$ oscillation grows, peaks, and then decays with little change in frequency until it terminates along the lower steady solution manifold. No further bifurcations were detected at $Re = 150$.

This section now proceeds to the $Re = 200$ case which corresponds to the bifurcation diagram shown in Figure 3.11. Figure 3.11 includes all 14 periodic solution branches detected on the presented interval. In essence, this analysis represents an extension of the steady flow dynamics considered in Figure 3.3 to the limit cycle solutions. Clearly, many more distinct limit cycles are present at $Re = 200$ than at $Re = 150$, indicating a dramatic rise in complexity. Nonetheless, it should again be emphasized that even more complex behavior is possible. The system may support or favor quasiperiodic and/or chaotic attractors over the purely periodic solutions considered here.

In section 3.1, it was shown that the quasi-columnar flow at $Re = 200$ supports several instabilities with $|m| = 2$ in addition to one $|m| = 1$ instability. The periodic solutions corresponding to these instabilities can be seen in Figure 3.11 as the periodic solution curves with nonzero amplitude at $S = 2$, *i.e.* curves 1-6 and 13. The solutions numbered 1 through 5 consist of spatially-extensive $|m| = 2$ oscillations which rotate in both directions. This "family" of solutions consists of co-winding $|m| = 2$ spiral structures which slowly absorb kinetic energy from the jet over an extensive axial range. It is worth noting that the periodic solutions on branch 2 stem from the same neutral curves associated with the $|m| = 2$ solution branches studied at other Reynolds numbers earlier. Regardless, oscillations 1-5 have little influence on the fluid motion near the pipe exit and primarily serve to aid downstream mixing. These branches disappear one-by-one as the penetration depth of the jet decreases with increasing S due to the higher entrainment and, eventually, the emergence of the central stagnation region. Solution branch 6, an $|m| = 1$ oscillation, stems from

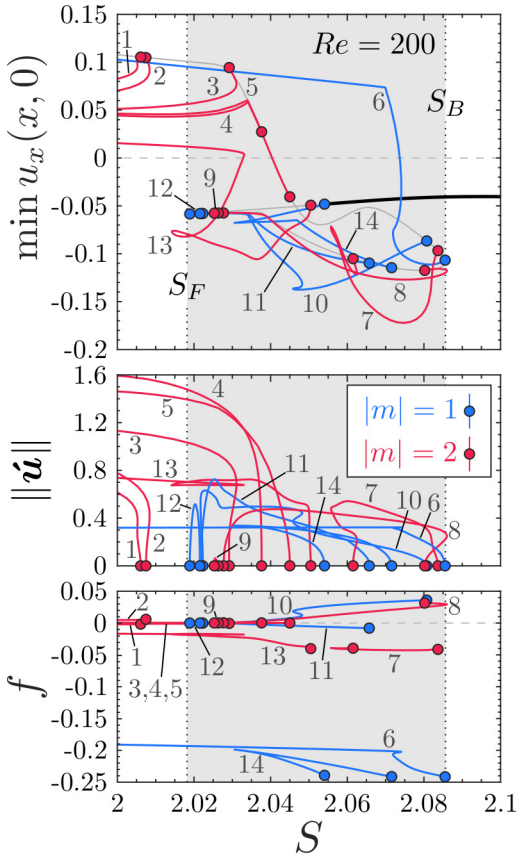

Figure 3.11: Bifurcation diagram for the steady and periodic solutions at $Re = 200$ and intermediate swirl showing the evolution of the minimum centreline velocity, amplitude, and frequency with S. The periodic solution branches are labeled sequentially in the order of appearance of their *terminal* bifurcation points along the steady flow solution curve.

the same neutral curve as the $|m| = 1$ instabilities of the quasi-columnar flow seen earlier. Neither the morphology nor the frequency of the counter-rotating, co-winding $|m| = 1$ oscillations change significantly from the $Re = 150$ case. Nonetheless, one notable dynamical difference from the earlier case is a pleated pair of saddle-node bifurcations in the solution curve which occur as the central recirculation zone emerges. The final periodic solution branch present in the quasi-columnar flow regime and relevant to the intermediate swirl dynamics corresponds to an $|m| = 2$ oscillation numbered 13. Unlike solution curves 1-6 whose periodic oscillations consist of convective structures which dissipate as the mean flow undergoes vortex breakdown, solution curve 13 bypasses the familiar breakdown process described in section 3.1.

Visualizations of the flow structures on branch 13 are shown in Figure 3.12. Beginning in the quasi-columnar flow regime at $S = 2$, the solution curve is locally single-valued, and the unsteady motion takes the form of a counter-rotating flow structure which features significant oscillations along the wall near the pipe exit and which develops into a co-winding spiral further downstream. Even when the flow along the centreline is everywhere positive, these strong near-wall velocity fluctuations produce powerful Reynolds stresses which greatly assist entrainment and dramatically distort the mean flow in comparison to the steady flow. Consequently, the mean flow exhibits a small separation vortex around the pipe exit as well as a larger recirculation vortex outside the first. As S increases, the growing interactions between the near-wall fluctuations and the mean flow reduce the penetration of the jet and cause the outer recirculation features to further dominate the flow dynamics. At $S = 2.033$, these dynamics reach a crux signaled by the appearance of a saddle-node bifurcation followed almost immediately by stagnation of the on-axis flow. As S decreases from this point, the separation vortex overwhelmingly dominates the flow behavior, rapidly pulling the initial stagnation point open into a massive region of reversed flow which deflects the jet radially-outwards. The completion of this transition to the wall-jet flow topology is marked by a second saddle-node bifurcation at $S = 2.014$. Beyond

this point, the periodic solutions consist of counter-rotating $|m| = 2$ spirals superposed upon a wall-jet type mean flowfield. The solution curve eventually terminates in a Hopf bifurcation along the lower solution manifold of the steady flow at $S = 2.051$.

Moving on, the periodic solution branches numbered 7-12 in Figure 3.11 bifurcate from the steady flow solution curve after the emergence of the central recirculation zone but do not ever exhibit a wall-jet type solution. These solution curves consist of co- and counter-rotating and co- and counter-winding $|m| = 1$ and $|m| = 2$ oscillations within non-columnar mean flowfields. Proceeding along the steady flow solution curve, the first such instability to appear is solution curve 10, which bifurcates at $S = 2.081$ and corresponds to a co-rotating $|m| = 1$ oscillation. Visualizations of representative solutions along this curve are shown in Figure 3.13. Immediately after its birth, solution curve 10 proceeds in the direction of decreasing S, bypassing the turning point of the steady flow at $S = S_B$. Initially, the morphology of its solutions take the form of a gently azimuthally-precessing ellipsoidal 'bubble' recirculation region with a counter-winding spiral tail similar to the structure described in the simulations of Ruith et al. [39]. It is clear by comparison with the steady flow solutions along the intermediate manifold that these $|m| = 1$ oscillations dramatically limit the size of the mean recirculation zone. However, as S decreases in this unconfined flow, a pair of pleated saddle-node bifurcations occur near $S = 2.045$. Beyond this pleat, the small recirculation bubble rapidly opens up into a much larger asymmetric cone structure resembling the observations of Billant et al. [31]. As S further decreases toward the forward turning point at $S = S_B$, the asymmetry of the central recirculation gradually fades, and the oscillation eventually succumbs to a stabilizing Hopf bifurcation at $S = 2.022$. Note that the amplitude peak apparent in the diagram shortly before the lower extent in S of solution curve 10 is caused by the increase in the oscillation's spatial extent associated with the rapid expansion of the recirculation zone. It is not due to any strengthening of the local velocity fluctuations.

Continuing along the steady flow solution curve after the start of branch 10, the next

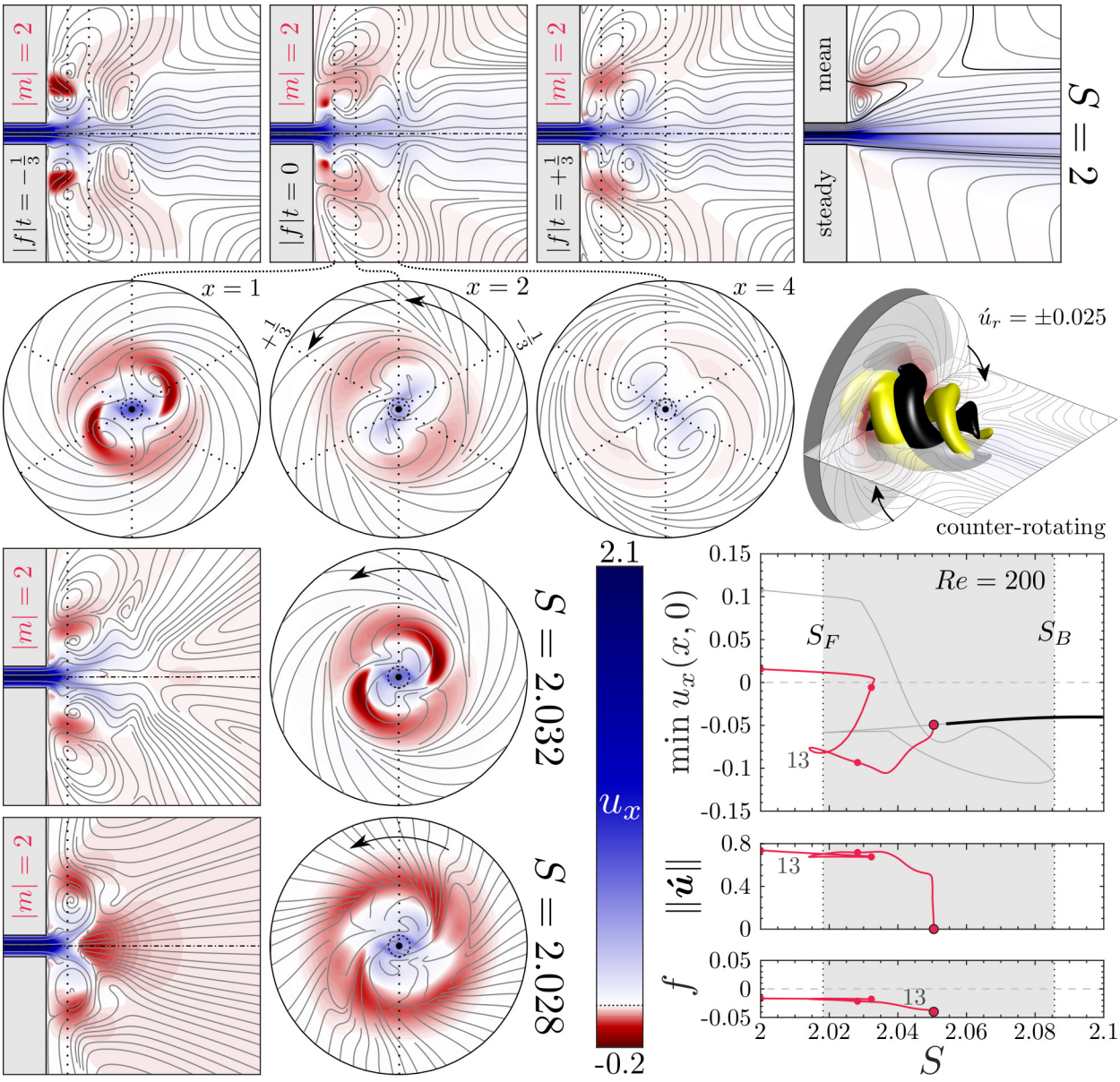

Figure 3.12: Visualization of the flow structures at three points along branch 13 using the format of Figure 3.7. The locations of the chosen flowfields on the solution branch are indicated on the bifurcation diagram. All representations are extracted from within the volume $(x, r, \theta) \in [-2, 10] \times [0, 6] \times [0, 2\pi]$.

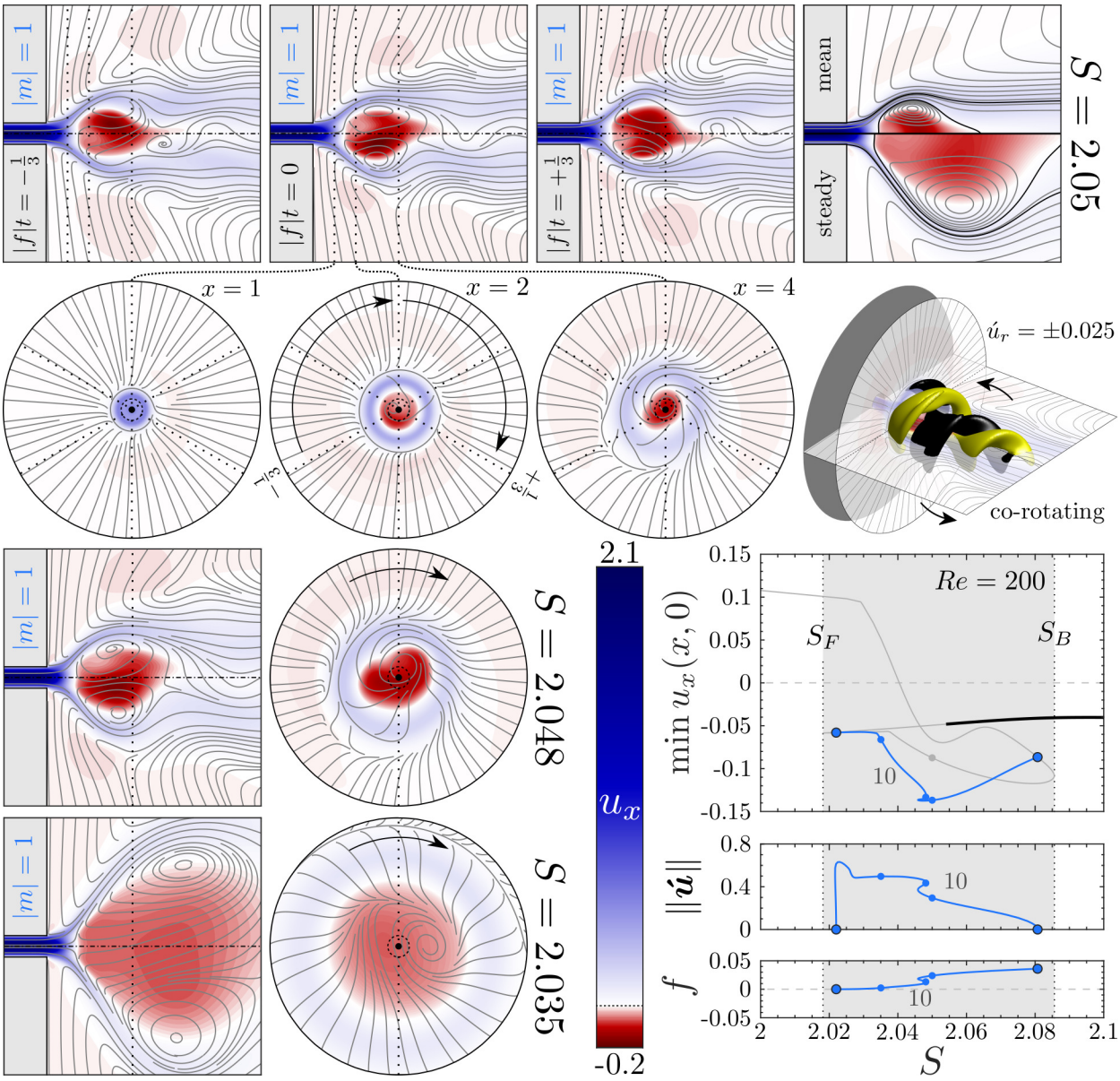

Figure 3.13: Visualization of the flow structures at three points along branch 10 using the format of Figure 3.7. The locations of the chosen flowfields on the solution branch are indicated on the bifurcation diagram. All representations correspond to the same visualization volume of $(x, r, \theta) \in [-2, 10] \times [0, 6] \times [0, 2\pi]$. In this figure, the yellow and black surfaces in the isometric view represent the respective $u_x - \bar{u}_x = \pm 0.025$ isocontours.

periodic solution branch to appear is number 7. Solution branch 7, which corresponds to counter-rotating $|m| = 2$ oscillations, bifurcates from the steady flow along the upper portion of the steady solution manifold at $S = 2.084$, just before the first saddle-node bifurcation of the steady flow at $S = S_B$. Visualizations of representative solutions along curve 7 are shown in Figure 3.14. The unsteady structures on curve 7 take the form of vortex filaments arranged in a co-winding spiral concentrated along the shear layers between the jet and the inner and outer recirculation zones. These shear layer fluctuations greatly enhance the mixing of the jet with its surroundings. At first, these oscillations primarily entrain fluid from the central recirculation zone, causing the time-averaged central recirculation zone to radially compress and axially elongate relative to the corresponding steady flowfield. This 'squeezing' of the central bubble allows the solutions along curve 7 to exhibit the more negative velocities along the axis than the steady flow and stalls the expansion of the central bubble with decreasing swirl. However, as rotation further decreases and the central recirculation bubble begins to swell, the oscillations begin to instead favor entrainment from the outer recirculation zone. This transition reverses the previous trend whereby the mean central vortex bubble is compressed, rather causing the central recirculation zone to expand to a larger size than is seen in the steady flow. Nonetheless, this expansion of the central vortex weakens the oscillation, leading to a complex chain of nonlinear behaviors which manifest a pleated pair of saddle-node bifurcations at $S = 2.056$ and $S = 2.063$ and ultimately result in the demise of the solution curve at $S = 2.062$.

The remaining periodic solution curves branch from the intermediate steady flow solution manifold as S decreases from S_B to S_F. Of these, periodic solution branch 8, which bifurcates at $S = 2.080$, is the first to appear after the backwards turning point at S_B. Solution 8 is a co-rotating $|m| = 2$ instability as shown by the representative visualizations in Figure 3.15. The solutions on branch 8 can be interpreted as the $|m| = 2$ analogue of the $|m| = 1$ solutions on branch 10. That is, they correspond to oscillatory motions featuring a pulsating, non-axisymmetric ellipsoidal recirculation bubble with a counter-winding spiral

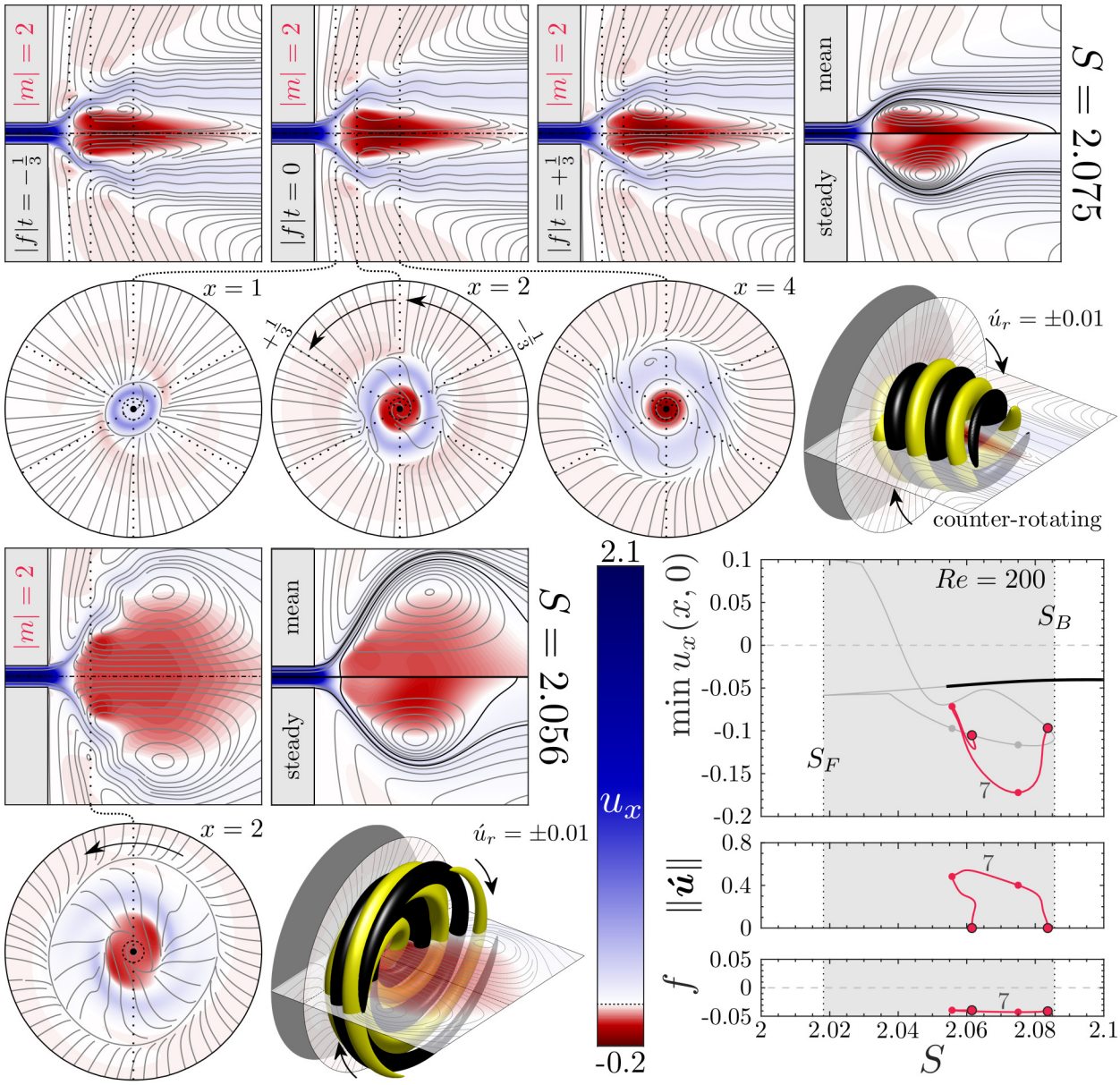

Figure 3.14: Visualization of the flow structures at two points along branch 7 using the format of Figure 3.7. The locations of the chosen flowfields on the solution branch are indicated on the bifurcation diagram. All representations correspond to the same visualization volume of $(x, r, \theta) \in [-2, 10] \times [0, 6] \times [0, 2\pi]$.

tail. This structure closely resembles the 'double-helical' breakdown mode described in the Grabowski-Berger vortex simulations of Ruith et al. [39]. Much like the solutions on branch 10, these oscillations retard the expansion of the time-average central recirculation zone as *S* decreases in comparison to the corresponding steady flow solutions. However, the branch 8 dynamics are simpler than those of branch 10, as there are no kinks or folds in the curve as *S* decreases. The oscillations weaken as *S* decreases until stabilizing in a Hopf bifurcation at $S = 2.028$. Interestingly, the eigenmode associated with this bifurcation briefly destabilizes again for a very small interval of *S* almost immediately after branch 8 restabilises. This 'blip' gives rise to branch 9 which represents a very small amplitude oscillation with the same characteristics as the solution on branch 8.

Just as the co-rotating oscillation on with $|m| = 1$ on branch 10 has an $|m| = 2$ counterpart, the counter-rotating oscillation with $|m| = 2$ on branch 7 has a slowly counter-rotating $|m| = 1$ cousin on branch 11. Visualizations of representative solutions along curve 11 are also shown in Figure 3.15. Branch 11 is born at a Hopf bifurcation from the intermediate steady flow manifold at $S = 2.066$. At this point, the central recirculation zone of the steady flow already measures several pipe diameters in radius and, unlike on branch 7, the $|m| = 1$ oscillations on branch 11 do not have a significant influence on the size of the recirculation zone of the mean flow as their amplitude increases with decreasing *S*. Nonetheless, these oscillations introduce a sizable non-axisymmetric component to the central recirculation zone. The unsteady structures on branch 11 represent a weak but spatially-extensive spiral vortex which appears as an asymmetric flapping along the back of the large central recirculation region when viewed from a meridional slice plane of the instantaneous flow. However, as *S* decreases further, the expansion of the central recirculation region apparently overpowers the growth of the oscillations, and the unsteady motions begin to dissipate. Branch 11 ends in a Hopf bifurcation at $S = 2.022$. However, as was the case with branches 8 and 9, the eigenmode associated with this stabilizing bifurcation briefly resurfaces again shortly after its initial disappearance. This recurrence gives rise to

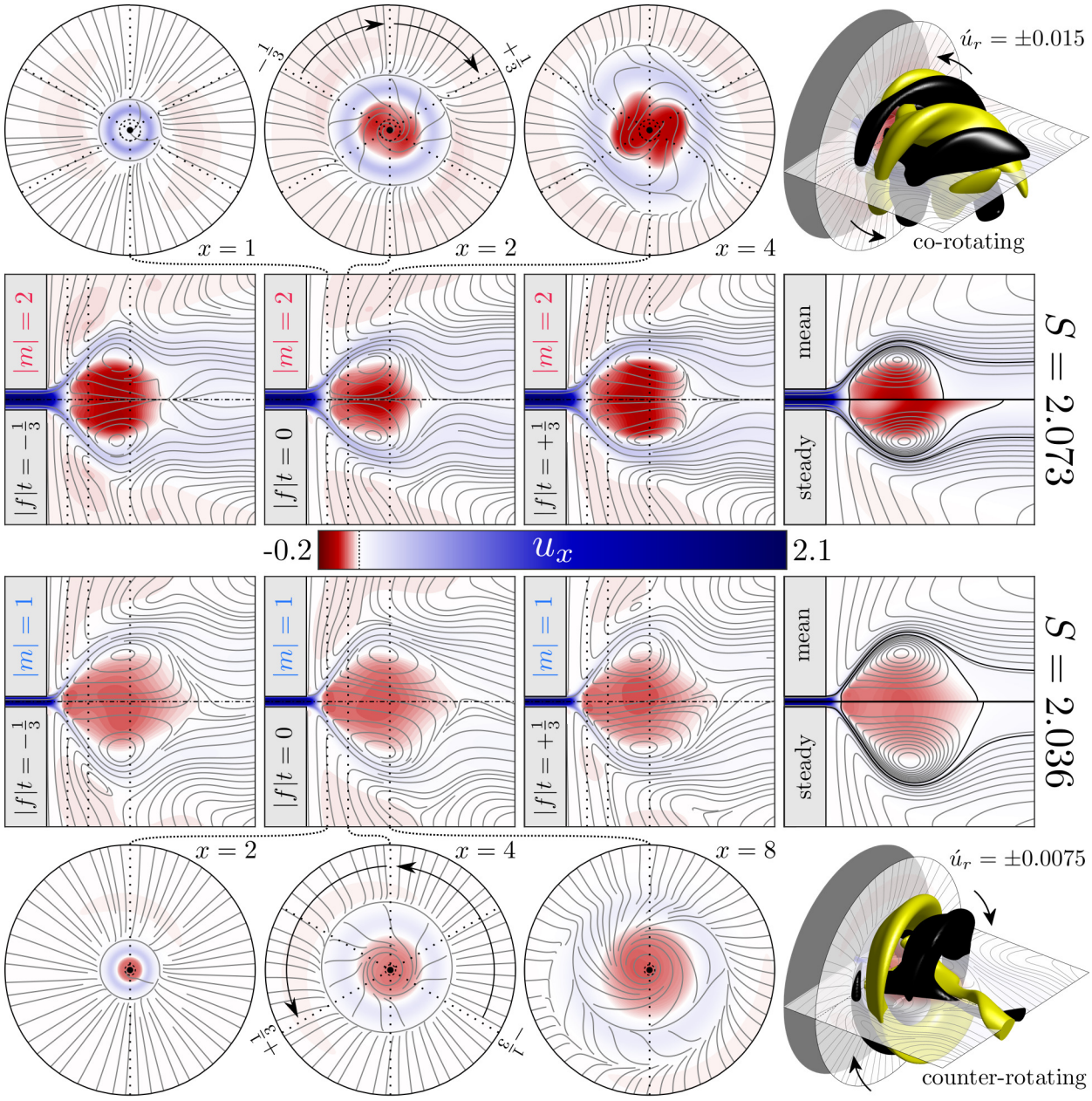

Figure 3.15: Visualization of the flow structures of branches 8 (top 2 rows) and 11 (bottom 2 rows) using the format of Figure 3.7. The representations from branch 8 and 11 correspond to the visualization volumes $(x, r, \theta) \in [-2, 10] \times [0, 6] \times [0, 2\pi]$ and $(x, r, \theta) \in [-4, 20] \times [0, 12] \times [0, 2\pi]$, respectively.

a short-lived solution branch numbered 12 whose solutions exhibit similar spatiotemporal characteristics to those of branch 11.

The final periodic solution branch which bifurcates from the steady flow solution manifold at $Re = 200$ is a counter-rotating $|m| = 1$ instability which exists along branch 14. Solution branch 14 is a direct extension of the post-breakdown $|m| = 1$ oscillation which was present at $Re = 150$, and its initial and final bifurcations lie on the same neutral curves as the $Re = 150$ case. It is thus unsurprising that both its dynamics and its structural appearance remain very similar to this lower *Re* case.

3.2.4 Discussion: Overall limit cycle characteristics

This subsection reviews the results of this analysis of the swirling jet's periodic solutions and discusses them in the context of existing literature. Just as in subsection 3.1.3, the various limit cycle solution curves can be interpreted as solution manifolds over the (Re, S) parameter space. However, many of these solution manifolds are multivalued over a significant portion of the parameter space due to subcritical bifurcation behaviors or other nonlinear effects and almost all overlap with other limit cycle manifolds in the (Re, S) space. These qualities make a clear, global visualization of the limit cycle dynamics analogous to Figure 3.5 difficult to realize. Nonetheless, the results show that a variety of different limit cycle structures ranging in periodicity from $0 \leq |m| \leq 5$ and exhibiting both co- and counter-rotating temporal behaviors and co- and counter-winding spatial behaviors exist over a large portion of the parameter space.

The fact that limit cycle states with different periodicities, rotation directions, and winding orientations exist at identical points in the parameter space is remarkable. Throughout the literature of swirling flows, there is a wide range of reported properties of the observed periodic structures. For example, Ruith et al. [39] noted in their survey that confined experiments have typically reported co-winding spiral structures while unconfined experiments have favored the counter-winding orientation. Liang & Maxworthy [35] have similarly

emphasized differences in the structures' observed rotation direction and speed across different studies. In this study, no evidence was found to support the idea that the limit cycle states have a global preferences for a single rotation or winding direction. However, this study has not carried out the Floquet analyses necessary to ascertain the limit cycles' stability characteristics, which could be biased toward particular rotation or winding traits. This indicates an important direction for future work.

Another important takeaway from this section is the significance of high-order bifurcation behaviors. Limit cycle oscillations stemming from supercritical Hopf bifurcations with a third-order normal form have been documented in swirling jets by several authors [35, 76, 42, 58]. However, there are no examples in the literature of swirling jets which have conclusively demonstrated the type of fifth- or higher-order Hopf bifurcations recorded here, though hysteresis behavior consistent with this idea has been reported [31, 33]. Aside from its physical implications, this is an important distinction because standard weakly-nonlinear methods which employ a third-order Stuart-Landau amplitude equation [130, 42, 58] cannot capture these types of bifurcation behaviors. Several of the bifurcations recorded in this study would require a higher-order weakly-nonlinear expansion (e.g. [131]) to be modeled appropriately. Moreover, these results did not show any specific link between the nature of a bifurcation and the azimuthal periodicity, rotation direction, or winding orientation of its ensuing limit cycle structures.

Lastly, the role of unsteady nonlinear interactions in the jet's limit cycle dynamics is considered. Harmonic interactions represent a key aspect of any nonlinear oscillation. However, as evidenced by Sipp & Lebedev [130], in certain cases, their dominant effect amounts to a steady Reynolds stress which only impacts the mean flow, while, in others, they also lead to significant Reynolds stress oscillations which directly influence the flow's oscillatory behavior. While modeling the latter situation requires nonlinear methods, in the former case, a linear analysis about the mean flow (based upon either a nonlinear calculation or an experimental measurement) can often characterize some aspects of the oscilla-

tion such as its linear stability, relative shape, and frequency with fair accuracy [132]. This raises an important practical question: is mean flow stability analysis a robust technique for characterizing the certain characteristics of limit cycle oscillations in swirling jets? A recent analysis by Manoharan et al. [58] has demonstrated that, in the specific situation of a turbulent swirling jet where the limit cycle oscillation appears at a supercritical Hopf bifurcation, the mean flow analysis approach is effective. However, it remains to be seen whether the same is true in general.

This question was addressed in this study by performing linear stability calculations on mean flowfields associated with the limit cycle states presented above at several representative conditions and comparing them with linear calculations from the steady flow and the fully-nonlinear results. The results of this analysis are tabulated in Table 3.1, along with the percentage of the unsteady kinetic energy contained in the limit cycle fundamental. Many of these cycles clearly do not satisfy the marginal stability property of [130], (i.e., $\sigma_M \approx 0$) implying that unsteady harmonic interactions do influence the limit cycle dynamics. Nonetheless, the results also indicate that, in most cases, surprisingly accurate estimates of the limit cycle oscillation frequency can be obtained using mean flow stability analysis, even when the growth rate is not small. Similar determinations have been reached for swirling jets in the turbulent regime by Oberleithner et al. [76], Tammisola & Juniper [77], and Mukherjee et al. [79], in addition to the more formal demonstration mentioned above by Manoharan et al. [58]. This outcome is particularly convenient for interpreting experimental data, where time averages are readily accessible. In particular, it supports the methods which will be adopted by this thesis in chapter 5 to analyze experiments of a turbulent reacting jet. Of course, for computations, the mean flow itself must be determined prior to applying this analysis.

Table 3.1: Comparison of selected nonlinear limit cycle results with frequency predictions from linear stability calculations about the mean flow. Here, $\%KE_f$ is the percentage of the unsteady kinetic energy contained in the limit cycle fundamental, f is the nonlinear limit cycle frequency and σ_M and f_M are the growth rate and frequency of the mean flow eigenvalue.

Re	*S*	$\|m\|$	Visualization	$\%KE_f$	f	σ_M	f_M
150	2.000	1	Figure 3.7	92.2	-0.1432	0.0417	-0.1501
150	2.000	2	Figure 3.7	74.3	0.0349	0.1383	0.0373
300	1.987	0	Figure 3.8	94.7	0.4618	-0.0625	0.4792
300	1.367	3	Figure 3.8	84.3	0.1011	0.0370	0.1033
300	2.766	1	Figure 3.9	99.2	0.7258	-0.0007	0.7258
200	2.000	2	Figure 3.12	77.3	-0.0167	-0.0109	-0.0227
200	2.050	1	Figure 3.13	84.3	0.0237	-0.0014	0.0247
200	2.075	2	Figure 3.14	88.3	-0.0427	-0.0103	-0.0415
200	2.073	2	Figure 3.15	93.0	0.0215	-0.0019	0.0225
200	2.036	1	Figure 3.15	97.6	-0.0021	-0.0002	-0.0021

3.3 Summary

This chapter characterized the dynamics of an unconfined, fully-developed, non-reacting swirling jet. It showed how variations in the swirl ratio *S* and Reynolds number *Re* affect the morphology of the system's steady and time-periodic solutions and how the state-space topology of the associated solution manifolds are linked to the physical structure of the flow. Numerical continuation of the steady solutions reveals that the flow morphology transitions from a quasi-columnar jet along the central axis at low *S* to a radial jet along the dump plane wall at high *S*. In between these limits, a nonlinear exchange of stability occurs due to a competition between two low pressure regions: a central region which is associated with vortex breakdown, and an outer region which forms due to entrainment of the ambient fluid exterior to the jet. This transition in flow structure is linked to a cusp bifurcation within the steady solution manifold which manifests parameter hysteresis over a small range of $S \sim 2$ for $Re > 47.1$.

Beyond certain critical parameter values, the steady solution manifold becomes unstable toward infinitesimal perturbations which break the time and azimuthal symmetry of

the steady system. Over the range of parameters investigated, the initial Hopf bifurcations are always associated with $|m| = 1$ or $|m| = 2$ disturbance modes. Additional instabilities corresponding to unsteady $m = 0$ and $|m| \geq 3$ perturbations only occur at points on the solution manifold where at least one $|m| = 1$ or $|m| = 2$ mode is already unstable. The neutral curves associated with each linear disturbance mode represent the intersections of the various periodic solution manifolds and the steady solution manifold in the state space. The nonlinear limit cycle solutions which stem from these neutral curves are associated with both super- and sub-critical bifurcation behavior. In the physical space, the limit cycle solutions display a wide array of three-dimensional, co- and counter-rotating flow structures which often exhibit very different time-averaged flow patterns compared to their steady counterparts at identical parameter values. Many of these structures bear strong resemblances to coherent structures reported in previous experiments. For example, the $|m| = 2$ limit cycle in the pre-breakdown regime at $Re = 150$ (see Figure 3.7) is reminiscent of the $|m| = 2$ instability detailed by Billant et al. [31]. Similar parallels may also be drawn between the $|m| = 1$ (Figure 3.13) and $|m| = 2$ (Figure 3.15) periodic solutions which occur in the vortex breakdown regime at $Re = 200$ and the single and double spiral forms of vortex breakdown reported in a broad range of swirling flows including top-hat jets [35], the Grabowski-Berger vortex [39], and confined vortex tubes [26], among others.

As remarked in chapter 1 and the previous paragraph, a unified framework that allows a global understanding of a general swirling flow configuration, and the similarities or distinctions between flow patterns across different flow configurations and parameter spaces, remains a key open challenge for the community. The present work contributes to this broader aim by definitively relating a suite of steady and time-periodic states in fully-developed laminar swirling jets with flush injection into a semi-infinite reservoir. Nonetheless, a number of questions requiring further research remain. These ideas will be discussed in chapter 7.

CHAPTER 4
BIFURCATION ANALYSIS OF FULLY-DEVELOPED SWIRLING FLAMES

This chapter builds on chapter 3 by considering the behaviors expressed by swirling jets undergoing lean premixed combustion. The configuration and methods used in this chapter are detailed in chapter 2. Overall, the setup is quite similar to that used in the experimental studies performed by Gotoda et al. [133, 46], but there are some notable differences. One such difference is that their investigation focused on rich premixed flames, while the flame model studied here is based on the assumption of a very lean reaction. In addition, Gotoda et al. [133, 46] focused on flames in a free-standing rotating Bunsen burner without any nearby walls. The setup used in this study, however, uses the same geometry adopted in chapter 3, which has a semi-infinite, adiabatic containing wall placed flush to the jet exit.

4.1 Scope and Context

To begin, a few comments are worthwhile in order to provide some preliminary context for this study and to limit its scope. While it may seem straightforward on the surface, the introduction of a flame greatly complicates the already quite complex dynamics of a swirling jet. Even the relatively simplistic single-step chemistry model considered in this thesis (see chapter 2) introduces four new independent parameters to the two which appear in the inert case, yielding a six-dimensional parameter space. Furthermore, the equations governing the reacting flow are comparatively larger and far more strongly nonlinear. It is beyond the scope of any single study to comprehensively characterize this enormous parameter space and equation system. In addition, an exhaustive analysis of this space would barely scratch the surface of physically-relevant conditions, as different flame models and boundary conditions will lead to different flame behaviors which are not accessible to the selected model. For example, rich stoichiometry, non-adiabatic walls, thermo-diffusive (i.e.

non-unity Lewis number) effects, detailed chemical pathways, and non-constant viscosity will all fundamentally alter the solutions admitted by the system. Instead, the purpose of this chapter is to demonstrate examples of the different ways that a generic lean premixed flame can affect the behavior of a swirling jet, with the aim of developing a foundational understanding of the physical processes underlying the considered dynamics.

All of the flames studied in this chapter are associated with a fixed Zeldovich number of $Ze = 10$. According to Seshadri & Göttgens [134], this value corresponds to a reasonable estimate for *Ze* in the context of lean hydrocarbon-air flames at standard (atmospheric) conditions. This choice should be contrasted with the previous investigations discussed in chapter 1 by Rusak, Kapila, & Choi [47, 48]. In those studies, the asymptotically low flame temperatures resulted in $Ze \sim 1$ – a value far lower than any usual flame. (Recall that the Zeldovich number appears in the exponential heat release term, so a factor of ten difference is quite dramatic.) Even though the Zeldovich number will be fixed in the results of this study, the flame speed, temperature, and thickness may still be freely manipulated by varying *Da*, *Pe* and ΔT. This is important, as these factors are intertwined with the flame speed, the flame thickness, and the density ratio which are well-known to have a tremendous influence on the position, shape, and structure of a flame as well as the overall flow dynamics and stability characteristics.

4.1.1 Overview of the flame model

Before moving on to the main results, the main effects of the various flame parameters on the structure of the flame are considered. A sample of four different flames in non-swirling conditions at $Re = 200$ are tabulated in Table 4.1 and visualized in Figure 4.1. These flames have a variety of different properties in order to demonstrate how the parameters influence the overall flame structure. In addition to the flame parameters and *a priori* flame speed and flame thickness estimates from Equation 2.3, Table 4.1 also reports the flame length L_F. Here, L_F is evaluated *a posteriori* from the numerical solution and is defined as the

Table 4.1: Table of sample flames considered to demonstrate the properties of the chemistry model. Here, S_L^0 and δ_F^0 are *a priori* estimates for the unstretched laminar flame speed and thickness given by Equation 2.3, and L_F is evaluated *a posteriori* from the solution.

Label	*Re*	*S*	ΔT	*Ze*	*Da*	*Pe*	S_L^0	δ_F^0	L_F
Flame A	200	0	3	10	400	100	0.257	0.0389	2.80
Flame B	200	0	3	10	200	50	0.257	0.0778	2.30
Flame C	200	0	3	10	200	200	0.129	0.0389	5.51
Flame D	200	0	5	10	423	100	0.257	0.0389	3.07

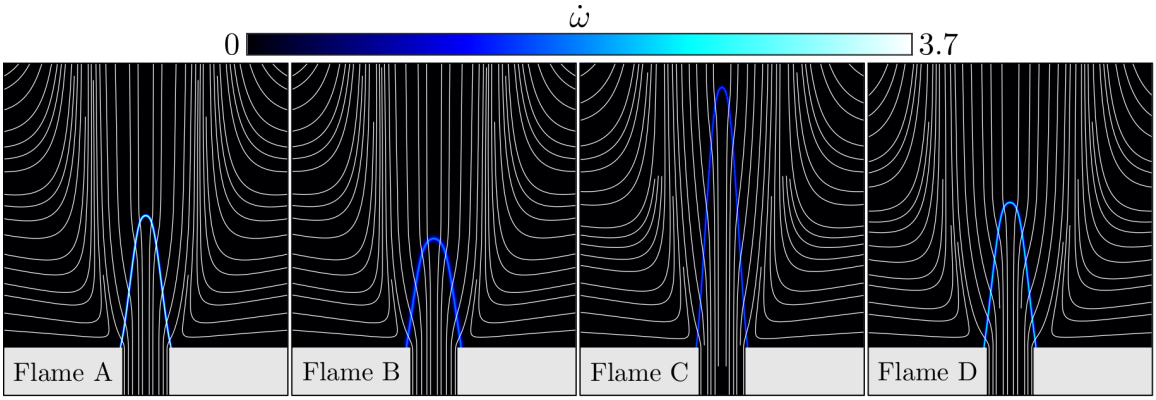

Figure 4.1: Meridional visualizations of the steady, axisymmetric, non-swirling flames from Table 4.1 via reaction rate contours (blue) and velocity streamlines (white) over $(x, r) \in [-1, 6] \times [0, 3]$. Here, the jet's x-axis is oriented vertically to allow easy, side-by-side comparisons.

position of peak heat release along the centerline (i.e. the location of $\max \dot{\omega}(x, 0)$ where $\dot{\omega}$ is the local heat release).

The data in Table 4.1 and Figure 4.1 showcase several important details of the flame model. For example, it is clear that the S_L^0 estimate is only somewhat correlated with the resulting flame length. While part of this disagreement may stem from errors associated with the approximations used to derive Equation 2.3, it is worth pointing out that in this axisymmetric model, the flames exhibit local curvature everywhere and can not be assumed to be unstretched even in the "cone" region of the flame. In addition to this, the tip region of the flames is highly sensitive to a number of key physical effects which preclude a one-to-one relationship between S_L^0 and L_F. For instance, flames with lower values of *Pe* (e.g. Flame B) are associated with more rounded flame tips due to the increased relative role of

diffusion. Another key effect is associated with the role of thermal expansion. Comparing Flame D (the hottest flame) with the others, it is clear that the post-flame jet has the largest cross-sectional area due to its high heat release and the resulting dilatation. Finally, it should be mentioned that all of these flames have essentially the same spatially-integrated reaction rate (i.e. $\int_\Omega \dot{\omega}\,\mathrm{d}\Omega$) due to the chosen chemistry model. Thus, any variations in the local reaction rate are compensated by changes in the overall volume of the reaction zone. Flames B and C in particular have noticeably lower local reaction rates which are compensated for by an increased thickness and length of the reaction zone, respectively, in comparison to the others.

4.2 Characterization of the reacting jet

As in chapter 3, the nonlinear solution branches presented below are traced using the Moore-Penrose continuation method described in chapter 2. Once again, the minimum velocity along the centerline $\min u_x\,(x,0) < 0$ is monitored to identify the emergence of central recirculation features as the parameters are varied. Additionally, in order to monitor the evolution of the steady flame, the flame length L_F is extracted from each solution. Once the steady solutions are identified, their linear stability is determined using eigenvalue calculations, and any apparent instabilities are tracked to their corresponding bifurcation points.

4.2.1 Rotation effects

The dynamics of the steady reacting jet under variations in *S* will be considered throughout this chapter alongside other parameters. Nonetheless, in order to demonstrate a somewhat typical evolution of the reacting jet under changing rotation rates, a bifurcation diagram obtained for Flame A with varying *S* is shown in Figure 4.2 for reference. From the bifurcation diagram, it is apparent that this steady reacting jet undergoes the same bifurcation sequence as its inert counterpart (compare against Figure 3.3). At low *S*, the flow exists

in the quasicolumnar regime. This yields a roughly cone-shaped flame (see Figure 4.1) which gradually decreases in length and bulges outwards into a more bulbous shape as the rotation rate and, thus, entrainment increases. In the case of Flame A, the central recirculation region associated with vortex breakdown emerges downstream of the flame front as *S* increases, causing the flame tip to widen in front of the central recirculation region. However, it will later be shown that at slower flame speeds, the central recirculation zone can form upstream of the flame, leading to a "flashback" phenomenon with increasing *S* which does not appear in the non-reacting flow. Regardless, at some critical *S* after the central stagnation point appears and the flame tip spreads in front of the recirculation region, a saddle-node bifurcation occurs at $S = S_B$. This gives rise to the same unstable intermediate manifold as the inert case, where the recirculation zone flares open as *S* decreases beyond the bifurcation. Eventually, like the non-reacting case, another saddle-node bifurcation is reached at $S = S_F$, and the flowfield attains its wall-jet morphology. This flow topology leads to very wide, flat flame shapes at high levels of swirl which closely resemble the high-swirl "plateau" flame structure observed experimentally by Gotoda et al. [46] (see Figure 1.4).

4.2.2 Reynolds number effects

While the effect of the Reynolds number is not a focus of this chapter, a few observations are still worth mentioning. Like the rotation rate, the Reynolds number has a similar qualitative effect on both the reacting and non-reacting jets. Namely, increases in *Re* reduces viscous dissipation, allowing sharper velocity gradients that promote hydrodynamic instabilities. However, the specific critical values of *Re* can change dramatically between the reacting and non-reacting jets. For example, at $Re = 200$, Figure 4.2 indicates that Flame A remains stable toward unsteady and non-axisymmetric disturbances over the full range of rotation rates investigated as no Hopf bifurcations exist in the diagram. In contrast, Figure 3.3 indicated several different instabilities for the inert case at the same Reynolds

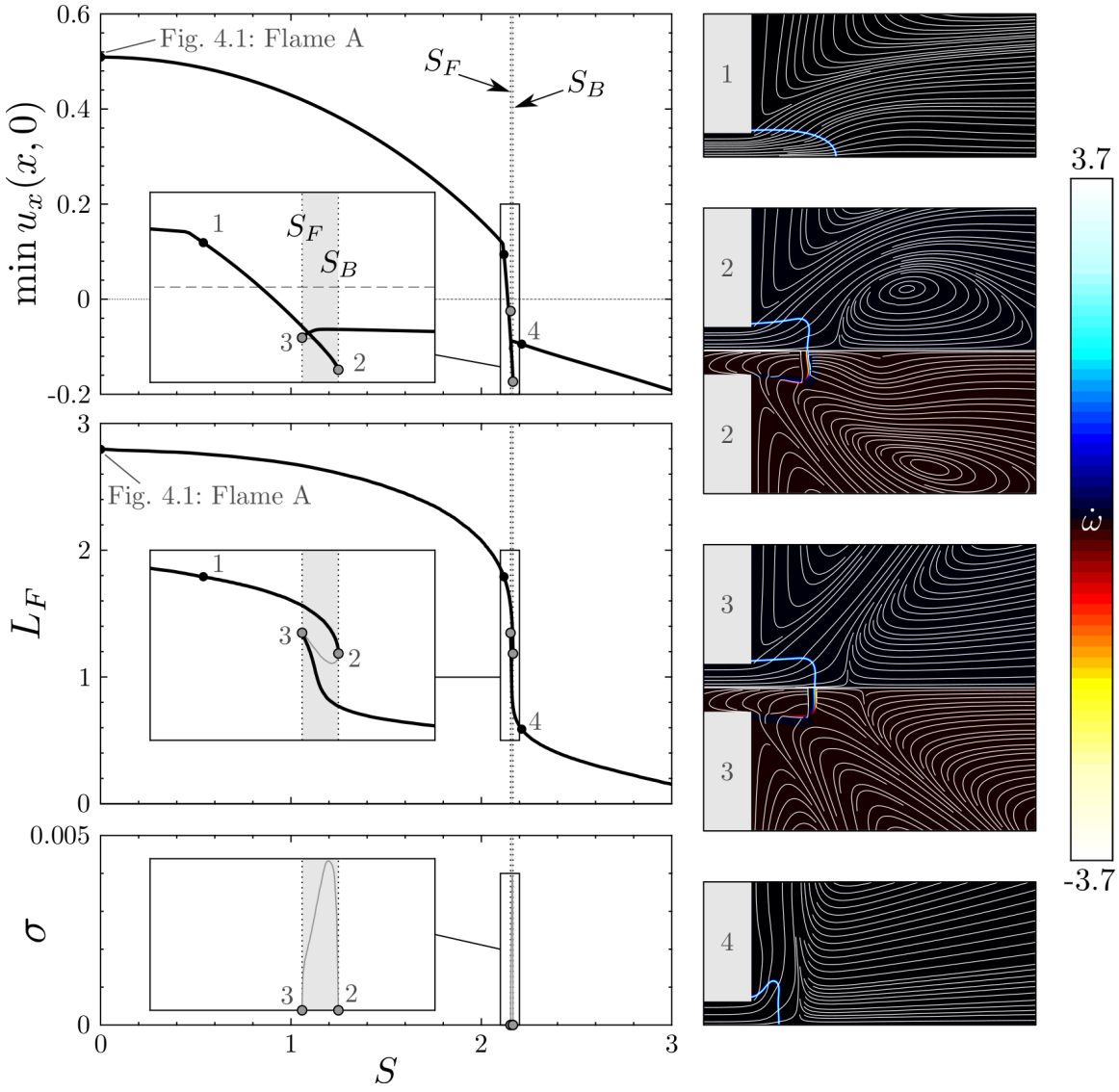

Figure 4.2: Bifurcation diagram showing the evolution of the minimum velocity along the axis, the flame length, and the growth rate of the non-stable eigenvalues for Flame A at $Re = 200$ with varying S. The thin gray portion of the solution curve corresponds to the unstable intermediate saddle which connects the two stable portions of the solution indicated by the thick black curves. Note that the only unstable modes are axisymmetric and steady (i.e. $m = f = 0$). Meridional projections of the axisymmetric reaction rate contours and velocity streamlines are shown over $(x, r) \in [-1, 6] \times [0, 3]$ for selected steady flow fields corresponding to points indicated on the diagrams. Critical eigenmodes (arbitrary amplitude) are also shown in the lower half plane for points 2 and 3 indicated in the diagrams. These results can be compared against the non-reacting case in Figure 3.3.

number.

To briefly demonstrate the effect of *Re* in the reacting jet, an analysis of Flame A at a fixed rotation rate of $S = 2.05$ and varying *Re* is given in Figure 4.3. These results, which may be compared against the inert results in Figure 3.4, show that the critical $Re = Re_U$ for Flame A at $S = 2.05$ is approximately four times higher than in the corresponding non-reacting case. In this example, the primary instability is associated with a co-rotating, counter-winding $|m| = 1$ mode which is also visualized in Figure 4.3. More generally, the frequency and structural properties of the bifurcating modes and the critical Reynolds number all vary significantly depending on the specific combination of the reacting jet parameters. As such, aside from noting a *destabilizing* effect of elevated *Re* in this example, no further effort will be made to characterize the effect of *Re* on reacting swirling jets.

4.2.3 Heat release effects

Next, the effect of the exothermicity on the behavior of the reacting swirling jet flowfield is considered. Branch continuation analyses were performed across a range of ΔT and S values at constant $Re = 200$, $S_L^0 = 0.257$, $Ze = 10$, and $\delta_F^0 = 0.0389$ in order to isolate the effect of exothermicity and avoid confounding heat release effects with variations in the flame speed and flame thickness. Here, S_L^0 and δ_F^0 are held constant by adjusting *Da* to compensate for changes in the flame speed associated with varying ΔT at a constant value of *Pe*=100. The chosen flame properties match the parameters of Flame A at $\Delta T = 3$ and Flame D at $\Delta T = 5$ for $S = 0$. The results of this analysis are summarized in the bifurcation diagrams and stability map shown in Figure 4.4. Note that the results at $\Delta T = 0$ and $\Delta T = 3$ correspond exactly to the bifurcation diagrams shown in Figure 3.3 and Figure 4.2, respectively. Thus, the neutral curves displayed in the stability map of Figure 4.4 are direct extensions of the Hopf bifurcation points from the inert case shown in Figure 3.3, and no "new" instability modes are apparent.

Based on Figure 4.4, it is clear that the overall effect of heat release is largely a stabi-

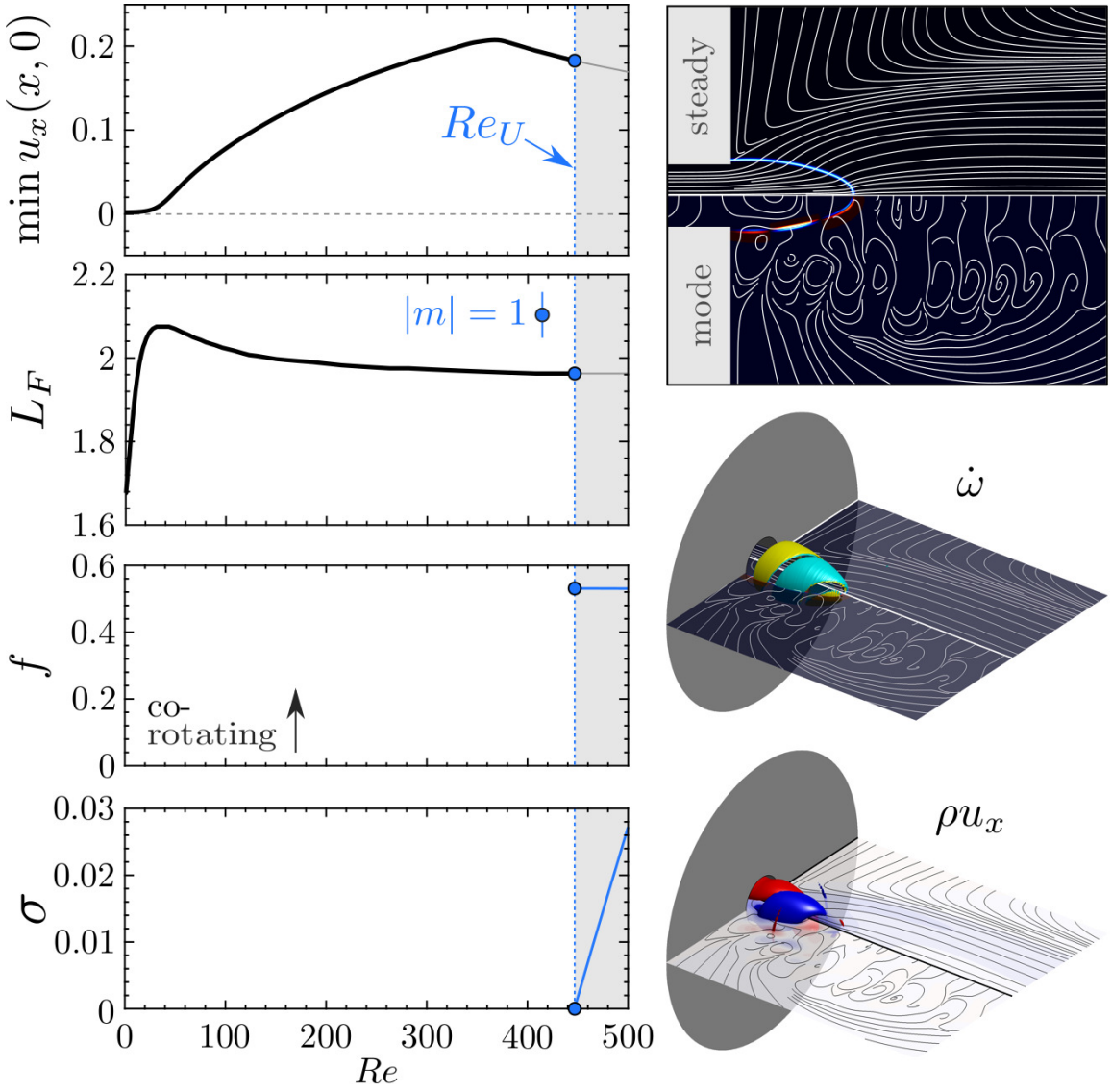

Figure 4.3: (left) Bifurcation diagrams showing the evolution of the minimum velocity along the axis, the flame length, and the growth rate and frequency of the non-stable eigenvalues for Flame A at $S = 2.05$ with varying *Re*. (top-right) Meridional projections of the reaction rate contours and velocity streamlines corresponding to the bifurcation point indicated on the diagrams are shown over $(x, r) \in [-1, 6] \times [0, 3]$ for the steady flow field and the real part of the critical disturbance mode. Three-dimensional isocontour representations of the reaction rate (middle-right) and axial mass flux fields (bottom-right) are also shown.

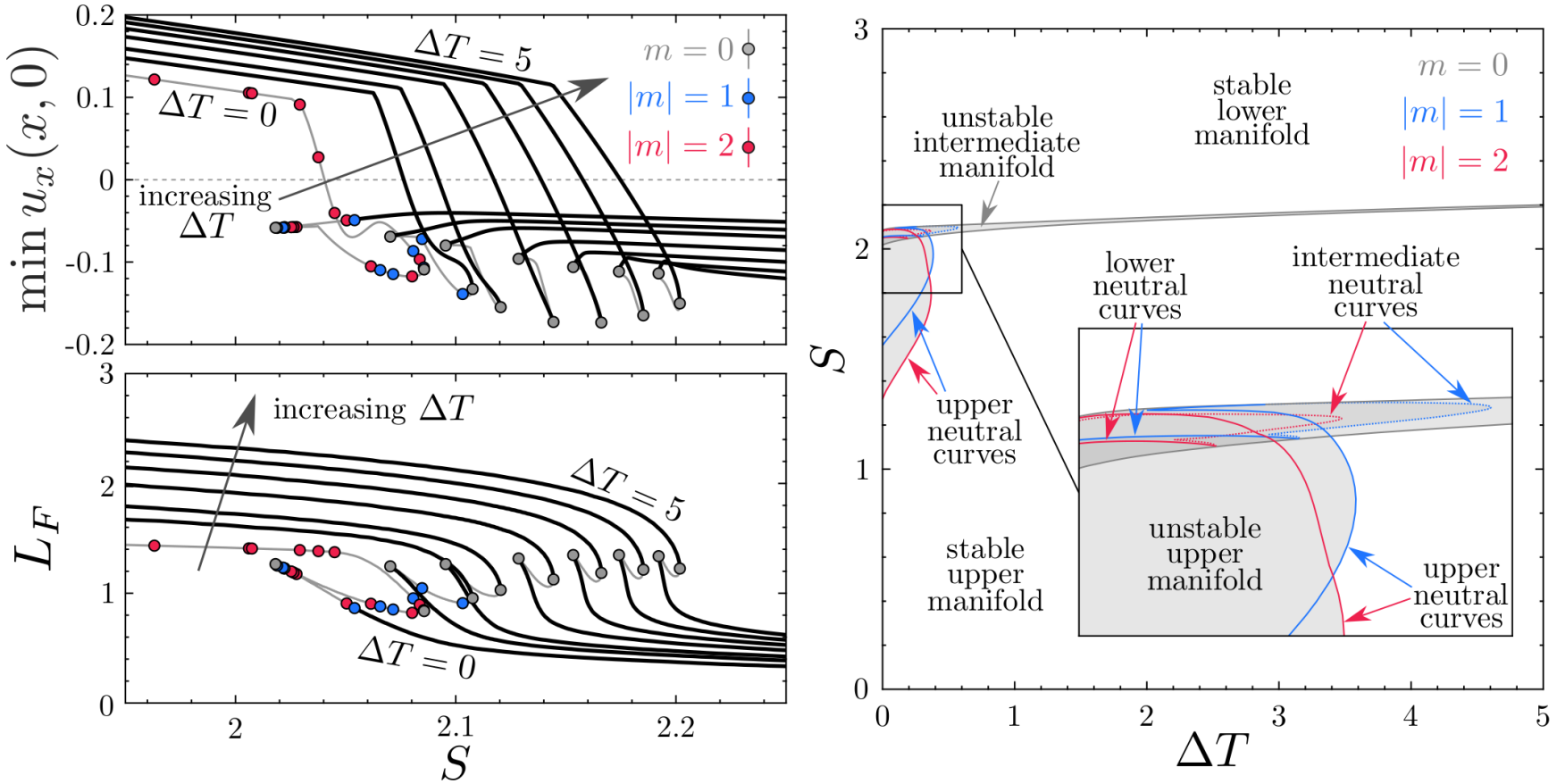

Figure 4.4: (left) Bifurcation diagrams showing the evolution of the minimum centerline velocity and flame length for $\Delta T = [0, 0.5, 1, 2, 3, 4, 5]$ with varying S at constant $Re = 200$, $S_L^0 = 0.257$, and $\delta_F^0 = 0.0389$. (right) Corresponding stability map in the $(\Delta T, S)$ parameter space.

lizing one. While flow instabilities associated with $|m| = 1$ and $|m| = 2$ modes do exist for the given flame parameters at low exothermicity values, all of these instabilities are quenched beyond $\Delta T \gtrsim 0.6$ in this case. It should be noted that the neutral curves shown in Figure 4.4 are dependent on other factors besides just *S* and ΔT, such as the flame speed and thickness. In later subsections, instabilities will be shown to exist at exothermicity values higher than $\Delta T = 0.6$ under different flame conditions. Nonetheless, even in those cases, elevated exothemicity was determined to have a stabilizing effect, as both the peak growth rates and the range of parameters over which the disturbance modes are unstable are reduced with increasing ΔT.

In addition to resisting instability, higher heat release rates also delay the onset of vortex breakdown, as indicated by the larger rotation rates required to achieve flow stagnation at high ΔT values in Figure 4.4. This result seems intuitive based on classical flame theory, where the thermal expansion associated with heat release may be expected to accelerate the jet in the direction normal to the flame. In the case of an axisymmetric jet, this accelerates the jet axially and radially but not azimuthally, thereby decreasing the local ratio of the azimuthal and axial momentum flux and stalling vortex breakdown. Evidence of this dilatation-induced acceleration is shown in Figure 4.4 by the increased values of $\min u_x(x, 0)$ and L_F at higher ΔT values. However, an asymptotic result reviewed in chapter 1 concerning inviscid reacting swirling flows in pipes by Rusak, Kapila, & Choi [47, 48] suggests an opposite outcome – at least for asymptotically small exothermicity values in diffuse flames. While the inclusion of viscosity, a more complex flow geometry, and higher exothermicity values could all potentially explain this discrepancy, one additional difference between the present setup and the configuration considered in that group of studies is worth emphasizing. Namely, the flame studied by those authors is similar in thickness to the overall diameter of the pipe itself, causing the thermal gradients to be relatively weak and allowing large-scale flow structures to significantly influence the internal structure of the reaction zone. This scale similarity is a fundamental aspect of their asymptotic analysis

alongside the selected perturbation orders. It implies that baroclinic effects due to flame-induced thermal gradients (i.e. the second term on the right-hand side of equation (75) in [47]) are of the same order of magnitude as vortex stretching effects resulting from velocity gradients (i.e. the first term on the right-hand side of equation (75) in [47]). This is a reasonable approximation for the diffuse, low *Ze* flames considered in that study. However, more typical flames, such as those studied here, have sharp reaction fronts with strong, highly-localized thermal gradients compared to typical fluid mechanic length scales. In such a thin flame, the two terms mentioned above may be expected to have very different magnitudes, prohibiting an asymptotic comparison like the one considered by those authors and implying that their result does not extend to reacting flows with steep-fronted flames.

4.2.4 Flame speed effects

The effect of flame speed is considered across four cases separated by factors of two ranging from four times slower than flame A to two times faster. This portion of the study is performed at fixed values of $\Delta T = 3$, $Ze = 10$, and $Re = 200$, and the flame speed S_L^0 is controlled by simultaneously varying *Da* and *Pe* such that $\delta_F^0 = 0.0389$ is held constant. These properties are chosen such that the flame parameters correspond to Flame A at $S_L^0 = 0.257$ and Flame C at $S_L^0 = 0.129$ for $S = 0$. The results of branch continuation over S for each of these cases are displayed in Figure 4.5 along with selected visualizations of corresponding flame and flow fields.

Before addressing some more specific details, it is worthwhile to point out two general trends which are made apparent by the bifurcation diagrams in Figure 4.5. First, as should be intuitively expected, the flame speed is inversely related to L_F. Second, it is clear that flames with higher flame speeds tend to resist the emergence of vortex breakdown. This effect is attributed to the effect of acceleration due to thermal expansion and the angle of the flame. In the case of a very slow flame, the flame is nearly parallel to the jet axis and the resulting flow acceleration normal to the flame is oriented primarily in the radial direction.

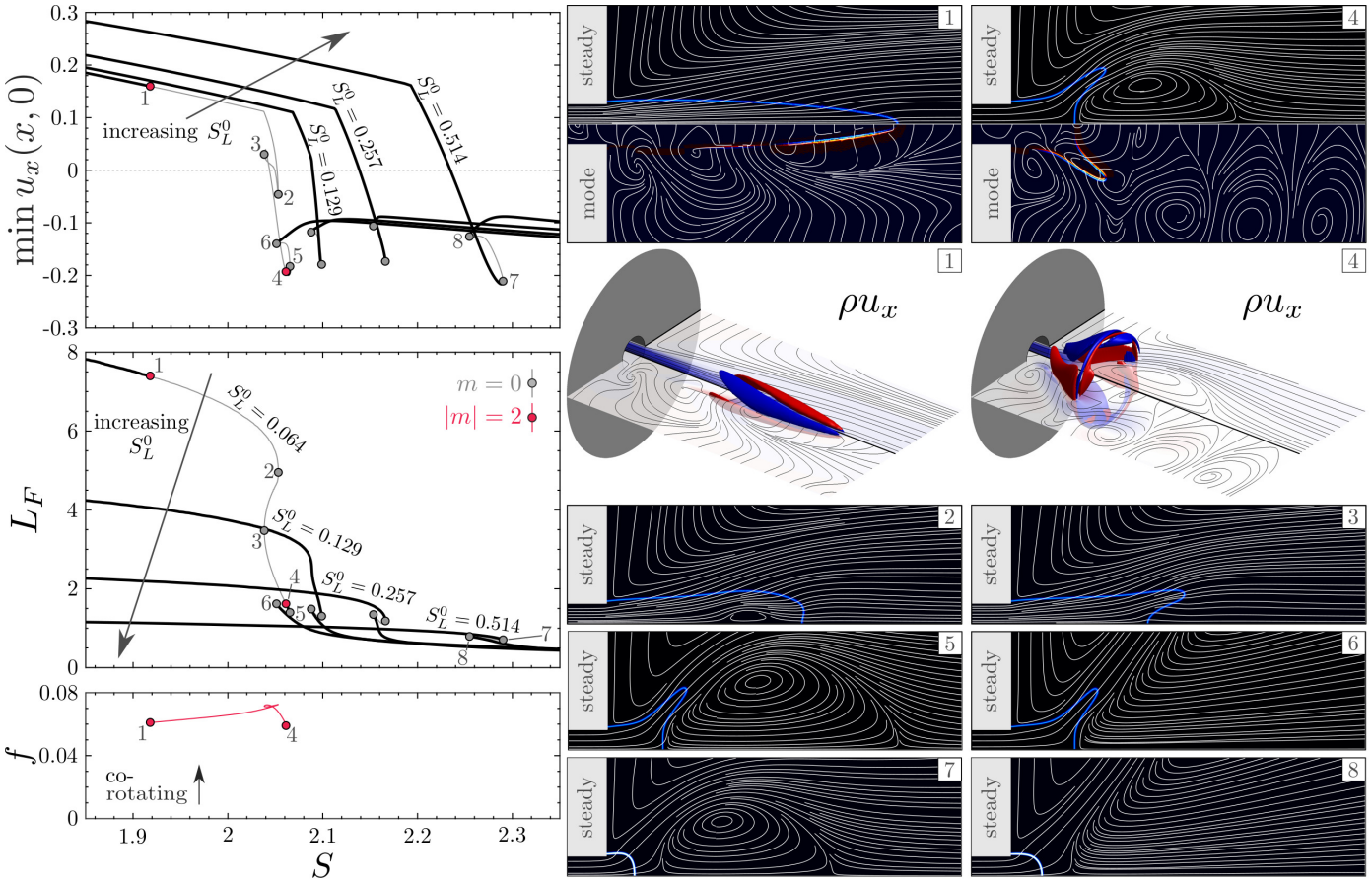

Figure 4.5: (left) Bifurcation diagrams for $S_L^0 = [0.064, 0.129, 0.257, 0.514]$ showing the evolution of the minimum centerline velocity, flame length, and the frequency of the unstable mode with varying S at constant $Re = 200$, $\Delta T = 3$, and $\delta_F^0 = 0.0389$. (right) Visualizations of meridional projections of the reaction rate contours and velocity streamlines corresponding to the steady, axisymmetric flow at the bifurcation points indicated on the diagrams are shown over $(x, r) \in [-1, 9] \times [0, 3]$. Here, points 1-6 correspond to $S_L^0 = 0.064$ while point 7 and 8 correspond to $S_L^0 = 0.514$. In addition to the steady flow visualizations, the $|m| = 2$ Hopf bifurcation modes at points 1 and 4 are also given using meridional projections of the reaction rate and streamlines and a three-dimensional isocontour view of the axial mass flux field based on the real part of the mode.

This radial acceleration does not strongly affect the jet's local ratio of azimuthal and axial momentum flux and therefore does not significantly alter the critical swirl needed to achieve vortex breakdown. Conversely, in the case of a fast flame, the short flame length causes the normal acceleration across the flame to have a significant axial component, thereby increasing the relative flux of axial momentum and stalling vortex breakdown.

From the diagrams, it is clear that the case with the slowest flame speed (i.e. the case with $S_L^0 = 0.064$) undergoes a qualitatively different bifurcation sequence compared to the cases with faster flames. For example, this case experiences a linear instability associated with a co-rotating $|m| = 2$ mode with $f \sim 0.06$ which is not seen at higher flame speeds. Though its critical S is somewhat larger and its frequency is nearly seven times higher, a branch-tracing analysis confirmed that this instability is isomorphic to an $|m| = 2$ bifurcation which is also present in the non-reacting case (i.e. when $\Delta T = 0$) where it occurs at $S = 1.62$ with $f \sim 0.008$. In the reacting case studied here, the $|m| = 2$ instability occurs in the quasicolumnar regime at $S = 1.91$ (point 1) where it exhibits a co-winding helical structure and persists until $S = 2.04$ (point 4), well after the emergence of the central recirculation zone. Note that at point 4, the mode's winding structure cannot be easily defined as it exhibits both co- and counter-winding structures. As shown in Figure 4.5, this instability mode is associated with mass flux fluctuations which feature large amplitudes along the flame front and peak near the flame tip. These characteristics suggest that the nonlinear limit cycle solution branch which stems from this instability is likely to include substantial heat release fluctuations. However, this is merely a hypothesis as no attempt is made in this thesis to characterize the nonlinear limit cycle oscillations which arise due to instabilities of the reacting flow.

Even beyond the existence of an oscillatory instability, however, the steady solution curve for the slowest flame speed contains an extra pair of saddle-node bifurcations (points 2 and 3) which are not present at higher flame speeds. This extra "pleat" in the solution curve reveals bistable behavior associated with a flashback phenomenon, which is inter-

preted as follows. In the case of sufficiently low flame speed, as the rotation rate increases, the initial emergence of the vortex breakdown recirculation zone occurs inside of the flame cone. As the rotation rate continues to increase, this recirculation "bubble" gradually grows in size until a critical point is reached where the flame behind the central bubble cannot be kinematically balanced by the nearly stagnant flow near the rear stagnation point of recirculation region. At this point (labeled 2 in Figure 4.5), a bifurcation occurs and the flame front, unable to stabilize behind the bubble, must propagate through the recirculation zone until it reaches a new stabilization point in front of the stagnation zone. This process has a drastic effect on both the flame shape and the entire flow field. At forward turning point (labeled 3 in Figure 4.5), the flame exhibits a strong inward curvature and velocity along the centerline is seen to be everywhere downstream. This phenomenon is explained by the effect of thermal expansion through the flame causing the flow to accelerate towards the centerline and suppressing the formation of the central recirculation zone. Nonetheless, as the rotation rate increases beyond point 3, the thermal expansion effect is eventually overpowered, leading to the formation of the recirculation zone. Shortly thereafter, another saddle-node bifurcation occurs due to the same nonlinear processes which govern the inert flow, whereby the flow transitions from a quasicolumnar jet to a wall jet. As apparent by comparing the flow visualizations at points 5 and 6 in Figure 4.5, this transition has a dramatic effect on the flowfield topology but a minimal effect on the flame structure. This insensitivity of the flame shape to the flowfield during the quasicolumnar to wall jet transition is consistent – at least qualitatively – across all of the flame speeds investigated.

4.2.5 Flame thickness effects

Before ending this chapter, the effect of flame thickness on the dynamics of the swirling jet is also briefly analyzed. Four cases are considered with flame thickness estimates separated by factors of two and ranging from four times thicker than flame A to two times thinner. Branch continuation analyses over S are performed at fixed values of $\Delta T = 3$, $Ze = 10$ and

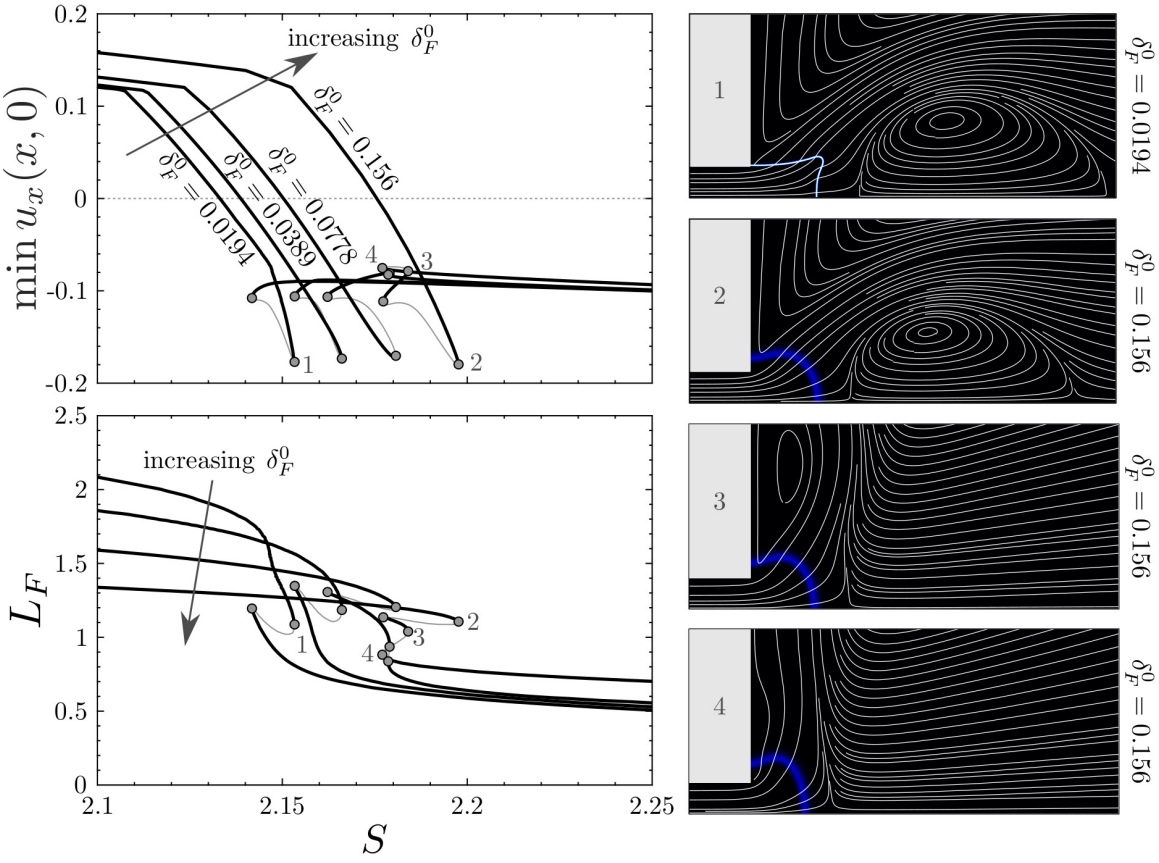

Figure 4.6: (left) Bifurcation diagrams for $\delta_F^0 = [0.0194, 0.0389, 0.0778, 0.156]$ showing the evolution of the minimum centerline velocity and flame length with varying *S* at constant *Re* $= 200$, $\Delta T = 3$, and $S_L^0 = 0.257$. (right) Visualizations of meridional projections of the reaction rate contours and velocity streamlines over $(x, r) \in [-1, 6] \times [0, 3]$ corresponding to the steady, axisymmetric fields indicated on the diagrams. Note that, as mentioned in subsection 4.1.1, the local heat release intensity of the thinnest flame (visualization 1) is approximately eight times that of the thickest flame (visualization 2).

Re $= 200$, and the flame thickness δ_F^0 in each case is controlled by simultaneously varying *Da* and *Pe* such that $S_L^0 = 0.257$ is held constant. These properties are chosen such that the flame parameters correspond to Flame A at $\delta_F^0 = 0.0389$ and Flame B at $\delta_F^0 = 0.0778$ for $S = 0$. The results are summarized in Figure 4.6.

Figure 4.6 indicates that the flame thickness does influence the vortex breakdown process as thicker flames are shown to resist the onset of vortex breakdown. In this study, where the flame thickness is controlled by varying *Pe*, this phenomenon can be understood as follows. In thin flames, the role of mass and thermal diffusion is relatively weak, allow-

ing the resulting flame front to support a relatively strongly-curved reaction zone (see point 1). In contrast, the stronger effect of diffusion in thicker flames results in a "smoother" flame which cannot support sharp cusps in the reaction front (see points 2-4). It should be emphasized, however, that the flame thickness may be controlled through other methods, such as by varying the Zeldovich number. Such possibilities are not studied here, but since the main effects reported here seem to be diffusion-driven, it seems plausible that a variable-*Ze* scenario may lead to different behaviors.

The cases with thicker flames also exhibit an extra pair of saddle-node bifurcations which occur in the wall-jet regime. The resulting pleat in the solution curve indicates an interval of bistability and hysteresis between wall-jet solutions characterized by an outer recirculation zone with a large separation vortex (point 3) and a more strongly attached solution where the separation vortex is suppressed (point 4). This effect is apparently spurred by a slight change in the attachment point of the flame along the outer wall due to the interaction between the expansion of the flow across the thickened flame and the recirculating flow which pushes back against the flame. The physical relevance of this transition is unclear, however, for two major reasons. First, this transition is likely only possible due to the assumption of an adiabatic wall. In a less-idealistic scenario where thermal losses are present, the flame will be quenched along the wall, resulting in a different flame structure. Second, real flames in typical burners are generally quite thin in comparison to the diameter of the injector, suggesting that conditions where the flame is thick enough to support these dynamics may not be realizable in practice.

4.3 Summary

In summary, this chapter has systematically considered the effects of lean premixed reactions on the nonlinear dynamics of steady swirling jets and their linear instabilities. It shows how variations in the exothermicity ΔT, the flame speed S_L^0, and the flame thickness δ_F^0 change the evolution of the swirling jet's structure with respect to the rotation rate *S*, and

interprets the physical effects underlying these differences. In particular, the heat release due to the flame is shown to have quite different effects toward the steady flow than may be suggested by the earlier analyses for diffuse swirling flames in pipes by Rusak, Kapila, and Choi [47, 48]. These effects vary significantly depending on the structure and orientation of the flame as determined by its speed and thickness. Indeed, even the fundamental bifurcation structure of the swirling flow may also be altered due to reactions. For example, flashback was shown to occur during the vortex breakdown process for sufficiently slow flame speeds. In addition, the presence of the flame was observed to have a uniformly stabilizing effect toward oscillatory linear instabilities of the swirling jet over all cases considered in this chapter as the instabilities are either completely suppressed or the parameter interval over which they are unstable is reduced. However, further work will be needed to completely characterize the reacting swirling jet's linear dynamics.

The results also lend deeper insights into the experimental observations of Gotoda et al. [133, 46]. In particular, this numerical continuation study yielded flowfields which closely resembled all of the key flame topologies described in that study, in addition to others at conditions not considered in their experiments. Furthermore, [133, 46] reported stable flames at low and high rotation rates and unsteady, fluctuating flames at intermediate rotation which is qualitatively consistent with the linear stability calculations performed here.

CHAPTER 5
HYDRODYNAMIC RESPONSE ANALYSIS OF A FORCED TURBULENT SWIRLING FLAME

5.1 Introduction

In engineering applications, the combustion instability phenomenon negatively impacts emissions, performance, and even structural integrity. Resonant acoustic modes associated with a combustion system's geometry can filter pressure fluctuations from the turbulent broadband, leading to a significant narrowband forcing effect [2, 65]. This motivates efforts to understand how reacting turbulent swirling flows respond to narrowband forcing.

The influence of external forcing on a given flowfield is a strong function of the flow's natural dynamics and the strength and structure of the forcing. Fundamentally, shear flows tend to behave either as self-excited oscillators with intrinsic dynamics or as noise amplifiers that act to filter extrinsic dynamics. When clear coherent structures appear without imposed forcing, the turbulent system is self-excited and, according to the argument presented in chapter 1, may be interpreted to lie in the vicinity of a low-dimensional attractor in phase space. This "noisy" attractor must be somewhat robust to perturbations, as turbulent fluctuations would otherwise carry the system away from it [135]. Under such conditions, narrowband excitation with an improper frequency, insufficient amplitude, or incorrect spatial pattern is unlikely to have a significant effect on the flow dynamics [74]. However, if external forcing with a sufficiently high amplitude, an appropriate temporal distribution, and a suitable spatial arrangement is applied, the system may bifurcate to a new set of dynamics governed by a different attractor. This is known as the "lock-in" phenomenon [136, 137].

On the other hand, noise amplifier flows that naturally exhibit more broadband spa-

tiotemporal behavior generally do not show such clear bifurcations. In these flows, forcing, even at small amplitudes and with low authority, can fundamentally alter the flow response by directly introducing narrowband coherent structures to the flow [74]. In noise amplifier flows, the scale of the response typically depends directly on both the amplitude of the imposed forcing and the flow's underlying receptivity to the forcing frequency and structure [137, 113, 138]. This sensitivity implies a linear relationship between the imposed acoustic field and the dominant flow response, provided the forcing amplitude is sufficiently small to permit a linear approach. Consequently, theoretical pursuit of the response problem with small-amplitude forcing for noise-amplifier flows based on linear theory has been quite successful at qualitative predictions of flow dynamics [76, 139].

This chapter investigates the effects of acoustic excitation on the flow dynamics of a multi-nozzle swirl-stabilized combustor. This flow was selected because it behaves as a non-self-excited noise amplifier, such that a linear response analysis as argued above is applicable. The analysis will be based on the weakly-global framework described in chapter 2 and compared with experiments described below.

A portion this chapter has been published previously in the Proceedings of the 2018 AIAA Aerospace Sciences Meeting, in an article I co-authored with Travis Smith, Benjamin Emerson, Kiran Manoharan, Santosh Hemchandra, and Timothy Lieuwen [140].

5.2 Overview of experiments

5.2.1 Test conditions

The measurements which form the basis of this chapter have been previously described in the works of Smith [113, 114, 6], and were performed in the experimental facility described in chapter 2. These experiments utilized high-speed planar stereoscopic PIV and synchronized OH-PLIF measurements for flow and flame characterization. The specific test cases investigated here include an unforced single-nozzle flow and transversely-forced triple-nozzle flows. To obtain three-dimensional flow information, measurements were

Table 5.1: Measurement conditions for experiments analyzed in this work. For the single-nozzle cases, flow to the outer nozzles is blocked and only the central nozzle is open. In the triple-nozzle cases, all three nozzles are open, but diagnostics are only performed on the central nozzle.

Transverse Acoustics	**Imaging Rate** [kHz]	**Flow Rate** [m/s]	**Preheat** [K]	**Stoichiometry** [-]
unforced	3.0	$\otimes$ – 25 – $\otimes$	$\otimes$ – 500 – $\otimes$	$\otimes$ – 0.85 – $\otimes$
IP @ 390 Hz	5.0	25 – 25 – 25	500 – 500 – 500	0.6 – 0.85 – 0.6
OP @ 390 Hz	5.0	25 – 25 – 25	500 – 500 – 500	0.6 – 0.85 – 0.6

performed on the central jet in its meridional plane as well as four separate axial planes at $x = 0.15$, $x = 0.67$, $x = 1.2$, and $x = 1.7$. In the transversely-forced cases, the lateral speakers were set to oscillate either In Phase (IP) or Out of Phase (OP) to generate standing transverse acoustic waves in the combustor box which correspond either to pressure antinodes or nodes, respectively, at the central nozzle. A list of the experimental test conditions is provided in Table 5.1, and representative images from the cameras used for stereoscopic PIV and OH-PLIF are shown in Figure 5.1. As shown in the figure, a cylindrical coordinate system is adopted with the origin centered on the dump plane at the central nozzle. Further experimental details and descriptions of post-processing methods can be found in the works of Smith [113, 114, 6].

5.2.2 Flow characterization

This investigation will focus solely on the flow through the center nozzle. In all of the test cases, the nominal conditions of this central flow are identical. It consists of a lean ($\phi = 0.85$) mixture of preheated methane and air injected from an annular nozzle with an outer diameter of $D^\star = 36.83\,\mathrm{mm}$. The nominal flow velocity based on the mass flux is $U^\star = 25\,\mathrm{m/s}$ and the equilibrium properties of the reactants at the preheat temperature of $T_R^\star = 500\,\mathrm{K}$ are: $\rho_R^\star = 0.6776\,\mathrm{kg/m^3}$, $\mu_R^\star = 2.62 \times 10^{-5}\,\mathrm{kg/(m \cdot s)}$, $\mathcal{D}_R^\star = 4.8355 \times 10^{-5}\,\mathrm{m^2/s}$, $c_{p,R}^\star = 1\,126\,\mathrm{kJ/(kg \cdot K)}$, where the stars denote dimensional quantities. The Reynolds and Péclet numbers which result from these properties are $Re = 23\,813$ and

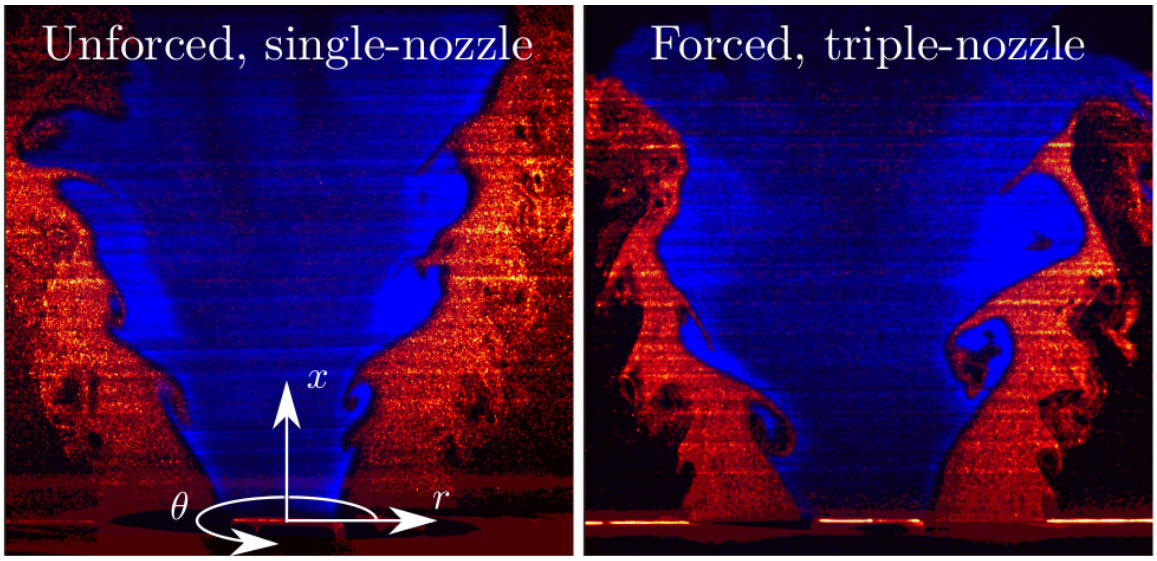

Figure 5.1: Overlay of typical Mie scattering (orange) and OH-PLIF (blue) snapshots from the meridional plane of the unforced single-nozzle experiment (left) and the IP transversely-forced triple-nozzle experiment (right). The PLIF signal indicates the approximate location of the flame, and the Mie scattering from the seeded flow through the nozzle provides a particle tracer visualization of the fluid motion.

$Pe = 19\,041$. Note that chemical equilibrium calculations based on this reactant mixture yield an adiabatic flame temperature of $T_P^\star = 2\,192\,\mathrm{K}$, which corresponds to $\Delta T = 3.38$. As discussed in chapter 2, no attempt is made to determine approximate *Da* and *Ze* values for these flames.

To identify coherent structures within the measurements, the harmonic content is first analyzed on the basis of its energy spectra. The kinetic energy associated with each frequency is characterized by the spatial average of the squared magnitude of each Fourier component. This quantity represents a Power Spectral Density (PSD) which is shown in Figure 5.2. These results show that the unforced flow does not exhibit any clear energy peaks, indicating that the flow is not self-excited. It also demonstrates that transverse acoustic forcing has a controlling effect on the flow dynamics as it introduces strong narrowband energy content at the forcing frequency. Finally, the results indicate that OP forcing yields a stronger response from an kinetic energy perspective than IP forcing. Note that the Fourier modes associated with the marked frequencies in Figure 5.2 will henceforth be identified

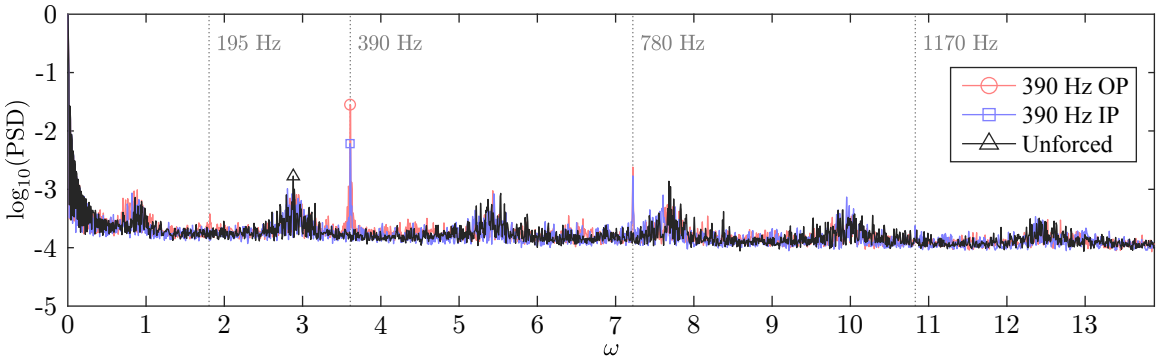

Figure 5.2: Spatially-integrated power spectrum for the measured flowfields contrasting the forced and unforced cases.

as the coherent part of their respective cases.

Next, the flow and flame motions are considered from a structural perspective. Each case is visualized in Figure 5.3 by an instantaneous snapshot of the flow field and the mean and coherent components of the triple decomposition from Equation 2.31. For the decomposition, instantaneous three-dimensional velocity vectors come directly from the processed stereoscopic PIV image pairs, and the instantaneous flow properties come from methane-air chemical equilibrium calculations based on instantaneous product/reactant fields inferred from binarized OH-PLIF measurements. All of the data considered in this chapter comes from the interval $x \in [0.1, 1.2]$, which corresponds to the dimension of the window for which reliable simultaneous PLIF and PIV measurements are available. Several aspects of the data presented in Figure 5.3 are worthy of comment. To begin, the figure shows that the mean flow field is essentially unaffected by forcing as the mean flow is similar across all cases. The coherent parts, however, differ greatly. While the unforced flow does not indicate any significant coherent oscillations, the forced cases do present a clear response at the forcing frequency $\omega_f = 3.61$. Specifically, the OP case shows a clear asymmetric shear layer response which is indicative of asymmetric helical shear layer oscillations. These flow oscillations then manifest themselves on the flame, which is kinematically dependent on the flow, as shown by the staggering of the phase-mean PVF contours. Conversely, the IP case exhibits a symmetric response which is indicative of symmetric helical or ring-like

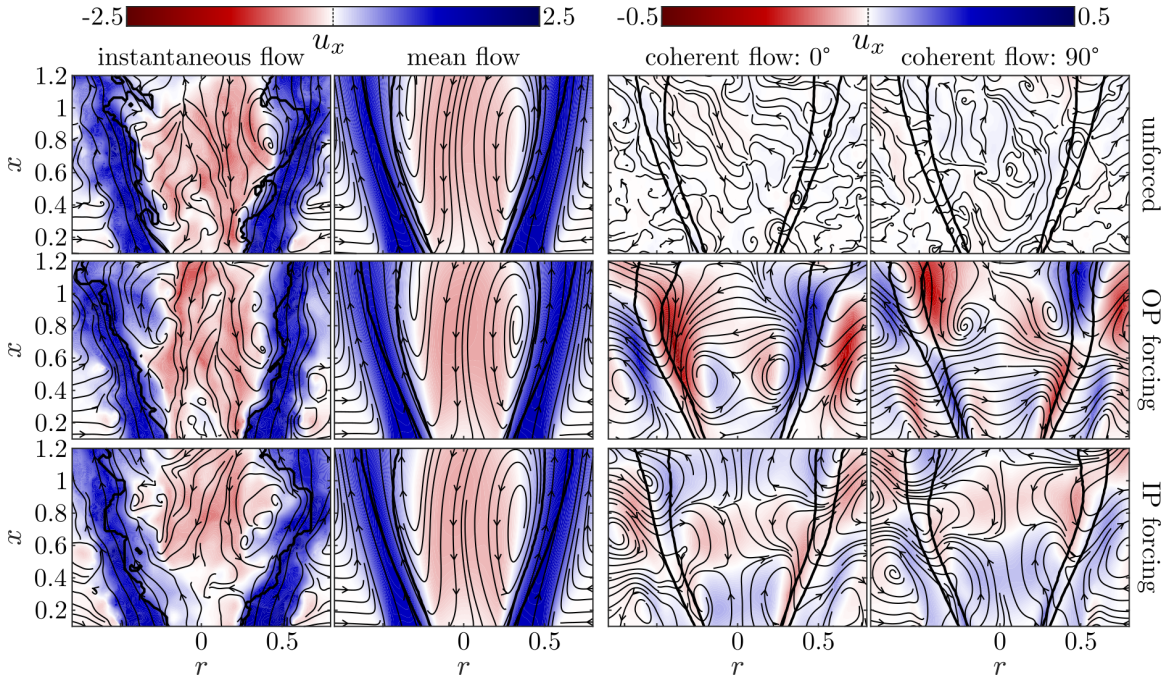

Figure 5.3: Flow visualization in the meridional measurement plane via axial velocity contours (colors), flow streamlines, and flame PVF contours (thick black lines). In the instantaneous flow, the PVF contours indicate the instantaneous boundary between reactants and products deduced from the binarized OH-PLIF measurements. In the mean and coherent flow visualizations, the thick black lines correspond to the 20% and 80% PVF contours.

shear layer oscillations. The dominant response of the flow to asymmetric OP-forcing, rather than symmetric IP-forcing, suggests an underlying preference of the flow response toward asymmetric helical disturbances. This will be discussed further after the presentation of the linear response predictions.

5.3 Hydrodynamic stability analysis

5.3.1 Mean Flow

The mean flow used for the stability analysis is derived entirely from the unforced single-nozzle experiment. Previous experimental investigations have shown the mean flow from this single-nozzle experiment approximates that of the three-nozzle experiment, and that both cases have similar axial disturbance profiles [114]. The single-nozzle dataset consists of 2 727 synchronized stereoscopic PIV and OH-PLIF measurements which are used to

identify the Favré-averaged mean flow state as described in chapter 2 and shown in Figure 5.3. After the mean velocity and flame progress variable fields are determined from the images, they are spatially-averaged by reflection across the centerline to yield an azimuthally homogeneous mean flow state.

As indicated in chapter 2, the Boussinesq hypothesis will be used to model turbulent transport in the hydrodynamic modeling approach. This eddy viscosity is determined directly from the measured Reynolds stress tensor using the projection of Equation 2.39. For present data set, the overdetermined system yielded a spatially-varying eddy viscosity which was negative in some regions. Though certain conditions do exist where this may be physically significant [141, 142], in this work, the negative eddy viscosity values will be set to zero such that $\overline{\mu}_T = \overline{\mathcal{D}}_T \geq 0$. This is consistent with the approach taken by previous studies in swirling flows which have employed eddy viscosity models [76, 77, 78].

Near the maximum radius of the experimental measurement window, the mean flowfield is always comprised of pure reactants and is nearly stagnant. Therefore, the velocities outside of the window are assumed to be negligible and the local fluid properties are chosen as those of the reactants. A continuous representation of the data is obtained by fitting a two-dimensional piecewise-cubic spline curve to the azimuthally-averaged and Favré-averaged basic flow. A two-dimensional Gaussian smoothing filter was also applied to the turbulent dissipation fields. This results in the smooth, axisymmetric basic flow shown in Figure 5.4 which is directly based on the experimental flow profile rather than an assumed model profile equation.

Profiles of the axisymmetric, Favré-averaged mean flow used for the stability analysis are shown in Figure 5.4. It shows first that the axial component displays a significant amount of reverse flow in the central recirculation region, as well as very clear inner and outer shear layers. Inviscid theory suggests that such features heavily influence the inertial instability mechanisms of swirling flows. Second, the presence of the central recirculation region caused by the combined effects of vortex breakdown and the center body wake

causes the average rotating component to rapidly transition from a well-defined azimuthal jet at the dump plane to a more radially-distributed vortex profile, even as the axial velocity profile retains its jet-like character. Third, the time-average of the binarized OH-PLIF signals forms a mean flame PVF which shows that the flame exists primarily within the inner shear layer. The presence of the flame here has a drastic effect on turbulent transport. Compared to other studies, which are based a mean flow derived from an unweighted Reynolds-averaging approach instead of the density-weighted Favré-averaging approach adopted by this study, the density stratification introduced by the flame greatly diminishes the Reynolds stress in the inner shear layer, which is reflected in the resultant eddy viscosity.

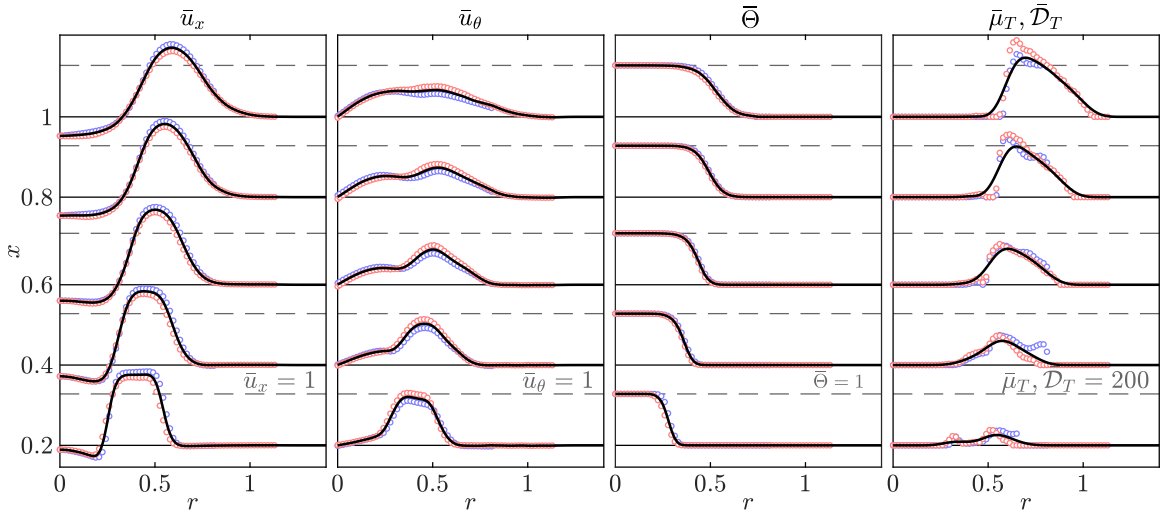

Figure 5.4: Mean flow derived from unforced single-nozzle stereoscopic PIV and OH-PLIF data. Blue and red points represent normalized data from the right and left half-planes, respectively. Dashed lines indicate scale and solid black curves show the axisymmetric cubic spline interpolation based on the average of the points from both half-planes.

5.3.2 Local analysis

Temporal analysis

In the local temporal stability analysis framework, complex-valued frequencies are sought for imposed real wavenumbers. In more physical terms, this form of stability analysis

corresponds to interrogating the time evolution of perturbations to the mean flow from the perspective of a moving reference frame which travels with each perturbation. In that sense, the temporal stability analysis indicates a "worst case" scenario for instability, since a perturbation that does not grow in its own reference frame cannot appear to grow in any other reference frame.

The temporal analysis is performed over a range of axial and azimuthal wavenumbers at all axial locations to identify all of the possibly relevant instability modes, which are then set aside for further analysis. Each perturbation has an axial phase velocity ω/k, an azimuthal phase velocity ω/m, and a helical winding orientation $-k/m$. Due to the chosen sign convention of $m \leq 0$, this indicates that $\omega > 0$ is counter-rotating, $k > 0$ is co-winding, and vice versa. Complementary to their azimuthal and axial phase velocities and winding orientation, each mode may be further classified according to its radial velocity distribution. However, unlike the phase velocities and helix orientation classifications which have precise definitions, these distinctions are somewhat subjective. A given mode may be a center mode that displays its peak oscillatory amplitude in the central recirculation region, a shear layer mode that peaks within the annular jet shear layers, a ring mode which peaks in the fluid surrounding the jet, or, more generally, a combination of these [125, 143, 144]. An example of a temporal eigenvalue spectrum obtained at $x = 0.25$ for $k = -3.61$ and $|m| = 1$ is plotted in Figure 5.5 along with some notable mode shapes. The chosen example is representative of the eigenvalue spectrum and mode shapes that are found at other axial locations, azimuthal periodicities, and wavenumbers.

A more complete depiction of the local temporal stability analysis at $x = 0.25$ is shown in Figure 5.6 for $|k| \leq 20$ and $|m| \leq 2$. Higher wavenumber perturbations were also analyzed, but are not shown as they were found to always be less unstable than the modes shown with $|m| \leq 2$ and $|k| \leq 20$. These results, which are consistent with results from other axial locations, indicate that the most temporally unstable axisymmetric modes have a downstream axial phase velocity (i.e. they are co-propagating), and that the most tempo-

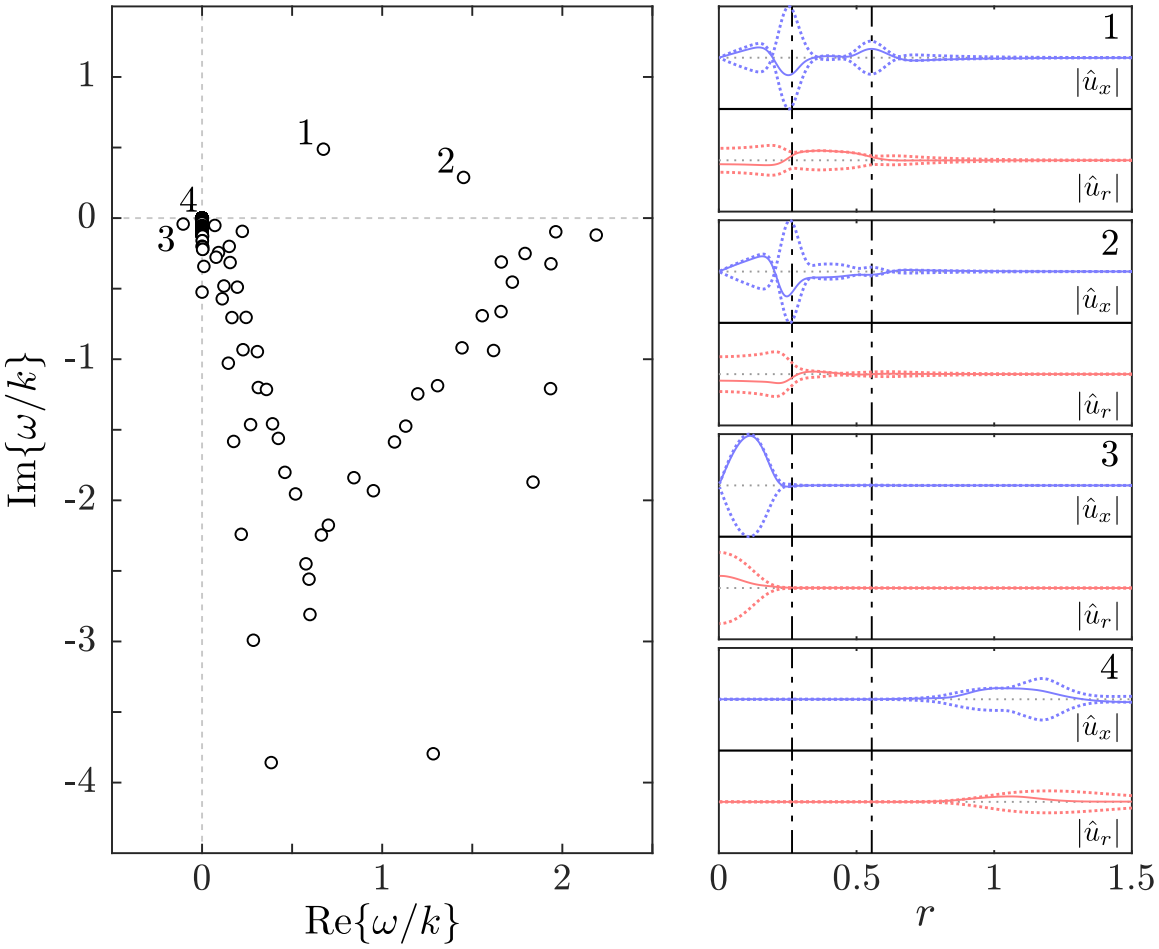

Figure 5.5: Example of a characteristic solution of the temporal eigenvalue problem at $z = 0.25$ with $|m| = 1$ and $k = -3.61$. In this case, there are two temporally unstable modes, numbered 1 and 2. According to the eigenvalues and wavenumbers, these modes both correspond to co-rotating, counter-winding singly-helical structures. On the left, the converged eigenvalue spectrum is represented in the phase velocity space. On the right, mode shapes corresponding to the labeled eigenvalues are shown as a function of the radial coordinate. The solid blue and red curves represent the real part of the respective axial and radial velocity components, and the corresponding dotted lines show each mode's amplitude envelope. Broken vertical lines indicate the radial positions of the inflection points in the inner and outer shear layers of the swirling annular jet mean flow.

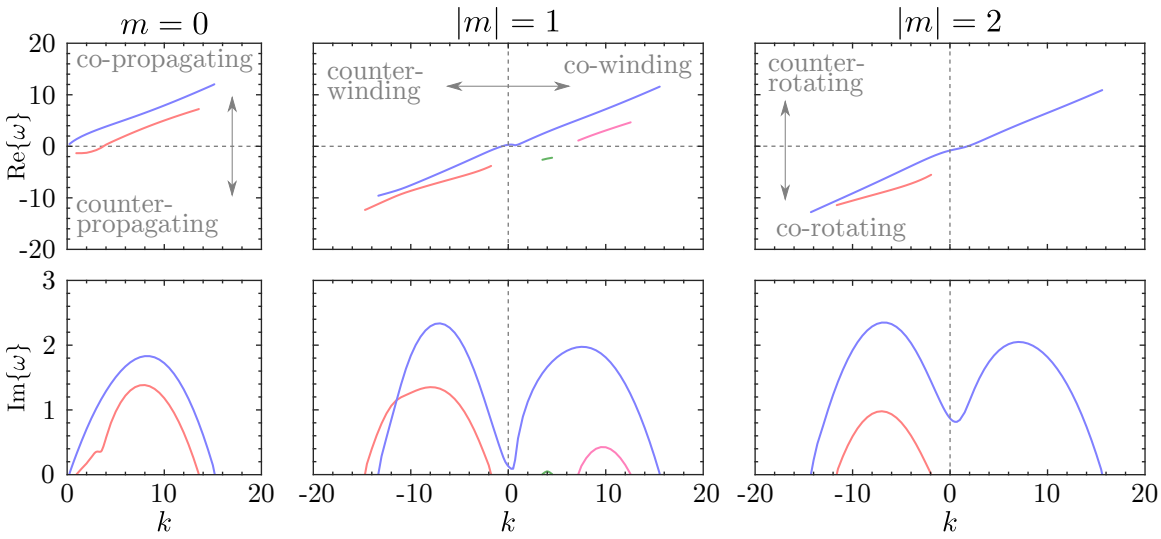

Figure 5.6: Plot of representative temporal stability analysis eigenvalues obtained at $x = 0.25$ as a function of real k. Colors are only used to distinguish distinct branches of eigenvalues from each other, and do not imply any other physical significance. Note that $\text{Im}\{\omega\} = \sigma$ and $\text{Re}\{\omega\} = -2\pi f$ from the previous sections. Only unstable eigenvalues are shown.

rally unstable helical modes rotate and wind in opposite directions. In all cases, the dominant axial wavenumbers associated with the largest temporal growth rates corresponds to wavelengths on the order of one nozzle diameter (i.e. $2\pi/k \sim O(1)$). Furthermore, all cases exhibit up to two unstable modes at each k. The unstable modes all feature significant oscillations of the annular jet's inner and outer shear layers, but, in certain cases, also exhibit elements of center or ring modes. As such, no attempt to classify these modes in terms of their radial velocity distributions will be attempted.

Spatiotemporal analysis

In the local spatiotemporal stability analysis framework, perturbations are considered with complex-valued frequencies and wavenumbers in order to assess the linear system's impulse response. As discussed in chapter 2, the validity of the chosen spatial stability analysis-based response framework depends on the coherent system being unable to manifest self-excited behavior, such that the external acoustic disturbances introduced at the burner lips represent the sole wavemaker in the domain. The previous subsection showed

that certain perturbations exhibit exponential temporal amplification in their own reference frame. However, these perturbations represent propagating dispersive waves with group velocities which may or may not enable them to grow in time at a fixed point of impulse. Thus, the purpose of the spatiotemporal analysis performed here is to confirm that all perturbations decay to zero at any point of impulse in order to rule out the possibility of self-excited global instability.

A spatiotemporal analysis was performed for all of the temporally unstable modes identified above at all axial locations using the variant of Deissler's algorithm described in chapter 2. In this framework, it is essential to ensure that the all of the identified stationary points where $\partial\omega/\partial k = 0$ satisfy causality. This is ensured using the Briggs-Bers"pinch-point" criterion, which requires that the dominant saddle corresponds to a stationary wave "pinched" between upstream and downstream propagating waves [74]. The results of the spatiotemporal analysis at the location $x = 0.25$ and for $|m| \leq 2$ are shown in Figure 5.7, and these results are representative of the results at other axial locations and azimuthal wavenumbers. The analysis reveals that all of the stationary points correspond to situations where $\text{Im}\{\omega\} < 0$, indicating that the impulse response decays at any point of perturbation. Thus, in the stability analysis vernacular, the flow is – at most – *convectively* unstable, and cannot sustain the absolute instability necessary to manifest self-excited behavior. This indicates that the signaling problem is well-posed, allowing further analysis in the spatial stability framework considered below.

Spatial analysis

In the spatial analysis, perturbations are considered with real frequencies and complex wavenumbers. This situation physically represents a signaling problem, where harmonic perturbations are introduced at a point, and the analysis determines whether the perturbations grow or decay along the streamwise direction. A representative result of the local spatial stability analysis at $x = 0.25$ is shown in Figure 5.8 for $|\omega| \leq 20$ and $|m| \leq 2$. While

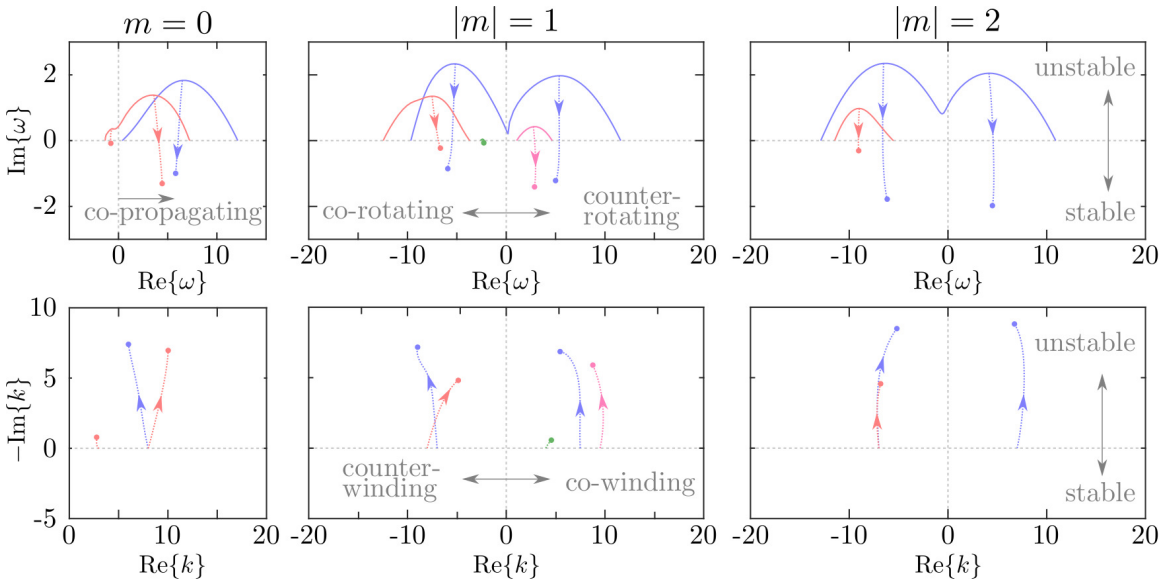

Figure 5.7: Plot of representative spatiotemporal stability analysis results obtained at $x = 0.25$ in the complex ω-plane (top) and complex k-plane (bottom). The temporal eigenvalue branches are shown in the ω-plane using the same colors from Figure 5.6. The path of steepest descent follows the dotted lines to the saddle points located at the end of the steepest descent paths. All of the saddles are shown to correspond to $\text{Im}\{\omega\} < 0$, indicating that the flow is only convectively unstable and does not support self-excited behavior.

this analysis has a different physical interpretation compared to the temporal analysis considered earlier, the overall characteristics of the spatially-unstable coherent perturbations are qualitatively quite similar to their temporal analogs. In particular, the dominant instabilities still tend to represent helical waves which wind and rotate in opposite directions or axisymmetric waves which propagate downstream. These structures are shown to exhibit spatial amplification for a range of frequencies with $|\omega| \lesssim 10$.

5.3.3 Weakly-global analysis

Building on the results of the local analysis methods described above, the WKBJ approach can now be used to derive weakly-global linear response predictions. Following the argument in chapter 2, as no natural absolute instability exists to generate sustained intrinsic coherent oscillations, the acoustic coupling which occurs near the burner lips is interpreted to represent the flow's sole wavemaker. This external excitation locally excites small, pure-

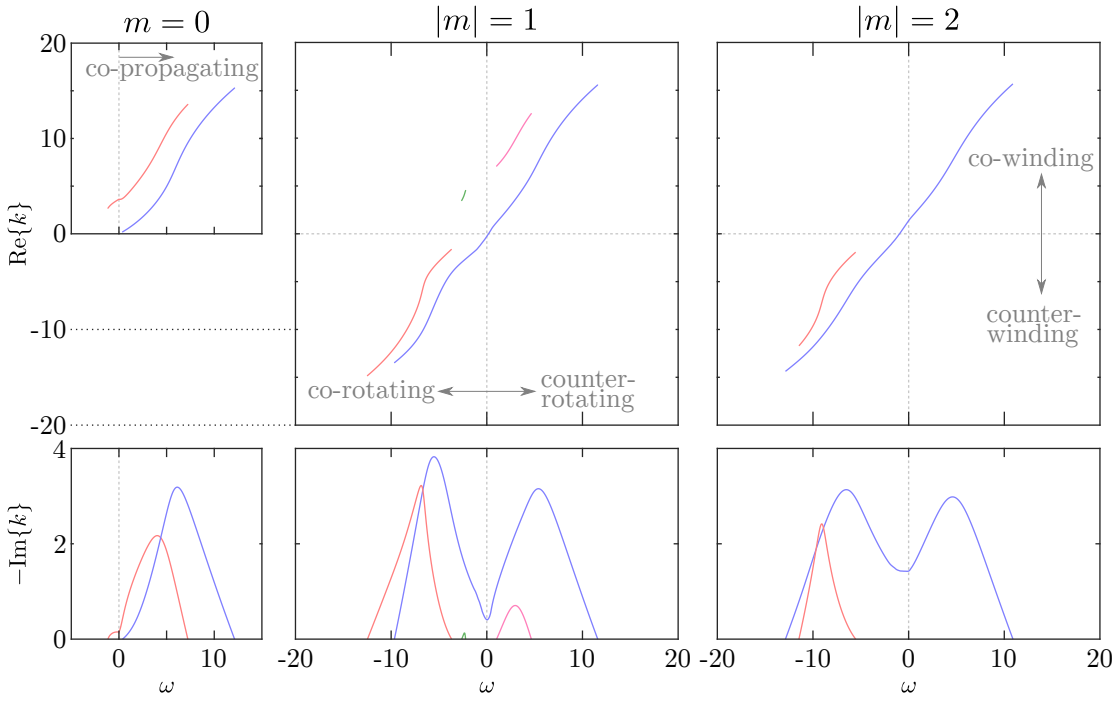

Figure 5.8: Plot of representative spatial stability analysis eigenvalues obtained at $x = 0.25$ as a function of real ω. The same colors are used from the previous plots. Note that $\mathrm{Im}\{k\} < 0$ is required for instability in the spatial framework so $-\mathrm{Im}\{k\}$ is plotted on the lower axes. Only unstable eigenvalues are shown.

tone perturbations at $x = 0$ which may then be spatially amplified by hydrodynamic instability as they convect downstream.

Based on this physical model, the weakly global modes are constructed from a sequence of local analyses conducted at 55 axial locations evenly distributed over the measurement interval $x \in [0.1, 1.2]$. The eigenvalues of the spatial stability analysis results at the forcing frequency of 390 Hz, which corresponds to a dimensionless angular frequency of $|\omega| = 3.61$, are shown in Figure 5.9 for each x. Using these independent eigenvalues, the spatial stability results are assimilated through the WKBJ approximation of Equation 2.42 with $x_0 = 0.1$ to determine the streamwise evolution of each weakly-global mode's amplitude and phase. This information is also presented in Figure 5.9 for the $|m| \leq 3$ modes which experience linear spatial amplification in any part of the measurement interval. The analysis reveals that the turbulent swirling annular reacting jet exhibits a wide range of convectively unstable weakly-global modes associated with coherent oscillations at the forcing frequency. If all modes are excited equally, the results indicate that the dominant response is associated with a co-rotating, counter-winding $|m| = 1$ mode. Note that higher wavenumber modes with $|m| \geq 4$ were considered in this analysis, but were determined to be more stable than the presented modes and are therefore not shown.

In addition to the axial amplitude and phase variation discussed above, the weakly-global analysis also provide insight into structural characteristics of the linear response. Visualizations of the leading weakly-global $|\omega| = 3.61$ response modes for $|m| \leq 3$ are shown in Figure 5.10. The visualizations reveal a variety of ring ($m = 0$) and helical ($m \neq 0$) vortical structures which are concentrated along the annular jet and particularly its shear layers. According to Figure 5.9, the counter- and co-rotating structures correspond to co- and counter-winding helical vortex structures, respectively. Since the flame stabilizes along the jet's inner shear layer, these response modes clearly imply a hydrodynamic connection between the acoustic forcing and the flame response.

It should be emphasized at this point that the linear response modes considered in Fig-

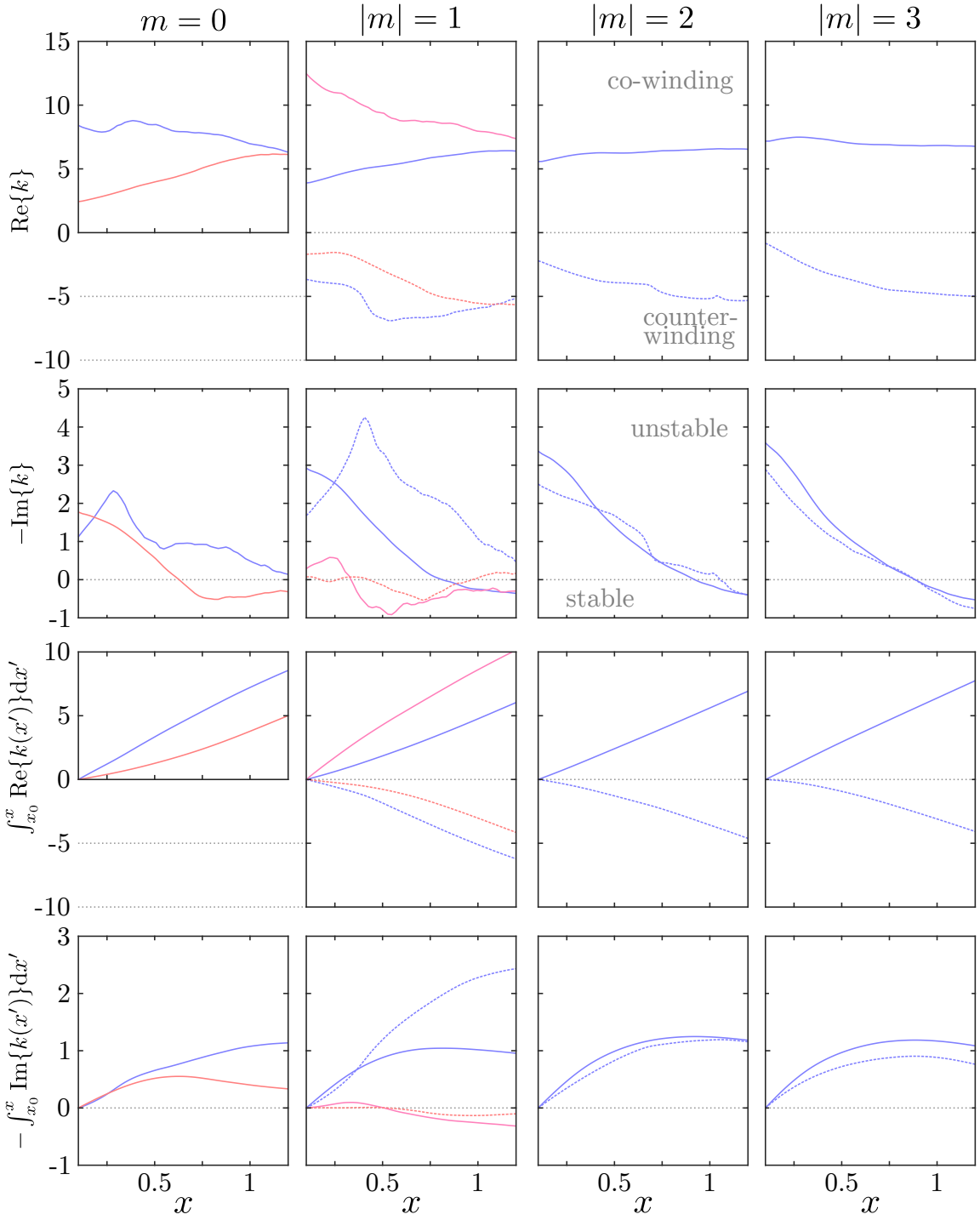

Figure 5.9: Eigenvalues and WKBJ phase resulting from the weakly-global analysis as a function of x. Top two rows show the real and imaginary parts of the complex wavenumbers at the forcing frequency $|\omega| = 3.61$. The bottom two rows show the real and imaginary parts of the axial phase function resulting from the WKBJ approximation. In all cases, the line colors for each solution branch are consistent with the previous figures. Solid lines correspond to $\omega = 3.61$ (counter-rotating for non-axisymmetric disturbances) and dashed lines correspond to $\omega = -3.61$ (co-rotating).

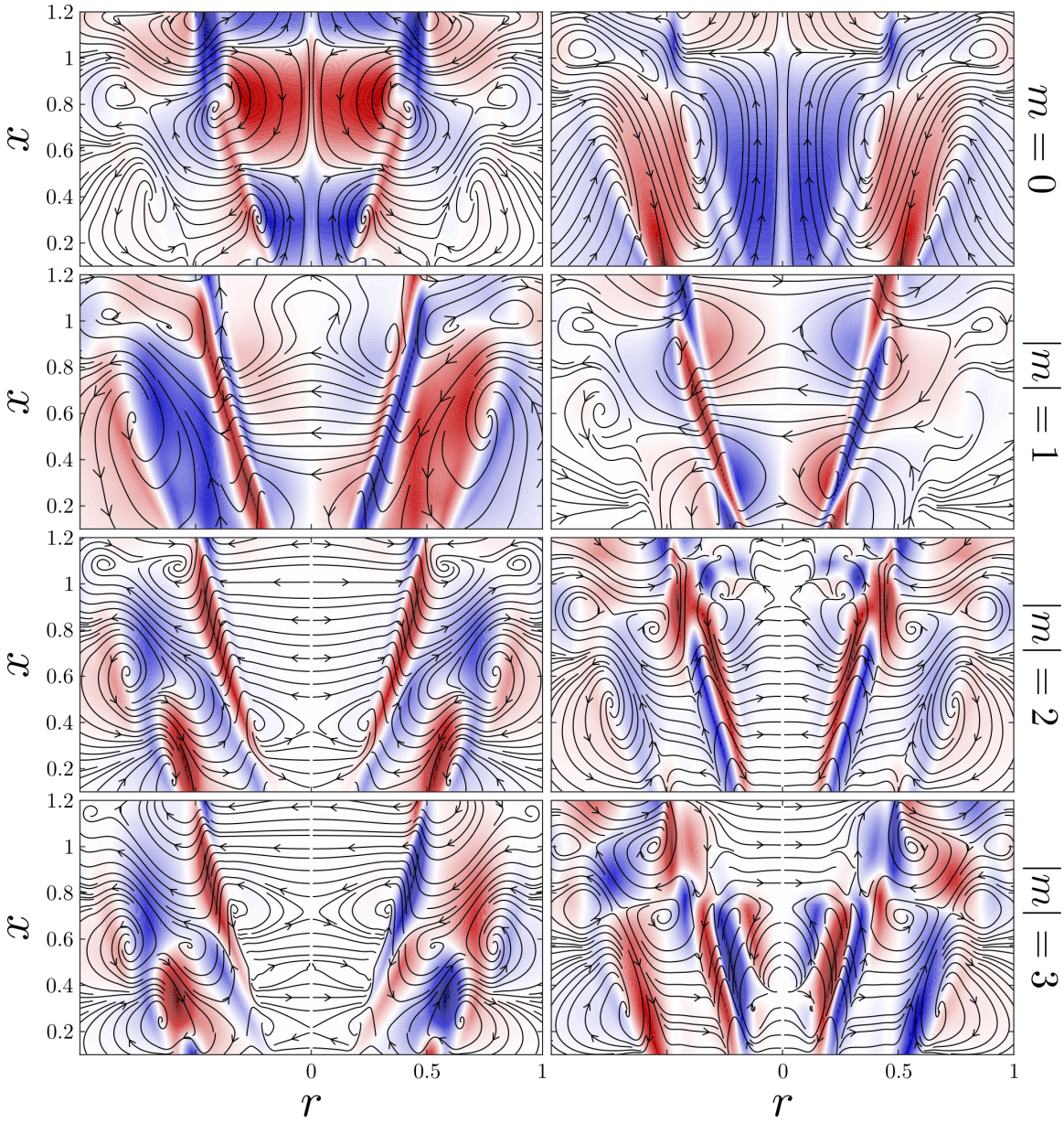

Figure 5.10: Visualizations of perturbation streamlines and axial velocity contours in the meridional plane for the two most-dominant weakly-global linear response modes at $|\omega| = 3.61$ for each $|m| \leq 3$. For $m = 0$, the left and right columns correspond to the blue and red curves in Figure 5.9, respectively. For $m \neq 0$, the left and right columns corresponds to the dominant counter-rotating and co-rotating modes, respectively. Note that the overall amplitude and phase of each weakly-global mode is arbitrary.

ure 5.9 and Figure 5.10 are based only on the forcing frequency and not on any structural characteristics of the forcing itself. This is a crucial distinction as the transverse acoustic forcing used in the experiments features important structural characteristics which do not evenly excite all disturbances. In particular, the OP and IP cases are designed to preferentially excite modes with odd and even m, respectively. This will be discussed further in the following, where the pointwise linear response predictions described in this section are compared with the measured response.

5.4 Comparison with experiments

As mentioned above, the structure of the IP and OP forcing patterns considered in the forced experiments were selected to elicit a specific flow response. In the IP case, the nozzle center coincides with a pressure anti-node of a standing planar acoustic wave in the combustor, leading to a symmetric fluctuation in pressure with respect to the anti-nodal line. Expanding this planar symmetric fluctuation in a Taylor series, it can be shown that IP forcing is also axisymmetric ($m = 0$) to leading order at the central nozzle. Conversely, for the OP case, the nozzle center lies at a pressure node, causing an asymmetric pressure response with a 180° phase difference across the nodal line. In this case, the leading order effect of the planar asymmetric OP forcing is the excitation of two superposed $|m| = 1$ waves of equal strength which rotate in opposite directions.

Hence, even though the hydrodynamic response modes do indicate a preference for the co-rotating, counter-winding $|m| = 1$ shear layer mode if all azimuthal periodicities are excited equally, the transverse forcing used in the experimental studies introduces a clear bias toward structures with specific periodicities which must be taken into consideration. For the $|\omega| = 3.61$ forcing considered in this chapter, the jet may be considered to be acoustically-compact as the wavelengths associated with the transverse acoustics are *O(100)* times larger than the diameter of the nozzle [145]. This assumption allows the higher-order terms associated with the Taylor series expansions of the IP and OP forcing

patterns to be discarded, such that the leading order response consists only of $m = 0$ and $|m| = 1$ structures for the IP and OP cases, respectively. It should also be pointed out that the acoustically compact assumption also implies that the amplitude of the OP forcing is significantly weaker than the IP forcing [65].

As noted at the beginning of this chapter, the experimental response to forcing has been thoroughly detailed in the works of Smith [113, 6]. In part of his analysis, Smith identified and isolated azimuthally-periodic structures in each axial (i.e. r-θ) plane and charted their spatial evolution as a function of x. These results are recounted in Figure 5.11 and compared with the linear response predictions. However, as noted in the caption, the radially-integrated helical mode coefficients used by Smith [113] have a distinct physical interpretation from the relative amplitudes of the weakly-global modes which result from the stability analysis, meaning that the comparisons are only qualitative. Nonetheless, the linear predictions do match several important characteristics of the observed response. For example, the hydrodynamic stability analysis and measured response under OP forcing both indicate a relative dominance of the co-rotating $|m| = 1$ in comparison to its counter-rotating analog. This provides evidence that the co-rotating instability is dominant due to an underlying hydrodynamic instability of the mean flow profile, not due to other effects such as a biased excitation of only the co-rotating oscillation mode or a nonlinear competition between the $|m| = 1$ modes. Additionally, the growth and decay trends of the predicted modes with respect to the axial coordinate are similar to the measurements. In particular, the $m = 0$ mode appears to grow uniformly as a function of x in the IP case for both prediction and measurement. On the other hand, the $|m| = 1$ modes do not grow uniformly. Both the co- and counter-rotating $|m| = 1$ modes exhibit an interval of nearly equal spatial amplification for $0.1 \lesssim x \lesssim 0.5$. However, beyond $x \gtrsim 0.5$ the amplitudes diverge. For the co-rotating mode, the amplitude continues to increase while the counter-rotating mode experiences a decay.

To further aid comparison, the spatial distribution of the linear response are also com-

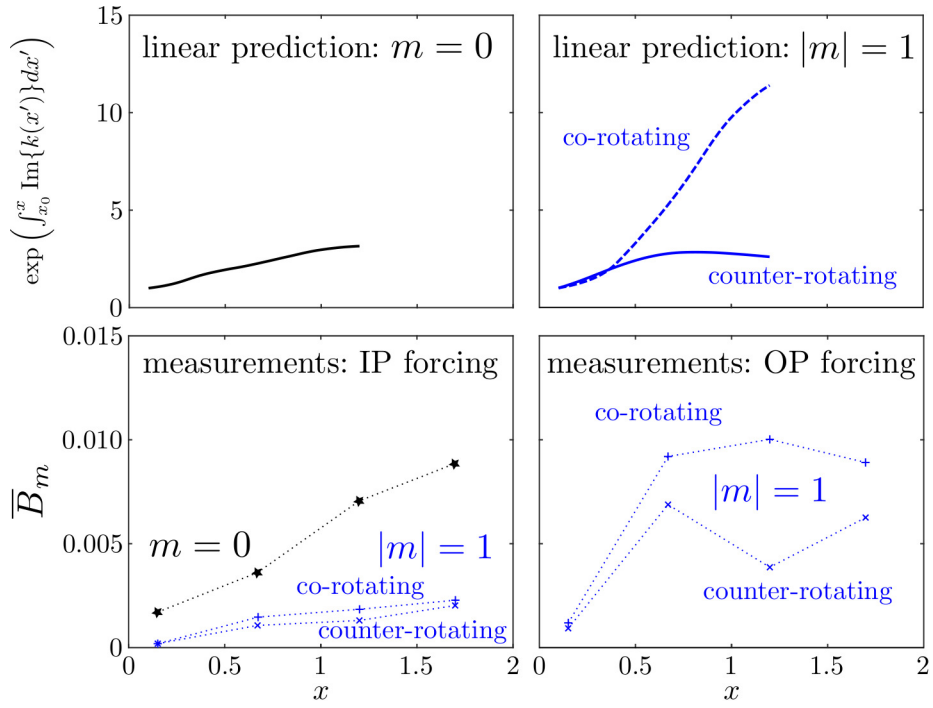

Figure 5.11: Relative modal amplitude profiles predicted by the WKBJ linear response analysis for $m = 0$ and $|m| = 1$ (top) and measured integrated helical mode coefficients $\overline{B}_m$ at each axial measurement plane for IP and OP forcing conditions reproduced from Smith [6] (bottom). Note that these metrics are not equivalent and are only suitable for qualitative comparisons.

pared against the measured coherent component of the test cases with IP and OP forcing in Figure 5.12. Under IP forcing, Figure 5.11 showed that the measured flow exhibits a primarily axisymmetric response with small $|m| = 1$ components which may arise due to unintentional excitation of the $|m| = 1$ modes due to imperfections in the combustor geometry or forcing conditions. This mostly symmetric behavior is also indicated by the spatial structure shown in Figure 5.12. The spatial distribution of the predicted $m = 0$ mode is clearly very similar to the measured response. In particular, both consist of axisymmetric vortical structures of similar axial wavelengths (and therefore axial phase speeds k/ω) which cascade downstream along the inner and outer shear layers of the mean flow. Here, it should be emphasized that the predicted dominance of the $m = 0$ mode under IP forcing is completely unrelated to the usual thermoacoustic feedback loop as the linear weakly-global analysis does not allow for two-way streamwise feedback due to the locally-parallel assumption, and Equation 2.41 does not account for heat release perturbations as discussed in chapter 2. In the case of OP forcing, the predicted response consists of independent co- and counter-rotating $|m| = 1$ modes. As shown in Figure 5.11, the co-rotating $|m| = 1$ mode prevails in both the experimental and predicted response beyond $x \gtrsim 0.5$, but the amplitudes of both modes remain significant throughout the domain. The spatial distribution of the $|m| = 1$ response modes differ slightly from the measured response. In particular, the predicted $|m| = 1$ modes seem to overemphasize the strength of velocity fluctuations along the inner shear layer where the mean flame is located compared to the measured response. Nonetheless, the behavior of the perturbation streamlines and the axial wavenumber (which also corresponds to a helical pitch angle) is largely similar between the measured coherent flow and the dominant modes. Overall, these comparisons suggest that the linear response predictions made by weakly-global hydrodynamic stability analysis capture all of the major aspects which control the evolution of coherent acoustic disturbances to the turbulent swirling annular jet flame.

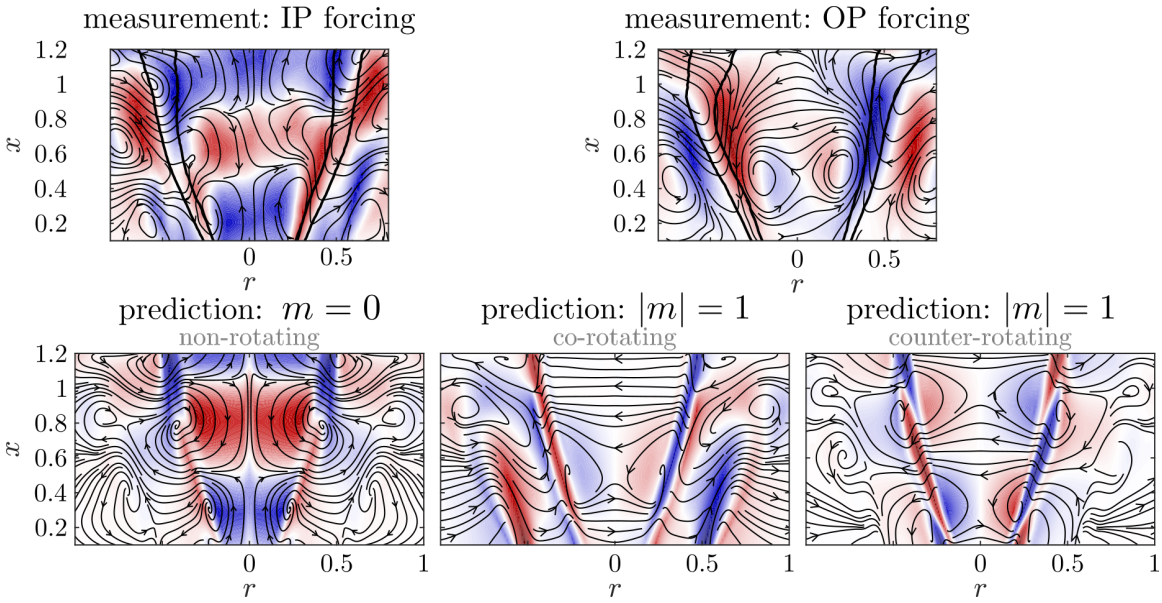

Figure 5.12: Comparison of the spatial velocity distribution of the measured coherent response against the predicted linear response. Note that the phase and amplitude of the predicted mode shapes is arbitrary.

5.5 Summary

In this chapter, a weakly-global hydrodynamic stability analysis was used to model the response of a measured turbulent swirling reacting annular jet to external acoustic forcing. The unforced flow was shown to lack any significant degree of coherent self-excited behavior, supporting its interpretation as a noise amplifier which can be analyzed appropriately in a linear framework. The mean flow field associated with this unforced flow was then used as the basis for hydrodynamic stability analyses based on the formulation and numerical methods developed in chapter 2. Local temporal, spatiotemporal, and spatial stability analyses were conducted at various axial stations within the measurement domain. Consistent with observations, these spatiotemporal stability analyses established that the flow is nowhere absolutely unstable, indicating that it behaves as a convectively unstable system in which disturbances may grow or decay in space as they are advected away from a point of impulse. Based on the local analyses, a weakly-global stability analysis was performed to determine the flow response under pointwise acoustic forcing at the forcing frequency

$|\omega_f| = 3.61$ used in the experiments.

The results of the weakly-global analysis indicated a co-rotating, counter-winding $|m| = 1$ spiral shear layer oscillation to be the dominant response mode under unbiased pointwise forcing at $|\omega| = 3.61$. This response mode exhibits spatial growth throughout the measurement region and features a downstream phase velocity which gradually decreases with increasing x. However, as discussed above, the linear response predicted from hydrodynamic stability analysis does not account for the selective characteristics of transverse forcing, which does not evenly excite all disturbances. In the particular situations of OP and IP transverse forcing considered in the experiments, the acoustics' spatial distribution primarily excites structures with $|m| = 1$ or $m = 0$ azimuthal symmetries, respectively. By accounting for this biased excitation, it was shown that the predicted weakly-global response mode are in good agreement with the measured response.

CHAPTER 6
EXPERIMENTAL CHARACTERIZATION OF TURBULENCE IN ANNULAR SWIRLING JETS AND FLAMES

This chapter is motivated by the lack of experimental tests of turbulence models for high Reynolds number, reacting shear flows in industrially-relevant flow configurations. It is based on a novel, dual-plane PIV technique which is leveraged to characterize the macro-properties of turbulence interactions in swirling annular jet flows and flames under forced and unforced conditions.

Much of the content of this chapter has been published previously in the Journal of Engineering for Gas Turbines and Power, in an article I co-authored with Jamie Lim, Travis Smith, Benjamin Emerson, Timothy Lieuwen, Naibo Jiang, Christopher Fugger, Tony Yi, Joseph Felver, Sukesh Roy, and James Gord [146].

6.1 Experimental methods

6.1.1 Facility

This experimental data considered in this chapter were obtained in the same facility as in chapter 5, namely, the multi-nozzle combustor facility detailed by Smith in [6]. To be clear, even though the facility is largely the same, the experiments described in this chapter are different from the cases discussed earlier. For the particular work considered here, the seeded flow was preheated to $T^\star = 500\,\mathrm{K}$ and passed through the same central nozzle as in chapter 5 at a nominal velocity of $U^\star = 25\,\mathrm{m/s}$. Flow to the outer two nozzles was blocked for all of the test cases, and no transverse acoustic forcing was applied. A table of test cases is presented in Table 6.1. Only air was supplied to the rig for the non-reacting cases (1 and 2). In the reacting cases (3 and 4), air and natural gas were premixed at an equivalence ratio

Table 6.1: List of experimental test cases.

Case #	ϕ (if reacting)	$f_0^\star$ (if forced)
1	–	–
2	–	390 Hz
3	0.85	–
4	0.85	390 Hz

of 0.85 before entering the combustor at atmospheric pressure. In the forced cases 2 and 4, the flow was longitudinally acoustically forced at 390 Hz. This forcing was applied in the premixing tube upstream of the swirler, and the frequency was selected to match the first longitudinal mode of the premixing tube to gain augmented forcing authority.

6.1.2 Diagnostics

A schematic of the diagnostics setup is shown in Figure 6.1. Note that this chapter will make use of a Cartesian coordinate system to avoid ambiguity Cartesian instead of high-speed dual-plane stereoscopic PIV was utilized to characterize the velocity field. For this measurement, a double-pulsed hybrid flash lamp and diode-pumped Nd:YAG-based (532 nm) high-speed burst-mode Master Oscillator Power Amplifier (MOPA) with a pulse separation of 15.0 µs was split into two sheets with orthogonal polarization to illuminate sub-micron TiO_2 particles. Four Complementary Metal Oxide Semiconductor (CMOS) cameras, each with a viewing angle 25° from the laser sheet normal and with 1.0 MP resolution, captured polarization interference filtered scattering from the tracer particles. Due to operational requirements of the burst-mode MOPA, the image pairs for each test case were captured in ten 10 kHz bursts lasting 16.5 ms each and separated by 12 s.

To complement the velocity measurements, synchronized 10 kHz OH-PLIF measurements were obtained to characterize the flame in the reacting cases (3 and 4). For this, a CMOS camera with a high-speed gated intensifier recorded OH fluorescence induced by the Nd:YAG laser (532 nm), which pumped a dye laser system to a wavelength of 283.4502 nm. The synchronized OH-PLIF measurements were captured during the 15.0 µs delay between

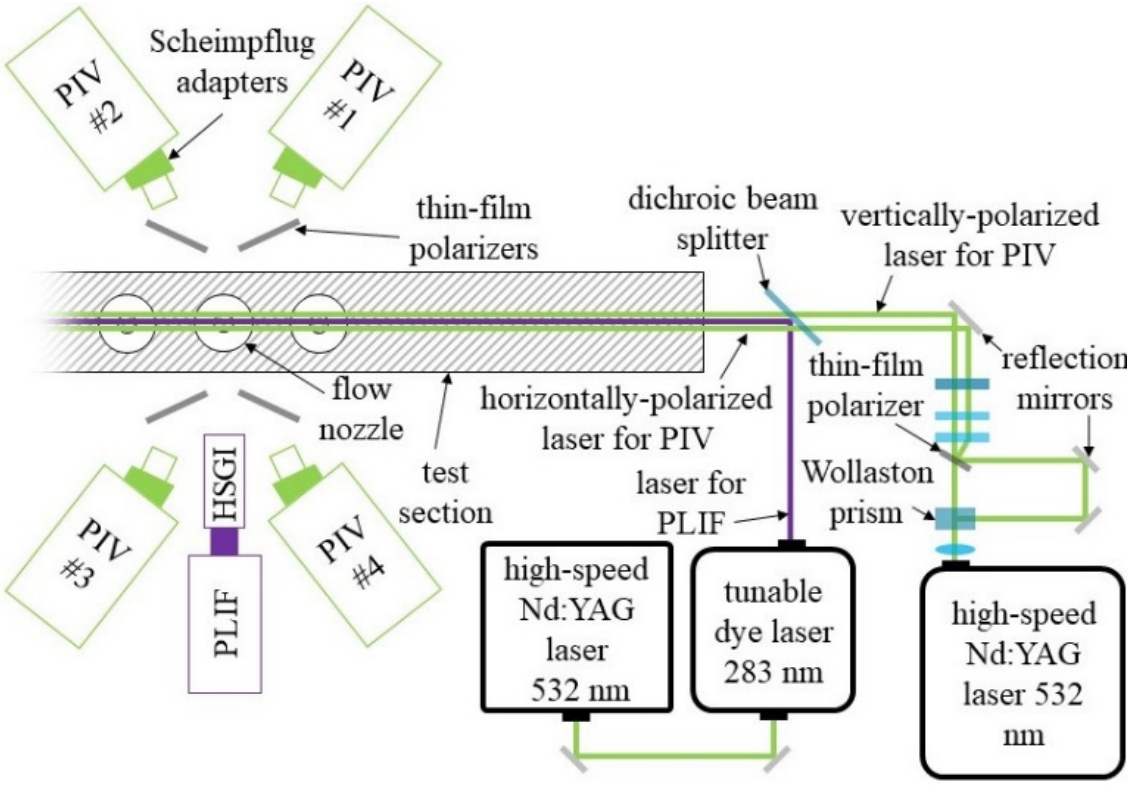

Figure 6.1: Schematic of the diagnostics layout used for the experiments (not to scale).

the PIV laser pulses while the PIV cameras were shuttered.

The lasers are conditioned before being combined into sheets and passed into the combustor. The PIV laser sheets are 1.7 mm thick and parallel, positioned symmetrically about the combustor centerline, and separated by a 2.0 mm gap from peak to peak. The PLIF laser sheet is 2 mm thick and parallel to the PIV lasers, passing directly over the nozzle centerline and between the two PIV laser sheets. The total span between the outer edges of the PIV lasers is 3.7 mm, which is considered to be small compared to the 36.8 mm diameter of the nozzle.

6.1.3 Post-processing

Calibration of each camera and processing of dual-plane stereoscopic PIV image pairs and OH-PLIF images were performed using LaVision DaVis imaging software. For each test

case, a total of 1650 stereoscopic PIV image pairs (165 per burst) were stored for each plane. Due to a weaker laser pulse intensity near the beginning and end of each burst, the first 6 and last 19 image pairs from each burst were discarded, leaving 1400 usable image pairs per plane for each test case. In the reacting cases, a total of 3390 OH-PLIF images were stored. Those images which were not temporally synchronized to the usable PIV image pairs were discarded, leaving 1400 usable OH-PLIF images. These PLIF images were then binarized to estimate the instantaneous reactant-product fields and determine the instantaneous flame position.

Due to the complexity of the optical setup and combustor hardware, localized laser light reflections from the combustor's dump plane were captured in the Mie scattering image pairs used for PIV. For the vertically polarized PIV laser sheet, a sliding minimum filter was used to minimize the background noise in the image pairs. However, for the horizontally polarized PIV laser sheet, a sliding minimum filter was insufficient and a POD background subtraction scheme [147] was implemented instead.

For each of the two measurement planes, a LaVision dual- plane dot pattern target was used to register the cameras and complete the initial calibration. Self-calibration was applied to compensate for slight misalignment between each laser sheet and the registration target facial plane. Both calibration and PIV processing were performed using LaVision DaVis 8.3.1 imaging software. Pre-processing included sliding minimum subtraction to reduce background interference and particle size normalization to enhance the PIV code sensitivity. Multiple passes with decreasing interrogation windows sizes starting at 32×32 pixels were used, and the final window size weighting function was an optimized non-uniform function. The final window size was 16×16 pixels with an overlap of 25%, yielding a vector spacing of 1.34 mm.

6.1.4 Triple decomposition

In chapter 2, it was shown that after applying the triple decomposition (Equation 2.31) to the governing system, the Favré averaging process resulted in nonlinear terms on the right hand side of Equation 2.36 associated with the statistical effect of coherent and incoherent fluctuations on the coherent flow. In the momentum equation, this term is referred to as the "Reynolds stress," and its divergence represents a force density due to turbulent fluctuations acting on the mean or coherent momentum. Similar terms arise in other equations whenever nonlinear terms are averaged through the triple decomposition (e.g. Equation 2.36c). Regardless, this chapter will focus on the Reynolds stress specifically as the velocity measurements derived from the experiment are particularly well-suited for this purpose.

After applying the triple decomposition, the Reynolds stress appears in the governing system as an unsteady quantity with nonzero mean, coherent, and incoherent parts, just as the other flow variables. For this work, the time-mean Reynolds stress is defined as,

$$\overline{\boldsymbol{\tau}}^R = \overline{\rho\left(\boldsymbol{u}-\overline{\boldsymbol{u}}\right)\left(\boldsymbol{u}-\overline{\boldsymbol{u}}\right)}, \tag{6.1}$$

where $\boldsymbol{\tau}^R$ is the Reynolds stress tensor. Similarly, the coherent Reynolds stress is,

$$\widetilde{\boldsymbol{\tau}}^R = \left\langle\rho\left(\boldsymbol{u}-\overline{\boldsymbol{u}}\right)\left(\boldsymbol{u}-\overline{\boldsymbol{u}}\right)\right\rangle - \overline{\boldsymbol{\tau}}^R. \tag{6.2}$$

Note that according to the definitions in chapter 2, Equation 6.2 has zero time mean.

In this chapter, as in chapter 5, the time-mean fields are determined by directly computing the time average using Equation 2.32 over all 1400 stored images. For the reacting cases, the flame PVF is defined by the binarized OH-PLIF images to identify the instantaneous boundary between reactants and products. By averaging, this instantaneous binarized flame PVF, a continuous PVF is obtained which may be used to identify the flame brush. The binarized PVF is also used to infer the instantaneous local fluid density through the

equilibrium properties of the reactants and products, which are nominally the same as in chapter 5.

Determination of the coherent part of the fluctuating fields is more difficult than in chapter 5, where a Fourier transform could be used due to the constant sampling frequency. In this chapter, the phase averaging operation is performed in the time domain since the image pairs were acquired in separate bursts staggered in time. Furthermore, exact phase repetitions are not available in the measurements due to the incommensurate ratio of the 10 kHz image acquisition rate and the 390 Hz forcing frequency which results in ~ 25.6 phase points per forcing period. To ensure that all of the stored images were included in the phase averaging procedure, a phase tolerance of up to $\pm 7.0^{\circ}$ was allowed, yielding an average ensemble size of 54.6 images for each point of phase.

Since the image pairs were acquired in temporally-staggered bursts, it was also necessary to identify a means to phase-reference the start of each burst. Uncertainty in timing between the recorded forcing signal and laser bursts prevents a direct phase-synchronization from the forcing signal. Similarly, the 12 s spacing between bursts was not precise enough to obtain an accurate phase shift between sequential bursts. Instead, the bursts are synchronized to the forcing signal by using a standard beamforming technique. This process is straightforward for the forced cases since the forcing introduces harmonic oscillations to the PIV data. In the forced cases, measurements from different bursts at arbitrary timings are phase referenced by minimizing the integrated root-mean-square deviations between the ensemble-averaged coherent structures in the initial burst and those in each subsequent burst. In the unforced cases, synchronization is still possible (e.g. [146]), but the analysis of the coherent oscillations in this chapter will focus on the forced cases since they display more prominent coherent structures.

6.2 Discussion of the dual-plane measurement

This chapter presents novel results regarding the behavior of harmonically-forced turbulent premixed swirling flames. However, one of the features which makes this work unique is the multiple-plane experimental method. An example of the instantaneous vector field and binarized OH-PLIF contour from Case 3, obtained using this method, is presented in Figure 6.2. While the spatiotemporal behavior of the two flow field sequences appears very similar at a glance, it is their differences that are of particular interest. This technique is intended to allow measurement of out-of-plane gradients inaccessible to standard stereoscopic PIV techniques. Nonetheless, quantification of these out-of-plane gradients requires finite-differences across the small plane-to-plane offset, which introduces a substantial multiplication of experimental uncertainty. Unfortunately, due to greater experimental uncertainty in the horizontally-polarized versus the vertically-polarized stereoscopic PIV planes, a meaningful analysis of the out-of-plane velocity gradients was not possible based on this experiment. Instead, this section will discuss some of the key challenges that must be overcome to effectively make such measurements.

6.2.1 Challenges

One of the major difficulties of the dual-plane method is uncertainty management, which can cloud the extraction of the novel quantities offered by this technique. Therefore, the challenges encountered during this campaign that promote such uncertainties are briefly enumerated.

Firstly, the laser reflections observed by PIV necessitated an appropriate background subtraction scheme. Both of the background subtraction schemes implemented introduced some degree of meaningful data subtraction in addition to removal of the unwanted contamination from the background environment. While great care was taken to avoid and control reflections, the complexity of the diagnostics setup for this experiment makes it

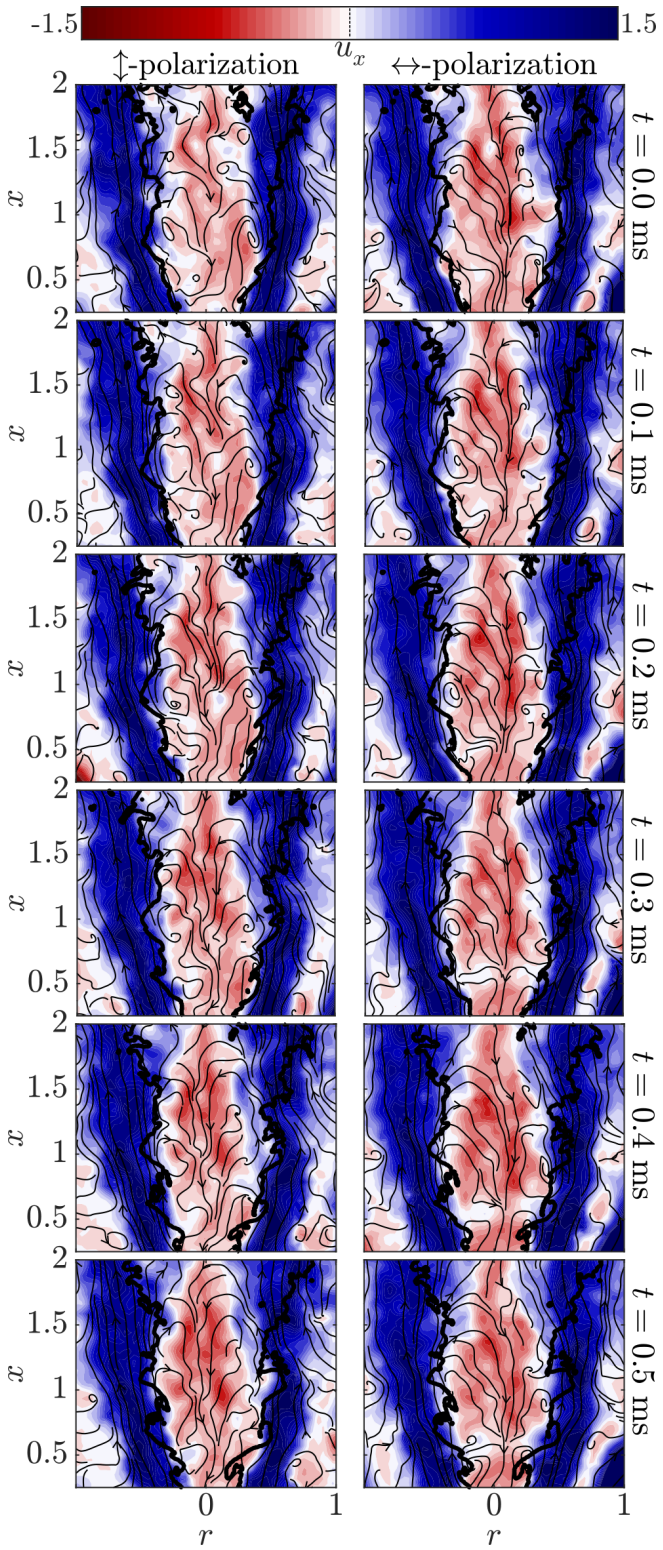

Figure 6.2: Sequential instantaneous flow snapshots obtained by dual-plane stereoscopic PIV and OH-PLIF for Case 3. The flow fields in both planes at each instance are measured simultaneously. The color map represents the axial velocity, black streamlines indicate the in-plane velocities, and thick black lines show the instantaneous flame position.

difficult to predict and remove them completely. This is worsened by the fact that reflections are not revealed until the post-processing stage (transferring images from the cameras is a nontrivial operation). This problem could be addressed by using a live diagnostic to assess reflections during preliminary runs and taking appropriate corrective actions during the experimental campaign instead of during post-processing.

Secondly, the tracer particles will de-polarize a portion of the laser light during the Mie scattering process. This introduces a "phantom particle" effect as depolarized scattering can be detected by the wrong pair of cameras or both pairs of cameras. This could be solved by staggering the timing of the laser sheets and associated cameras at the expense of additional complexity in the diagnostics setup and simultaneity of the measurement. A more auspicious solution is the use of differently-colored lasers instead of differently-polarized lasers for the dual-plane measurement. This is because a photon's wavelength is robust during the Mie scattering process, unlike its polarization.

Thirdly, finite-differences, which are used to compute the strain rate tensor, will greatly amplify random errors for in-plane differences, as well as both bias and random errors for out-of-plane differences. Uncertainty management is an important consideration when planning experimental campaigns intended for finite-difference based analyses, as the number of ensembles available for averaging becomes a critical factor. Random error diminishes the signal-to-noise ratio for any measurement, which requires substantial levels of time- or phase-averaging to raise the signal from the noise floor. While the random error, which is inversely proportional to the square root of the number of independent samples, is driven to zero by averaging, bias errors introduce a constant offset which may not be correctable via statistical analysis.

In traditional stereoscopic PIV, the dominant bias errors introduced by the spatial calibrations, laser sheet placement, peak-locking, loss of pairs, laser-hardware reflections, and flow tracer fidelity are sufficiently small for most applications. However, in this work, it was found that the influence of bias errors on dual-plane out-of-plane gradient measure-

ments can be significant. An interesting consequence of this sensitivity is that it does offer a special opportunity for *in situ* assessment of bias errors. In other words, rather than repeating the experiment, which captures uncertainty in the stereoscopic PIV methodology as well as the repeatability of the experiment itself, dual-plane PIV enables uncertainty quantification by implementing two nearly independent PIV setups & analyses on the same run of the experiment. This provides an opportunity to assess bias errors in the time-averaged velocity field when the two measurement planes are arranged about a line of symmetry, as in the current study.

6.2.2 Applications

The sensitivity of the out-of-plane gradients to small bias errors in the independent PIV measurements from separately-calibrated cameras has several important implications on what can and cannot be extracted from analysis of such methods. For example, the sensitivity to bias errors discussed in the previous section has an important implication for bias error detection. In effect, dual-plane measurement offers the opportunity to perform a repeatability study, with two independent diagnostic setups applied to the exact same experimental situation, but without sensitivity to repeatability of the experiment. As such, this technique can self-report an estimate of its bias error field. For example, the time-averaged dilatation field should be essentially null for non-reacting, incompressible flows, and only indicate positive dilatation near the flame for reacting flows. Furthermore, due to the symmetry of experimental setup relative to the placement of the two measurement planes, the time-averaged out-of-plane gradients should be nearly zero. The high sensitivity of these gradient-based quantities to experimental uncertainties provides an opportunity for iterative experimental refinement (of both the setup and the PIV processing).

Another possible application of the dual-plane measurement technique is for analysis of instantaneous strain rates, which may be much larger and less prone to small bias errors than their time- or phase-averaged counterparts. The high sensitivity of the out-of-plane

gradients to bias due to the close spacing of PIV measurement planes highlights an important pitfall of this technique, which is that experimental characterization of low-level out-of-plane gradients is quite difficult. However, an analysis of the *instantaneous* strain rate field, where strain rates are orders of magnitude greater than the bias error-induced uncertainty can be much more practical. This has important applications for combustor flow fields, where the instantaneous, dynamical strain rates induced by large-scale coherent structures and smaller eddies can strongly influence what locations qualify as flame anchoring points.

6.3 Results and analysis

In this section, the experimental data is analyzed and its relevance is discussed in the context of existing literature on turbulent swirling jets and flames. All of the velocity field measurements analyzed in this section are obtained from the vertically-polarized PIV sheet due to the challenges noted above.

6.3.1 Characterization of the mean flow

Velocity field

The Favré averaged mean velocity fields along each of the cardinal directions for each test case are presented in Figure 6.3. At the risk of slight abuse of notation, this chapter will make use of cylindrical coordinates throughout. However, it should be recognized that the measurements are planar and include data for $r < 0$. These planar velocity fields are reported as measured, with no adjustments made to account for the parity of the individual components across the centerline.

As shown in Figure 6.3, the non-reacting cases exhibit an annular swirling jet profile with a narrow recirculation zone in the center of the domain due to the combined effect of the centerbody wake and the vortex breakdown phenomenon. In the reacting cases, a V-shaped flame anchors itself in the inner shear layer in the same manner as the flows in

chapter 5. Compared to the non-reacting cases, combustion causes the flow speeds in the jet cores to increase and more than doubles the diameter of the central recirculation region. The doubling of the recirculation zone diameter corresponds to a fourfold increase in the fluid's specfic volume at constant pressure, which is consistent with the thermal expansion ratio of 4.38 derived from equilibrium calculations. This effect may therefore be attributed to the dilatation associated with the heat release causing the flow to expand and deflect the annular jet flow away from the centerline. In addition to accelerating and expanding the fluid, combustion also extends the region of reverse flow further upstream than the nonreacting cases, a phenomenon which has been seen in prior works in the context of combustion-induced vortex breakdown [148]. After testing, seeding particles were observed that had deposited themselves along the surface of the inner wall of the annulus just before the dump plane, indicating a flow stagnation/separation point. This suggests that the mean recirculation zone in the reacting cases extends slightly upstream into the nozzle. Comparing the forced and unforced cases in Figure 6.3, only a marginal effect of longitudinal harmonic forcing on the time-mean velocity field is observed. This resemblance is similar to the observations of Smith [6] which were discussed in the last chapter, and provides rationale for the application of the unforced mean field as a linearization reference for the mean-flow hydrodynamic stability analysis considered in chapter 5. However, the linear approach is only strictly valid if the Reynolds stresses are also unmodified by forcing, which will be shown not to be the case for the strong longitudinal forcing considered in this chapter.

Reynolds stress fields

Figure 6.4 shows the time-mean Reynolds stress tensor derived from each test case. As may be expected, the highest physical values of each of the mean Reynolds stress components generally occurs in the jet shear layers. Notably, the mean Reynolds stress tensor does show signatures of the background subtraction scheme utilized to process the PIV data.

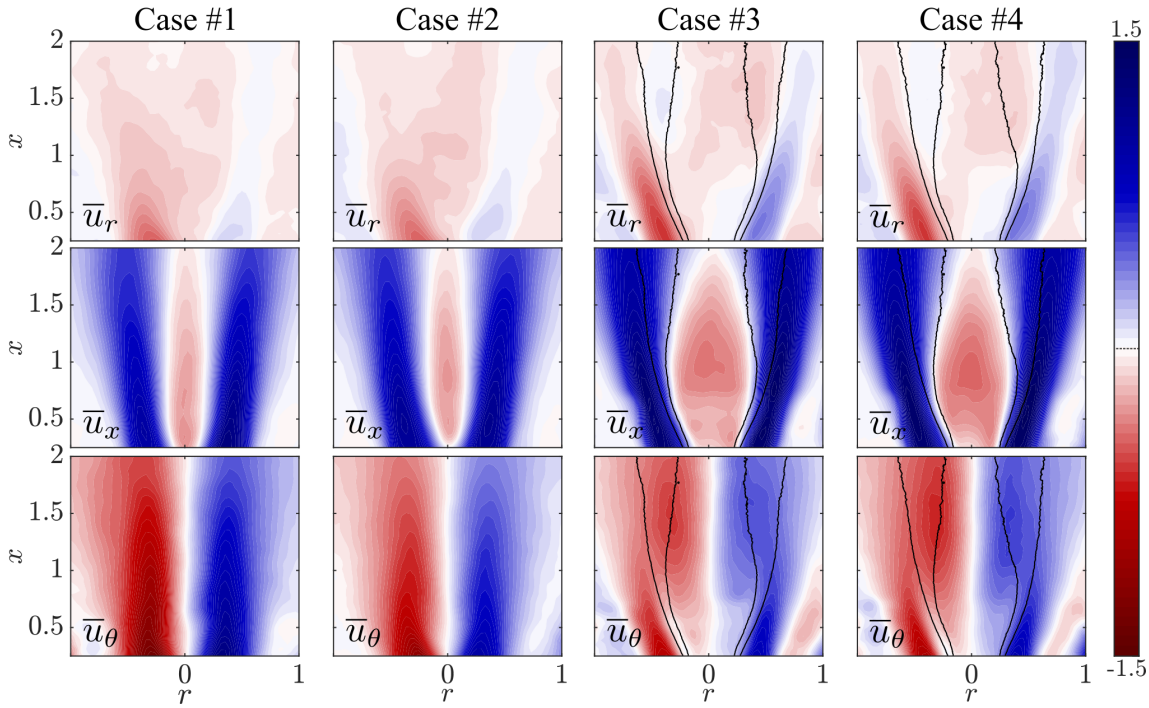

Figure 6.3: Measured mean velocity field for each of the four cases. For the reacting cases, black lines show the 20% and 80% flame PVF contours derived from the OH-PLIF measurements. Velocities are normalized by the nominal flow speed of 25 m/s

Cases 3 and 4 show "hot spots" in the $\tau^R_{r\theta}$ and $\tau^R_{\theta\theta}$ Reynolds stress components where laser reflections occurred, and Case 1 shows a strong peak near the centerline (particularly in the $\tau^R_{\theta\theta}$ component) which is not believed to be physical. Nonetheless, these effects are local in nature and are unlikely to have any significant effect on the data obtained in the rest of the measurement window. Surprisingly, the amplitude of the Reynolds stresses in the forced and unforced cases are quite similar, suggesting that the presence of longitudinal forcing does not significantly alter the time-mean transport of turbulent momentum for either the reacting or non-reacting cases.

It is also interesting to note the differences in the spatial distribution of the mean Reynolds stress between the reacting and non-reacting cases. In particular, while the non-reacting cases show significant Reynolds stresses which occur in the recirculation zone near the centerline, these Reynolds stresses are greatly reduced in the reacting cases. This is likely due to a combination of at least two effects. First, due to the presence of the flame,

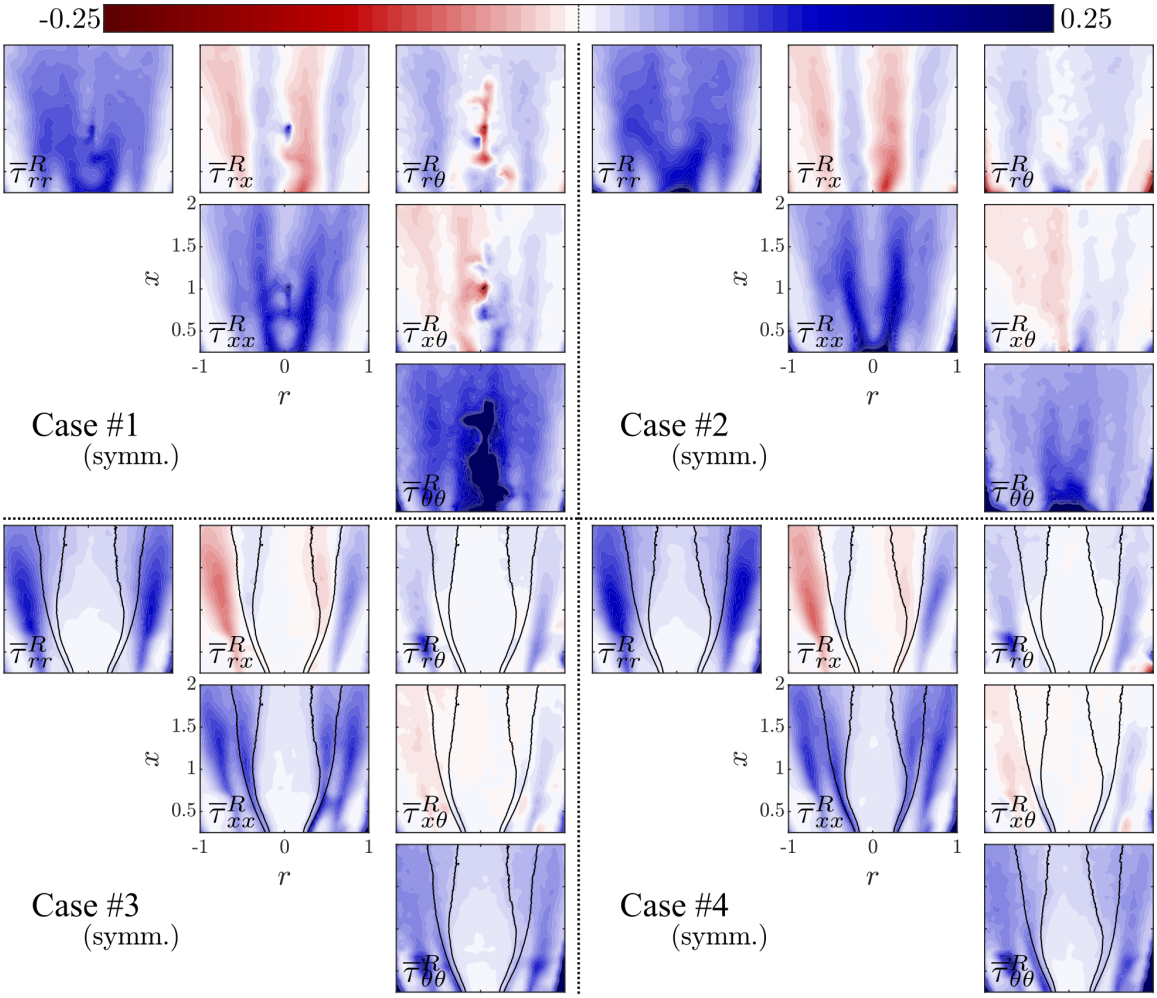

Figure 6.4: Measured time-mean Reynolds stress tensors for each test case. Flame PVF contours are overlaid in black for the reacting cases.

the density within the recirculation region is significantly reduced in the reacting cases compared to the non-reacting ones. This is important as, per Equation 6.1, the local density has a key influence on the local Reynolds stress values. Second, dilatation which occurs due to thermal expansion results in a sharp decrease in the strength of the local turbulent velocity fluctuations as they are transported across the flame. This phenomenon can be understood by considering the vorticity transport equation, where positive dilatation acts as a local vorticity sink, diminishing the amplitude of vortical fluctuations. Note that this is a separate effect from the former density effect which results as a direct consequence of the local density values and not due to a transport phenomenon as in the latter.

The fact that the peak mean Reynolds stresses tend to occur in the shear layers where the local strain rate is high hints that the Boussinesq hypothesis may provide a reasonable approximation of the local Reynolds stress. To test this idea, the Reynolds stress is modeled using the eddy viscosity via Equation 2.37 under the additional assumption of an axisymmetric mean flow. However, instead of using typical turbulence modeling equations such as the well-known k-ε closure [149, 150] to model $\overline{\mu}_T$ and $\overline{k}$, the comparison considered here will use Equation 2.39 and the definition of TKE to directly determine $\overline{\mu}_T$ and $\overline{k}$ from the measurements. As indicated in chapter 2, this approach results in a mathematically-optimal projection of the data onto the eddy viscosity, providing, in some sense, a best-case scenario for the Boussinesq eddy viscosity to accurately capture the turbulent behavior.

The modeled mean Reynolds stress fields based on the empirically-determined eddy viscosity for each test case are presented in Figure 6.5. These results can be directly compared with the measured mean Reynolds stresses reported in Figure 6.4. Overall, the results show good agreement with the measurements, as most of the main qualitative features of the Reynolds stress fields are accurately reproduced by the approximation. Thus, these results support the application of the Boussinesq hypothesis for the purposes of low-order modeling in this turbulent swirling annular jet flame. In particular, this may be interpreted to validate the approach taken in chapter 5, where an eddy viscosity was used to model the effect of incoherent fluctuations on the unforced turbulent flow (which did not display meaningful coherent dynamics) in order to formulate the stability analysis. However, it is important to emphasize that this empirically-determined eddy viscosity model is not based on any turbulence model equation. These results indicate that the Boussinesq hypothesis itself provides a good low-order approximation for the effect of turbulence on the mean flow, but the ability of model equations to predict this optimal eddy viscosity was not tested. Indeed, in this experimental framework, it would be challenging to form a well-posed problem for any turbulence closure equations as the flow boundaries lie outside of the measurement domain.

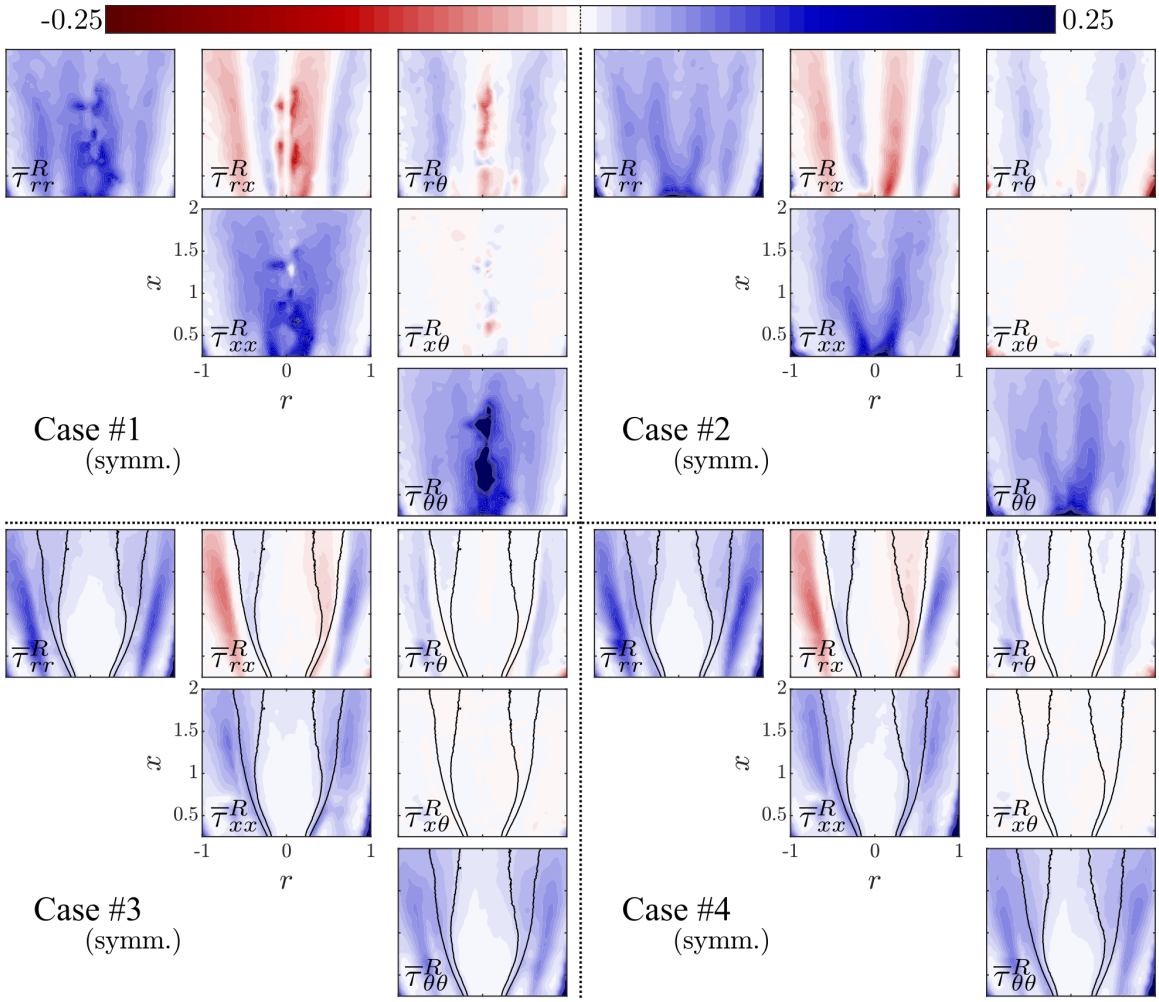

Figure 6.5: Eddy-viscosity modeled time-mean Reynolds stress tensors for each test case. Flame PVF contours are overlaid in black for the reacting cases. These results may be directly compared with the measured mean Reynolds stresses from Figure 6.4.

6.3.2 Characterization of the coherent flow

Velocity field

The coherent part extracted from the measured velocity fields of the forced experiments are shown in Figure 6.6. Due to the relatively small number of available samples, the coherent structures presented here contain a high degree of background turbulence and noise. Nonetheless, the non-reacting and reacting forced flows both exhibit coherent structures which are clearly visible above the turbulent background. The nominally-axisymmetric coherent structures incited by the longitudinal acoustics grow in amplitude as they are advected downstream along the jet For the reacting case, the phase-averaged PVF contours are overlaid in the figure to demonstrate the effect of these coherent oscillations on the flame position. From the flame PVF, it is clear that forcing has a substantial effect on the flame dynamics. Near the dump plane, where the amplitude of the oscillations is small, very little flame motion is visible. However, by $x \sim 1$ clear flame wrinkles are visible which grow and propagate along with the coherent velocity oscillations. Even though the forcing strength is identical in both cases, it is clear that the reacting case exhibits a far more robust response than its non-reacting counterpart.

The increase in the relative amplitudes of the coherent oscillations between Cases 2 and 4 indicates a notable sensitivity of the jet's forced response toward the presence of a flame which motivates deeper consideration. Several different factors come into play to influence whether or not a given flow responds positively to forcing. Strongly swirling jets typically exhibit spiraling natural instability modes (see chapter 3 and chapter 4 for laminar examples, or [136, 57, 135, 113] for turbulent studies), and, since the unforced reacting flow of case 3 is nominally the same as the unforced flow considered in chapter 5, the dominant linear response mode for this flow is also an $|m| = 1$ spiral. However, as discussed in chapter 5 and shown again here, the nature of the imposed forcing can preselect both the frequency and the azimuthal periodicity of the leading-order response [136, 115,

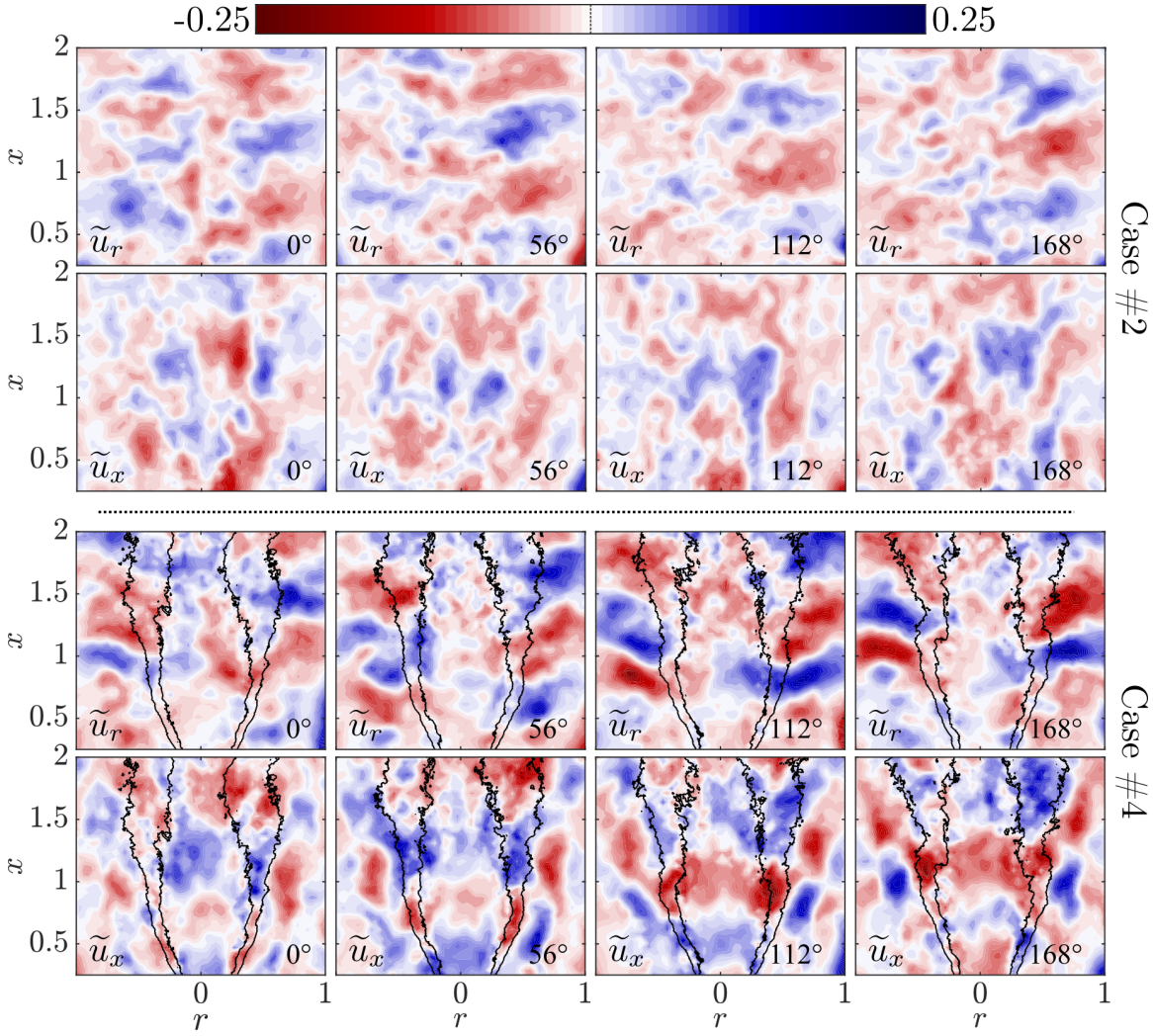

Figure 6.6: Coherent part of the in-plane velocity fields at four phase points for each of the two longitudinally-forced test cases. For the reacting cases, black lines show the 20% and 80% phase-averaged flame PVF contours.

145]. In this case, the strong longitudinal acoustics introduce axisymmetric perturbations. It is plausible that the axisymmetric flame wrinkles introduced by forcing help to resist dissipation of the vortex rings via some weak thermoacoustic effect [151], or that flame wrinkling somehow couples to the flow field via some non-local flow "memory" effect which decreases phase-jitter [152]. However, a more compelling hypothesis is that the non-reacting flow is simply less receptive to spatial amplification of 390 Hz axisymmetric hydrodynamic structures.

Reynolds stress fields

The coherent Reynolds stress tensor derived from each of the forced test cases is presented in the upper panels of Figure 6.7. The divergence of this tensor characterizes a force density which acts directly upon the coherent momentum equation (see Equation 2.36b). In other words, just as the time-mean Reynolds stress indicates the contribution of unsteady structures to the time-mean momentum transport, the coherent Reynolds stress tensor indicates the contribution of unsteady structures to coherent momentum oscillations. As shown in Figure 6.7, the reacting flow shows larger-amplitude oscillations in the coherent Reynolds stress than the non-reacting flow, particularly for $x \sim 1$ and further downstream. Thus, as may be expected, the strength of the coherent Reynolds stress oscillations is correlated with the strength of the coherent velocity oscillations. In addition, much like in the results from the time-mean field, the presence of flame has a significant effect on the local amplitude of the coherent Reynolds stress. This is likely a consequence of the same physical mechanisms discussed in subsection 6.3.1, namely a combined effect of the lower local density in the post-flame region and the stabilizing influence of dilatation on vortical fluctuations.

The bottom panels of Figure 6.7 show the variation in the xx-component of the coherent Reynolds stress as a function of phase angle for the forced cases. From this phase evolution, it is clear that the Reynolds stress fields exhibit clear structures which appear to closely follow the motion of the coherent velocity fluctuations visualized in Figure 6.6.

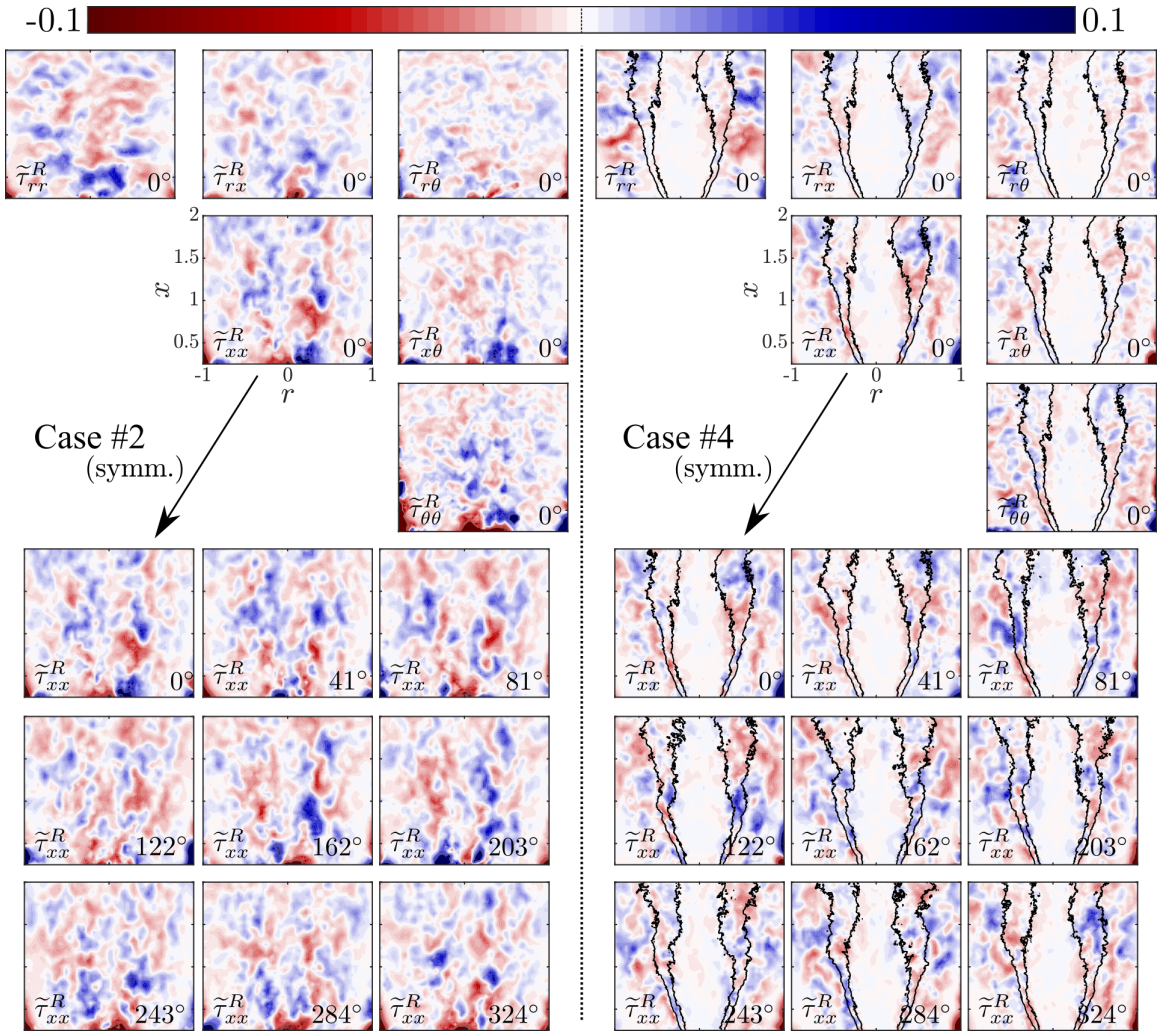

Figure 6.7: Measured coherent Reynolds stress tensors at the reference phase point for the forced test cases (top) and phase evolution of the xx-component of the coherent Reynolds stress (bottom). Phase-averaged PVF contours are overlaid in black for the reacting case.

However, it should be emphasized that interactions among these coherent velocity oscillations do not directly contribute to the coherent Reynolds stress oscillations, as the sum and difference nonlinear interactions act along different Fourier components than the fundamental oscillation (see Equation 2.22). Rather, the dominant effect captured by the coherent Reynolds stress is likely due to phase-jitter, whereby incoherent fluctuations cause cycle-to-cycle variations in the spatial location of otherwise coherent structures [80]. This therefore demonstrates a *modulation* of the coherent structures and their harmonics by the broadband turbulence. Nonetheless, the incoherent fluctuations themselves are also modulated by the coherent structures. An example of how this process might occur can be understood based on the classical turbulent energy cascade. In this interpretation, the apparent advection of peaks and valleys as a function of phase in the coherent Reynolds stress of Figure 6.7 is a consequence of smaller-scale eddies being energized by the periodic passage of the larger coherent vortices. These mechanisms represent only some of the plausible explanations for the observed coherent Reynolds stress oscillations, and it seems likely that several other effects would contribute to the phenomenon.

Comparing Figure 6.7 with Figure 6.4, in regions where the flow shows significant coherent features, the amplitudes of the coherent Reynolds stress oscillations can be up to 75% of the time-averaged Reynolds stress. This indicates a major contribution by unsteady structures to the dynamics of the coherent flow which motivates an analysis of the Boussinesq closure model's ability to capture these physics. This is tested using the coherent eddy viscosity model of Equation 2.38, which was proposed by [77] based on the work of [117]. As in subsection 6.3.1, no specific eddy viscosity model will be adapted in this work. The necessary inputs to determine the value of $\overline{\mu}_T$ are all obtained directly from the measurements, under the assumption that the dominant response is axisymmetric. Note that, for the current planar measurements, this assumption is essential, as out of plane gradients cannot be resolved. However, if the dual-plane measurement technique were to be successfully adapted in future work, this assumption of axisymmetry would not be necessary, and the

comparison could be extended to non-axisymmetric disturbance fields.

The modeled coherent Reynolds stress tensor based on the empirically-determined eddy viscosity for the forced test cases is presented in Figure 6.8. These results can be directly compared with the measured coherent Reynolds stresses reported in Figure 6.7. Unlike the time-mean results given in subsection 6.3.1, the modeled results for the coherent Reynolds stress tensor indicate far weaker stresses than the measurements. Despite this quantitative disagreement, certain qualitative aspects of the coherent Reynolds stresses are reproduced. For example, in the reacting case, the phase evolution of the peaks and valleys of coherent Reynolds stress shown in Figure 6.8 does agree the results in Figure 6.7, even if though oscillation amplitudes do not. Nonetheless, it is worth re-emphasizing that the methodology adopted here represents an optimal scenario for agreement between the measured stresses and the predictions from an eddy-viscosity model. In practical situations where the determination of the TKE and eddy viscosity rely on model equations with assumed coefficients and boundary conditions, the predictions would almost certainly be inferior. This therefore suggests that Boussinesq closure models, while suitable for modeling mean flow behavior, may not be appropriate for flows undergoing strong coherent oscillations, at least when $\widetilde{k}$ and $\widetilde{\mu}_T$ are neglected.

6.4 Summary

This chapter presents an experimental investigation of the flow field in longitudinally-forced premixed swirling annular jet flames. The chapter begins by describing a recently-developed high-speed, multi-plane simultaneous stereoscopic PIV and OH-PLIF experimental procedure for characterizing swirling flames. While this technique shows promise toward unlocking an additional dimension of velocity field measurements, several challenges remain to be solved before the approach can reach its full potential. The chapter detailed these challenges and suggested potential solutions which may allow them to be overcome in future work.

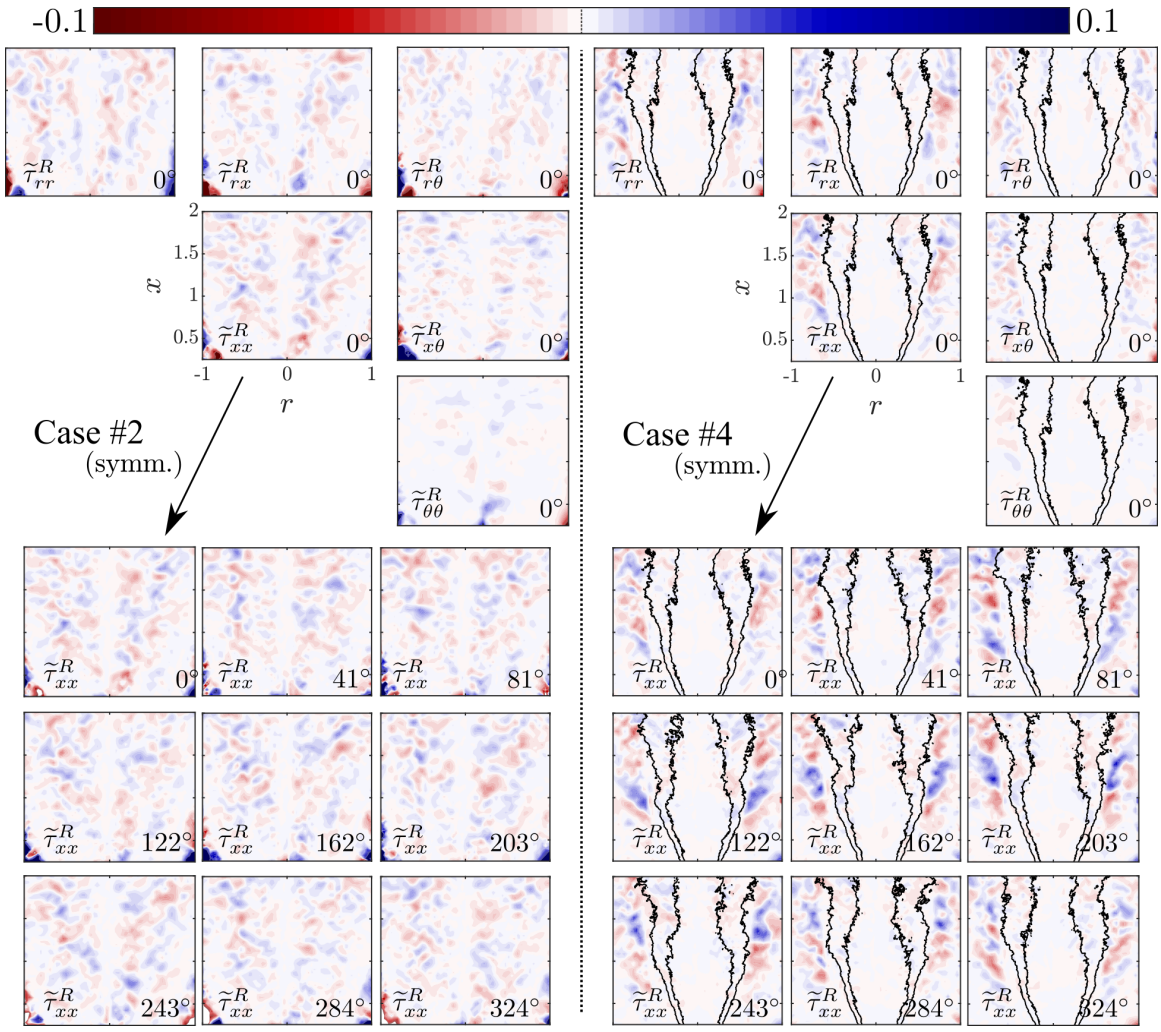

Figure 6.8: Eddy-viscosity modeled coherent Reynolds stress tensors at the reference phase point for the forced test cases (top) and phase evolution of the xx-component of the coherent Reynolds stress (bottom). Phase-averaged PVF contours are overlaid in black for the reacting case. These results may be directly compared with the measured coherent Reynolds stresses from Figure 6.7.

Next, the effects of forcing and combustion on the Favré-averaged mean velocity fields and the mean Reynolds stress tensor components were investigated using a single PIV measurement plane from the dual-plane measurement technique. The results indicated a minimal effect of longitudinal forcing on the mean flow and the mean Reynolds stress. However, dramatic effects were observed due to combustion on both the mean flowfields and the mean Reynolds stress distribution. Additionally, the measured mean Reynolds stresses were compared with predictions based on an empirically-determined eddy viscosity obtained by projecting the measured Reynolds stresses onto a Boussinesq closure model. The comparison indicated good agreement between the measured and modeled Reynolds stresses within the resolution of the measurements.

Finally, the coherent dynamics measured in the forced test cases were also characterized. As expected, the coherent velocity field indicated a clear response to longitudinal forcing. This response was significantly more pronounced in the reacting case than the non-reacting case. Characterization of the coherent Reynolds stress tensor was also performed. These results demonstrated harmonic modulation of incoherent flow features via periodic oscillations in the coherent Reynolds stress. This suggests mutual modulation of the coherent and incoherent flow structures through effects such as phase-jitter, leading to a coherent nonlinear interaction between the organized structures and broadband turbulence. It was further shown that the "best-case" Boussinesq eddy viscosity model failed to accurately capture these coherent Reynolds stress oscillations. This finding has important implications toward modeling of organized structures in reduced-order computational approaches, which often incorporate similar turbulence models.

CHAPTER 7
CONCLUDING REMARKS

This chapter summarizes the main contributions of this thesis. It outlines the particular significance of this research toward understanding the physics of swirling jets and flames, as well as its more general implications towards the overall role of hydrodynamic instability in unsteady combustion processes. Additionally, it addresses some important questions raised by this work and provides recommendations to future researchers aiming to build on these ideas.

7.1 Summary of contributions

7.1.1 Dynamics of laminar swirling jets and flames

The first major contribution of this work is the development of a large-scale numerical bifurcation analysis framework and its application to swirling jets and flames. As discussed in chapter 1, even for an inert flow in the laminar regime, the swirling jet parameter space is topologically very complex. Despite several thorough studies at specific conditions, prior investigations have not yielded a unified framework for understanding the relationships between different swirling jet behaviors. A key reason for this is the computational expense associated with numerical branch tracing calculations in large fluid mechanics and combustion problems. The parallel implementations of the equilibrium, bifurcation, and limit-cycle continuation algorithms described in chapter 2 synthesize existing ideas from the field of dynamical systems with modern, high-performance computing libraries which greatly expands applied capabilities on this front. It should also be emphasized that these numerical methods are not limited to swirling jets or even fluid systems. They are generic approaches which extend beyond this field to much broader classes of time-evolving non-

linear systems in irregular geometries.

Using this numerical bifurcation analysis framework, chapter 3 elucidated the steady and time-periodic behavior of non-reacting fully-developed swirling jets under variations in the Reynolds number *Re* and swirl ratio *S*. Within the $(0, 0) \leq (Re, S) \leq (300, 3)$ range, the steady, axisymmetric flow was shown to exhibit several distinct patterns ranging from a quasicolumnar jet along the central axis at low *S* to a radial jet attached to the containing wall at high *S* with various forms of vortex breakdown in between. At intermediate swirl conditions, a competition occurs between an inner low pressure region associated with the vortex breakdown phenomenon and an outer low pressure region associated with entrainment of the ambient fluid. Beyond a threshold Reynolds number of $Re = 47$, this mechanism triggers bistable behavior over a small range of *S* before the onset of flow instability. While bistability has been previously detailed in swirling flows in pipes (e.g. [128, 97]) and less precisely demonstrated in experimental (e.g. [31, 35]) and numerical (e.g. [32, 33]) studies of swirling jets, this work is the first to thoroughly characterize it in an unconfined jet using a proper bifurcation analysis.

Beyond the jet's steady dynamics, chapter 3 also considered the instability of the steady flow and the consequential nonlinear limit cycle oscillations. Over the parameter range considered, criticality of the steady flow was linked to eigenmodes which were singly ($|m| = 1$) or doubly ($|m| = 2$) azimuthally periodic, though additional instabilities with other azimuthal wavenumbers occured at (Re, S)-values beyond the leading neutral curves. The various branches of limit cycle solutions which stemmed from these neutral curves were associated with both super- and sub-critical Hopf bifurcations, revealing multivaluedness which further demonstrates the intricacy of the swirling jet parameter space. The resulting limit cycles oscillations exhibited a wide array of three-dimensional rotating flow structures, and comparisons between the time-averaged and steady flow patterns highlighted the role of these unsteady nonlinear interactions on the overall behavior of swirling jets.

Building on these findings, the swirling jet bifurcation analysis was extended to include

a simple high-*Ze* lean premixed flame model in chapter 4. While the enormous size of the reacting jet's parameter space discouraged a comprehensive study analogous to the inert case, a range of specific examples were considered in order to demonstrate how variations in the temperature, speed, and thickness of a swirling Bunsen-type flame configuration alter its behavior. The analysis focused on the jet's steady solutions and stability characteristics with varying S and the discussion emphasized the roles of the different physical mechanisms underlying these dynamics. For example, flame propagation, diffusion, and thermal expansion were all observed to play key roles in the jet's dynamical behavior. Overall, these results should serve as a caution to future researchers as they demonstrate that the dynamics of swirling jet flames are highly case-dependent and are intricately linked to the specifics of the flame configuration and parameters.

7.1.2 Hydrodynamic instabilities of turbulent swirling jets and flames

The second major contribution of this thesis concerns low-order descriptions of turbulent swirling flames. This portion of the work focused on analyzing and interpreting experimental measurements from a lean premixed flame in a high-*Re* swirling annular jet configuration. These measurements detailed a turbulent flow which naturally exhibits extremely high-dimensional "incoherent" turbulence. However, under imposed harmonic acoustic forcing, which may simulate the effect of thermoacoustic feedback present in an industrial combustor, significant time-periodic and spatially-coherent flow and flame structures were introduced.

In chapter 5, a weakly-global linear stability analysis was developed into a low-order predictive tool for determining the aforementioned coherent acoustic-hydrodynamic response of the swirling reacting jet to external acoustics. By accounting for the flowfield's spatial stability characteristics as well as the frequency and spatial distribution of the forcing, the predictions achieved good agreement with the measured flow response. Thus, while more advanced "global" stability approaches (such as those considered in the laminar por-

tion of this thesis) have become increasingly popular over the past decade, these methods all require extensive knowledge of the global mean flow field and boundary conditions which are often not possible to determine in experimentally-derived flow situations. In addition, fully-global stability analyses are far more computationally expensive. Thus, in nearly-parallel, convectively-unstable flows, the weakly-global analysis approach demonstrated in this thesis actually has several advantages over global methods (i.e. resolvent analysis in this context) when the mean flow conditions and/or boundary conditions are unresolved or are subject to high uncertainties.

Finally, in chapter 6, attention was turned to experimental characterizations of the turbulent flow and flame system with a particular emphasis on the implications toward low-order modeling. These results offer insight into the interplay among coherent vortices, broadband turbulence, and unsteady flames, which all contribute to the overall low-order dynamics within a turbulent combustor environment. Additionally, the presented experimentally-measured Reynolds stress fields serve as a platform from which to evaluate turbulence models for future low-order modeling efforts in swirling flames.

7.2 Recommendations for future work

7.2.1 Future work toward laminar swirling jets and flames

As remarked both above and in chapter 1, a unified framework for understanding the similarities and distinctions between flow patterns and behaviors across different swirling flow configurations and parameter spaces remains a key open challenge for the fluids and combustion communities. The present work contributes to this broader aim by definitively relating a suite of steady and time-periodic states in fully-developed laminar swirling jets with flush injection into a semi-infinite reservoir. Nonetheless, a number of questions requiring further research remain which are enumerated below.

Non-reacting setting

First, this work should be extended to a broader range of temporal dynamics. For example, a Floquet analysis of the periodic orbits identified in this study would determine the stability of the limit cycle solutions and precisely identify transitions to quasiperiodic behaviors. Then, a multiple-frequency harmonic balance approach could enable the nonlinear branches of quasiperiodic solutions to be traced through the parameter space in much the same way as the single-frequency approach was used for limit cycle solutions. However, the development of suitable preconditioners would be essential to making such an effort computationally tractable. Another relevant direction under this theme concerns the possible (and indeed almost certain) existence of attractors which are disconnected from the steady solution manifold. In particular, as briefly noted in subsubsection 2.1.3, pseudoresonant, nonmodal amplification of small perturbations [107] can divert even a linearly-stable system onto a new basin of attraction through nonlinear processes [106]. Montagnani & Auteri [108] have begun to address this issue for a co-axial swirling jet configuration at low swirl, but a similar analysis on a broader class of swirl flows, and across a wider parametric range, could provide important insights into the role of non-modal linear dynamics in swirling jet behaviors.

Second, work is needed to generalize these results to jet profiles with thinner boundary layers. As noted in subsection 3.2.1, a jet's boundary layer thickness dramatically influences the relative linear growth rates of its $m = 0$ and $|m| = 1$ modes, as well as the role of shear instabilities relative to other inviscid instability mechanisms. By introducing a boundary layer thickness parameter to the flow configuration, a similar continuation-type analysis could trace the nonlinear dynamics of jets across the gamut of boundary layer thicknesses.

Third, work is needed to explore the effects of lateral confinement. In the laterally-unconfined flow considered in this thesis, steady vortex breakdown occurs gradually and smoothly as S is increased and hysteresis occurs between the vortex breakdown and wall-

jet states. However, as discussed in subsection 3.1.3, the nonlinear evolution of the unconfined flow considered here is markedly different from that seen in confined flows where steady vortex breakdown appears and disappears abruptly due to hysteresis between columnar and breakdown states. While this study does not directly address the role of confinement, it is worth mentioning that steady solutions identified in our work from the vortex breakdown and wall-jet regimes exhibit streamline patterns and velocity magnitudes which would clearly be affected by the introduction of a solid lateral wall with a diameter $O(10)$ times larger than the jet as typically seen in experimental studies [31, 35]. This suggests that lateral confinement may play a larger role in the behaviors observed in existing swirling jet experiments than perhaps thought. Future research on this subject, which could also be tackled with continuation analyses based on variation of a confinement parameter, would be particularly useful for relating results from unconfined flows such as those examined here to computational studies and experiments of flows where varying degree of lateral confinement are present.

Fourth, important questions also come to mind related to the influence of the ambient fluid surrounding the swirling jet. For example, an alteration of the injection depth (*i.e.* the distance between the pipe exit and the containing wall) would substantially alter the near-field entrainment of the ambient fluid which could, in turn, lead to important differences in the jet's overall behavior. As noted in subsection 2.1.1, the flush jet considered here differs in this regard from the setups used in some experimental studies [31, 35]. Indeed, the 'opposite' limit of the configuration examined here would be a jet injected into a completely open domain with no containing wall, which would simulate a rotating pipe flow injected into a large open volume. This distinction implies that further work on the role of injection depth is also needed to fully understand the relation between these results (where a wall jet is a prominent flow feature at high S-values) and other studies. In a similar vein, changes to the jet's entrainment characteristics may also occur if the jet were placed in a co-axial configuration where the ambient fluid was endowed with an axial co-flow. In subsection 3.1.3,

it was hypothesized, based on comparisons between the present results and vortex models with strong and weak axial co-flow velocities, that the formation of an outer recirculation zone is necessary for bistable behavior of the steady flow in unconfined swirling flows. Future studies toward the role of co-flow in the dynamics of co-axial swirling jets could evaluate the validity of this hypothesis.

Finally, it is worth considering the effects of flow turbulence and bridging the gap between the laminar and turbulent portions of this work. As discussed in chapter 1, the phenomenon of spatiotemporal coherence in turbulent flows is fundamentally linked to the influence of low-dimensional invariant solution manifolds (which include steady and time-periodic solution manifolds such as those identified in this study) on the system's state space trajectory [68, 66]. As shown in chapter 5, this connection can be exploited in low-order modeling approaches by leveraging the triple decomposition to separate the mean and coherent part of the flow (which are usually of primary interest) from the incoherent fluctuations (whose effects may be modeled using, for example, the eddy-viscosity hypothesis). Thus, even though the Reynolds numbers investigated in chapter 3 lie an order of magnitude or more below the actual values associated with most turbulent applications, the effective Reynolds numbers associated with low-order turbulence models may actually be quite similar in magnitude to the *Re* values used here at pertinent spatial locations. Several existing studies which leverage this approach, including the analysis in chapter 5, have resorted to linear models of the coherent dynamics which neglect the role of harmonic interactions on the coherent oscillations [76, 77, 58]. As pointed out by Tammisola & Juniper [77], this simplifying assumption is applicable in certain cases. Nonetheless, the results of chapter 6 demonstrated significant coherent Reynolds stress oscillations, indicating non-negligible unsteady harmonic interactions which cannot be captured without considering nonlinear effects [146]. The harmonic balance approach adopted here, if coupled with a suitable model for incoherent turbulent fluctuations, offers a more general approach for modeling coherent oscillations when harmonic interactions are not negligible. Such ef-

forts could represent a meaningful direction for future work addressing low-dimensional behavior in turbulent flows.

Reacting setting

The questions raised above in the context of inert swirling jets also directly extend to the reacting case. However, the work performed here also broaches many additional questions which are specific to swirling jet flames.

First, it should be noted that even within the relatively limited confines of the lean premixed flame model considered in this thesis, the present study was restricted to only a small portion of the overall parameter space. For example, while $Ze = 10$ (which was held constant throughout this work) may be a fair approximation of a typical flame, additional work is needed to understand how variations in *Ze* interact with the other parameters to influence the overall flow behavior. Additionally, the approach should be extended to non-adiabatic boundary conditions in order to gain additional insight into how quenching and the resulting destabilization of the flame along cold walls can influence the flame shape and flame/flow dynamics.

Second, this study only considered a very simple flame model, with several limiting physical assumptions such as constant specific heats, viscosity, and diffusion coefficients. Future work should extend this type of bifurcation analysis to higher-order reaction models which include a broader suite of physics such as differential diffusion and thermophoresis and which incorporate non-constant flow properties in order to better understand how these factors influence the jet dynamics. For instance, recent work has emphasized the role that non-constant viscosities have on the dynamics and instabilities of a variety of flow systems including reacting ones [153]. Such effects could easily be incorporated into this model with a Sutherland-type law scaling for viscosity and/or thermal transport at the expense of only some additional parameters (which do not impact computational cost).

Third, in the reacting case, the work in this thesis focused only on the steady flow and

its linear stability. Future work should address the role of nonlinearity in flow oscillations which arise after instability in the reacting flow. This could be accomplished using an approach similar to that pursued in the non-reacting portion of the study.

7.2.2 Future work toward turbulent swirling jets and flames

Throughout this thesis, the importance of developing a unified physical understanding of swirling jets and flames across different parameter conditions and flow configurations has been repeatedly emphasized. Both strong parallels and clear distinctions exist between the low-dimensional coherent structures which appear in turbulent flows and the laminar dynamics which can be more easily understood. As noted above, consolidating this knowledge should represent a core theme for future work in this area. While the work discussed in chapter 5 and chapter 6 do contribute to this larger goal, it also raises several more specific questions which should be targeted by future work.

First, more work is needed to determine the limitations of the weakly-global linear acoustic-hydrodynamic response model advanced in chapter 5. For example, how "parallel" must the mean flow be in order for the analysis to deliver useful results? Is the current method robust enough to handle more complex acoustic forcing conditions which cannot be understood based on forcing interactions restricted to the burner lips? Is there a frequency or amplitude limit beyond which this linear method breaks down? Answers for all of these questions will be required to safely interpret results from this type of analysis without direct experimental validation as given in this study.

Second, the results indicated a relatively gradual decrease in the amplitude of the linear response at high wavenumbers (see, for example, Figure 5.9). This suggests that the primary factor influencing their lack of appearance in the response is not due to inherently weaker linear stability characteristics, but rather due to a lack of excitation of these particular instability modes by the forcing patterns. Future work should test this hypothesis by introducing forcing which directly excites $|m| \geq 2$ disturbances and measuring the

response.

Finally, as discussed extensively in section 6.2, the experimental work faced a series of technical challenges which prevented the measured data set from yielding a sufficiently-precise characterization of the 3-D strain rate tensor. This effort should not be abandoned based on these challenges, however, as such a measurement would have enormous implications for the assessment of low-order turbulence models. Future work should consider and adapt to the challenges faced in that experimental campaign in order to someday successfully characterize this important quantity.

Appendices

APPENDIX A

DERIVATION OF GOVERNING EQUATIONS

In this appendix, the governing system for the reacting flow model described in chapter 2 is derived. The governing equations for reacting flows consist of conservation of mass, species, momentum, and energy and the equations of state. Assuming a Newtonian mixture of N thermally perfect gases and neglecting external volume forces and energy sources and radiative heating, these may be expressed in their dimensional differential form as,

$$\frac{\partial \rho^\star}{\partial t^\star} + \boldsymbol{\nabla}^\star \cdot \boldsymbol{u}^\star = 0, \tag{A.1a}$$

$$\frac{\partial \rho^\star Y_k^\star}{\partial t^\star} + \boldsymbol{\nabla}^\star \cdot \left(\rho^\star \left(\boldsymbol{u}^\star + \boldsymbol{v}_k^\star\right) Y_k^\star\right) = \dot{\omega}_k^\star, \tag{A.1b}$$

$$\frac{\partial \rho^\star \boldsymbol{u}^\star}{\partial t^\star} + \boldsymbol{\nabla}^\star \cdot \left(\rho^\star \boldsymbol{u}^\star \boldsymbol{u}^\star\right) = -\boldsymbol{\nabla}^\star p^\star + \boldsymbol{\nabla}^\star \cdot \boldsymbol{\tau}^\star, \tag{A.1c}$$

$$\begin{aligned}\frac{\partial \rho^\star E^\star}{\partial t^\star} + \boldsymbol{\nabla}^\star \cdot \left(\rho^\star \boldsymbol{u}^\star E^\star\right) &= -\boldsymbol{\nabla}^\star \cdot \left(\boldsymbol{u}^\star p^\star\right) + \boldsymbol{\nabla}^\star \cdot \left(\boldsymbol{u}^\star \cdot \boldsymbol{\tau}^\star\right) - \sum \Delta h_{f,k}^{0\star} \dot{\omega}_k^\star \\ &\quad + \boldsymbol{\nabla}^\star \cdot \left(\mathcal{D}^\star \boldsymbol{\nabla}^\star T^\star - \sum \rho^\star h_{s,k}^\star Y_k^\star \boldsymbol{v}_k^\star\right),\end{aligned} \tag{A.1d}$$

$$p^\star = \sum \frac{\rho_k^\star Y_k^\star}{W_k^\star} R_u^\star T^\star, \tag{A.1e}$$

$$e_s^\star = \sum \int_{T_{\mathrm{ref}}^\star}^{T^\star} c_{v,k}^\star Y_k^\star \, \mathrm{d}T^\star, \tag{A.1f}$$

$$\begin{aligned}\boldsymbol{\tau}^\star &= \mu^\star \left(\boldsymbol{\nabla}^\star \boldsymbol{u}^\star + \left(\boldsymbol{\nabla}^\star \boldsymbol{u}^\star\right)^{\mathrm{T}}\right) \\ &\quad + \left(\kappa^\star - \frac{2\mu^\star}{3}\right) \boldsymbol{I} \left(\boldsymbol{\nabla}^\star \cdot \boldsymbol{u}^\star\right),\end{aligned} \tag{A.1g}$$

where $\rho^\star$ is the density, $\boldsymbol{u}^\star$ is the velocity vector, $Y_k^\star$ is the mass fraction of species k, $\dot{\omega}_k^\star$ is reaction rate of species k, $\boldsymbol{v}_k^\star$ is the diffusion velocity of species k, $p^\star$ is the static pressure, $E^\star = e_s^\star + \frac{1}{2}\boldsymbol{u}^\star \cdot \boldsymbol{u}^\star$ is the sum of sensible and kinetic energies, $\Delta h_{f,k}^{0\star}$ is the formation enthalpy of species k, $\mathcal{D}^\star$ is the thermal diffusivity, $T^\star$ is the temperature, $h_{s,k}^\star$ is the sensible enthalpy of species k, $\rho_k^\star$ and $W_k^\star$ are the density and atomic weight of species

k, $R_u^\star$ is the universal gas constant, $c_{p,k}^\star$ is the specific heat at constant pressure of species k, $T_{\text{ref}}^\star$ is the reference temperature, $h_s^\star$ is the total sensible enthalpy, $\mu^\star$ is the total dynamic shear viscosity, and $\kappa^\star$ is the total second (volume) viscosity. Here, asterisks are used to denote dimensional variables.

Next, a series of approximations are made to reduce Equation A.1 to a more tractable system. First, the chemistry is modeled by a single-step, irreversible, fuel-limited exothermic reaction with a rate determined by the Arrhenius law. Second, Soret, Dufour, and pressure gradient diffusion effects are all neglected such that the diffusion velocity $\boldsymbol{v}_k^\star$ is determined directly from Fick's Law. Third, the products and reactants are assumed to have equal molecular weights and to have identical, constant heat capacity and diffusivity properties which yield a Lewis number of one. With these assumptions, Equation A.1 becomes,

$$\frac{\partial \rho^\star}{\partial t^\star} + \boldsymbol{\nabla}^\star \cdot (\rho^\star \boldsymbol{u}^\star) = 0, \tag{A.2a}$$

$$\frac{\partial \rho^\star Y^\star}{\partial t^\star} + \boldsymbol{\nabla}^\star \cdot (\rho^\star \boldsymbol{u}^\star Y^\star) = -\mathcal{A}^\star \rho^\star Y^\star \exp\left(\frac{-{T_a}^\star}{T^\star}\right) + \mathcal{D}^\star \nabla^{\star 2} Y^\star, \tag{A.2b}$$

$$\frac{\partial \rho^\star \boldsymbol{u}^\star}{\partial t^\star} + \boldsymbol{\nabla}^\star \cdot (\rho^\star \boldsymbol{u}^\star \boldsymbol{u}^\star) = -\boldsymbol{\nabla}^\star p^\star + \boldsymbol{\nabla}^\star \cdot \boldsymbol{\tau}^\star, \tag{A.2c}$$

$$\begin{aligned}\frac{\partial \rho^\star E^\star}{\partial t^\star} + \boldsymbol{\nabla}^\star \cdot (\rho^\star \boldsymbol{u}^\star E^\star) = &-\boldsymbol{\nabla}^\star \cdot (\boldsymbol{u}^\star p^\star) + \Delta h_f^{0\star} \mathcal{A}^\star \rho^\star Y^\star \exp\left(\frac{-{T_a}^\star}{T^\star}\right) \\ &+\mathcal{D}^\star \nabla^{\star 2} T^\star + \boldsymbol{\nabla}^\star \cdot (\boldsymbol{u}^\star \cdot \boldsymbol{\tau}^\star),\end{aligned} \tag{A.2d}$$

$$p^\star = \rho^\star R^\star T^\star, \tag{A.2e}$$

$$e_s^\star = c_v^\star T^\star, \tag{A.2f}$$

$$\begin{aligned}\boldsymbol{\tau}^\star = &\mu^\star \left(\boldsymbol{\nabla}^\star \boldsymbol{u}^\star + (\boldsymbol{\nabla}^\star \boldsymbol{u}^\star)^{\mathrm{T}}\right) \\ &+ \left(\kappa^\star - \frac{2\mu^\star}{3}\right) \boldsymbol{I} (\boldsymbol{\nabla}^\star \cdot \boldsymbol{u}^\star),\end{aligned} \tag{A.2g}$$

where $\mathcal{A}^\star$ is the Arrhenius frequency factor, ${T_a}^\star$ is the Arrhenius activation temperature, and $R^\star$ is the specific gas constant.

To further simplify, the dimensional variables that have been used in the previous equa-

tions are scaled by the reference properties of the reactants (subscript R) and the velocity and length scale of the flow ($U^\star$ and $D^\star$, respectively). These reference quantities are chosen such that the dimensionless quantities remain $O(1)$ for any Mach number defined by $M \equiv \frac{U^\star\sqrt{\rho_R^\star}}{\sqrt{p_R^\star}}$ (which differs from the traditional Mach number definition by a factor of $\sqrt{\gamma}$ where $\gamma = \frac{c_p^\star}{c_v^\star}$ is the specific heat ratio). The scaled, dimensionless quantities are defined by

$$\rho = \frac{\rho^\star}{\rho_R}^\star,\ Y = \frac{Y^\star}{Y_R^\star},\ \boldsymbol{u} = \frac{\boldsymbol{u}^\star}{U^\star},\ E = \frac{\rho_R^\star E^\star}{p_R^\star},\ p = \frac{p^\star}{p_R^\star},\ T = \frac{T^\star}{T_R^\star},\ h_s = \frac{\rho_R^\star h_s^\star}{p_R^\star},$$
$$\boldsymbol{x} = \frac{\boldsymbol{x}^\star}{D^\star},\ t = \frac{U^\star t^\star}{D^\star}, \boldsymbol{\tau} = \frac{D^\star \boldsymbol{\tau}^\star}{\mu_R^\star U^\star},\ \mu = \frac{\mu^\star}{\mu_R^\star},\ \kappa = \frac{\kappa^\star}{\mu_R^\star},\ \mathcal{D} = \frac{\mathcal{D}^\star}{\mathcal{D}_R^\star},\ c_p = \frac{c_p^\star}{c_{p,R}^\star}.$$

Note that, since the specific heat and thermal diffusivity (which is equivalent to the mass diffusivity by the unity Lewis number assumption) were assumed constant, $\mathcal{D} = c_p = 1$. Substituting these definitions into (Equation A.2) yields the dimensionless equations,

$$\frac{\partial \rho}{\partial t} + \boldsymbol{\nabla}\cdot(\rho \boldsymbol{u}) = 0, \tag{A.3a}$$
$$\frac{\partial \rho Y}{\partial t} + \boldsymbol{\nabla}\cdot(\rho \boldsymbol{u} Y) = -\mathit{Da}'\rho Y \exp\left(\frac{-\mathit{Ta}}{T}\right) + \frac{1}{\mathit{Pe}}\nabla^2 Y, \tag{A.3b}$$
$$\frac{\partial \rho \boldsymbol{u}}{\partial t} + \boldsymbol{\nabla}\cdot(\rho \boldsymbol{u}\boldsymbol{u}) = -\frac{1}{\mathit{M}^2}\boldsymbol{\nabla} p + \frac{1}{Re}\boldsymbol{\nabla}\cdot\boldsymbol{\tau}, \tag{A.3c}$$
$$\frac{\partial \rho E}{\partial t} + \boldsymbol{\nabla}\cdot(\rho \boldsymbol{u} E) = -\boldsymbol{\nabla}\cdot(\boldsymbol{u} p) + \frac{\gamma \mathit{Da}'\Delta T}{\gamma - 1}\rho Y \exp\left(\frac{-\mathit{Ta}}{T}\right) + \frac{\gamma}{(\gamma-1)\mathit{Pe}}\nabla^{\star 2} T + \frac{\tilde{M}^2}{Re}\boldsymbol{\nabla}\cdot(\boldsymbol{u}\cdot\boldsymbol{\tau}), \tag{A.3d}$$
$$p = \rho T, \tag{A.3e}$$
$$e_s = \frac{T}{\gamma - 1}, \tag{A.3f}$$
$$\boldsymbol{\tau} = \mu\left(\boldsymbol{\nabla}\boldsymbol{u} + (\boldsymbol{\nabla}\boldsymbol{u})^{\mathrm{T}}\right) + \left(\kappa - \frac{2\mu}{3}\right)\boldsymbol{I}(\boldsymbol{\nabla}\cdot\boldsymbol{u}), \tag{A.3g}$$

where the following dimensionless parameters have been defined: the unscaled Dahmköler number, $\mathit{Da}' \equiv \mathcal{A}^\star D^\star/U^\star$; the exothermicity, $\Delta T \equiv Y_R^\star \Delta h_f^{\star 0}/(c_{p,R}^\star T_R^\star)$; the normalized activation temperature, $\mathit{Ta} \equiv {\mathit{Ta}}^\star/T_R^\star$; the Péclet number, $\mathit{Pe} \equiv U^\star D^\star/\mathcal{D}^\star$; and the Reynolds

number, $Re \equiv \rho_R^\star U^\star D^\star / \mu_R^\star$. Note that the Mach number also appears in the dimensionless non-chemical energy where $E = e_s + \frac{1}{2}M^2 \boldsymbol{u} \cdot \boldsymbol{u}$.

To derive the low-Mach number form of the equations, each flow variable is expanded in orders of the Mach number, i.e.

$$\psi = \psi_{(0)} + M\psi_{(1)} + M^2\psi_{(2)} + O(M^3).$$

Here, ψ represents an arbitrary flow variable. Substituting the asymptotic expansion into Equation A.3 and collecting only the equations which do not vanish in the limit of zero Mach number yields,

$$\begin{aligned}
\frac{\partial \rho_{(0)}}{\partial t} + \boldsymbol{\nabla} \cdot \left(\rho_{(0)} \boldsymbol{u}_{(0)}\right) &= 0, && \text{(A.4a)}\\
\frac{\partial \rho_{(0)} Y_{(0)}}{\partial t} + \boldsymbol{\nabla} \cdot \left(\rho_{(0)} \boldsymbol{u}_{(0)} Y_{(0)}\right) &= -Da' \rho_{(0)} Y_{(0)} \exp\left(\frac{-T_a}{T_{(0)}}\right) + \frac{1}{Pe}\nabla^2 Y_{(0)}, && \text{(A.4b)}\\
0 &= -\boldsymbol{\nabla} p_{(0)}, && \text{(A.4c)}\\
\frac{\partial \rho_{(0)} \boldsymbol{\nabla} \boldsymbol{u}_{(0)}}{\partial t} + \boldsymbol{\nabla} \cdot \left(\rho_{(0)} \boldsymbol{u}_{(0)} \boldsymbol{u}_{(0)}\right) &= -\boldsymbol{\nabla} p_{(2)} + \frac{1}{Re} \boldsymbol{\nabla} \cdot \boldsymbol{\tau}_{(0)}, && \text{(A.4d)}\\
\frac{\partial \rho_{(0)} E_{(0)}}{\partial t} + \boldsymbol{\nabla} \cdot \left(\rho_{(0)} \boldsymbol{u}_{(0)} E_{(0)}\right) &= -\boldsymbol{\nabla} \cdot \left(\boldsymbol{u}_{(0)} p_{(0)}\right) + \frac{\gamma Da' \Delta T}{\gamma - 1} \rho_{(0)} Y_{(0)} \exp\left(\frac{-T_a}{T_{(0)}}\right) \\
&\qquad + \frac{\gamma}{(\gamma - 1) Pe} \nabla^2 T_{(0)}, && \text{(A.4e)}\\
p_{(0)} &= \rho_{(0)} T_{(0)}, && \text{(A.4f)}\\
E_{(0)} &= \frac{T_{(0)}}{\gamma - 1}, && \text{(A.4g)}\\
\boldsymbol{\tau}_{(0)} &= \mu_{(0)} \left(\boldsymbol{\nabla} \boldsymbol{u}_{(0)} + \left(\boldsymbol{\nabla} \boldsymbol{u}_{(0)}\right)^{\mathrm{T}}\right) \\
&\qquad + \left(\kappa_{(0)} - \frac{2\mu_{(0)}}{3}\right) \boldsymbol{I} \left(\boldsymbol{\nabla} \cdot \boldsymbol{u}_{(0)}\right). && \text{(A.4h)}
\end{aligned}$$

Thus, as a consequence of the $O(M^{-2})$ momentum equation (Equation A.4c), the leading-order pressure must be spatially constant. Using the equation of state (Equation A.4f), this implies that the product $\rho_{(0)} T_{(0)}$ should also be spatially uniform. With these constraints, the pressure $p_{(2)}$ now represents a purely hydrodynamic component of pressure that is fully

decoupled from the spatially-uniform thermodynamic pressure at leading order. Additionally, the leading order energy is proportional to the the temperature. Applying these restrictions to Equation A.4 and dropping the subscripts denoting the expansion orders for all variables except the pressure returns,

$$\begin{aligned}
\frac{\partial \rho}{\partial t} + \boldsymbol{\nabla} \cdot (\rho \boldsymbol{u}) &= 0, && \text{(A.5a)} \\
\frac{\partial \rho Y}{\partial t} + \boldsymbol{\nabla} \cdot (\rho \boldsymbol{u} Y) &= -Da' \rho Y \exp\left(\frac{-T_a}{T}\right) + \frac{1}{Pe} \nabla^2 Y, && \text{(A.5b)} \\
\frac{\partial \rho \boldsymbol{u}}{\partial t} + \boldsymbol{\nabla} \cdot (\rho \boldsymbol{u} \boldsymbol{u}) &= -\boldsymbol{\nabla} p_{(2)} + \frac{1}{Re} \boldsymbol{\nabla} \cdot \boldsymbol{\tau}, && \text{(A.5c)} \\
\frac{1}{\gamma} \frac{\mathrm{d} p_{(0)}}{\mathrm{d} t} + p_{(0)} \boldsymbol{\nabla} \cdot \boldsymbol{u} &= Da' \Delta T \rho Y \exp\left(\frac{-T_a}{T}\right) + \frac{1}{Pe} \nabla^2 T, && \text{(A.5d)} \\
p_{(0)} &= \rho T, && \text{(A.5e)} \\
\boldsymbol{\tau} &= \mu \left(\boldsymbol{\nabla} \boldsymbol{u} + (\boldsymbol{\nabla} \boldsymbol{u})^{\mathrm{T}} \right) + \left(\kappa - \frac{2\mu}{3} \right) \boldsymbol{I} \left(\boldsymbol{\nabla} \cdot \boldsymbol{u} \right). && \text{(A.5f)}
\end{aligned}$$

Next, the thermodynamic pressure is assumed to be subject to time-invariant boundary conditions. This implies that $p_{(0)}$ is identically one, which simplifies the energy equation and the equation of state. A significant simplification to the viscous stress tensor in the momentum equation can also be realized by assuming μ to be constant and redefining the hydrodynamic pressure as $p = p_{(2)} - Re^{-1} \left(\kappa + \mu/3 \right) \left(\boldsymbol{\nabla} \cdot \boldsymbol{u} \right)$. This substitution is a particular advantage of the low-Mach number expansion. It is possible because the normal viscous stresses act along the gradient with the hydrodynamic pressure, and can thus be absorbed into the pressure term without any other change to the overall equations. With

these changes, Equation A.5 reduces to,

$$\begin{aligned}
\frac{\partial \rho}{\partial t} + \boldsymbol{\nabla} \cdot (\rho \boldsymbol{u}) &= 0, && \text{(A.6a)}\\
\frac{\partial \rho Y}{\partial t} + \boldsymbol{\nabla} \cdot (\rho \boldsymbol{u} Y) &= -Da' \rho Y \exp\left(\frac{-T_a}{T}\right) + \frac{1}{Pe}\nabla^2 Y, && \text{(A.6b)}\\
\frac{\partial \rho \boldsymbol{u}}{\partial t} + \boldsymbol{\nabla} \cdot (\rho \boldsymbol{u}\boldsymbol{u}) &= -\boldsymbol{\nabla} p + \frac{1}{Re}\nabla^2 \boldsymbol{u}, && \text{(A.6c)}\\
\boldsymbol{\nabla} \cdot \boldsymbol{u} &= Da' \Delta T \rho Y \exp\left(\frac{-T_a}{T}\right) + \frac{1}{Pe}\nabla^2 T, && \text{(A.6d)}\\
1 &= \rho T. && \text{(A.6e)}
\end{aligned}$$

Even further simplification is possible when the chemical and thermal state of the fluid can be completely determined by a flame PVF. When this is true, the species equation in Equation A.6 becomes linearly dependent. The progress variable $\Theta \equiv (T-1)/\Delta T$ can then be defined such that Θ varies from zero in the reactants to one in the products, resulting in the identity that $Y + \Theta = 1$ everywhere. In this way, the T and Y dependence is reduced to a dependence on only the new progress variable Θ. Then Equation A.6 can be simplified by substituting $\rho \to 1/(1+\Delta T\Theta)$, $T \to 1 + \Delta T\Theta$, and $Y \to 1 - \Theta$, i.e.,

$$\begin{aligned}
\frac{1}{1+\Delta T\Theta}\left(\frac{\partial \Theta}{\partial t} + \boldsymbol{u} \cdot \boldsymbol{\nabla}\Theta\right) &= Da\left(\frac{1-\Theta}{1+\Delta T\Theta}\right)\exp\left(\frac{-T_a}{1+\Delta T\Theta}\right) + \frac{1}{Pe}\nabla^2\Theta, && \text{(A.7a)}\\
\frac{1}{1+\Delta T\Theta}\left(\frac{\partial \boldsymbol{u}}{\partial t} + \boldsymbol{u} \cdot \boldsymbol{\nabla}\boldsymbol{u}\right) &= -\boldsymbol{\nabla} p + \frac{1}{Re}\nabla^2 \boldsymbol{u}, && \text{(A.7b)}\\
\boldsymbol{\nabla} \cdot \boldsymbol{u} &= \frac{\Delta T}{1+\Delta T\Theta}\left(\frac{\partial \Theta}{\partial t} + \boldsymbol{u} \cdot \boldsymbol{\nabla}\Theta\right). && \text{(A.7c)}
\end{aligned}$$

Finally, the numerical properties of Equation A.7 can be improved by defining the Zeldovich number $Ze = T_a \Delta T/(1+\Delta T)^2$ and defining $Da = Da' \exp\left(-Ze(1+\Delta T)/\Delta T\right)$. This conveniently rescales the reaction rate term such that rounding errors due to finite-precision arithmetic do not significantly affect the solver at high Zeldovich numbers. Making these substitutions in Equation A.7, the final governing system of Equation 2.2 is derived.

It is also worthwhile to point out that in the specific case of $\Delta T = 0$, Equation A.7 is equivalent to Equation 2.1, plus a passive scalar equation for Θ, i.e.,

$$\frac{\partial \Theta}{\partial t} + \boldsymbol{u} \cdot \boldsymbol{\nabla} \Theta = Da\,(1-\Theta)\exp\left(-T_a(1-\Theta)\right) + \frac{1}{Pe}\nabla^2\Theta, \tag{A.8a}$$

$$\frac{\partial \boldsymbol{u}}{\partial t} + \boldsymbol{u} \cdot \boldsymbol{\nabla} \boldsymbol{u} = -\boldsymbol{\nabla} p + \frac{1}{Re}\nabla^2 \boldsymbol{u}, \tag{A.8b}$$

$$\boldsymbol{\nabla} \cdot \boldsymbol{u} = 0. \tag{A.8c}$$

APPENDIX B

MESH SENSITIVITY ANALYSIS

This appendix serves to assess the sensitivity of the presented results to the properties of the computational mesh. To achieve this, comparative non-reacting calculations were performed against the primary mesh M, shown in Figure B.1, using four test meshes A_0-A_3 listed in Table B.1. The properties of these test meshes were selected to separately assess specific details of the discretization chosen for the primary mesh. In particular, the meshes A_0 and A_1 are used to assess the sensitivity of the results to the position of the respective inlet and open boundaries, while A_2 and A_3 gauge the sensitivity of the results to refining and coarsening the mesh, respectively.

Bifurcation diagrams for $Re = 200$ with varying S were computed on each mesh to quantify the dependence of the results on the mesh properties. The curves are almost indistinguishable from each other due to their similarity. To illustrate, the critical S values associated with the bifurcation points are tabulated in Table B.1. This data indicates excellent agreement across the various meshes as most numerical values are identical down to at least three significant digits. Consequently, the results obtained on mesh M are considered to be well-converged.

It should be remarked that mesh M was chosen due to its robustness across a wide range of parameter conditions. In the convergence study, it was observed that the required domain size (i.e. the necessary value of R_∞) to avoid confinement effects increases with *Re*. The key physical process which limits the possible degree of domain truncation is the transition from a bubble-type vortex breakdown region to a wall jet, where the initially quasi-columnar jet fans open and exits the domain along the radial direction instead of along the axis. Increasing *Re* also results in a general steepening of flow gradients, which require finer discretizations to be resolved accurately.

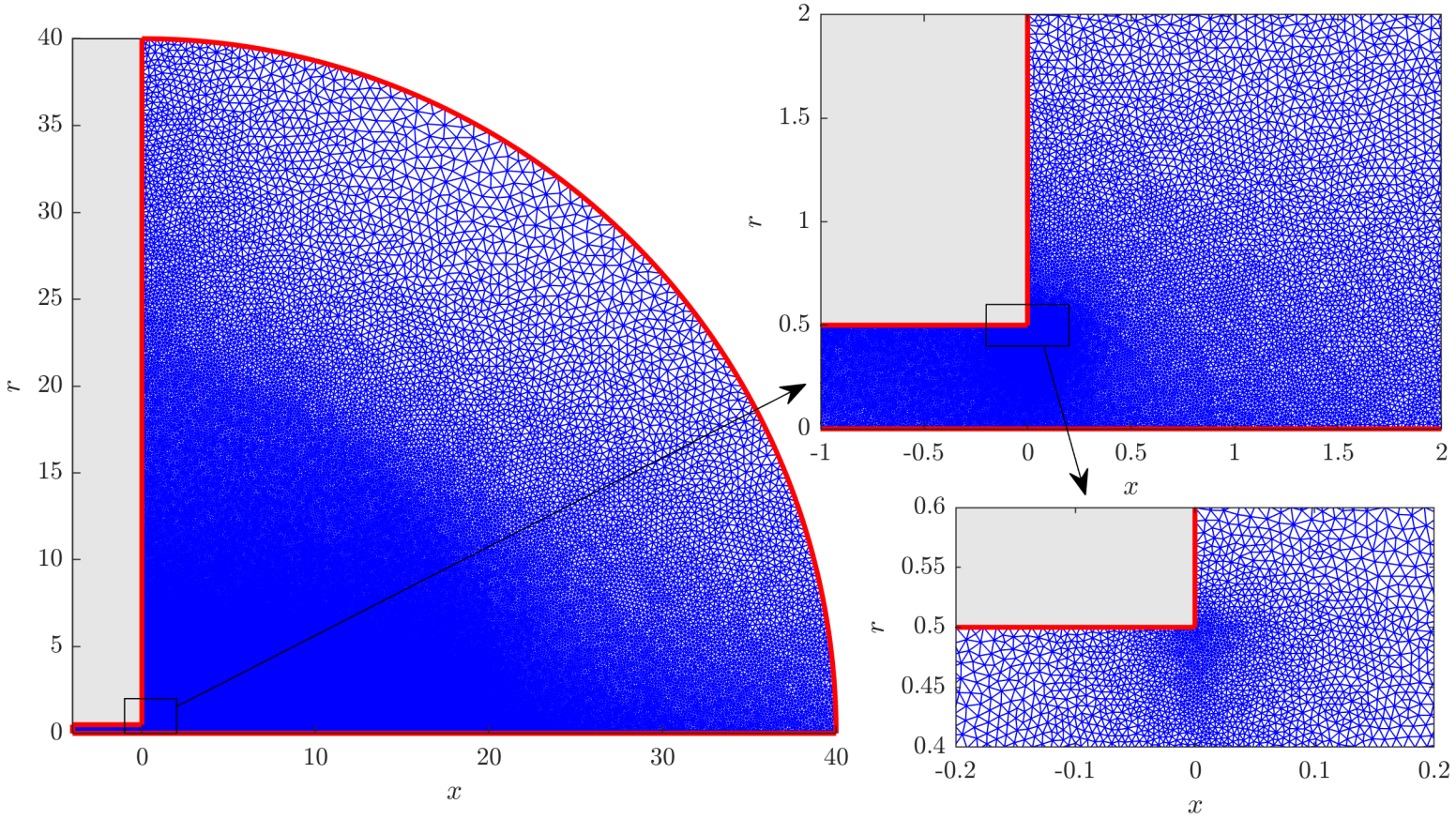

Figure B.1: Visualization at various detail levels of the primary computational mesh M used to obtain the numerical results presented in chapter 3 and chapter 4. The mesh properties are detailed in Table B.1.

Table B.1: Comparison of mesh properties and critical S values along the $Re = 200$ steady solution curves. Here, r_h is the mesh refinement factor relative to M based on edge vertex density, n_t is the total number of triangles, and DOF is the total number of discrete degrees of freedom. As indicated in section section 3.1, the saddle-node bifurcations at S_B and S_F are associated with axisymmetric modes, while the Hopf bifurcations at S_U and S_L are associated with $|m| = 2$ and $|m| = 1$ modes, respectively.

Mesh	ℓ	R_∞	r_h	n_t	DOF	S_B	S_F	S_U	S_L
M	4	40	–	140 055	915 839	2.0856	2.0182	1.3174	2.0540
A_0	6	40	1.0	151 854	993 481	2.0856	2.0182	1.3174	2.0540
A_1	4	60	1.0	179 845	1 175 463	2.0856	2.0190	1.3212	2.0541
A_2	4	40	1.5	312 875	2 041 894	2.0876	2.0197	1.3256	2.0552
A_3	4	40	0.8	90 396	591 972	2.0836	2.0166	1.3124	2.0528

APPENDIX C

LIST OF OPERATORS

This appendix lists the strong forms of the various operators used in chapter 2.

C.1 Non-reacting case

In the non-reacting case, the state vector is given by $\boldsymbol{q} = (\boldsymbol{u}, p, p_o)^{\mathrm{T}}$.

C.1.1 Mass Operator

$$\mathcal{M}(\boldsymbol{q}) = \begin{pmatrix} 1 & 0 & 0 \\ 0 & 0 & 0 \\ 0 & 0 & 0 \end{pmatrix} \tag{C.1}$$

C.1.2 Steady system operator

$$\mathcal{R}(\boldsymbol{q}) = \begin{pmatrix} \boldsymbol{u} \cdot \boldsymbol{\nabla} \boldsymbol{u} + \boldsymbol{\nabla} p - \dfrac{1}{Re} \nabla^2 \boldsymbol{u} \\ \boldsymbol{\nabla} \cdot \boldsymbol{u} \\ \boldsymbol{\nabla} p \cdot \boldsymbol{t} - \dfrac{u_\theta^2}{r} \end{pmatrix} \tag{C.2}$$

C.1.3 Jacobian operator

$$\mathcal{J}_m(\boldsymbol{q}_0) = \begin{pmatrix} \boldsymbol{u}_0 \cdot \boldsymbol{\nabla}_m(\bullet) + (\bullet) \cdot \boldsymbol{\nabla}_0 \boldsymbol{u}_0 - \dfrac{1}{Re} \nabla_m^2(\bullet) & \boldsymbol{\nabla}_m(\bullet) & 0 \\ \boldsymbol{\nabla}_m \cdot (\bullet) & 0 & 0 \\ -\dfrac{2u_{\theta,0}}{r}(\bullet) \cdot \boldsymbol{e}_\theta & 0 & \boldsymbol{\nabla}_m(\bullet) \cdot \boldsymbol{t} \end{pmatrix} \tag{C.3}$$

C.1.4 Hessian operator

$$\mathcal{H}_{m+n}\left(\hat{\boldsymbol{q}}_m\right) = \begin{pmatrix} \hat{\boldsymbol{u}}_m \cdot \boldsymbol{\nabla}_n(\bullet) + (\bullet) \cdot \boldsymbol{\nabla}_m \hat{\boldsymbol{u}}_m & 0 & 0 \\ 0 & 0 & 0 \\ -\dfrac{2\hat{u}_{\theta,m}}{r}(\bullet) \cdot \boldsymbol{e}_\theta & 0 & 0 \end{pmatrix}. \tag{C.4}$$

C.2 Laminar reacting case

In the laminar reacting case, the state vector is given by $\boldsymbol{q} = (\Theta, \boldsymbol{u}, p, p_o)^{\mathrm{T}}$.

C.2.1 Mass Operator

$$\mathcal{M}\left(\boldsymbol{q}\right) = \begin{pmatrix} \dfrac{1}{1+\Delta T\Theta} & 0 & 0 & 0 \\ 0 & \dfrac{1}{1+\Delta T\Theta} & 0 & 0 \\ -\dfrac{\Delta T}{1+\Delta T\Theta} & 0 & 0 & 0 \\ 0 & 0 & 0 & 0 \end{pmatrix} \tag{C.5}$$

C.2.2 Steady system operator

$$\mathcal{R}\left(\boldsymbol{q}\right) = \begin{pmatrix} \dfrac{\boldsymbol{u}\cdot\boldsymbol{\nabla}\Theta}{1+\Delta T\Theta} - Da\left(\dfrac{1-\Theta}{1+\Delta T\Theta}\right)\exp\left(\dfrac{-T_a}{1+\Delta T\Theta}\right) - \dfrac{1}{Pe}\nabla^2\Theta \\ \dfrac{\boldsymbol{u}\cdot\boldsymbol{\nabla}\boldsymbol{u}}{1+\Delta T\Theta} + \boldsymbol{\nabla}p - \dfrac{1}{Re}\nabla^2\boldsymbol{u} \\ \boldsymbol{\nabla}\cdot\boldsymbol{u} - \dfrac{\Delta T\left(\boldsymbol{u}\cdot\boldsymbol{\nabla}\Theta\right)}{1+\Delta T\Theta} \\ \boldsymbol{\nabla}p_o\cdot\boldsymbol{t} - \dfrac{1}{1+\Delta T\Theta}\left(\dfrac{u_\theta^2}{r}\right) \end{pmatrix} \tag{C.6}$$

C.2.3 Jacobian operator

$$\mathcal{J}_m\left(\boldsymbol{q}_0\right) = \begin{pmatrix} J_{11} & \dfrac{(\bullet)\cdot\boldsymbol{\nabla}_0\Theta_0}{1+\Delta T\Theta_0} & 0 & 0 \\ J_{21} & \dfrac{\boldsymbol{u}_0\cdot\boldsymbol{\nabla}_m(\bullet)+(\bullet)\cdot\boldsymbol{\nabla}_0\boldsymbol{u}_0}{1+\Delta T\Theta_0}-\dfrac{1}{Re}\nabla_m^2(\bullet) & \boldsymbol{\nabla}_m(\bullet) & 0 \\ J_{31} & \boldsymbol{\nabla}_m\cdot(\bullet)-\dfrac{\Delta T\left((\bullet)\cdot\boldsymbol{\nabla}_0\Theta_0\right)}{1+\Delta T\Theta_0} & 0 & 0 \\ J_{41} & -\dfrac{2u_{\theta,0}(\bullet)\cdot\boldsymbol{e}_\theta}{r\left(1+\Delta T\Theta_0\right)} & 0 & \boldsymbol{\nabla}_m(\bullet)\cdot\boldsymbol{t} \end{pmatrix}, \tag{C.7}$$

where

$$\begin{aligned} J_{11} &= \frac{1}{1+\Delta T\Theta_0}\left[\boldsymbol{u}_0\cdot\boldsymbol{\nabla}_m(\bullet)-\frac{\Delta T(\bullet)\left(\boldsymbol{u}_0\cdot\boldsymbol{\nabla}_0\Theta_0\right)}{1+\Delta T\Theta_0}\right]-\frac{1}{Pe}\nabla_m^2(\bullet) \\ &\quad -\frac{Da(\bullet)}{1+\Delta T\Theta_0}\left[\frac{\Delta T(1-\Theta_0)}{1+\Delta T\Theta_0}+\frac{T_a\Delta T(1-\Theta_0)}{\left(1+\Delta T\Theta_0\right)^2}-1\right]\exp\left(\frac{-T_a}{1+\Delta T\Theta_0}\right), \\ J_{21} &= -\frac{\Delta T(\bullet)\left(\boldsymbol{u}_0\cdot\boldsymbol{\nabla}_0\boldsymbol{u}_0\right)}{\left(1+\Delta T\Theta_0\right)^2}, \\ J_{31} &= \frac{\Delta T}{1+\Delta T\Theta_0}\left[\frac{\Delta T(\bullet)\left(\boldsymbol{u}_0\cdot\boldsymbol{\nabla}_0\Theta_0\right)}{1+\Delta T\Theta_0}-\boldsymbol{u}_0\cdot\boldsymbol{\nabla}_m(\bullet)\right], \\ J_{41} &= \frac{\Delta T(\bullet)}{\left(1+\Delta T\Theta_0\right)^2}\frac{u_{\theta,0}^2}{r}. \end{aligned}$$

C.2.4 Hessian operator

$$\mathcal{H}_{m+n}\left(\hat{\boldsymbol{q}}_m\right) = \begin{pmatrix} H_{11} & H_{12} & 0 & 0 \\ H_{21} & H_{22} & 0 & 0 \\ H_{31} & H_{32} & 0 & 0 \\ H_{41} & H_{42} & 0 & 0 \end{pmatrix}. \tag{C.8}$$

where

$$
\begin{aligned}
H_{11} &= -\frac{2\mathrm{i}\pi f\Delta T(\bullet)\hat{\Theta}}{(1+\Delta T\Theta_0)^2}+\frac{\Delta T(\bullet)\left(\boldsymbol{u}_0\cdot\boldsymbol{\nabla}_m\hat{\Theta}_m\right)}{(1+\Delta T\Theta_0)^2}-\frac{\Delta T\hat{\Theta}_m\left(\boldsymbol{u}_0\cdot\boldsymbol{\nabla}_n(\bullet)\right)}{(1+\Delta T\Theta_0)^2}\\
&\quad+\frac{2\Delta T^2(\bullet)\hat{\Theta}_m\left(\boldsymbol{u}_0\cdot\boldsymbol{\nabla}_0\Theta_0\right)}{(1+\Delta T\Theta_0)^3}+\frac{2DaT_a\Delta T\hat{\Theta}_m(\bullet)}{(1+\Delta T\Theta_0)^3}\exp\left(\frac{-T_a}{1+\Delta T\Theta_0}\right)\\
&\quad-\frac{DaT_a{}^2\Delta T^2(1-\Theta_0)\hat{\Theta}_m(\bullet)}{(1+\Delta T\Theta_0)^5}\exp\left(\frac{-T_a}{1+\Delta T\Theta_0}\right)\\
&\quad+\frac{2Da\Delta T^2\hat{\Theta}_m(\bullet)}{(1+\Delta T\Theta_0)^3}\left[1-\Theta_0+\frac{T_a(1-\Theta_0)}{1+\Delta T\Theta_0}\right]\exp\left(\frac{-T_a}{1+\Delta T\Theta_0}\right)\\
&\quad+\frac{\hat{\boldsymbol{u}}_m\cdot\boldsymbol{\nabla}_n(\bullet)}{1+\Delta T\Theta_0}-\frac{\Delta T(\bullet)\hat{\boldsymbol{u}}_m\cdot\boldsymbol{\nabla}_0\Theta_0}{(1+\Delta T\Theta_0)^2},\\
H_{12} &= \frac{(\bullet)\cdot\boldsymbol{\nabla}_m\hat{\Theta}_m}{1+\Delta T\Theta_0}-\frac{\Delta T\hat{\Theta}_m\left((\bullet)\cdot\boldsymbol{\nabla}_0\Theta_0\right)}{(1+\Delta T\Theta_0)^2},\\
H_{21} &= \frac{2\Delta T^2\hat{\Theta}_m(\bullet)\left(\boldsymbol{u}_0\cdot\boldsymbol{\nabla}_0\boldsymbol{u}_0\right)}{(1+\Delta T\Theta_0)^3}-\frac{\Delta T(\bullet)\left(\boldsymbol{u}_0\cdot\boldsymbol{\nabla}_m\hat{\boldsymbol{u}}_m+\hat{\boldsymbol{u}}_m\cdot\boldsymbol{\nabla}_0\boldsymbol{u}_0\right)}{(1+\Delta T\Theta_0)^2},\\
H_{22} &= -\frac{2\mathrm{i}\pi f\Delta T(\bullet)\hat{\boldsymbol{u}}_m}{(1+\Delta T\Theta_0)^2}+\frac{(\bullet)\cdot\boldsymbol{\nabla}_m\hat{\boldsymbol{u}}_m+\hat{\boldsymbol{u}}_m\cdot\boldsymbol{\nabla}_n(\bullet)}{1+\Delta T\Theta_0}\\
&\quad-\frac{\Delta T\hat{\Theta}_m\left((\bullet)\cdot\boldsymbol{\nabla}_0\boldsymbol{u}_0+\boldsymbol{u}_0\cdot\boldsymbol{\nabla}_n(\bullet)\right)}{(1+\Delta T\Theta_0)^2},\\
H_{31} &= \frac{2\mathrm{i}\pi f\Delta T^2(\bullet)\hat{\Theta}}{(1+\Delta T\Theta_0)^2}+\frac{\Delta T^2\hat{\Theta}_m\left(\boldsymbol{u}_0\cdot\boldsymbol{\nabla}_n(\bullet)\right)}{(1+\Delta T\Theta_0)^2}-\frac{2\Delta T^3\hat{\Theta}_m(\bullet)\left(\boldsymbol{u}_0\cdot\boldsymbol{\nabla}_0\Theta_0\right)}{(1+\Delta T\Theta_0)^3}\\
&\quad+\frac{\Delta T^2(\bullet)\left(\boldsymbol{u}_0\cdot\boldsymbol{\nabla}_m\hat{\Theta}_m+\hat{\boldsymbol{u}}_m\cdot\boldsymbol{\nabla}_0\Theta_0\right)}{(1+\Delta T\Theta_0)^2}-\frac{\Delta T\left(\hat{\boldsymbol{u}}_m\cdot\boldsymbol{\nabla}_n(\bullet)\right)}{1+\Delta T\Theta_0},\\
H_{32} &= \frac{\Delta T}{1+\Delta T\Theta_0}\left(\frac{\Delta T\hat{\Theta}_m\left((\bullet)\cdot\boldsymbol{\nabla}_0\Theta_0\right)}{1+\Delta T\Theta_0}-(\bullet)\cdot\boldsymbol{\nabla}_m\hat{\Theta}_m\right),\\
H_{41} &= \frac{2\Delta Tu_{\theta,0}}{r\left(1+\Delta T\Theta_0\right)^2}\left(\hat{u}_{\theta,m}(\bullet)-\frac{\Delta Tu_{\theta,0}\hat{\Theta}_m(\bullet)}{1+\Delta T\Theta_0}\right),\\
H_{42} &= \frac{2}{r\left(1+\Delta T\Theta_0\right)}\left(\frac{\Delta T\hat{\Theta}_m}{1+\Delta T\Theta_0}u_{\theta,0}(\bullet)\cdot\boldsymbol{e}_\theta-\hat{u}_{m,\theta}(\bullet)\right).
\end{aligned}
$$

C.3 Turbulent reacting case

C.3.1 Turbulent reacting case

In the case of the local stability analysis, p_o is not part of the formulation. Therefore, the state vector is given by $\boldsymbol{q} = (\rho, \boldsymbol{u}, p)^{\mathrm{T}}$.

C.3.2 Mass Operator

$$\mathcal{M}(\boldsymbol{q}) = \begin{pmatrix} 1 & 0 & 0 \\ 0 & \rho & 0 \\ 0 & 0 & 0 \end{pmatrix} \tag{C.9}$$

C.3.3 Jacobian operator

$$\mathcal{J}_m(\overline{\boldsymbol{q}}_0) = \begin{pmatrix} \boldsymbol{\nabla}_m \cdot ((\bullet)\overline{\boldsymbol{u}}_0) & \boldsymbol{\nabla}_m \cdot (\overline{\rho}_0(\bullet)) & 0 \\ (\bullet)\overline{\boldsymbol{u}}_0 \cdot \boldsymbol{\nabla}_0 \overline{\boldsymbol{u}}_0 & J_{22} & \boldsymbol{\nabla}_m(\bullet) \\ \dfrac{1}{\mathit{Pe}} \boldsymbol{\nabla}_m \cdot \left[\left(1 + \overline{\mathcal{D}}_{T,0}\right) \boldsymbol{\nabla}_m \left(\dfrac{(\bullet)}{\overline{\rho}_0^2} \right) \right] & \boldsymbol{\nabla}_m \cdot (\bullet) & 0 \end{pmatrix}, \tag{C.10}$$

where

$$J_{22} = \overline{\rho}\left((\bullet) \cdot \boldsymbol{\nabla}\overline{\boldsymbol{u}}_0 + \overline{\boldsymbol{u}}_0 \cdot \boldsymbol{\nabla}_m(\bullet)\right) - \frac{1}{\mathit{Re}} \boldsymbol{\nabla}_m \cdot \left(\left(1 + \overline{\mu}_{T,0}\right) \boldsymbol{\nabla}_m(\bullet) \right). \tag{C.11}$$

C.3.4 Local stability operators

The local stability operators are written for an almost parallel, axisymmetric mean flow where $\partial\overline{(\bullet)}/\partial x \approx \partial\overline{(\bullet)}/\partial\theta \approx 0$ and $\overline{u}_{r,0} \approx 0$. Here, it is convenient to expand the vector equations and write the system in cylindrical coordinates. Using the WKBJ ansatz (Equation 2.42), the local stability operators are,

$$\mathcal{A}_0 = \begin{pmatrix} \frac{\mathrm{i}m(\bullet)\overline{u}_{\theta,0}}{r} & 0 & \frac{1}{r}\frac{\mathrm{d}\left(r\overline{\rho}_0(\bullet)\right)}{\mathrm{d}r} & \frac{\mathrm{i}m\overline{\rho}_0(\bullet)}{r} & 0 \\ 0 & A_{0,22} & \overline{\rho}_0(\bullet)\frac{\mathrm{d}\overline{u}_{x,0}}{\mathrm{d}r} & 0 & 0 \\ -\frac{(\bullet)\overline{u}_{\theta,0}^2}{r} & 0 & A_{0,33} & A_{0,34} & \frac{\mathrm{d}(\bullet)}{\mathrm{d}r} \\ 0 & 0 & A_{0,43} & A_{0,33} & \frac{\mathrm{i}m(\bullet)}{r} \\ A_{0,51} & 0 & \frac{1}{r}\frac{\mathrm{d}\left(r(\bullet)\right)}{\mathrm{d}r} & \frac{\mathrm{i}m(\bullet)}{r} & 0 \end{pmatrix}, \tag{C.12}$$

$$\mathcal{A}_1 = \begin{pmatrix} \mathrm{i}(\bullet)\overline{u}_{x,0} & \mathrm{i}\overline{\rho}_0(\bullet) & 0 & 0 & 0 \\ 0 & \mathrm{i}\overline{\rho}_0\overline{u}_{x,0}(\bullet) & 0 & 0 & \mathrm{i}(\bullet) \\ 0 & 0 & \mathrm{i}\overline{\rho}_0\overline{u}_{x,0}(\bullet) & 0 & 0 \\ 0 & 0 & 0 & \mathrm{i}\overline{\rho}_0\overline{u}_{x,0}(\bullet) & 0 \\ 0 & \mathrm{i}(\bullet) & 0 & 0 & 0 \end{pmatrix}, \tag{C.13}$$

$$\mathcal{A}_2 = \begin{pmatrix} 0 & 0 & 0 & 0 & 0 \\ 0 & \frac{\left(1+\overline{\mu}_{T,0}\right)(\bullet)}{\boldsymbol{Re}} & 0 & 0 & 0 \\ 0 & 0 & \frac{\left(1+\overline{\mu}_{T,0}\right)(\bullet)}{\boldsymbol{Re}} & 0 & 0 \\ 0 & 0 & 0 & \frac{\left(1+\overline{\mu}_{T,0}\right)(\bullet)}{\boldsymbol{Re}} & 0 \\ -\frac{\left(1+\overline{\mathcal{D}}_{T,0}\right)(\bullet)}{\boldsymbol{Pe}\,\overline{\rho}_0^2} & 0 & 0 & 0 & 0 \end{pmatrix}, \tag{C.14}$$

where

$$\begin{aligned} A_{0,22} &= \frac{\mathrm{i}m\overline{\rho}_0\overline{u}_{\theta,0}(\bullet)}{r} - \frac{1}{\boldsymbol{Re}}\left[\frac{1}{r}\frac{\mathrm{d}}{\mathrm{d}r}\left(r\left(1+\overline{\mu}_{T,0}\right)\frac{\mathrm{d}(\bullet)}{\mathrm{d}r}\right) - \frac{m^2\left(1+\overline{\mu}_T\right)(\bullet)}{r^2}\right], \\ A_{0,33} &= \frac{\mathrm{i}m\overline{\rho}_0\overline{u}_{\theta,0}(\bullet)}{r} - \frac{1}{\boldsymbol{Re}}\left[\frac{1}{r}\frac{\mathrm{d}}{\mathrm{d}r}\left(r\left(1+\overline{\mu}_{T,0}\right)\frac{\mathrm{d}(\bullet)}{\mathrm{d}r}\right) - \frac{\left(1+m^2\right)\left(1+\overline{\mu}_T\right)(\bullet)}{r^2}\right], \\ A_{0,34} &= -\frac{2\overline{\rho}_0\overline{u}_{\theta,0}(\bullet)}{r} + \frac{1}{\boldsymbol{Re}}\frac{2\mathrm{i}m\left(1+\overline{\mu}_T\right)(\bullet)}{r^2}, \\ A_{0,43} &= \frac{\overline{\rho}_0\overline{u}_{\theta,0}(\bullet)}{r} + \overline{\rho}_0(\bullet)\frac{\mathrm{d}\overline{u}_{\theta,0}}{\mathrm{d}r} - \frac{1}{\boldsymbol{Re}}\frac{2\mathrm{i}m\left(1+\overline{\mu}_T\right)(\bullet)}{r^2}, \\ A_{0,51} &= \frac{1}{\boldsymbol{Pe}}\left[\frac{1}{r}\frac{\mathrm{d}}{\mathrm{d}r}\left(r\left(1+\overline{\mathcal{D}}_{T,0}\right)\frac{\mathrm{d}}{\mathrm{d}r}\left(\frac{(\bullet)}{\overline{\rho}_0^2}\right)\right) - \frac{m^2\left(1+\overline{\mathcal{D}}_{T,0}\right)(\bullet)}{r^2\,\overline{\rho}_0^2}\right]. \end{aligned}$$

REFERENCES

[1] S. Sivasegaram and J. H. Whitelaw, "Combustion in swirling flows: A review," *Combustion and Flame*, vol. 23, pp. 195–205, 1991.

[2] T. C. Lieuwen and V. Yang, *Combustion Instabilities In Gas Turbine Engines: Operational Experience, Fundamental Mechanisms, and Modeling*. American Institute of Aeronautics and Astronautics, 2006.

[3] Y. Huang and V. Yang, "Dynamics and stability of lean-premixed swirl-stabilized combustion," *Progress in Energy and Combustion Science*, vol. 35, pp. 293–364, 2009.

[4] T. C. Lieuwen, *Unsteady Combustor Physics*. Cambridge University Press, 2012.

[5] J. O'Connor, "Response of a swirl-stabilized flame to transverse acoustic excitation," Ph.D. dissertation, School of Aerospace Engineering, Georgia Institute of Technology, Dec. 2011.

[6] T. E. Smith, "Experimental investigation of transverse acoustic instabilities," Ph.D. dissertation, School of Aerospace Engineering, Georgia Institute of Technology, Dec. 2017.

[7] S. Leibovich, "Vortex stability and breakdown - survey and extension," *AIAA Journal*, vol. 22, no. 9, pp. 1192–1206, 1984.

[8] R. L. Ash and M. R. Khorrami, "Vortex stability," in *Fluid Vortices*. Dordrecht: Springer Netherlands, 1995, pp. 317–372, ISBN: 978-94-011-0249-0.

[9] N. C. Lambourne and D. W. Bryer, "The bursting of leading edge vortices – some observations and discussion of the phenomenon," Aeronautical Research Council, Tech. Rep. R & M No. 3282, 1962.

[10] L. Rayleigh, "On the dynamics of revolving fluids," *Proceedings of the Royal Society of London. Series A, Containing Papers of a Mathematical and Physical Character*, vol. 93, no. 648, pp. 148–154, 1917.

[11] J. L. Synge, "The stability of heterogeneous liquids," *Transactions of the Royal Society of Canada*, p. 18, 1933.

[12] L. N. Howard and A. S. Gupta, "On the hydrodynamic and hydromagnetic stability of swirling flows," *Journal of Fluid Mechanics*, vol. 14, no. 3, pp. 463–476, 1962.

[13] S. Leibovich and K. Stewartson, "A sufficient condition for the instability of columnar vortices," *Journal of Fluid Mechanics*, vol. 126, pp. 335–356, 1983.

[14] P. Billant and F. Gallaire, "A unified criterion for the centrifugal instabilities of vortices and swirling jets," *Journal of Fluid Mechanics*, vol. 734, pp. 5–35, 2013.

[15] L. R. S. R.S., "On the instability of cylindrical fluid surfaces," *The London, Edinburgh, and Dublin Philosophical Magazine and Journal of Science*, vol. 34, no. 207, pp. 177–180, 1892.

[16] G. K. Batchelor and A. E. Gill, "Analysis of the stability of axisymmetric jets," *Journal of Fluid Mechanics*, vol. 14, no. 4, pp. 529–551, 1962.

[17] F. Gallaire and J.-M. Chomaz, "Instability mechanisms in swirling flows," *Physics of Fluids*, vol. 15, no. 9, pp. 2622–2639, 2003.

[18] J. E. Martin and E. Meiburg, "On the stability of the swirling jet shear layer," *Physics of Fluids*, vol. 6, no. 1, pp. 424–426, 1994.

[19] L. Kelvin, "Vibrations of a columnar vortex," *The London, Edinburgh, and Dublin Philosophical Magazine and Journal of Science*, vol. 10, no. 61, pp. 155–168, 1880.

[20] H. Squire, "Analysis of the 'vortex breakdown' phenomenon: Part i," Imperial College of Science and Technology, Aeronautics Department, Tech. Rep. No. 102, 1960.

[21] T. B. Benjamin, "Theory of the vortex breakdown phenomenon," *Journal of Fluid Mechanics*, vol. 14, no. 4, pp. 593–629, 1962.

[22] S. Wang and Z. Rusak, "The dynamics of a swirling flow in a pipe and transition to axisymmetric vortex breakdown," *Journal of Fluid Mechanics*, vol. 340, pp. 177–223, 1997.

[23] S. Wang, Z. Rusak, R. Gong, and F. Liu, "On the three-dimensional stability of a solid-body rotation flow in a finite-length rotating pipe," *Journal of Fluid Mechanics*, vol. 797, pp. 284–321, 2016.

[24] N. A. Chigier and A. Chervinsky, "Experimental Investigation of Swirling Vortex Motion in Jets," *Journal of Applied Mechanics*, vol. 34, no. 2, pp. 443–451, Jun. 1967.

[25] J. K. Harvey, "Some observations of the vortex breakdown phenomenon," *Journal of Fluid Mechanics*, vol. 14, no. 4, pp. 585–592, 1962.

[26] T. Sarpkaya, "On stationary and travelling vortex breakdowns," *Journal of Fluid Mechanics*, vol. 45, no. 3, pp. 545–559, 1971.

[27] H. U. Vogel, "Experimentelle ergebnisse über die laminare strömung in einem zylindrischen gehäuse mit darin rotierender scheibe, bericht / max-planck-institut für strömungsforschung," Ph.D. dissertation, Zugl.: Göttingen, Univ., Dipl.-Arb., Göttingen, 1968.

[28] S. Farokhi, R. Taghavi, and E. J. Rice, "Effect of initial swirl distribution on the evolution of a turbulent jet," *AIAA Journal*, vol. 27, no. 6, pp. 700–706, 1989.

[29] J. Panda and D. K. McLaughlin, "Experiments on the instabilities of a swirling jet," *Physics of Fluids*, vol. 6, no. 1, pp. 263–276, 1994.

[30] J. E. Martin and E. Meiburg, "Nonlinear axisymmetric and three-dimensional vorticity dynamics in a swirling jet model," *Physics of Fluids*, vol. 8, no. 7, pp. 1917–1928, 1996.

[31] P. Billant, J.-M. Chomaz, and P. Huerre, "Experimental study of vortex breakdown in swirling jets," *Journal of Fluid Mechanics*, vol. 376, pp. 183–219, 1998.

[32] G. Ogus, M. Baelmans, and M. Vanierschot, "On the flow structures and hysteresis of laminar swirling jets," *Physics of Fluids*, vol. 28, no. 12, p. 123 604, 2016.

[33] P. Moise, "Bistability of bubble and conical forms of vortex breakdown in laminar swirling jets," *Journal of Fluid Mechanics*, vol. 889, A31, 2020.

[34] T. Loiseleux and J.-M. Chomaz, "Breaking of rotational symmetry in a swirling jet experiment," *Physics of Fluids*, vol. 15, no. 2, pp. 511–523, 2003.

[35] H. Liang and T. Maxworthy, "An experimental investigation of swirling jets," *Journal of Fluid Mechanics*, vol. 525, pp. 115–159, 2005.

[36] H. Liang and T. Maxworthy, "Experimental investigations of a swirling jet in both stationary and rotating surroundings," *Experiments in Fluids*, vol. 45, no. 2, pp. 283–293, 2008.

[37] F. Gallaire and J.-M. Chomaz, "Mode selection in swirling jet experiments: A linear stability analysis," *Journal of Fluid Mechanics*, vol. 494, pp. 223–253, 2003.

[38] F. Gallaire, S. Rott, and J.-M. Chomaz, "Experimental study of a free and forced swirling jet," *Physics of Fluids*, vol. 16, no. 8, pp. 2907–2917, 2004.

[39] M. R. Ruith, P. Chen, E. Meiburg, and T. Maxworthy, "Three-dimensional vortex breakdown in swirling jets and wakes: Direct numerical simulation," *Journal of Fluid Mechanics*, vol. 486, pp. 331–378, 2003.

[40] W. J. Grabowski and S. A. Berger, "Solutions of the navier-stokes equations for vortex breakdown," *Journal of Fluid Mechanics*, vol. 75, no. 3, pp. 525–544, 1976.

[41] E. Vyazmina, J. W. Nichols, J.-M. Chomaz, and P. J. Schmid, "The bifurcation structure of viscous steady axisymmetric vortex breakdown with open lateral boundaries," *Physics of Fluids*, vol. 21, no. 7, p. 074 107, 2009.

[42] P. Meliga, F. Gallaire, and J.-M. Chomaz, "A weakly nonlinear mechanism for mode selection in swirling jets," *Journal of Fluid Mechanics*, vol. 699, pp. 216–262, 2012.

[43] U. A. Qadri, D. Mistry, and M. P. Juniper, "Structural sensitivity of spiral vortex breakdown," *Journal of Fluid Mechanics*, vol. 720, pp. 558–581, 2013.

[44] S. Pasche, F. Avellan, and F. Gallaire, "Onset of chaos in helical vortex breakdown at low reynolds number," *Physical Review Fluids*, vol. 3, p. 064 701, 6 Jun. 2018.

[45] P. Moise and J. Mathew, "Bubble and conical forms of vortex breakdown in swirling jets," *Journal of Fluid Mechanics*, vol. 873, pp. 322–357, 2019.

[46] H. Gotoda, T. Ueda, and R. K. Cheng, "Dynamic motion of rotating bunsen flame tip in microgravity," *AIAA journal*, vol. 42, no. 7, pp. 1485–1489, 2004.

[47] Z. Rusak, A. K. Kapila, and J. J. Choi, "Effect of combustion on near-critical swirling flow," *Combustion Theory and Modeling*, vol. 6, no. 4, pp. 625–645, 2002.

[48] J. J. Choi, Z. Rusak, and A. K. Kapila, "Numerical simulation of premixed chemical reactions with swirl," *Combustion Theory and Modeling*, vol. 11, no. 6, pp. 863–887, 2007.

[49] C. O. U. Umeh, Z. Rusak, and E. Gutmark, "Vortex breakdown in a swirl-stabilized combustor," *Journal of Propulsion and Power*, vol. 28, no. 5, pp. 183–219, 2012.

[50] U. A. Qadri, "Global stability and control of swirling jets and flames," Ph.D. dissertation, University of Cambridge, 2014.

[51] S. T. Lee and J. S. T'ien, "A numerical analysis of flame flashback in a premixed laminar system," *Combustion and Flame*, vol. 48, pp. 273–285, 1982.

[52] S. Ishizuka, "Flame propagation along a vortex axis," *Progress in Energy and Combustion Science*, vol. 28, pp. 477–542, 2002.

[53] A. K. M. F. Hussain and W. C. Reynolds, "The mechanics of an organized wave in turbulent shear flow," *Journal of Fluid Mechanics*, vol. 41, no. 2, pp. 241–258, 1970.

[54] N. Syred, "A review of oscillation mechanisms and the role of the precessing vortex core (pvc) in swirl combustion systems," *Progress in Energy and Combustion Science*, vol. 32, pp. 93–161, 2006.

[55] F. Martinelli, A. Olivani, and A. Coghe, "Experimental analysis of the precessing vortex core in a free swirling jet," *Experiments in Fluids*, vol. 42, pp. 827–839, 2007.

[56] C. M. Coats, "Coherent structures in combustion," *Progress in Energy and Combustion Science*, vol. 22, pp. 427–509, 1996.

[57] A. Steinber, C. Arndt, and W. Meier, "Parametric study of vortex structures and their dynamics in swirl-stabilized combustion," *Proceedings of the Combustion Institute*, vol. 34, no. 2, pp. 3117–3125, 2013.

[58] K. Manoharan, M. Frederick, S. Clees, J. O'Connor, and S. Hemchandra, "A weakly nonlinear analysis of the precessing vortex core oscillation in a variable swirl turbulent round jet," *Journal of Fluid Mechanics*, vol. 884, A29, 2020.

[59] Y. Huang and V. Yang, "Effect of swirl on combustion dynamics in a lean-premixed swirl-stabilized combustor," *Proceedings of the Combustion Institute*, vol. 30, no. 2, pp. 1775–1782, 2005.

[60] M. Stöhr, I. Boxx, C. D. Carter, and W. Meier, "Experimental study of vortex-flame interaction in a gas turbine model combustor," *Combustion and Flame*, vol. 159, pp. 2636–2649, 2012.

[61] Q. An, W. Y. Kwong, B. D. Geraedts, and A. M. Steinberg, "Coupled dynamics of lift-off and precessing vortex core formation in swirl flames," *Combustion and Flame*, vol. 168, pp. 228–239, 2016.

[62] I. Boxx, M. Stöhr, C. Carter, and W. Meier, "Temporally resolved planar measurements of transient phenomena in a partially pre-mixed swirl flame in a gas turbine model combustor," *Combustion and Flame*, vol. 157, pp. 1510–1525, 2010.

[63] M. Kröner, T. Sattelmayer, J. Fritz, F. Kiesewetter, and C. Hirsch, "Flame propagation in swirling flows — effect of local extinction on the combustion induced vortex breakdown," *Combustion Science and Technology*, vol. 179, no. 7, pp. 1385–1416, 2007.

[64] I. Chterev, B. Emerson, and T. Lieuwen, "Velocity and stretch characteristics at the leading edge of an aerodynamically stabilized flame," *Combustion and Flame*, vol. 193, pp. 92–111, 2018.

[65] J. O'Connor, V. Acharya, and T. Lieuwen, "Transverse combustion instabilities: Acoustic, fluid mechanic, and flame processes," *Progress in Energy and Combustion Science*, vol. 49, pp. 1–39, 2015.

[66] B. Suri, J. Tithof, R. O. Grigoriev, and M. F. Schatz, "Forecasting fluid flows using the geometry of turbulence," *Physical Review Letters*, vol. 118, p. 114 501, 2017.

[67] S. B. Pope, "Small scales, many species and the manifold challenges of turbulent combustion," *Proceedings of the Combustion Institute*, vol. 34, pp. 1–31, 2013.

[68] G. Kawahara, M. Uhlmann, and L. van Veen, "The significance of simple invariant solutions in turbulent flows," *Annual Review of Fluid Mechanics*, vol. 44, no. 1, pp. 203–225, 2012.

[69] B. O. Koopman, "Hamiltonian systems and transformations in hilbert space," *Proceedings of the National Academy of Sciences*, vol. 17, no. 5, pp. 315–318, 1931.

[70] I. Mezić, "Analysis of fluid flows via spectral properties of the koopman operator," *Annual Review of Fluid Mechanics*, vol. 45, pp. 357–378, 2013.

[71] S. Bagheri, "Koopman-mode decomposition of the cylinder wake," *Journal of Fluid Mechanics*, vol. 726, pp. 596–623, 2013.

[72] I. Mezić, "Spectral properties of dynamical systems, model reduction and decompositions," *Nonlinear Dynamics*, vol. 41, pp. 309–325, 2005.

[73] C. W. Rowley, I. Mezić, S. Bagheri, P. Schlatter, and D. S. Henningson, "Spectral analysis of nonlinear flows," *Journal of Fluid Mechanics*, vol. 641, pp. 115–127, 2009.

[74] P. Huerre and P. A. Monkewitz, "Local and global instabilities in spatially developing flows," *Annual Review of Fluid Mechanics*, vol. 22, pp. 473–537, 1990.

[75] L. Rukes, C. O. Paschereit, and K. Oberleithner, "An assessment of turbulence models for linear hydrodynamic stability analysis of strongly swirling jets," *European Journal of Mechanics - B/Fluids*, vol. 59, pp. 205–218, 2016.

[76] K. Oberleithner, M. Sieber, C. N. Nayeri, C. O. Paschereit, C. Petz, H.-C. Hege, B. R. Noack, and I. Wygnanski, "Three-dimensional coherent structures in a swirling jet undergoing vortex breakdown: Stability analysis and empirical mode construction," *Journal of Fluid Mechanics*, vol. 679, pp. 383–414, 2011.

[77] O. Tammisola and M. P. Juniper, "Coherent structures in a swirl injector at re = 4800 by nonlinear simulations and linear global modes," *Journal of Fluid Mechanics*, vol. 792, pp. 620–657, 2016.

[78] K. Manoharan, T. Smith, B. Emerson, C. M. Douglas, T. Lieuwen, and S. Hemchandra, "Velocity field response of a forced swirl stabilized premixed flame," in *Proceedings of ASME Turbo Expo 2017: Turbomachinery Technical Conference and Exposition*, Charlotte, North Carolina, U.S.A., 2017.

[79] A. Mukherjee, N. Muthichur, C. More, S. Gupta, and S. Hemchandra, "The Role of the Centerbody Wake on the Precessing Vortex Core Dynamics of a Swirl Nozzle," *Journal of Engineering for Gas Turbines and Power*, vol. 143, no. 5, Mar. 2021, 051019.

[80] S. J. Shanbhogue, M. Seelhorst, and T. Lieuwen, "Vortex phase-jitter in acoustically excited bluff body flames," *International Journal of Spray and Combustion Dynamics*, vol. 1, no. 3, pp. 365–387, 2009.

[81] A. O. Nieckele, R. L. Thompson, and G. Mompean, "Anisotropic reynolds stress tensor representation in shear flows using dns and experimental data," *Journal of Turbulence*, vol. 17, no. 6, pp. 602–632, 2016.

[82] B. Ganapathisubramani, E. K. Longmire, I. Marusic, and S. Pothos, "Dual-plane piv technique to determine the complete velocity gradient tensor in a turbulent boundary layer," *Experiments in Fluids*, vol. 39, no. 2, pp. 222–231, Aug. 2005.

[83] J. A. Mullin and W. J. A. Dahm, "Dual-plane stereo particle image velocimetry measurements of velocity gradient tensor fields in turbulent shear flow. ii. experimental results," *Physics of Fluids*, vol. 18, no. 3, p. 035 102, 2006.

[84] B. Coriton, A. M. Steinberg, and J. H. Frank, "High-speed tomographic piv and oh plif measurements in turbulent reactive flows," *Experiments in Fluids*, vol. 55, no. 6, p. 1743, Jun. 2014.

[85] C. W. Foley, I. Chterev, J. Seitzman, and T. Lieuwen, "High resolution particle image velocimetry and ch-plif measurements and analysis of a shear layer stabilized flame," *Journal of Engineering for Gas Turbines and Power*, vol. 138, no. 3, p. 031 603, 2016.

[86] Q. Zhang, S. J. Shanbhogue, Shreekrishna, T. Lieuwen, and J. O'Connor, "Strain characteristics near the flame attachment point in a swirling flow," *Combustion Science and Technology*, vol. 183, no. 7, pp. 665–685, 2011.

[87] S. Chaudhuri, S. Kostka, M. W. Renfro, and B. M. Cetegen, "Blowoff dynamics of bluff body stabilized turbulent premixed flames," *Combustion and Flame*, vol. 157, no. 4, pp. 790–802, 2010.

[88] T. Poinsot and D. Veynante, *Theoretical and Numerical Combustion*, 3rd ed. 2011.

[89] Z. Rusak, J. Choi, N. Bourquard, and S. Wang, "Vortex breakdown in premixed reacting flows with swirl in a finite-length circular open pipe," *Journal of Fluid Mechanics*, vol. 793, pp. 749–776, 2016.

[90] F. Williams, *Combustion Theory: The Fundamental Theory of Chemically Reacting Flow Systems*, 2nd ed. CRC Press, 1985.

[91] Z. Rusak, "The interaction of near-critical swirling flows in a pipe with inlet azimuthal vorticity perturbations," *Physics of Fluids*, vol. 10, no. 7, pp. 1672–1684, 1998.

[92] J. Boyd, *Chebyshev and Fourier Spectral Methods: Second Revised Edition*, ser. Dover Books on Mathematics. Dover Publications, 2013, ISBN: 9780486141923.

[93] M. Ruith, P. Chen, and E. Meiburg, "Development of boundary conditions for direct numerical simulations of three-dimensional vortex breakdown phenomena in semi-infinite domains," *Computers and Fluids*, vol. 33, no. 9, pp. 1225–1250, 2004.

[94] C.-H. Bruneau and P. Fabrie, "Effective downstream boundary conditions for incompressible navier–stokes equations," *International Journal for Numerical Methods in Fluids*, vol. 19, no. 8, pp. 693–705, 1994.

[95] M. Braack and P. Mucha, "Directional do-nothing condition for the navier-stokes equations," *Journal of Computational Mathematics*, vol. 32, pp. 507–521, 2014.

[96] C. Bertoglio, A. Caiazzo, Y. Bazilevs, M. Braack, M. Esmaily, V. Gravemeier, A. L. Marsden, O. Pironneau, I. E. Vignon-Clementel, and W. A. Wall, "Benchmark problems for numerical treatment of backflow at open boundaries," *International Journal for Numerical Methods in Biomedical Engineering*, vol. 34, no. 2, e2918, 2018, e2918 cnm.2918.

[97] P. Meliga and F. Gallaire, "Control of axisymmetric vortex breakdown in a constricted pipe: Nonlinear steady states and weakly nonlinear asymptotic expansions," *Physics of Fluids*, vol. 23, no. 8, p. 084 102, 2011.

[98] C. Geuzaine and J.-F. Remacle, "Gmsh: A 3-d finite element mesh generator with built-in pre- and post-processing facilities," *International Journal for Numerical Methods in Engineering*, vol. 79, no. 11, pp. 1309–1331, 2009.

[99] F. Hecht, "New development in freefem++," *J. Numer. Math.*, vol. 20, no. 3-4, pp. 251–265, 2012.

[100] J. Moulin, P. Jolivet, and O. Marquet, "Augmented lagrangian preconditioner for large-scale hydrodynamic stability analysis," *Computer Methods in Applied Mechanics and Engineering*, vol. 351, pp. 718–743, 2019.

[101] S. Balay, S. Abhyankar, M. F. Adams, J. B. P. Brune, K. Buschelman, L. Dalcin, A. Dener, V. E. W. D. Gropp, D. Kaushik, M. G. Knepley, D. A. M. L. C. McInnes, R. T. Mills, T. Munson, K. R. P. Sanan, B. F. Smith, S. Zampini, H. Zhang, and H. Zhang, "PETSc users manual," Argonne National Laboratory, Tech. Rep. ANL-95/11 - Revision 3.13, 2020.

[102] P. Amestoy, I. S. Duff, J. Koster, and J.-Y. L'Excellent, "A fully asynchronous multifrontal solver using distributed dynamic scheduling," *SIAM Journal on Matrix Analysis and Applications*, vol. 23, no. 1, pp. 15–41, 2001.

[103] H. B. Keller, "Global homotopies and newton methods," in *Recent Advances in Numerical Analysis*, C. DE BOOR and G. H. GOLUB, Eds., Academic Press, 1978, pp. 73–94, ISBN: 978-0-12-208360-0.

[104] E. L. Allgower and K. Georg, "Steplength adaptations for the predictor," in *Numerical Continuation Methods: An Introduction*. Berlin, Heidelberg: Springer Berlin Heidelberg, 1990, pp. 44–60, ISBN: 978-3-642-61257-2.

[105] V. Hernandez, J. E. Roman, and V. Vidal, "SLEPc: A scalable and flexible toolkit for the solution of eigenvalue problems," *ACM Trans. Math. Software*, vol. 31, no. 3, pp. 351–362, 2005.

[106] L. N. Trefethen, A. E. Trefethen, S. C. Reddy, and T. A. Driscoll, "Hydrodynamic stability without eigenvalues," *Science*, vol. 261, no. 5121, pp. 578–584, 1993.

[107] P. J. Schmid, "Nonmodal stability theory," *Annual Review of Fluid Mechanics*, vol. 39, no. 1, pp. 129–162, 2007.

[108] D. Montagnani and F. Auteri, "Non-modal analysis of coaxial jets," *Journal of Fluid Mechanics*, vol. 872, pp. 665–696, 2019.

[109] A. G. Salinger, N. M. Bou-Rabee, R. Pawlowsky, E. D. Wilkes, E. A. Burroughs, R. B. Lehoucq, and L. A. Romero, "Loca 1.1: Library of continuation algorithms: Theory and implementation manual," Sandia National Laboratories, Tech. Rep., 2002.

[110] K. C. Hall, K. Ekici, J. P. Thomas, and E. H. Dowell, "Harmonic balance methods applied to computational fluid dynamics problems," *International Journal of Computational Fluid Dynamics*, vol. 27, no. 2, pp. 52–67, 2013.

[111] Y. A. Kuznetsov, *Elements of Applied Bifurcation Theory (2nd Ed.)* Berlin, Heidelberg: Springer-Verlag, 1998, ISBN: 0387983821.

[112] Y. Saad and M. H. Schultz, "Gmres: A generalized minimal residual algorithm for solving nonsymmetric linear systems," *SIAM Journal on Scientific and Statistical Computing*, vol. 7, no. 3, pp. 856–869, 1986.

[113] T. E. Smith, C. M. Douglas, B. L. Emerson, and T. C. Lieuwen, "Axial evolution of forced helical flame and flow disturbances," *Journal of Fluid Mechanics*, vol. 844, pp. 323–356, 2018.

[114] T. E. Smith, I. P. Chterev, B. L. Emerson, D. R. Noble, and T. C. Lieuwen, "Comparison of single- and multinozzle reacting swirl flow dynamics," *Journal of Propulsion and Power*, vol. 34, no. 2, pp. 384–394, 2018.

[115] J. O'Connor and T. Lieuwen, "Disturbance field characteristics of a transversely excited burner," *Combustion Science and Technology*, vol. 183, no. 5, pp. 427–443, 2011.

[116] A. K. M. F. Hussain and W. C. Reynolds, "The mechanics of an organized wave in turbulent shear flow. part 2. experimental results," *Journal of Fluid Mechanics*, vol. 54, no. 2, pp. 241–261, 1972.

[117] W. C. Reynolds and A. K. M. F. Hussain, "The mechanics of an organized wave in turbulent shear flow. part 3. theoretical models and comparisons with experiments," *Journal of Fluid Mechanics*, vol. 54, no. 2, pp. 263–288, 1972.

[118] J.-M. Chomaz, P. Huerre, and L. G. Redekopp, "A frequency selection criterion in spatially developing flows," *Studies in Applied Mathematics*, vol. 84, no. 2, pp. 119–144, 1991.

[119] M. P. Juniper and B. Pier, "The structural sensitivity of open shear flows calculated with a local stability analysis," *European Journal of Mechanics - B/Fluids*, vol. 49, pp. 426–437, 2015, Trends in Hydrodynamic Instability in honour of Patrick Huerre's 65th birthday.

[120] P. G. Drazin and W. H. Reid, *Hydrodynamic Stability*, 2nd ed., ser. Cambridge Mathematical Library. Cambridge University Press, 2004.

[121] P. Schmid and D. Henningson, *Stability and Transition in Shear Flows*, ser. Applied Mathematical Sciences. Springer New York, 2012, ISBN: 9781461301851.

[122] M. R. Khorrami, M. R. Malik, and R. L. Ash, "Application of spectral collocation techniques to the stability of swirling flows," *Journal of Computational Physics*, vol. 81, no. 1, pp. 206–229, 1989.

[123] L. Parras and R. Fernandez-Feria, "Spatial stability and the onset of absolute instability of batchelor's vortex for high swirl numbers," *Journal of Fluid Mechanics*, vol. 583, pp. 27–43, 2007.

[124] M. R. Khorrami, "A chebyshev spectral collocation method using a staggered grid for the stability of cylindrical flows," *International Journal for Numerical Methods in Fluids*, vol. 12, no. 9, pp. 825–833, 1991.

[125] D. Fabre and L. Jacquin, "Viscous instabilities in trailing vortices at large swirl numbers," *Journal of Fluid Mechanics*, vol. 500, pp. 239–262, 2004.

[126] R. J. Deissler, "The convective nature of instability in plane poiseuille flow," *The Physics of Fluids*, vol. 30, no. 8, pp. 2303–2305, 1987.

[127] C. M. Douglas, B. L. Emerson, and T. C. Lieuwen, "Nonlinear dynamics of fully-developed swirling jets," *Journal of Fluid Mechanics*, 2021.

[128] J. M. Lopez, "On the bifurcation structure of axisymmetric vortex breakdown in a constricted pipe," *Physics of Fluids*, vol. 6, no. 11, pp. 3683–3693, 1994.

[129] A. Michalke, "Survey on jet instability theory," *Progress in Aerospace Sciences*, vol. 21, pp. 159–199, 1984.

[130] D. Sipp and A. Lebedev, "Global stability of base and mean flows: A general approach and its applications to cylinder and open cavity flows," *Journal of Fluid Mechanics*, vol. 593, pp. 333–358, 2007.

[131] D. Barkley, L. S. Tuckerman, and M. Golubitsky, "Bifurcation theory for three-dimensional flow in the wake of a circular cylinder," *Phys. Rev. E*, vol. 61, pp. 5247–5252, 5 May 2000.

[132] Barkley, D., "Linear analysis of the cylinder wake mean flow," *Europhys. Lett.*, vol. 75, no. 5, pp. 750–756, 2006.

[133] H. Gotoda, K. Maeda, T. Ueda, and R. K. Cheng, "Periodic motion of a bunsen flame tip with burner rotation," *Combustion and Flame*, vol. 134, no. 1, pp. 67–79, 2003.

[134] K. Seshadri and J. Göttgens, "Structure of the oxidation layer for stoichiometric and lean methane-air flames," in *Reduced Kinetic Mechanisms and Asymptotic Approximations for Methane-Air Flames*. Springer-Verlag Berlin, 1991, pp. 111–136.

[135] S. Roy, T. Yi, N. Jiang, G. H. Gunaratne, I. Chterev, B. Emerson, T. Lieuwen, A. W. Caswell, and J. R. Gord, "Dynamics of robust structures in turbulent swirling reacting flows," *Journal of Fluid Mechanics*, vol. 816, pp. 554–585, 2017.

[136] A. Lacarelle, T. Faustmann, D. Greenblatt, C. O. Paschereit, O. Lehmann, D. M. Luchtenburg, and B. R. Noack, "Spatiotemporal characterization of a conical swirler flow field under strong forcing," *Journal of Engineering for Gas Turbines and Power*, vol. 131, no. 3, p. 031 504, 2009.

[137] B. Emerson, J. O'Connor, M. Juniper, and T. Lieuwen, "Density ratio effects on reacting bluff-body flow field characteristics," *Journal of Fluid Mechanics*, vol. 706, pp. 219–250, 2012.

[138] S. Hemchandra, S. Shanbhogue, S. Hong, and A. F. Ghoniem, "Role of hydrodynamic shear layer stability in driving combustion instability in a premixed propane-air backward-facing step combustor," *Phys. Rev. Fluids*, vol. 3, p. 063 201, 6 Jun. 2018.

[139] K. Manoharan, S. Hansford, J. O'Connor, and S. Hemchandra, "Instability mechanism in a swirl flow combustor: Precession of vortex core and influence of density gradient," in *Turbo Expo: Power for Land, Sea, and Air*, Montreal, Canada, 2015.

[140] C. Douglas, T. Smith, B. L. Emerson, K. Manoharan, S. Hemchandra, and T. C. Lieuwen, "Hydrodynamic receptivity predictions and measurements of an acoustically forced multi-nozzle swirl combustor," in *Proceedings of 2018 AIAA Aerospace Sciences Meeting: AIAA SciTech Forum*, Orlando, Florida, U.S.A., 2018.

[141] G. Sivashinsky and V. Yakhot, "Negative viscosity effect in large-scale flows," *The Physics of Fluids*, vol. 28, no. 4, pp. 1040–1042, 1985.

[142] G. I. Sivashinsky and A. L. Frenkel, "On negative eddy viscosity under conditions of isotropy," *Physics of Fluids A: Fluid Dynamics*, vol. 4, no. 8, pp. 1608–1610, 1992.

[143] C. J. HEATON, "Optimal growth of the batchelor vortex viscous modes," *Journal of Fluid Mechanics*, vol. 592, pp. 495–505, 2007.

[144] C. J. HEATON and N. PEAKE, "Transient growth in vortices with axial flow," *Journal of Fluid Mechanics*, vol. 587, pp. 271–301, 2007.

[145] J. Blimbaum, M. Zanchetta, T. Akin, V. Acharya, J. O'Connor, D. R. Noble, and T. Lieuwen, "Transverse to longitudinal acoustic coupling processes in annular combustion chambers," *International Journal of Spray and Combustion Dynamics*, vol. 4, no. 4, pp. 275–297, 2012.

[146] C. Douglas, J. Lim, T. Smith, B. Emerson, T. Lieuwen, N. Jiang, C. Fugger, T. Yi, J. Felver, S. Roy, *et al.*, "Measurements of periodic reynolds stress oscillations in a forced turbulent premixed swirling flame," *Journal of Engineering for Gas Turbines and Power*, vol. 141, no. 1, 2019.

[147] M. Mendez, M. Raiola, A. Masullo, S. Discetti, A. Ianiro, R. Theunissen, and J.-M. Buchlin, "Pod-based background removal for particle image velocimetry," *Experimental Thermal and Fluid Science*, vol. 80, pp. 181–192, 2017.

[148] M. Kröner, J. Fritz, and T. Sattelmayer, "Flashback limits for combustion induced vortex breakdown in a swirl burner," *Journal of Engineering for Gas Turbines and Power*, vol. 125, no. 3, pp. 693–700, 2003.

[149] K. Hanjalić and B. E. Launder, "A reynolds stress model of turbulence and its application to thin shear flows," *Journal of Fluid Mechanics*, vol. 52, no. 4, pp. 609–638, 1972.

[150] K. Hanjalić and B. Launder, *Modelling Turbulence in Engineering and the Environment: Second-Moment Routes to Closure*. Cambridge University Press, 2011.

[151] V. S. Acharya, D.-H. Shin, and T. Lieuwen, "Premixed flames excited by helical disturbances: Flame wrinkling and heat release oscillations," *Journal of Propulsion and Power*, vol. 29, no. 6, pp. 1282–1291, 2013.

[152] S. Hemchandra and T. Lieuwen, "Local consumption speed of turbulent premixed flames – an analysis of 'memory effects'," *Combustion and Flame*, vol. 157, no. 5, pp. 955–965, 2010.

[153] R. Govindarajan and K. C. Sahu, "Instabilities in viscosity-stratified flow," *Annual Review of Fluid Mechanics*, vol. 46, no. 1, pp. 331–353, 2014.